MULTIAXIAL CREEP OF ISOTROPIC AND ANISOTROPIC MATERIALS

By

ASHOK LAHANUJI RAMTEKE

A thesis submitted for the degree of
Doctor of Philosophy
of the
University of London
and for the
Diploma of Imperial College

September 1987

Department of Mechanical Engineering
Imperial College of Science & Technology
London SW7 2BX

ABSTRACT

The equations for effective stress and strain in an anisotropic material have been obtained assuming the material to be stiffer in the radial direction than the axial direction. A finite element program to calculate the steady-state stress distributions in axisymmetric bodies has been adapted to accommodate the anisotropy. A anisotropic thick-walled cylinder subjected to an internal pressure has been analysed and a good agreement between the analytical and numerical solution has been found, and the program for isotropic analysis has been modified to improve the rate of convergence. Solutions have been obtained for a range of circumferentially notched bar geometries for different values of creep index, n, using the finite element programs for isotropic and anisotropic materials. A good skeletal point has been observed for all the cases in both of the analyses. The difference between the isotropic and anisotropic analyses has been pointed out. It has been found that the stresses across the notch throat in isotropic materials redistribute faster than those in anisotropic materials.

Creep data have been obtained for plain and notched bars of 304-H stainless steel at 760±2 ^{0}C and for plain and notched bars of DS Mar M002 at 900 ±4 ^{0}C. Creep data for 2-1/4 Cr Mo steel have been obtained from the literature. These data are then used to characterize the overall behaviour of the material under multiaxial stress conditions using different theoretical models. Constant load curves have been predicted from the constant stress curves. Good agreement has been found between the predicted and experimental constant load curve in the case of DS material, but in the case of 2-1/4 Cr Mo steel the predicted curve underestimated the experimental curve.

A metallographic analysis has been carried out on the selected notched bar geometries of 304-H stainless steel , 2-1//4 Cr Mo steel and DS Mar M002. A major difference between the failure behaviour of 304-H stainless steel and 2-1/4 Cr Mo steel has been pointed out. A failure pattern in DS Mar M002 under multiaxial stress conditions has been studied. It has been found that the failure in DS Mar M002 material

occurs at an angle to the solidification direction away from the notch root plane where the maximum effective stress exists.

ACKNOWLEDGEMENT

No words can express my deep sense of gratitude for my supervisors Dr. G. A. Webster, Dr. R. T. Fenner and Dr. B. F. Dyson for three years of patience, invaluable guidance, continuous encouragement, honest criticism and help. Working with them was a wonderful experience since it was characterized by innumerable, regular and detailed discussions through which they constantly corrected me and improved my confidence.

I also gratefully thank Mr. M. S. Loveday for helping me to overcome different problems in the experimental work at NPL.

I thank Mr. Nick Taylor and Mr. D. K. Willis for their assistance in the experimental work and Miss. Edna Archer for providing the best facilities in the library.

CONTENTS

Description	Page No
Title Page	1
Abstract	2
Acknowledgement	4
Contents	5
List of Figures	9
List of Tables	15
Nomenclature	16
Introduction	19
Chapter-1 : General Theory of Creep	22
1. Introduction	22
1.1 Uniaxial creep deformation and failure	22
1.1.1 Hoff's theory of ductile fracture	23
1.1.2 Robinson's cumulative damage rule	24
1.2 Multiaxial state of stress	25
1.2.1 Creep under multiaxial state of stress	27
1.3 Creep deformation mechanisms	28
1.4 Creep fracture mechanisms	30
1.4.1 Nucleation of cavities	30
1.4.2 Growth of cavities	32
1.4.3 Coalescence of cavities and final fracture	34
1.5 Necking of a tensile bar under creep test	35
1.6 Creep fracture under multiaxial state of stress	36
1.7 Continuum damage mechanism to creep failure	37
1.7.1 Kachanov and Robotnov continuum damage theory	37
1.7.2 Continuum damage analysis under multiaxial state of stress	38
1.7.3 Comparison between Ashby's void growth theory and the continuum theory of creep damage	40

1.8 Conclusions 44

Chapter-2 : Creep Resistant Alloys 52

2. Introduction 52

2.1 Isotropic alloys 52

2.2 Experimental methods for multiaxial creep tests 53

2.2.1 Theoretical prediction of notch rupture strength 54

2.3 Stress distribution of circumferentially notched bars 56

2.4 Directionally solidified alloys 58

2.5 Strengthening mechanisms in superalloys 59

2.6 Mechanical behaviour of superalloys 61

2.7 Friction stress in superalloys 63

2.8 Fracture of superalloys 66

2.9 Multiaxial state stress in superalloys 67

2.10 Conclusions 68

Chapter-3 : Creep Stress Analysis 75

3. Isotropic alloys 75

3.1 Non-linear finite element analysis (isotropic) 76

3.2 Anisotropy of materials 77

3.3 Present anisotropic effective stress and strain equations 77

3.4 Finite element analysis 83

3.4.1 The finite element formulation for linear elasticity 83

3.5 Treatment of non-linear problems 86

3.6 Comparison with an analytical solution 88

3.7 Conclusions 91

Chapter-4 : Specimens and Equipment 96

4. Introduction 96

4.1 Creep testing at Imperial College 96

4.1.1 Constant load creep machines 96

4.1.2 Experimental procedure 97

4.1.3 Cold loading 97

4.1.4 Hot loading 97

4.2 Creep testing at NPL 98

4.2.1 Constant load creep machines at NPL 98

4.2.2 Constant stress creep machines at NPL 98

4.2.3 Diametral strain measurement 99

4.3 Specimen geometries and manufacture 100

4.3.1 Specimen manufacture 100

Chapter-5 : Experimental Results and Analysis For Isotropic Materials 107

5. Introduction 107

5.1 Experimental results (Isotropic) 107

5.1.1 Uniaxial constant load creep tests 107

5.1.2 Uniaxial constant stress creep tests 108

5.1.2.1 Prediction of constant load creep curve from constant stress creep curve (Time Hardening) 108

5.1.2.2 Prediction of constant load creep curve from constant stress creep curve (Strain Hardening) 109

5.1.3 Multiaxial constant load creep tests 110

5.2 Data analysis 111

5.3 Numerical Analysis (Isotropic) 112

5.4 Mesh generation 113

5.5 Stress variation across a notch throat 113

5.6 Comparison of numerical and experimental deformation rate 115

5.7 Metallographic analysis 116

5.7.1 Quantitative metallography of 304-H stainless steel 117

5.8 Discussion 118

5.8.1 Discussion of experimental results 118

5.8.2 Discussion of numerical results 119

5.8.3 Discussion of metallographic analysis 121

5.9 Conclusions 122

Chapter-6 : Results and Analysis of DS MAR M002 Experiments 157

6. Introduction 157

6.1 Experimental results DS Mar M002 157

6.1.1 Uniaxial constant load creep tests 157

6.1.2 Uniaxial constant stress creep tests 158

6.1.3 Multiaxial constant load creep tests 159

6.1.4 Diametral strain measurement on notched bars 159

6.2 Numerical analysis 159

6.2.1 Stress variation across a notch throat 160

6.3 Comparison of isotropic and anisotropic stresses across a notch throat 161

6.4 Metallographic analysis 162

6.5 Results and Discussion 163

6.5.1 Discussion of experimental results 163

6.5.2 Discussion of numerical results 166

6.5.3 Discussion of metallographic analysis 168

6.6 Conclusions 169

Chapter-7

7.1 Conclusions 218

7.2 Recommendations for future work 219

References 221

Appendix-A 229

Appendix-B 234

Appendix-C 236

Appendix-D 238

LIST OF FIGURES

		Page No.
Figure - 1.1	: Standard creep curve	45
Figure - 1.2	: State of stress at a point	45
Figure - 1.3	: Stress components in cartesian and cylindrical coordinates	46
Figure - 1.4	: Stress space associated with principal stress coordinates	46
Figure - 1.5	: Relationship between steady state creep rate and applied stress	47
Figure - 1.6	: Models of intergranular cavity nucleation	47
Figure - 1.7	: Voids growing on grain boundaries in a polycrystal subjected to local stresses σ_1 , σ_3	48
Figure - 1.8	: The three simple mechanisms which control void growth	48
Figure - 1.9	: Void growth : (a) coupled boundary diffusion and power-law creep ; (b) coupled surface diffusion and power-law creep ; (c) coupled surface diffusion and boundary diffusion	49
Figure - 1.10	: Examples of cavity coalescence in plasticine and copper	50
Figure - 1.11	: Bridgman stress and strain distribution	50
Figure - 1.12	: Schematic illustration of a macroscopic crack initiation concept	51
Figure - 2.1	: Comparision on minimum strain rate for different structures	72
Figure - 2.2	: Variation of minimum creep rate with stress for different angle of fibre orientation	73
Figure - 2.3	: Variation of rupture time with stress for different angle of fibre orientation	73
Figure - 2.4	: Nucleation of voids and coalescence in conventionally cast IN738LC	74
Figure - 2.5	: Example of a crack initiation at carbides and growth through the grains in directionally solidified In738LC	74

Figure - 3.1	: Triangular finite element in a two- dimentional solution domain	92
Figure - 3.2a	: Simple finite element mesh for thick-walled cylinder problem : $R_2 = 2 R_1$	93
Figure - 3.2b	: Comparision of numerical and analytical stress distribution across a thick-walled cylinder	93
Figure - 3.3a	: Finite element mesh for a long Cylinder closed end problem	94
Figure - 3.3b	: Comparision of stresses in plane strain and closed end problem	94
Figure - 3.4	: Comparision of isotropic and anisotropic effective stress distribution across a thick-walled cylinder	95
Figure - 4.1	: Uniaxial creep testing machine at Imperial College	102
Figure - 4.2	: Uniaxial Constant stress and Constant load creep testind machine at NPL	103
Figure - 4.3	: Arrangement for the diametral strain measurement at NPL	104
Figure - 4.4	: Diamensions of the Uniaxial and Multiaxial test specimens	105
Figure - 4.5	: Correction of diametral strain	106
Figure - 5.1a	: Uniaxial constant load creep data for 304-H stainless steel at 760 $\pm 2\ ^0C$	125
Figure - 5.1b	: Uniaxial constant load creep data for 304-H stainless steel at 760 $\pm\ ^0C$	126
Figure - 5.2	: Log-Log plot of nominal stress versus time to fracture for 304-H stainless steel	127
Figure - 5.3	: Log-Log plot of minimum creep rate versus stress for 304-H stainless steel	128
Figure - 5.4	: Comparison of creep rupture data at different temperatures	129
Figure - 5.5	: Comparison of experimental constant load creep curve with the predicted constant load curve from constant stress curve 2-1/4 Cr Mo steel	130
Figure - 5.6	: Comparison of experimental data with different theoretical models for 304-H stainless steel	131

Figure - 5.7 :	Comparison of experimental data with different theoretical models for 2-1/4 Cr Mo steel	132
Figure - 5.8 :	Comparison of final a / R ratio with original a / R ratio	133
Figure - 5.9 :	Comparison of reduction of area of 304-H stainless steel and 2-1/4 Cr Mo steel for different a / R ratio	134
Figure - 5.10 :	Variation of normalised reduction in area with triaxiality	135
Figure - 5.11 :	Representstion of reduction of area by a void growth model 304-H stainless steel	136
Figure - 5.12 :	Representation of reduction of area by void growth model 2-1/4 Cr Mo steel	137
Figure - 5.13 :	General nomenclature of a notched bar	138
Figure - 5.14 :	Finite element mesh for b / a = 1.46 ; (a) a / R = 1.67 , (b) a / R = 9.30, (c) a / R = 21.60	139
Figure - 5.15 :	Establishment of a skeletal point for $n \geq 3$ b / a = 1.46 , a / R = 2.00	140
Figure - 5.16 :	Comparison of stresses across a notch throat from the present work ans ASAS-NL program , b / a = 1.46, a / R = 1.67	141
Figure - 5.17 :	Comparison of stresses across a notch throat from the present work and ASAS-NL program , b / a = 1.46, q / R = 9.30	142
Figure - 5.18 :	Comparison of stresses across a notch throat from the present work and ASAS-NL program , b / a = 1.46 , a / R = 21.60	143
Figure - 5.19 :	Variation of stresses across a notch throat ,b / a = 1.46, a / R = 1.67	144
Figure - 5.20 :	Variation of stresses across a notch throat., b / a = 1.46, a / R = 9.30	145
Figure - 5.21 :	Variation of stresses across a notch throat , b / a = 1.46, a / R = 21.60	146
Figure - 5.22 :	Variation of effective stress at a skeletal point with a / R for different b / a ratio	147

Figure - 5.23 : Variation of maximum principal stress at a skeletal point with a / R for different b / a ratio 147

Figure - 5.24 : Variation of hydrostatic stress at a skeletal point with a / R for different b / a ratio 148

Figure - 5.25 : Variation of triaxiality factor at a skeletal point with a / R for different b / a ratio 148

Figure - 5.26 : Variation of normalised stresses at a skeletal point with a / R ratio for b / a = 1.46 149

Figure - 5.27 : Variation of a constraint factor at a skeletal point with b / a ratio for different a / R ratio 150

Figure - 5.28 : Failure of a blunt notch of 304-H stainless steel 151

Figure - 5.29 : Failure of a sharp notch of 304-H stainless steel 152

Figure - 5.30 : Failure of a blunt notch of 2-1/4 Cr Mo steel 153

Figure - 5.31 : Failure of a sharp notch of 2-1/4 Cr Mo steel 154

Figure - 5.32 : Failure pattern in 304-H stainless steel and 2-1/4 Cr Mo steel 155

Figure - 5.33 : Final failure of a notched bar b / a = 1.46, a / R = 1.67 156

Figure - 6.1a : Uniaxial creep data at constant load for DS Mar M002 at 900±4 ^{0}C 175

Figure - 6.1b : Uniaxial creep data at constant load for DS Mar M002 at 900±4 ^{0}C 176

Figure - 6.2 : Log-Log plot of minimum strain rate versus stress for DS Mar M002 177

Figure - 6.3 : Log-Log plot of stress versus rupture time for DS Mar M002 178

Figure - 6.4 : Uniaxial creep data at constant stress for DS Mar M002 at 900±4 ^{0}C 179

Figure - 6.5 : Comparison of constant load and constant stress strain rate at 350 MPa 180

Figure - 6.6 : Comparison of experimental constant load, constant stress and predicted constant load creep curve 181

Figure - 6.7 : Variation of axial displacement with time for b / a = 1.46, a) a / R = 1.67, b) a / R = 4.60 182

Figure - 6.8	: Variation of axial displacement with time for b / a = 1.46, a) a / R = 9.30, b) a / R = 21.60	183
Figure - 6.9	: Comparison of notch strengthening ratio with different models	184
Figure - 6.10	: Variation of reduction of area with a / R ratio	185
Figure - 6.11	: Comparison of final a / R ratio with original a / R ratio	186
Figure - 6.12	: Variation of diametral strain with time for different notch geometries	187
Figure - 6.13a	: Finite element mesh b / a = 1.46, a) a / R = 0.5, b) a / R = 1.0 c) a / R = 1.67	188
Figure - 6.13b	: Finite element mesh for b / a = 1.46 , d) a / R = 2.60 e) a / R = 4.60 f) a / R = 9.30	189
Figure - 6.13c	: Finite element mesh for b / a = 1.46, g) a / R = 17.0 h) a / R = 21.60	190
Figure - 6.14	: Comparison of stresses across a notch throat from the present work and MARC program b / a = 1.46, a / R = 1.67	191
Figure - 6.15	: Comparison of stresses across a notch throat from the work and MARC program b / a = 1.46, a / R = 9.30	192
Figure - 6.16	: Comparison of stresses across a notch throat from the present work and MARC program b / a = 1.46 , a / R = 21.60	193
Figure - 6.17	: Variation of stresses across a notch throat b / a = 1.46, a / R = 1.67	194
Figure - 6.18	: Variation of stresses across a notch throat b / a = 1.46, a /R = 4.60	195
Figure - 6.19	: Variation of stresses across a notch throat b / a = 1.46, a / R = 9.30	196
Figure - 6.20	: Variation of stresses across a notch throat b / a = 1.46 a / R = 21.60	197
Figure - 6.21	: Variation of normalised effective stress along the notch profile for n = 8.2, b / a = 1.46 , a / R = 2.60	198
Figure - 6.22	: Comparison of theoretical and experimental diametral displacement rate	199

Figure - 6.23	: Comparison of maximum average effective stress away from the notch root with the effective stress at the skeletal point and the average effective stress in the notch root plane	200
Figure - 6.24	: Variation of stresses at a skeletal point across a notch throat	201
Figure - 6.25	: Comparison of multiaxial reduction in area with predicted reduction of area	202
Figure - 6.26	: Comparison of maximum principal stress , effective stress and hydrostatic stress in an isotropic and anisotropic analysis b / a = 1.46, a / R =1.67	203
Figure - 6.27	: Comparison of maximum principal stress, effective stress and hydrostatic stress in an isotropic and anisotropic analysis b / a = 1.46, a / R = 21.60	204
Figure - 6.28	: Comparison of isotropic and anisotropic effective stress across a notch throat for n = 1	205
Figure - 6.29	: Comparison of isotropic and anisotropic hydrostatic stress across a notch throat for n = 1	206
Figure - 6.30	: Comparison of isotropic and anisotropic maximum principal stress across a notch throat for n = 1	207
Figure - 6.31	: Comparison of isotropic and anisotropic effective stress across a notch throat for n = 8.2	208
Figure - 6.32	: Comparison of isotropic and anisotropic hydrostatic stress across a notch throat for n = 8.2	209
Figure - 6.33	: Comparison of isotropic and anisotropic maximum principal stress across a notch throat for n = 8.2	210
Figure - 6.34	: Fracture of a plain specimen	211
Figure - 6.35	: Damage in broken notch b / a = 1.46, a / R = 4.60	212
Figure - 6.36	: Damage in unbroken notch b / a = 1.46, a / R = 4.60	213
Figure - 6.37	: Damage along a longitudinal grain boundary b / a = 1.46 a / R = 13.00	214
Figure - 6.38	: Damage in unbroken notch b / a = 1.46 , a / R = 13.00	215
Figure - 6.39	: Damage in unbroken notch b / a = 1.46, a / R = 21.60	216
Figure - 6.40	: Damage in unbroken notch b / a = 1.46, a / R = 21.60	217

LIST OF TABLES

		Page No.
Table-2.1:	Material properties of 304-H stainless stel at 760 ^{o}C	70
Table-2.2 :	Material properties of 2-1/4 Cr Mo steel at 538 ^{o}C	70
Table-2.3 :	Chemical composition of DS Mar M002	70
Table-2.4 :	Material properties of DS Mar M002 at 900 ^{o}C	71
Table-5.1 :	Uniaxial creep data for 304-H stainless steel	123
Table-5.2 :	Different notch geometries used in the numerical analysis	123
Table-5.3 :	Comparison of theoretical and experimental deformation rate for 304-H stainless steel	124
Table-6.1 :	Uniaxial constant load creep data of DS Mar M002 at 900±4 ^{o}C	172
Table-6.2 :	Constant stress uniaxial creep data for DS Mar M002 at 900±4 ^{o}C	172
Table-6.3 :	Different notch geometries used in the numerical analysis	173
Table-6.4 :	Notched bar creep data of DS Mar M002 at 900±4 ^{o}C	173
Table-6.5 :	Diametral strain rate and average effective stress for different notch geometries	174

NOMENCLATURE

a	:	notch throat radius
a_i , a_j , a_k	:	dimensions of triangular element
b	:	bar radius
b_i , b_j , b_k	:	dimensions of triangular element
$[B]$	:	element dimension matrix
$[D]$	:	element elastic property matrix
$[d]$	:	element dimension matrix
d	:	grain size
E	:	young's modulus
E'	:	effective modulus
$[F]$	:	vector of overall externally applied forces
F	:	relative stress concentration factor
f_h	:	area fraction of holes on grain boundary
f_i	:	initial area fraction of holes
f_c	:	area fraction of holes at which linkage occurs, taken as 0.25
f_t^d	:	area fraction of voids at transition from growth by boundary diffusion to power-law creep
f_t^s	:	area fraction of holes at transition from growth by surface diffusion to power-law creep
$2l$	:	centre-to-centre void spacing
n	:	stress index in creep law
P	:	pressure
R	:	notch profile radius

R_1 , R_2	:	internal and external radii of a thick-walled cylinder
r_h	:	radius of a growing void
S_s	:	notch to unnotched stress strength ratio
S_t	:	notch to unnotched time strength ratio
t_n	:	nucleation time
t_{no}	:	failure time of a notched specimen
t_{un}	:	failure time of a plain bar specimen
t_R	:	time to failure
u_i , u_j , u_k	:	element radial displacement component
w_i , w_j , w_k	:	element axial displacement component
α	:	parameter that measures the effect of stress state on void growth rate
α_0	:	value of a corresponding to simple tension
γ_s	:	surface free energy
Δ_m	:	element area
$[\delta]$, $[\delta]_m$	:	overall and element vector of displacement components
$\dot{\varepsilon}_0$, σ_0	:	creep constants
ε_R	:	strain to failure
ε_{zz} , $\varepsilon_{\theta\theta}$, ε_{rr}	:	axial, hoop and radial strains
ε_1 , ε_2, ε_3	:	principal strains
υ	:	Poisson's ratio
σ_{eff}	:	effective stress
σ_{mean}	:	hydrostatic stress
σ_∞	:	remote applied stress
σ_n	:	failure stress of a notched specimen
σ_{un}	:	failure stress of a plain bar specimen

σ_{zz} , $\sigma_{\theta\theta}$, σ_{rr} : axial, hoop and radial stresses

σ_1 , σ_2, σ_3 : principal stresses

ϕ_o : dimensionless material quantity which appears in Asby's boundary diffusion model

Ψ_0 : dimensionless material quantity which appears in Ashby's surface diffusion model

ω : measure of damage in continuum theory of creep damage

INTRODUCTION

The increasing need for high temperature thermal power plants, nuclear plants and gas turbine engines led to the birth of high temperature creep resisting alloys, superalloys and single crystal alloys. An assessment of better performance of these alloys in actual practice, at temperature greater than half the absolute melting temperature and under complex loading conditions, is an important factor. One of the major causes of failures in such materials is creep. "Creep" as a process can be defined as a gradual degradation of material strength in the course of time under various loading conditions. In many structures a triaxial state of stress prevails because of geometrical constraints, sharp changes of sections and complex loading conditions. Stresses generated due to triaxiality can govern the life of components in service. To prevent a catastrophe under service conditions, it is necessary to have an appropriate design procedure for complex structures. Apart from design standards and procedures, laboratory techniques are needed to assess the approximate life of such structures. As the problem of the influence of stress concentration on the lifetime of structures at high temperature is difficult this research has been undertaken to study stress state effect on the failure of such structures through the experimental and numerical (Finite Element) techniques.

Several researchers have tried to understand the behaviour of isotropic materials under triaxial stress state through the experimental and numerical techniques. Hayhurst and co-workers (1977) were the first to carry out detailed analyses on copper, aluminium and 316 stainless steel. In these materials it is observed mostly that the holes develop along the boundaries transverse to the tensile stress axis. In order to prevent the damage originating along the transverse grain boundaries the scientists decided to minimize the transverse grain boundaries by cahnging marphology of the grain structure. In this attempt the directionally solidified alloys have been developed and a trend is continuing to improve the creep properties of these alloys.

The directionally solidified alloys have found their application in gas turbine blades extensively. The triaxial state of stress exists in the fir tree root design of the blade. Apart from the triaxial state of stress they are subjected to different loading conditions. In isotropic or equiaxed materials maximum stress can occur at random direction to the crystallographic plane. Once the damage in the form of holes is developed along the grain boundaries they grow under the influence of the hydrostatic stress and the final failure is due to the coalescence of these holes. In the directionally solidified alloys, as the grains are aligned in one direction they are subjected to the maximum stress in that direction. Thus the chances of initiation of the damage at random directions are minimized.

A well known laboratory technique used to generate triaxial state of stress, is a circumferentially notched bar subjected to an axial tensile load. In this technique, the constraint of the shank produces a state of triaxial tension in the notch region which depends upon the notch geometry and creep properties of the material. Triaxiality can be varied by varying the notch root radius, keeping the other geometrical parameters constant and the failure can be studied under the influence of the different hydrostatic stress level. In the present work the same technique is used to generate triaxial state of stress. Several experimental investigations of this kind have revealed that both notch strengthening and notch weakening can be observed Ng et al. (1980), Al-Faddagh (1983). To explain this behaviour, a knowledge of how the state of stress parameters across the notch throat vary with notch sharpness and material properties are needed. The theoretical section of this thesis consists of the development of the constitutive effective stress and strain equations, with the anisotropy in the axial direction, for the creep analysis and the adaptation of these equations in the finite elemnt program. The stress distribution across a notch throat of several notch geometries for isotropic materials is presented. For this purpose a finite element program for isotropic analysis is modified and used. Stress distribution across a notch throat for anisotropic materials is carried out using the finite element program adapted with the anisotropic constitutive equations developed in this thesis. Further, comparison of the isotropic and anisotropic stress

distribution is presented.

The experimental section of this thesis consists of a series of creep tests carried out at 760 ^{0}C on notched specimens pulled in tension and having the same throat diameter as the plain tensile bars of 304 -H stainless steel. Creep data on 2-1/4 Cr Mo steel at 538 ^{0}C are taken from the literature. Similar tests are carried out on DS Mar M002 at 900 ^{0}C which is anisotropic in nature. Finally the failure pattern of isotropic and anisotropic materials is presented.

CHAPTER-1

1. Introduction

Creep is a time dependent deformation which occurs when a material is subjected to a load for a prolonged period of time. Creep occurs as a result of the motions of dislocations within grain, grain boundary rotation, and grain boundary sliding. It is sensitive to grain size, alloying additions, the initial condition of the material, heat treatment and test conditions. Generally creep is demonstrated by a "standard creep curve" Figure-1.1, which involves primary creep, secondary creep and tertiary creep. These three regions can be explained as follows ;

1) Primary creep ; a period of decreasing creep rate during which work hardening is taking place.

2) Secondary creep ; this is a pseudo steady state where a balance has been reached between work hardening and thermal softening.

3) Tertiary creep ; a period of accelerating creep rate culminating in fracture. It is associated with the onset of necking, cracking and overaging (metallurgical instability).

The occurrence of the final failure can be explained by successive events taking place during the course of time. These events are named by Svensson and Dunlop (1981) as :

1) Nucleation of cavities;

2) Growth of cavities;

3) Interlinkage to form larger cavities or cracks;

4) Crack propagation;

5) Final failure.

1.1 Uniaxial Creep Deformation and Failure

The phenomenon of creep was observed during the 19th century. Components in steam boilers and furnaces were often replaced by new spares because they deformed.

Andrade (1910) first investigated the creep of lead wires and introduced the term primary, secondary and tertiary creep as shown in Figure 1.1. He proposed the first creep law as follows :

$$l = l_0 (1 + B t^{1/3}) e^{kt} \qquad (1.1)$$

where l_0 and l are the initial and current lengths of the specimen respectively, and B and k are material constants. Since then, various empirical equations have been proposed for the stress, time and temperature dependence of creep of metals based on experimental observations. The steady- state region of the creep curve was studied in great detail. Baily and Norton [1929] suggested the empirical equation as follows :

$$\dot{\varepsilon}_s = C \sigma^n \qquad (1.2)$$

where C and n are material constants. Equation (1.2) is called Norton's creep law. In the long term tests when secondary creep dominates, the primary creep may be neglected. However, under large stresses, and especially at high temperatures, primary creep must be taken into account. Odqvist [1953] included the influence of primary creep and suggested the total creep rate :

$$\frac{d\varepsilon}{dt} = \frac{d}{dt} \left(\frac{\sigma}{\sigma_0} \right)^{n_0} + \left(\frac{\sigma}{\sigma_c} \right)^n \qquad (1.3)$$

where σ_0, n_0, σ_c and n are material constants.

1.1.1 Hoff's Theory of Ductile Fracture

In 1953, Hoff presented a theory which can predict creep failure times of uniaxial test specimen failing by geometrical instability or necking. The theory is based on the assumption that the initial cross- sectional area, A_0, of the test piece will shrink to zero under a constant load, P. Norton's equation with time function can be written as :

$$\varepsilon = C \sigma^n F'(t) = C \sigma^n t^m \tag{1.4}$$

Extending equation (1.4), to hold for finite deformation and neglecting primary creep.,

$$\dot{\varepsilon}_s = -\frac{1}{A}\frac{dA}{dt} = C \left(\frac{P}{A}\right)^n m\, t^{m-1} \tag{1.5}$$

where A is the cross-sectional area. Equation (1.5) can be integrated, assuming $A = A_0$ at $t = 0$, therefore

$$A_0^n - A^n = C\, n\, P^n\, t^m \tag{1.6}$$

Applying the basic assumption that A_0 will decrease to $A = 0$ in the finite time, the equation (1.6) becomes :

$$t_h = \left[\frac{1}{n C \sigma_0^n}\right]^{1/m} \tag{1.7}$$

The equation (1.7) reduces to Hoff's equation for ductile fracture when $m = 1$.

The stress, σ, will increase from its initial value , $\sigma_0 = P / A_0$, with time, according to the following equation :

$$\sigma = \sigma_0 \left(1 - \frac{t}{t_h}\right)^{-1/n} \tag{1.8}$$

σ will become infinite when $t = t_h$.

Equation (1.7) represents a straight line in a log / log plot between $\dot{\varepsilon}_s$ and t_h.

1.1.2 Robinson's Linear Cumulative Damage rule

Robinson [1952] proposed a practical solution for estimating life under variable conditions of stress or temperature. It is based on the assumption that the creep strain is a function of stress, temperature and the accumulated creep strain, ε_c :

$$\dot{\varepsilon} = f(\sigma, T, \varepsilon_c) \tag{1.9}$$

In a tensile creep test, if an applied stress , σ_1, is held for time t_1, it will produce damage, D_1, which, under steady conditions, is proportional to the fraction of total life, t_{R_1}:

$$D_1 = \frac{t_1}{t_{R_1}} \tag{1.10}$$

If the stress is changed to σ_2, then the second amount of damage incurred is :

$$D_2 = \frac{t_2}{t_{R_2}} \tag{1.11}$$

Assuming that the damage resulting from each loading period is independent of all other periods, Robinson's rule should be applicable for an unlimited number of variable temperature and stress conditions. The total damage, D, for all the period will then be :

$$D = \Sigma\left(\frac{t_i}{t_{R_i}}\right) = \int_0^{t_R} \frac{dt}{t_{R_i}} \tag{1.12}$$

At rupture, D = 1.

The advantage of this method is that it can be used to predict rupture times under variable conditions, using steady load data.

1.2 Multiaxial State of Stress

At an arbitrary point in a continuum, each force vector, T_i, is associated with a unit normal vector, n_i. This is illustrated in Figure -1.2, in which Δs is the surface of a small element having p as an interior point. The totality of all possible pairs of such vectors, T_i and n_i, at p defines the state of stress at that point. The nine components involved in describing the state of stress constitute a second order Cartesian tensor, σ_{ij}. Coordinate

transformation equations then serve to relate the stress vector on any other plane at the point to the three reference directions.

The nine components of the stress tensor , σ_{ij} , may be displayed in matrix form as follows :

$$\sigma_{ij} = \begin{bmatrix} \sigma_{11} & \sigma_{12} & \sigma_{13} \\ \sigma_{21} & \sigma_{22} & \sigma_{23} \\ \sigma_{31} & \sigma_{32} & \sigma_{33} \end{bmatrix} \qquad (1.13)$$

The stress tensor component may be displayed with respect to the coordinate planes, as shown in Figure-1.3a and 1.3b. The components perpendicular to the planes are called normal stresses. Those acting tangentially to the planes are called shear stresses.

A particular set of orthogonal planes could be found in which one of the normal stresses is a maximum and one is a minimum with respect to the rotation of coordinates. These normal stresses are the principal stresses, $\sigma_1 > \sigma_2 > \sigma_3$, the shear stresses on the principal stress planes are zero. Similarly, the planes for normal shear stresses could also be found, where $\tau_1 > \tau_2 > \tau_3$. However, the normal stresses on the principal shear stress planes are not zero.

The stress space shown in Figure- 1.4 has coordinate axes associated with the principal stresses. Every point in this space, for example, p (σ_1,σ_2,σ_3), corresponds to a different state of stress. The position vector of such point may be resolved into a component OA along the line OZ, which makes equal angles with the coordinate axes and a component OB in the plane known as the π-plane which is perpendicular to OZ and passes through the origin. The component along OZ, for which $\sigma_1 = \sigma_2 = \sigma_3$, represents the deviator portion of the stress state. The equation of the π plane is given by :

$$\sigma_1 + \sigma_2 + \sigma_3 = 0 \qquad (1.14)$$

For an isotropic material, the yield condition defines a surface called the " Yield Surface" which is a function of the principal stresses defined as follows :

$$f(\sigma_1, \sigma_2, \sigma_3) = \text{constant} \qquad (1.15)$$

Since the yield conditions are independent of the hydrostatic stress, such yield surface are general cylinders having their generators parallel to OZ. Those stress points which lie inside the cylindrical yield surface represent elastic stress states ; those which lie on the yield surface represent incipient plastic stress states.

In a true view of the π-plane , looking along OZ towards the origin O, the principal stress axes appear symmetrically placed 120^0 apart. The yield curves proposed by Tresca and Von-Mises are defined by the following equations.

$$\sigma_1 - \sigma_3 = 2\,\tau_{max} = \sigma_{eff} \qquad \text{(Tresca)} \qquad (1.16)$$

$$(\sigma_1 - \sigma_2)^2 + (\sigma_2 - \sigma_3)^2 + (\sigma_3 - \sigma_1)^2 = 2\,\sigma_{eff}^2$$

$$\text{(Von-Mises)} \qquad (1.17)$$

1.2.1 Creep Under Multi-axial State of Stress

Because creep strain is not linearly dependent on stress, the effects of stresses applied in different dimensions cannot be linearly superposed. Just as in classical plasticity theory, these effects can be described in terms of equivalent stresses and strains.

Experimentally it is found that ;

i) Hydrostatic stress does not affect creep

ii) Axes of principal stress and strain-rate are coincident,

iii) No volume change occurs during creep.

Hence the laws of classical plasticity can be applied to creep provided strain-rates are written in place of strains i. e. using the equation (1.17) and the corresponding equivalent strain rate

$$\dot{\varepsilon}_{eff} = \frac{\sqrt{2}}{3}\sqrt{[(\dot{\varepsilon}_1 - \dot{\varepsilon}_2)^2 + (\dot{\varepsilon}_2 - \dot{\varepsilon}_3)^2 + (\dot{\varepsilon}_3 - \dot{\varepsilon}_1)^2]} \qquad (1.18)$$

The Levy-Mises flow rule also becomes,

$$\frac{\dot{\varepsilon}_1}{\sigma_1 - \frac{1}{2}(\sigma_2 + \sigma_3)} = \frac{\dot{\varepsilon}_2}{\sigma_2 - \frac{1}{2}(\sigma_3 + \sigma_1)} = \frac{\dot{\varepsilon}_3}{\sigma_3 - \frac{1}{2}(\sigma_1 + \sigma_2)} = \text{constant} = \frac{\dot{\varepsilon}_{eff}}{\sigma_{eff}} \tag{1.19}$$

For uniaxial creep equation $\sigma_2 = \sigma_3 = 0$

$$\dot{\varepsilon}_1 = C\,\sigma_1^n \tag{1.20}$$

The corresponding complex stress expression is

$$\dot{\varepsilon}_{eff} = C\,\sigma_{eff}^n \tag{1.21}$$

and

$$\dot{\varepsilon}_1 = C\,\sigma_{eff}^{(n-1)}\left[\sigma_1 - \frac{1}{2}(\sigma_2 + \sigma_3)\right] \tag{1.22}$$

For uniaxial tension $\sigma_2 = \sigma_3 = 0$, Therefore $\sigma = \sigma_1$ and $\dot{\varepsilon}_1 = C\,\sigma^n{}_1$

The above analysis breaks if constant volume conditions are not maintained or if anisotropy develops. Similar expressions can be written down if the equation (1.16) and equivalent strain are used, i.e.

$$\sigma_{eff} = \sigma_1 - \sigma_3 \tag{1.23}$$

$$\dot{\varepsilon}_{eff} = \frac{2}{3}(\dot{\varepsilon}_1 - \dot{\varepsilon}_3) \tag{1.24}$$

1.3 Creep Deformation Mechanisms

The relationship between the steady-state creep rate and the applied stress for a wide range of polycrystalline materials can be represented by the common curve as shown in Figure-1.5. Sherby and Burke (1967) first showed that three different mechanisms are active at different stress levels.

In the region 1 , at low stresses, the strain rate is directly proportional to the applied stress and is expressed as ;

$$\dot{\varepsilon} = K\sigma \qquad (1.25)$$

This applies when creep occurs by a diffusional flux of vacancies from transverse to longitudinal grain boundaries, either by volume diffusion through the grains or by grain boundary diffusion around the grains. This mechanism may be inhibited by the presence of impurities or particles that may influence the efficiency of grain boundaries as sources and sinks of vacancies.

In the regime 2, over a wide intermediate stress range, at sufficient high temperature a steady state creep rate can be represented by a power-law function of stress. Strain rate in this region is given by the equation

$$\dot{\varepsilon} = K'\sigma^{n} \qquad (1.26)$$

Under these conditions deformation occurs by a combination of glide and climb of dislocations.

In regime 3, at sufficiently high stresses, the power-law representation of creep breaks down and creep strain rate, $\dot{\varepsilon}$, varies exponentially with the applied stress as ;

$$\dot{\varepsilon} = K'' \exp^{(B\sigma)} \qquad (1.27)$$

The important difference between this mechanism and low temperature yield by glide, is that a steady state dislocation structure can be maintained by rapid recovery processes such as dynamic recrystalization. Regime 2 and 3 may be regarded as extremes of a single mechanism whereby recovery processes create the cavities that allow the activation of glide events ; in regime 2, the recovery stage is slow and intermediate glide bursts are rapid; whereas, in regime 3, recovery is rapid relative to the viscous glide events and many more dislocation segments are in motion.

1.4 Creep Fracture Mechanisms

Many pure metals and industrial alloys can fracture by the formation of holes or cavities at grain boundaries. Most commonly, the holes appear on boundaries which lie roughly perpendicular to the maximum principal tensile stress direction. Their presence reduces the section and so accelerates the creep and this, in turn, increases the rate at which the damage grows. At low stresses the damage is void-like; at high, the voids may link to give grain-boundary cracks and thus the failure of the material. Creep fracture can be transcrystalline, intercrystalline , localized or spread over a wide area. Different steps which characterize the whole process are described in the following sections.

1.4.1 Nucleation of Cavities

Almost all materials are bound to have defects in their crystal structure. These defects are categorised as :

1) Point defects such as vacancies and interstitials ;

2) Line defects or dislocations ;

3) Planer defects such as grain boundaries ;

4) Volumetric defects such as precipitate particles and voids.

When these materials are exposed to service conditions or under laboratory conditions, a void nucleation process commences, as a result of decohesion of particle matrix interfaces or by cracking of the particles themselves. The decohesion may occur due to the high stress concentration generated at the defects listed above. According to Harris (1965), the number of possible sites at which suitable stress concentration can arise are

1) Triple junction of high angle grain boundaries ;

2) Sub boundary / grain boundary intersection ;

3) Grain boundary ledges (i. e. slip band intersections) ;

4) Second phase particles.

The stress conditions for the nucleation of cavities or cracks at obstacles to grain boundary sliding (e.g. second phase particles) have been modelled by Smith and

Barnby (1967) who endeavoured to explain that the voidage will be possible even under conditions of low applied creep stresses. They assumed that the precipitates fracture along a plane parallel to the sliding grain boundary, and for the actual situation no voidage will be produced. However, in practice, the clevage planes of precipitate will be inclined to the boundary and then it is immediately clear that voidage can be produced. Further, the concept of nucleation of the voids at grain boundaries have been refined by Fleck et al.(1975). They carried out the experiments with copper base alloy and found that cavity nucleation was associated with grain boundary particles. They found that the nucleation involves a critical sliding length whereby the product of the average rate of grain boundary sliding and time is constant. Dyson et al.(1976) concluded that the deviatoric or shear component of the stress tensor controls cavity nucleation in Ni 80A with the weight of evidence favouring grain interior slip as the responsible micromechanism. According to them, most cavities were on those grain boundaries which were parallel to the maximum principal stress axis. However, preferential cavity growth occurred during subsequent tensile creep and cavities on these parallel boundaries either remained constant in size or diminished while those on boundaries which were orthogonal to the applied stress axis grew relatively quickly. Raj and Ashby (1975) noticed that three types of void configurations are possible in clean boundaries and two types of void configurations at second phase particles. Using classical nucleation theory, they calculated the nucleation of the voids. According to them when no sliding is allowed the number of nuclei increase continuously with time but when stress concentration due to sliding is taken into account then nucleation is catastrophic i.e. full nucleation occurs at early stages of creep. The different intergranular cavity nucleation models are shown in Figure-1.6. Thomson and Hancock (1984) argued that nucleation is a statistical event which occurs by failure of the particle matrix interface. The first of these comprises particles not bonded to the matrix, that is, with zero interfacial strength. The second comprises particles well bonded to the matrix.

1.4.2 Growth of Cavities

The schematic diagram drawn by Cocks and Ashby (1980) represent the simplest way of modelling a grain boundary void subjected to the stress field σ_1, σ_2 and σ_3 as shown in Figure-1.7. The parameter 2l is the void spacing, d the grain size, and $2r_h$ is the void diameter. Under the above stress field, voids grow by three distinct micromechanisms ; these are :

a) Boundary diffusion mechanism .

b) Surface diffusion mechanism.

c) Power-law creep mechanism.

Figure-1.8 shows the simplest way of representing each mechanism in a unit structure.

Void growth by coupled mechanisms is also possible. They control the growth because the volumetric growth rate of a void is dependent upon the following parameters:

$$\dot{V} = f(\dot{\varepsilon}, T, V) \qquad (1.28)$$

where $\dot{\varepsilon}$ is the strain rate, T is the temperature, and V is the current volume of a void. One mechanism dominates for a period of time, then a switch to another mechanism will dominate until failure. Three types of coupled mechanisms can control the growth of voids ; these are :

a) Coupled boundary diffusion and power-law creep mechanism.

b) Coupled surface diffusion and power-law creep mechanism.

c) Coupled boundary and surface diffusion mechanism.

Figure-1.9 shows a void growing under the influence of a normal stress, σ_1, for each individual coupled mechanism.

The first detailed analysis of intergranular creep cavity growth by boundary diffusion was presented by Hull and Rimmer (1959). Their equation for void growth is :

$$\frac{\delta f_h}{\delta t} \alpha \left[\frac{\sigma}{1-f_h} - \frac{\gamma}{l}\sqrt{\frac{\pi}{f_h}} \right] \qquad (1.29)$$

where γ is the surface energy, and $f_h = r^2_h / l^2$

where r_h is the hole radius, 2l is their spacing, and f_h is the cross sectional area of voids per unit area.

They suggested that vacancies for void growth are produced by the tension across the grain boundaries rather than deformation inside the grain. The main assumption was based on the fact that the voids grow by the diffusion of atoms from the void surface along the grain boundary. Other theories and models for diffusion controlled void growth were proposed by Speight and Beer (1975), Raj et al. (1977), Chuang et al.(1979) and Cocks and Ashby (1982). In these theories, expressions for the rate of volumetric change of a void are given, based on the assumption :

a) Constancy of cavity density.

b) Grains do not deform plastically.

c) Cavities are a perfect vacancy sink and the normal stress is a perfect cavity source.

d) The applied load remains constant on each cavitated grain facet

In their analysis, Chuang et al. (1979) determined void shape as a part of the analysis, rather than assuming quasi equilibrium void shape. Thus they argued that when the surface diffusion is slower than grain boundary diffusion a cavity can change shape during growth and evolve into a more crack-like shape. Hence, a quasi equilibrium mode is favoured when the stress level is low, the cavity diameter and ratio of diameter to spacing are small, and when the parameter, Δ, (the ratio of surface to the grain boundary diffusivity) is large. The Cocks and Ashby (1980) void growth theory is explained in detail in Appendix-A.

The mechanism of void growth by power-law creep was first introduced by McClintock (1968) when studying a simple model of a hole growth during plastic deformation. His work was followed by many proposed theories for void growth by power-law creep (Rice and Tracey (1969), Hellan (1975), Dyson and Taplin (1976), Edward and Ashby (1979), Needleman and Rice (1980), and Cocks and Ashby (1980).

All these theories proposed an expression for calculating the rate of radius growth of a void under the influence of a remote uniform effective strain rate field, $\dot{\varepsilon}$, such as :

$$\dot{r} = r k \dot{\varepsilon} \qquad (1.30)$$

where k is the stress sensitivity parameter dependent on the particular theory adopted

The volumetric growth rate of a void is dependent on the three parameters, $\dot{\varepsilon}$, T, and V (equation 1.28). This makes it necessary to analyse a model in which voids grow by coupled mechanism. This was done by Beer and Speight (1978), Edward and Ashby (1979), Chuang, et al. (1979), and Cocks and Ashby (1980,1982). One example of a void growth by a coupled diffusion and power-law creep mechanism is shown in Figure-1.9. It shows the damage rate (df_h / dt) dependence on both the stress and the area fraction of holes, f_h. In this model a transition parameter, f_t, is introduced. The diffusion mechanism dominates from the initial area fraction of holes f_i to f_t and power-law creep dominates from f_t until fracture.

Many engineering components are subjected to multiaxial states of stress where the ratio of maximum principal stress to octahedral shear stress can vary substantially. In these components strain rates are of the order of 10^{-10} sec^{-1} because cavity growth rates in engineering structures are much slower than predicted by diffusion growth model. Bearing in mind this fact, Dyson (1976,1979) put forward a constrained cavity growth model, where cavity growth is controlled by deformation rate and is proportional to the octahedral shear stress raised to some positive power. In a statistical analysis of creep cavitation in AISI steel by Liu et al. (1984), cavity growth was found much less compared with the Hull and Rimmer (1959) cavity growth model. Cavities were observed to be statistically randomly distributed along the grain boundaries. This smaller cavity growth rate supported the phenomenon of constrained cavity growth by Dyson (1976,1979).

1.4.3 Coalescence of Cavities and Final Fracture

After nucleation cavities elongate along the major tensile axis and two neighbouring

cavities coalesce when their length has grown to the order of magnitude of their spacing. Figure-1.10 represents the general view of cavity coalescence in copper and in plasticine McClintock (1968). Failure by coalescence occurs when the ligaments between neighbouring voids have thinned down sufficiently. Such general coalescence is often observed in the centre of the neck in a round tensile bar. In other cases localization of plastic flow takes place so that the void induced failure occurs inside a narrow shear band by the formation of void sheet. Depending on the microstructure, stress state etc. the void volume fraction generally varies from 0.1 to 0.25.

A continuum model of the loss of stress carrying capacity due to void coalescence for a void containing ductile material is suggested by Tvegaard(1982). When the coalescence takes place in a small region of the material this part of the material has no more stress carrying capacity and the material possesses very low yield stress. Radhakrishnan (1985) studied void growth and fracture in power-law creep of 18-8 austenitic steel. He stated that Robinson's life summation rule equation (1.12) for cumulative damage will be valid if the same mechanism controls the void growth under different stress and temperature employed in cumulative damage.

1.5 Necking of a Tensile Bar Under Creep Test

Coalescence of voids results in the necking down of a round bar and thus final fracture. Bridgman (1952) first studied the stress distribution at the narrowest section of a necked down axisymmetric tension specimen and obtained a semi-empirical solution. His analysis was based on the assumption that the axial strain across the narrowest section was uniform. Chen (1971) calculated the shapes and deformation of a necked down tension specimen. He also found the stress and strain distributions in the specimen during its loading history. The distribution of effective stress calculated across the neck was found to be in good agreement with the Bridgman analysis, while the distribution of radial stress, σ_{rr}, and hoop stress, $\sigma_{\theta\theta}$, differed considerably. Figure-1.11 shows the stress distributions across a necked bar obtained by Bridgman. Needleman (1972)

calculated the stresses across the neck using a theory of bi-furcation. His results were in good agreement with Bridgman analysis. Peak values of the stress components remained on the axis of the bar. Furthermore, these peaks became attenuated as necking proceeded. Tvegaardand Needleman (1984) followed the inception of necking through the initiation and growth of voids in the centre of a neck which propagates across the specimen. The central crack once initiated follows the Zig-Zag path as it propagates across the specimen to the free surface, ultimately forming a cup-cone fracture. Levy (1986) studied the tertiary creep and necking of creep damaging bars in uniaxial tension. He tried to correlate the grain boundary cavitation with the necking of a bar under creep conditions. From the analysis of perfect and imperfect bars he concluded that in a perfect bar fracture occurs at a finite area while in an imperfect bar fracture occurs at the plane where the diameter is smaller with the formation of a highly localized neck just prior to fracture. This type of fracture is common in metals where intergranular fracture is dominant.

1.6 Creep Fracture Under Multiaxial Stress State

Coalescence of circular and elliptical holes in a plastic material under triaxial stress state was studied by McClintock (1968). From the analysis, he showed the strong interaction between triaxiality and strain hardening. He concluded that hole growth cannot occur in the tensile test before necking. Further analysis by Rice and Tracey (1969), Hancock and Mackenzie(1976) also indicates the strong dependence of ductility on the triaxial state of stress. All of them noted the exponential amplification of growth rate by stress triaxiality. Cocks and Ashby (1980) and Hancock and Brown (1983) carried out the same type of study and arrived at similar conclusions. Needleman and Tvegaard (1984) through their numerical analysis concluded that in most of the axisymmetric cases failure initiates at the center of the specimen. For sharp notches, the crack growth is confined to the minimum cross section due to the presence of high stress gradient across the notch throat. The geometrical constraint does not have any effect on the propagation of the crack. According to their findings, failure does not initiate at the notch surface but

is initiated slightly inside the notch root. This is actually expected since the stress free conditions on the notch surface lowers the stress level at the surface. Once initiated, the failure region propagates both backwards towards the notch and forwards into the material.

1.7 Continuum Damage Mechanism Approach to Creep Failure

At the microscale level, a good representation of physical mechanics can be introduced. But difficulties arise when those analyses have to be included in large scale structures to predict ductile failure. The main reason is the lack of accuracy of local stress calculations for a microscale level. Between that microscale level, say 10^{-3}-10^{-2}mm, and the structural scale level, say 10^{2}-10^{3} mm, there exists a macroscale level of constitutive equations for strain behaviour. At the macroscale level it is difficult to introduce much physics, but damage variable defined as an effective surface density of cracks or cavity intersecting a plane is easy to introduce in structural calculations, especially with the concept of effective stress. The schematic illustration of a macroscopic crack initiation concept is given in Figure-1.12.

1.7.1 Kachanov's and Robotnov's Continuum Damage Theory

An important contribution to creep mechanics was made by Kachanov in 1958. He proposed a theory of combined ductile and brittle creep rupture based on : (a) negligible elastic deformation, (b) creep rate , $\dot{\varepsilon}$, at steady-state is dependent on the applied uniaxial stress and temperature, and (c) deterioration with the time takes place whenever a metal is subjected to a state of tensile stress. The deterioration or damage represented by ;

$$\omega = 1 - (A_R / A_0) \qquad (1.31)$$

where A_R is the area after some damage has occurred and A_O is the initial area.

The value of ω increases monotonically from zero at $t = 0$ (damage free material) to unity at failure ; therefore, the strain rate in a standard Norton, equation (1.2), is now written as :

$$\dot{\varepsilon}_s = \frac{C\,\sigma^n}{(1-\omega)^q} \tag{1.32}$$

and the rate of change of ω is :

$$\dot{\omega} = \frac{B\sigma^m}{(1-\omega)^r} \tag{1.33}$$

where C, n, q, B, m and r are the material constants in equations (1.32) and (1.33)

Robotnov (1969) generalized these concepts to make predictions of creep strain accumulation, local damage and rupture times, assuming negligible primary creep, such as :

$$\frac{\varepsilon}{\varepsilon_R} = 1-\left(1-\frac{t}{t_R}\right)^{\frac{1+r-q}{1+r}} \tag{1.34}$$

and

$$(1-\omega)^{1+r} = 1-\frac{t}{t_R} \tag{1.35}$$

where the subscript R refers to rupture. Integrating equation (1.33) under the condition $\omega = 0$, $t = 0$ and $\omega = 1$, $t = t_f$ leads to an expression for uniaxial rupture time :

$$t_R = \frac{1}{B\,\sigma^m\,(1+r)} \tag{1.36}$$

Equation (1.36) corresponds with the linear plots of log σ against log t_R frequently used to present uniaxial creep data.

Creep damage-mechanics was further developed by Leckie and Hayhurst (1977). They correlated the physical damage, ε , to Kachanov's damage parameter ,ω ,through the equation

$$\dot{\varepsilon} = f(\sigma, \omega) \tag{1.37}$$

The rate of change of damage is given in terms of the nominal stress σ and the current value of ω by

$$\dot{\omega} = g(\sigma, \omega) \tag{1.38}$$

Simple forms of the strain rate and damage rate equations which can be used to describe uniaxial behaviour of low stress rupture are given by Hayhurst et al. (1984) as ;

$$\dot{\varepsilon} = G\left[\frac{\sigma}{(1-\omega)}\right]^n \tag{1.39}$$

and

$$\dot{\omega} = C\frac{\sigma^m}{(1-\omega)^r} \tag{1.40}$$

When material is undamaged, $\omega = 0$ and equation for strain rate reduces to Norton's law equation (1.1)

Rupture is defined by $\omega = 1$, when the strain rates are infinitely large, then the relation between failure time and applied stress is given by

$$t_f = \left[\frac{1}{C(1+r)}\right]\sigma^{-m} \tag{1.41}$$

1.7.2 Continuum Damage Analysis Under Multiaxial Stress State

Under multiaxial stress conditions, the rupture time is either dependent on principal tensile stress or maximum effective stress. Using the maximum principal stress criterion, the rate of increase of ω is expressed in terms of the principal stress σ_1 and given by (Hayhurst 1977)

$$\dot{\omega} = C\frac{\sigma_1^m}{(1-\omega)^r} \tag{1.42}$$

and with the maximum effective stress criterion, the corresponding relation is

$$\dot{\omega} = C\frac{\sigma_{eff}^m}{(1-\omega)^r} \tag{1.43}$$

A number of materials, including austenitic stainless steel, obey a mixed criterion of Leckie and Hayhurst (1977). In this situation, the rate of increase of ω may be expressed

as :

$$\dot{\omega} = C \frac{[\alpha \sigma_1 + (1-\alpha)\sigma_{eff}]^m}{(1-\omega)^r} \qquad (1.44)$$

where α is a factor to be determined from two sets of creep tests, each carried out under a different multiaxial stress state. Under the influence of non-proportional loading, creep defects can be distributed and oriented in planes perpendicular to the maximum principal stress. Based on this concept of anisotropy Chaboche (1984) developed the damage laws. He argued that the anisotropic damage laws made it possible to describe the behaviour of a damaged material more correctly, as well as the damage evolution and thus, variations in rupture conditions when the loading is not proportional. A model of isotropic ductile plastic fracture based on the effective stress concept and on the thermodynamics is derived by Lemaitre (1985). The general constitutive equation for ductile plastic damage rate is given by ;

$$\dot{\omega} = \left(\frac{K^2}{2 E S_0} \left[\frac{2}{3}(1+\upsilon) + 3(1-2\upsilon)\left(\frac{\sigma_{mean}}{\sigma_{eff}} \right)^2 \right] \varepsilon^{\frac{2}{M}} \right)^{s_0} \dot{\varepsilon}_s \qquad (1.45)$$

where E = Young's Modulus ; K and M = Material coefficients ; P = Plastic strain ; S_0 and s_0 are material and temperature dependent ; $\sigma_{mean} / \sigma_{eff}$ = Triaxiality factor ; υ = Poisson's ratio

He found that the damage rate is linear with the equivalent strain rate and shows a large influence of triaxiality by means of a damage equivalent stress

1.7.3 Comparison Between Ashby's Void Growth Theory and The Continuum Theory of Creep Damage

The general equation for damage rate and strain rate due to creep were given by equations (1.32 and 1.33). For the purpose of the present comparison, the equations are re-written using the assumption n = q and m = r (Penny (1974)) ; therefore :

$$\dot{\omega} = \dot{\omega}_0 \left(\frac{\sigma_1}{\sigma_0}\right)^m \left(\frac{1}{1-\omega}\right)^m \tag{1.46}$$

$$\dot{\varepsilon} = \dot{\varepsilon}_0 \left(\frac{\sigma_1}{\sigma_0}\right)^n \left(\frac{1}{1-\omega}\right)^n \tag{1.47}$$

where $\dot{\omega}_0$ is a temperature-dependent rate constant, like $\dot{\varepsilon}_0$

Equations (1.46 and 1.47) in their present form can be compared with Ashby's void growth equations of power-law creep and diffusion.

In simple tension, the shaded slab containing the void in Figure-1.8c extends at a rate determined by the net section stress $\sigma_{eff} / (1-f_h)$, while the rest of the cylinder (unshaded) extends at a rate determined by σ_{eff} alone. The result is that the shaded slab dilates, causing the holes to grow. Thus the damage rate and strain rate equations for voids growing by power-law creep are given by

$$\frac{1}{\varepsilon_0}\frac{df_h}{dt} = \frac{1}{\alpha}\left[\frac{1}{(1-f_h)} - (1-f_h)\right]\left(\frac{\bar{\sigma}}{\sigma_0}\right)^n \tag{1.48}$$

$$\frac{1}{\varepsilon_0}\frac{d\varepsilon}{dt} = \left\{1 + \frac{2\,r_h}{\alpha\, d}\left[\frac{1}{(1-f_h)} - 1\right]\right\}\left(\frac{\bar{\sigma}}{\sigma_0}\right)^n \tag{1.49}$$

In the equations (1.46) and (1.47), if m = n and $\dot{\omega}_0 = \dot{\varepsilon}_0$ and f_h is large, then the term ($1-f_h$) in equation (1.48) can be neglected. Therefore, it becomes identical to equation (1.46). However, if f_h is small, then the damage rate equations for the two theories become :

$$\dot{\omega} = \dot{\omega}_0 \left(\frac{\sigma_1}{\sigma_0}\right)^m \tag{1.50}$$

and $\qquad df_h / dt = 0$

According to the continuum damage theory, the damage rate equation (1.50) is finite, even if there is no damage ($\omega = 0$) , while Ashby's theory predicts zero damage rate (non-existent holes do not grow).

The time to rupture can also be compared by integrating the continuum damage rate equation (1.46) between the limits used in Ashby's power-law creep mechanism as :

$$f_h = f_i \qquad \text{at} \qquad t = t_n$$

$$f_h = f_c \qquad \text{at} \qquad t = t_R$$

Assuming $m = n$ and $\dot{\omega}_o = \dot{\varepsilon}_0$ the result is :

$$t_R = t_n + \frac{(1-f_i)}{(n+1)\,\dot{\varepsilon}_0} \left(\frac{\sigma_0}{\sigma_1}\right)^n \tag{1.51}$$

when f_i is large, equation (1.48) will be identical to the equation (A4, Appendix-A), because :

$$\frac{\alpha}{(n+1)\,\varepsilon_0} \ln\left[\frac{1}{(n+1)\,f_i}\right] \left(\frac{\sigma_0}{\sigma_1}\right)^n = \frac{(1-f_i)}{(n+1)\,\varepsilon_0} \left(\frac{\sigma_0}{\sigma_1}\right)^n \tag{1.52}$$

The rupture time will, therefore, be the nucleation time, t_n. However, when f_i is small, Ashby's power-law creep equation (A4) will predict much longer lives because the holes, when small, grow more slowly. Similar differences exist in rupture strains under the same conditions.

Under multiaxial loading conditions, the strain rate and the damage rate are accelerated in Ashby's power-law mechanism by two new terms which do not appear in continuum damage theory. These are the hydrostatic tension which enters through the term α (equation (A5)), and the grain size, d.

The boundary damage rate equation given by ;

$$\frac{1}{\varepsilon_0} \frac{df_h}{dt} = \frac{\phi_0}{f_h^{1/2} \ln\left(\frac{1}{f_h}\right)} \left(\frac{\sigma_1}{\sigma_0}\right) \tag{1.53}$$

can also be compared with the continuum damage equation (1.48), assuming $f_h = 1$, which makes the term $f_h^{1/2} \ln (1 / f_h) = (1 - f_h)$. Equation (1.49), with this assumption and $n = 1$ for diffusion, becomes :

$$\frac{df_h}{dt} = \phi_0 \varepsilon_0 \left(\frac{\sigma_1}{\sigma_0}\right)\left(\frac{1}{1-f_h}\right) \qquad (1.54)$$

If $\dot{\omega}_0 = \dot{\varepsilon}_0 \phi_0$, m = 1 and f_h approaches 1 , then equation (1.48) and (1.52) are identical. But when f_h is much less than 1, the two equations differ significantly. Equation (1.54) predicts the damage rate which decreases as damage grows while the continuum damage equation (1.48) predicts the steadily increasing damage rate.

Ashby's strain rate equation for boundary diffusion also becomes identical to the continuum damage equation (1.49) when f_h is close to 1 and the holes are randomly distributed, l = d. This makes the term $\ln (1 / f_h) = (1-f_h)$; therefore, equation

$$\frac{1}{\varepsilon_0}\frac{d\varepsilon}{dt} = \frac{2\phi_0}{\ln\left(\frac{1}{f_h}\right)}\left(\frac{1}{d}\right)\left(\frac{\sigma_1}{\sigma_0}\right) \qquad (1.55)$$

becomes $d\varepsilon / dt = 2\phi_0 \dot{\varepsilon}_0 (\sigma_1 / \sigma_0) (1 / 1-f_h)$

As before, the two equations differ when f_h is small.

The same conclusion holds for the surface diffusion void growth mechanism. When $f_h = 1$ it predicts identical results to that of the continuum mechanics theory but significantly different behaviour when f_h is small. The following conclusions are made from the two theories.

1) Both the theories are approximate.

2) When f_h or ω approach 1 , both theories predict identical behaviour.

3) When f_h or ω are small, the results divert significantly.

4) The physical processes which can lead to fracture due to uniaxial or multiaxial loading conditions can be explained more consistently when using Ashby's theory.

1.8 Conclusions

In this chapter a general phenomenon of creep fracture is reviewed. Different theories of fracture have been studied. The Cocks and Ashby's void growth theory is explained in detail and a continuum damage theory developed by different authors has been presented. Finally the comparison between the void growth theory and the continuum damage theory is studied. Under certain circumstances both the theories predict the similar answers.

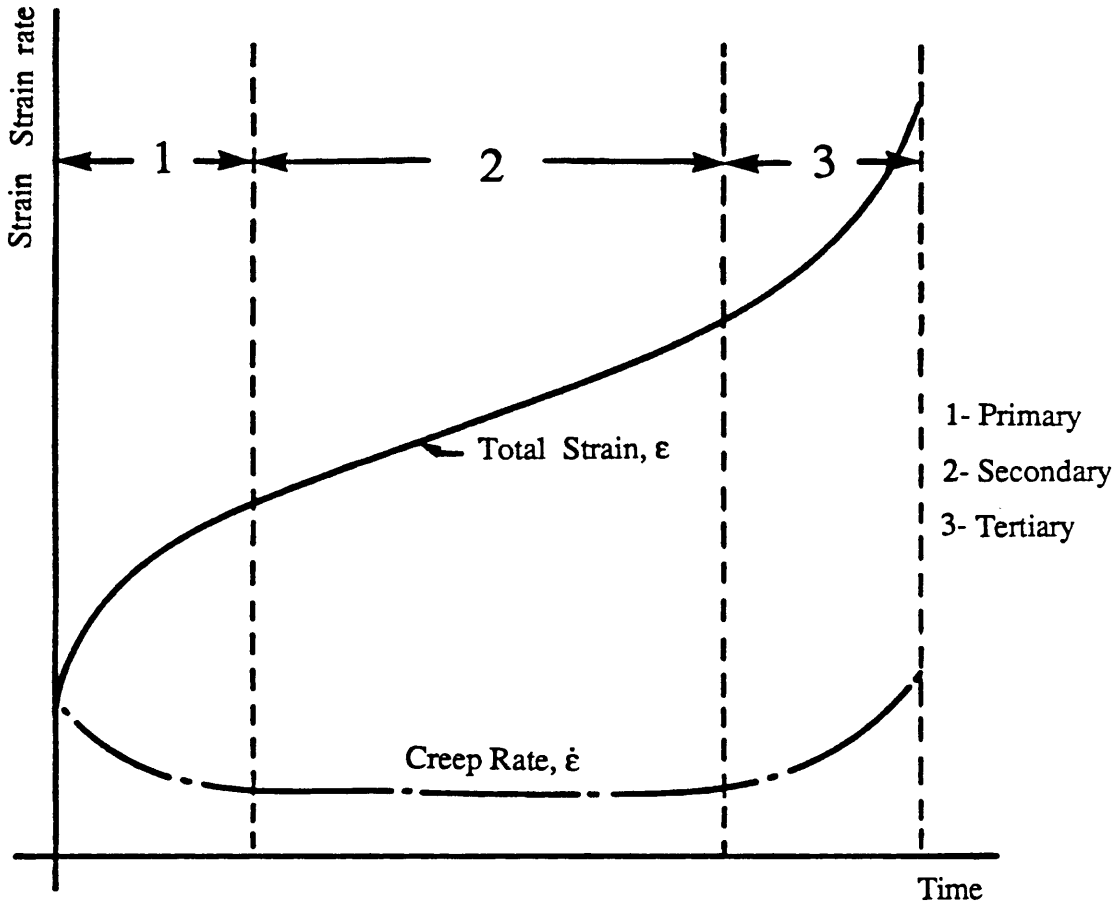


Figure 1.1 Standard creep curve

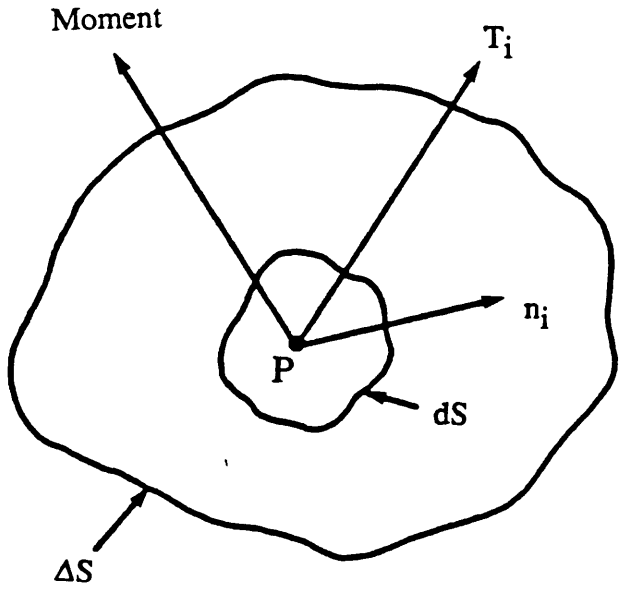
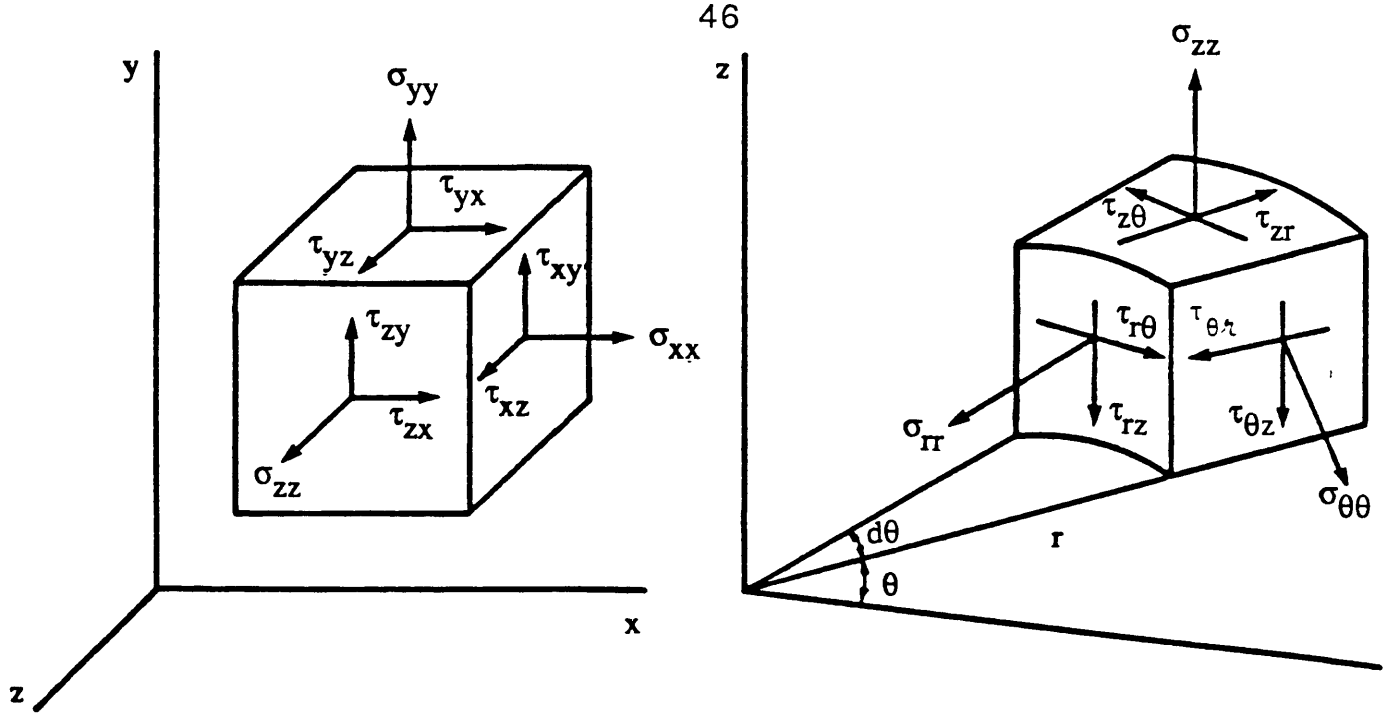


Figure 1.2 State of stress at a point



a- Cartesian coordinates

b- Cylindrical coordinates

Figure 1.3 Stress components in Cartesian and Cylindrical coordinates

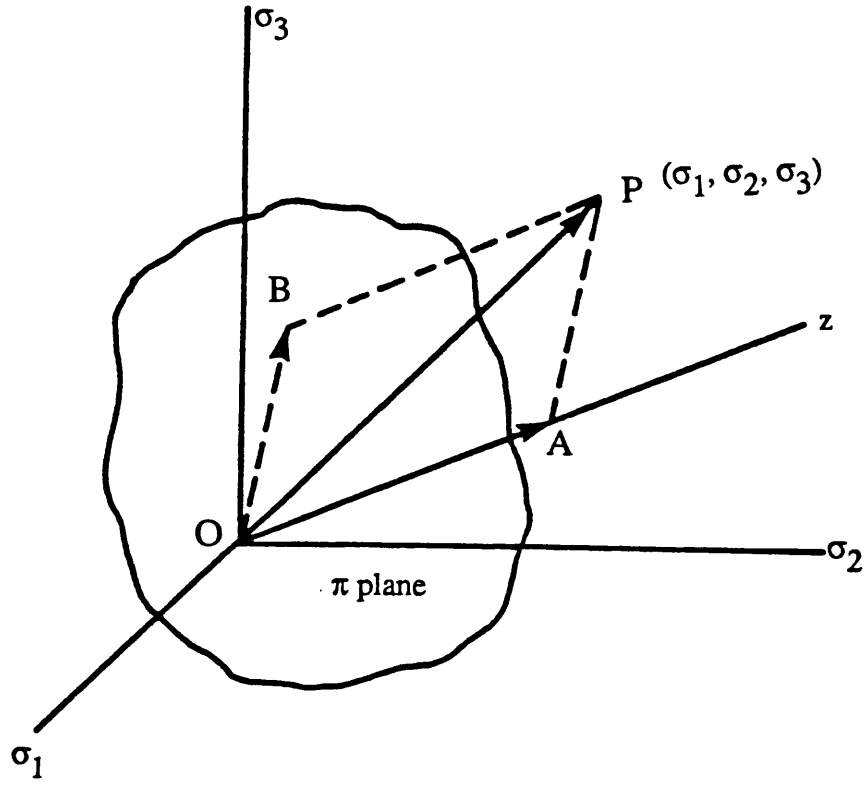


Figure 1.4 Stress space associated with principal stress coordinates.

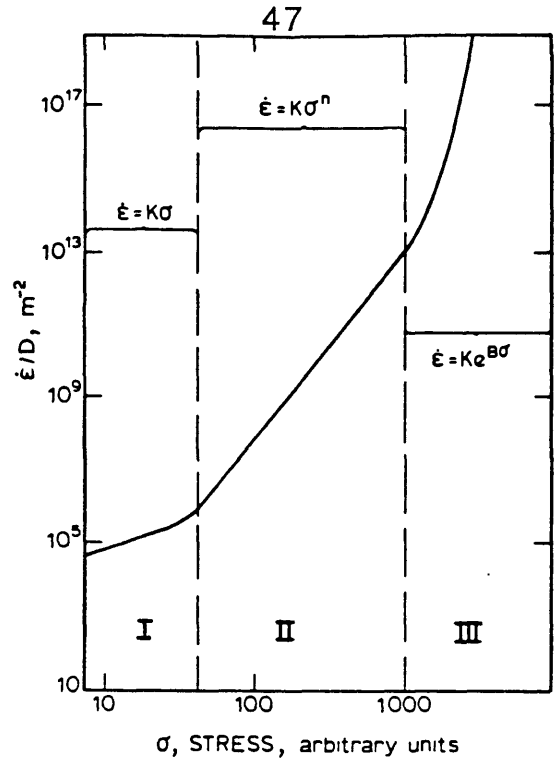


Figure 1.5 : Relationship between steady state creep rate and applied stress

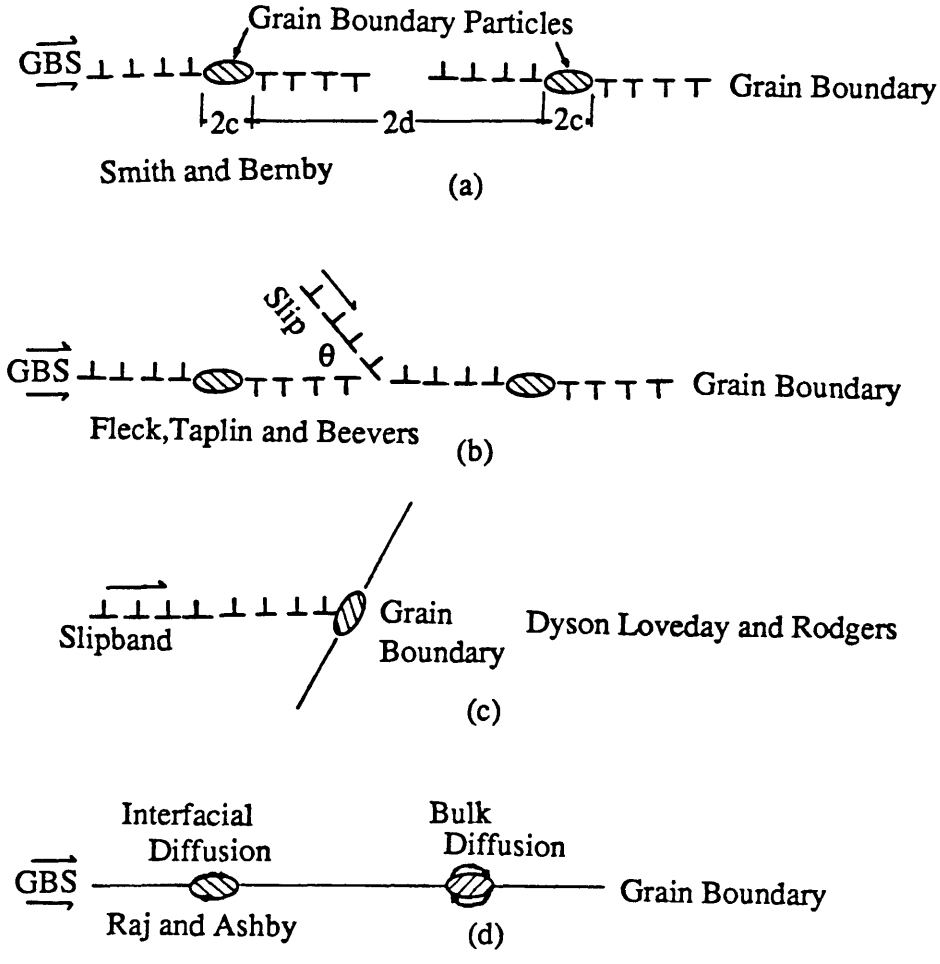


Figure 1.6 Models of intergranular cavity nucleation

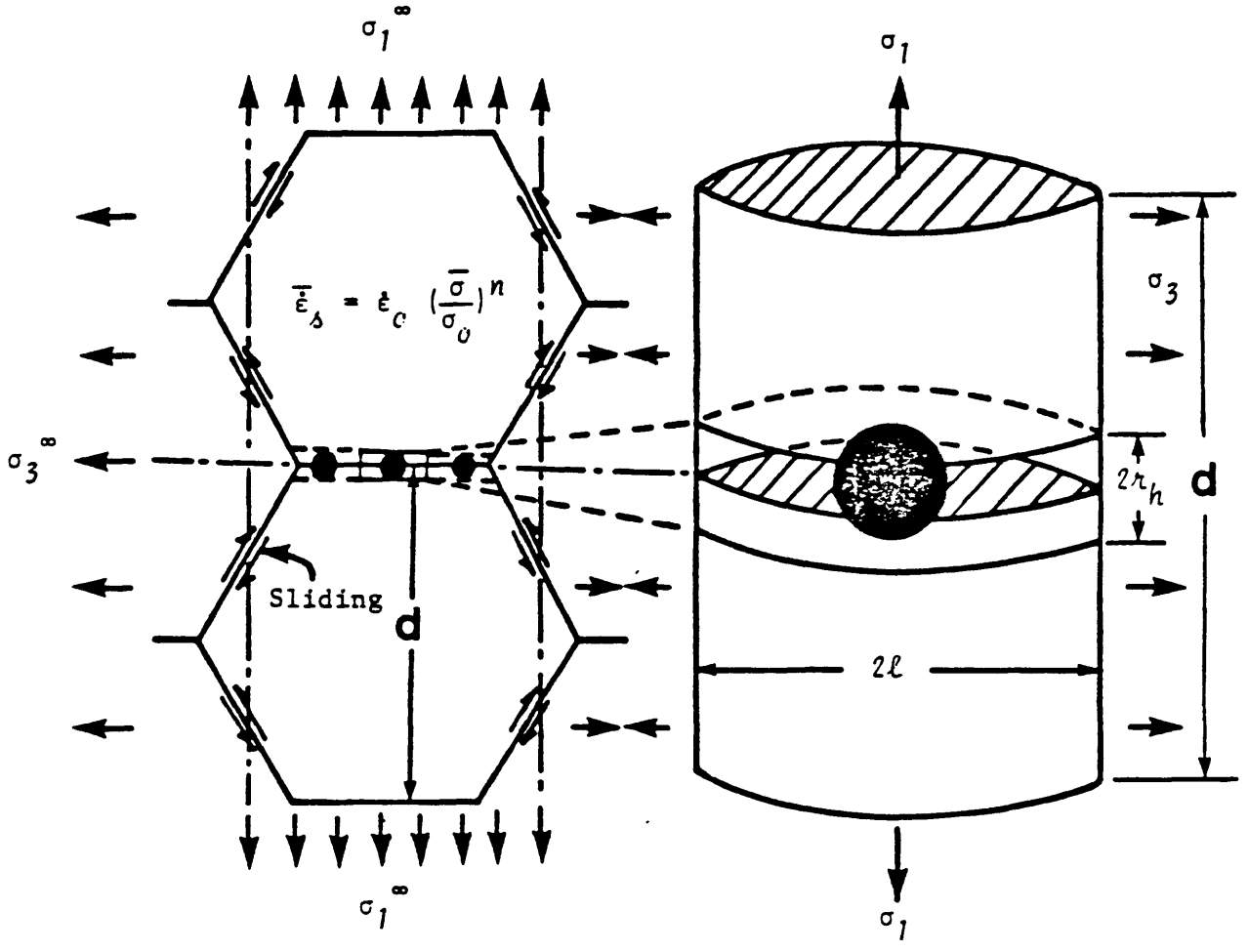


Figure 1.7 Voids growing on grain boundaries in a polycrystal subjected to local stresses σ_1, σ_3

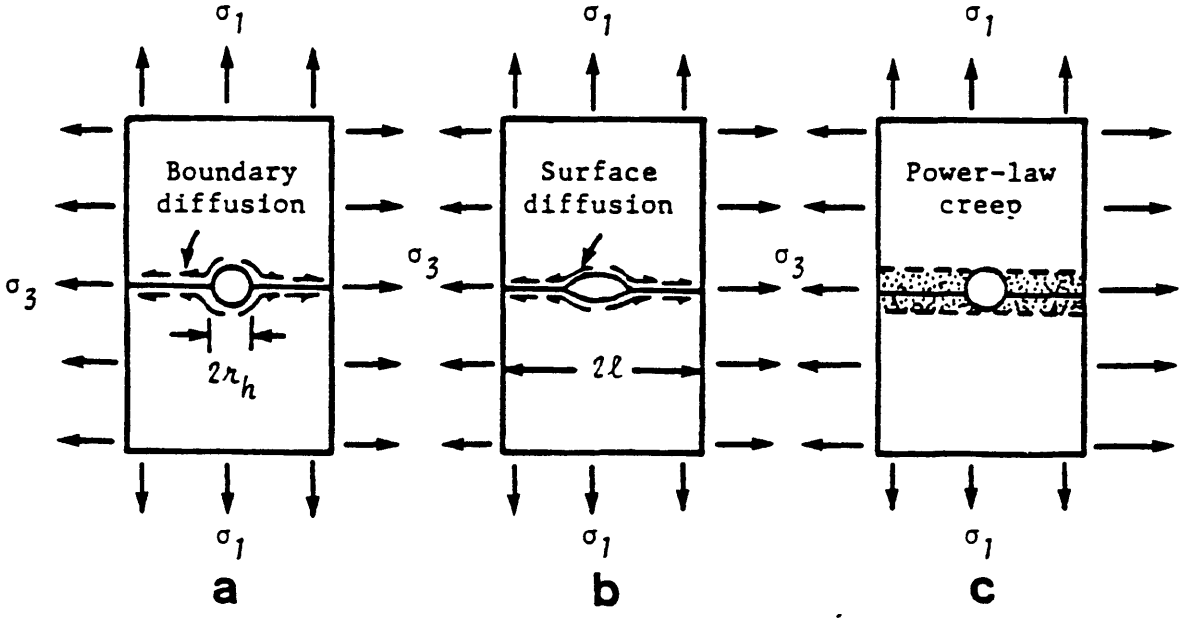


Figure 1.8 The three simple mechanisms which limit void growth

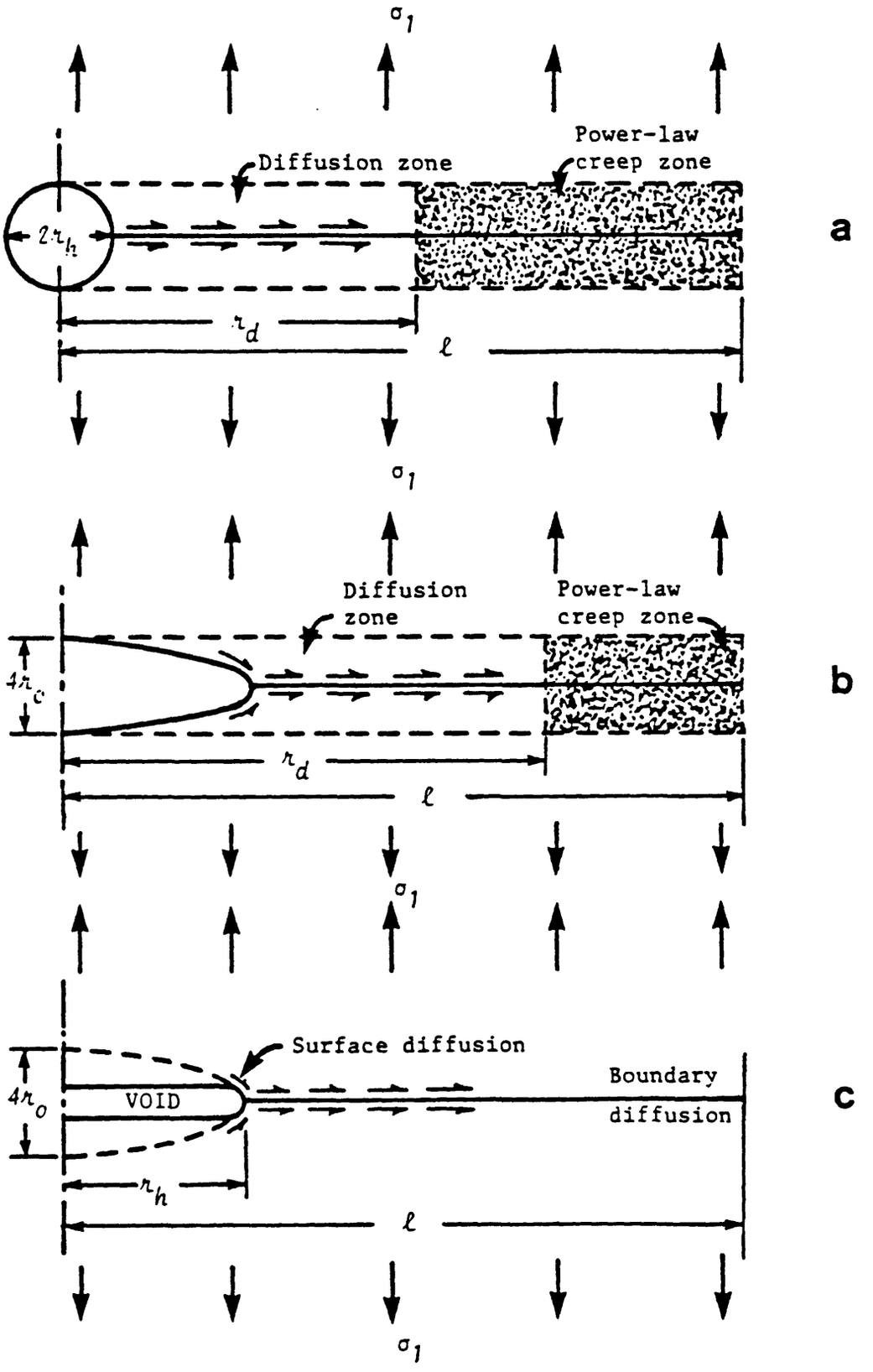
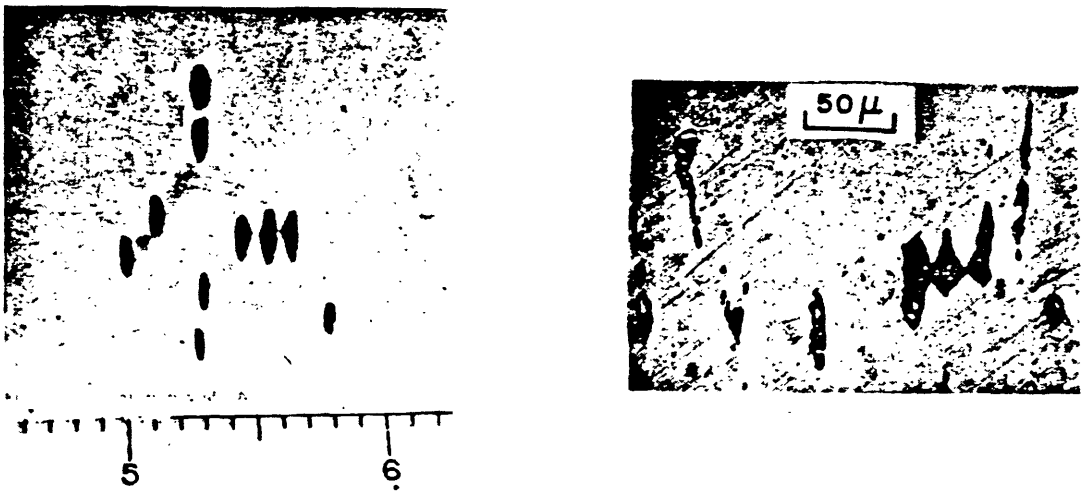


Figure 1.9 Void growth : (a) coupled boundary diffusion and power-law creep ; (b) coupled surface diffusion and power-law creep ; (c) coupled surface diffusion and boundary diffusion



(a) palsticine (b) copper

Figure 1.10 Examples of cavity coalescence in plasticine and copper

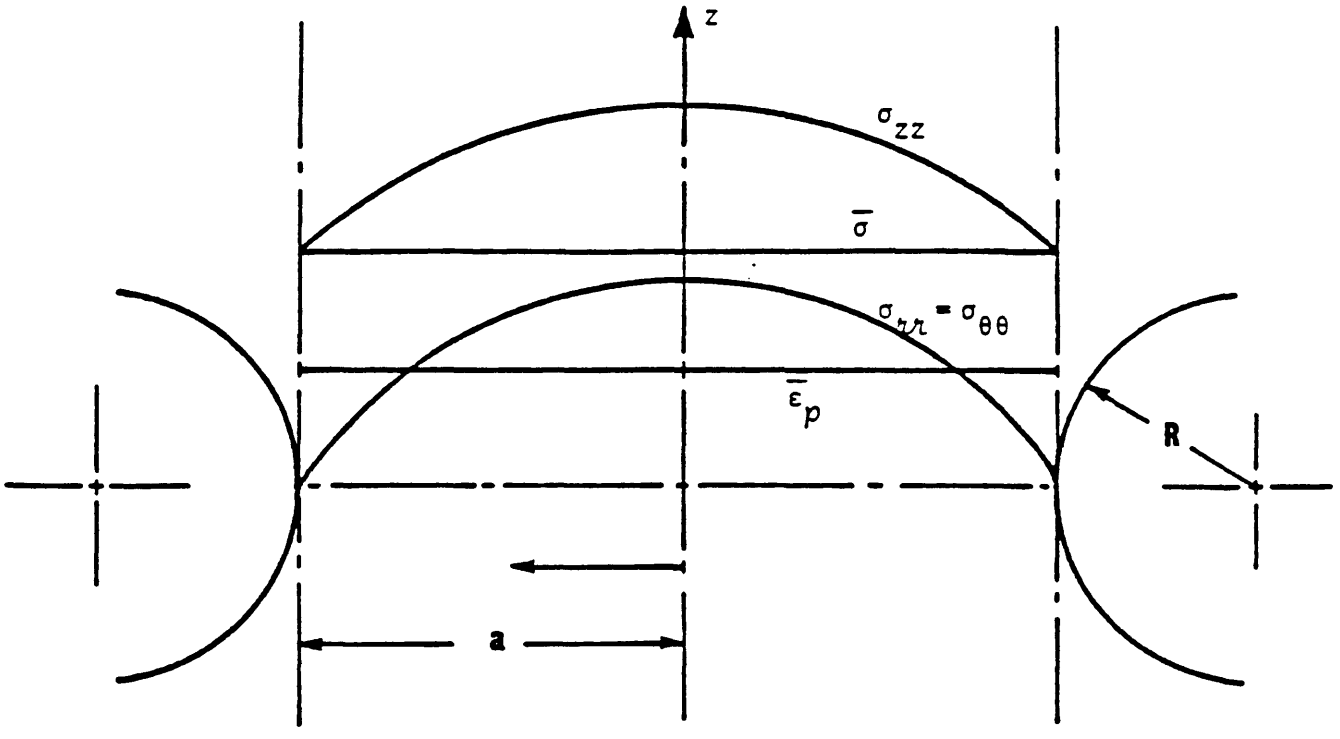


Figure 1.11 Bridgman stress and strain distributions

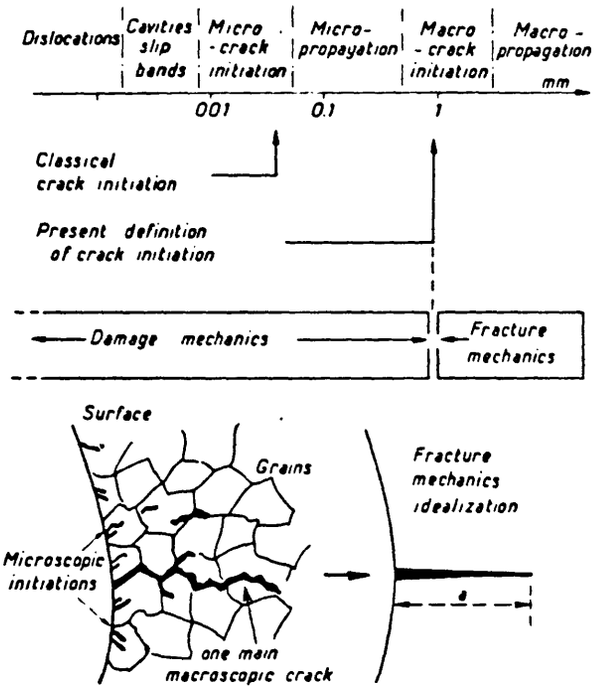


Figure 1.12 Schematic illustration of a macroscopic crack initiation concept

CHAPTER-2

CREEP RESISTANT ALLOYS

2.Introduction

Gas turbine engines , superheater header tubes, heat exchangers, nuclear fuel elements and many other such engineering structures are fabricated from metallic alloys of high creep resistance. This chapter is a brief description of the failure modes of such alloys under uniaxial and multiaxial stress condition is reviewed. A circumferentially notched bar technique is studied in detail and the necessity of carrying out the present work is explained.

2.1 Isotropic Alloys

Equipment operating at high temperature (above 0.5 times the absolute melting temperature) undergoes severedeformation during service. In such equipment creep resistant alloys have taken an important place. Common failures occurring in these alloys are :

1) Damage by loss of external section (necking).

2) Damage by loss of internal section (presence of voids or cracks)

3) Damage by degradation of microstructure.

4) Damage caused by interaction with the environment.

Several researchers have studied these failures while working with different alloys. Depending on the mode of a failure they categorised the materials as notch weakened or notch strengthened. The uniaxial ductility in notch weakened materials is higher than the multiaxial ductility while uniaxial ductility in notch strengthened materials is lower than the multiaxial ductility. For example, the notch weakening effect was observed in 1/2 Cr 1/2 Mo 1/4 V steel Ng et al. (1980) which is generally used in power plants. On the other hand, notch strengthening effect was observed in 2-1/4 Cr Mo steel at 538 ^{0}C by Al-Faddagh (1983). He carried out experiments on plain and notched bars.

He observed that the multiaxial ductility remained constant even though the notch sharpness was increased. In the present work the creep rupture data are collected on 304-H stainless steel at 760 ^{0}C and the major difference between the behaviour of 2-1/4 Cr Mo steel and 304-H stainless steel under multiaxial stress state is studied. The material properties of 304-H stainless steel are tabulated in Table-2.1 and the material properties of 2-1/4 Cr Mo steel are tabulated in Table-2.2.

2.2 Experimental Methods for Multiaxial Creep Tests

Equipment which operates over a long period of time at elevated temperatures may suffer excessive deformation or fracture due to creep. Since many components experience a triaxial state of stress as a result of a applied loading conditions or local sharp changes in section, there is a need to predict their life both theoretically and experimentally. Different techniques of simulating a multiaxial state of stress in the laboratory are summarised as ;

1) Torsion test of tubular and solid bars,

2) Double shear technique,

3) Circumferentially notched bar uniaxial technique,

4) Internally pressurized tubes,

5) Uniaxial tension plus hydrostatic pressure.

A uniaxial circumferentially notched bar technique is widely covered in the literature. The state of stress in the notch root can be altered systematically by changing the notch root radius. But the most important question is, how to measure this state of stress quantitatively through the experimental procedures. Numerical techniques (such as Finite Element method) provide the answer to this query. Thus, researchers have used the combination of uniaxial and notched bar rupture data with numerical data to predict the life of components in service.

2.2.1 Theoretical Prediction of Notch Rupture Strength

Results of experimental uniaxial and notched bar creep tests are usually interpreted in terms of notched to unnotched lives or strength ratios. When the time ratios are used in the presentation, the following condition is applied

$$\sigma_{nom} = \sigma_{un} \qquad (2.1)$$

therefore $$t_{no} / t_{un} = s_t \qquad (2.2)$$

where t_{no} is the failure time of a notched specimen due to an applied nominal stress, σ_{nom}, on the minimum section, and t_{un} is a failure time of a uniaxial specimen under a similar applied stress, $\sigma_{nom} = \sigma_{un}$.

Similarly when stress ratios are presented, the condition is ;

$$t_{no} = t_{un} \qquad (2.3)$$

therefore $$\sigma_{nom} / \sigma_{un} = s_s \qquad (2.4)$$

where σ_{nom} is the stress on the minimum section of a notched bar that fails in a time t_{no}, and σ_{un} is the stress in the uniaxial specimen that fails in the same time, t_{no} equal to t_{un}. The materials are said to be notch strengthened if s_t and s_s are greater than 1, but notch sensitive if s_t and s_s are less than 1.

Previous work has indicated that notch strengthening and notch weakening can both be observed, depending upon the material and test conditions. Detailed analysis of notch strengthening and notch weakening is presented by Davis and Manjoine (1967) in their work on different alloys. Their main conclusion is that, even though the materials have the same unnotched ductility, they do not necessarily have the same notch sensitivity. For metals with 10% or less unnotched elongation the notch effect may be strengthening or weakening depending on the notch sharpness. Examining the effect of grain size, they found that with the same unnotched ductility or hardness, the notch sensitivity of an alloy increases with increasing grain size. But, they showed a negligible size effect with a constant depth notch when the root area was varied by 36 %. Newman et al. (1953) were able to prove that the weakening effect of notches observed in stress rupture tests, is a time and

temperature dependent phenomenon. In addition they postulated that the notch sensitivity observed in a number of heat resistant alloys may be related to structural changes taking place during the course of the test. Garofalo (1959) extended the view of notch strengthening and weakening towards the austenitic stainless steels. He tested mainly 304, 316 and 321 stainless steels at two different temperatures. He showed the relationship between creep rupture strength and the instability which generally occurs in the relationship between the logarithm of rupture time for both notched and unnotched specimens. In very general terms, for materials exhibiting less than 10% elongation of unnotched bar, the presence of a mild notch usually causes notch strengthening. If a more severe notch is employed, notch embrittlement usually , but not always results. A study by Yoshida and Suwezawa (1962) on Mo Cr steel revealed that both single and double notched specimens were locally stretched considerably. In the case of single notched specimens the a / R ratio was decreased markedly , as a result of increasing radius R and decreasing diameter a. At the same time the structure was found to be stretched and oriented in the circumferential direction. In successive attempts to explore the facts about notch strengthening, Hanink (1962) proved that even the material with less than 1 % ductility permitted notch strengthening from mild notches. Thus peak rupture time depends on additional factors and is not a simple reflection of one specific notch geometry. A " Z " shaped stress-rupture time curve was observed by Couts et al. (1962) while dealing with V-57 alloy. They observed that transition from a lower leg of the curve to the upper one occurred over the range of nominal stresses where plastic strain near the notch load application became appreciable.

An atmospheric effect on notch strengthening and weakening was observed by Shainian (1964) with Nickel, Nichrome V, Udimet 500 and Inconel X under the vacuum and air at two different temperatures. The creep rupture strengths of all the alloys were either raised or lowered in an air atmosphere compared with in a vacuum

depending upon temperature, stress and microstructure. The greater atmospheric effect was due to the longer rupture lives experienced by notched bars. The atmospheric effect was found to be reversed in Inconel X by changing the microstructure. An air atmosphere was more prone to promote intergranular cracking.

Ellison and Wu (1983), while dealing with 1 Cr Mo V steel, observed the notch strengthening effect. Detailed experiments carried out by Al-Faddagh (1983) on 2-1/4 Cr Mo steel revealed considerable notch strengthening effect. An interesting part of the results is that, even after increasing constraint, rupture time was fairly constant. This indicates that the material is not notch sensitive under the conditions in which experiments were carried out. Recent work on SS 304 by Yoshida et al. (1986) confirmed that the notch strengthening effect prevailed in all notch geometries investigated. Maximum intergranular damage occurred in the centre of the blunt notch. Damage was more pronounced slightly ahead of the notch in sharp notch geometries. Some aged specimens were found to have very high critical damage , indicating intense cracking.

As mentioned in the literature above, some materials will always notch strengthen with an increase in constraint, while others will change from notch strengthening to notch weakening after a certain amount of constraint.

2.3 Stress Distribution In Circumferentially Notched Bars

Through the use of experimental results, it is possible to prove quantitatively, whether the material is notch strengthening or notch weakening under multiaxial stress conditions. But, from a design point of view, it is important to know the variation of effective stress , maximum principal stress and hydrostatic stress, which play a important role in final fracture across a neck of a notch. Bridgman (1952), first gave the detailed analysis for distribution of stresses across a neck of a bar. His

analysis was based on the slip line field method. He estimated the radial and hoop stresses to be the same. Flow stress which is generally used for the analysis was found to be less than the average tension. To obtain the correct value of flow stress, he introduced the correction factor by which the average tension has to be multiplied to get correct value of flow stress. This correction factor is given by,

$$\text{Correction Factor} = \{[\, 1+\frac{2R}{a}\,] \log [\, 1+ 0.5\, \frac{a}{R}\,]\,\}^{-1} \qquad (2.5)$$

The first step to find out the steady state stress across the notched bar, was taken by Hayhurst and co-workers (1977). Their successive findings led to the full understanding of variation of complex stress pattern across the notch. In the first published work by Hayhurst (1977), they suggested two types of notch geometries. One was the Bridgman notch (semicircular notch) and the second was the British standard notch. The notches were found to have different characteristics. The stationary state stress distribution in a semicircular notch was smooth and for some values of the stress index n was reasonably constant across the throat of the notch. The B. S. notch attained full constraint, only in the local sense, by the development of peaks in the stress distribution. In the region of peaks, considerable stress elevation occurred and a high ratio of $\sigma_{mean} / \sigma_{eff}$ was observed. In the subsequent paper by Hayhurst et al. (1977), they introduced three more notch geometries in order to investigate the change in axial stress variation with change in a / R. They confirmed that blunt notches are most suitable for use in subjecting volumes of material to multidimensional states of stress.

Ellison and Wu (1983), Al-Faddagh (1983) and Wu et al. (1984) studied a wide range of geometries. In all the studies mentioned above, a blunt notch shows uniform stress distribution across a notch throat, while a sharp notch shows high values of stresses near the notch root. Wu et al. (1984) argued that, in the case of less constrained geometries, since the stress distribution is fairly constant, creep spreads throughout the notch region. Thus the failure is a global event. In the case of

highly constrained notches, the creep zone is small and localized. Thus the failure is a local event.

The failure in these alloys is mostly due to void growth and coalescence along the grain boundaries perpendicular to the tensile stress axis. The complete phenomenon of failure of these alloys is explained in Chapter-1. To increase the creep resistance the transverse grain boundaries were eliminated by improving the solidification process and thus DS alloys and Single crystal alloys have been developed. Details of strengthening mechanisms of creep resistant alloys are given in section 2.5.

2.4 Directionally Solidified Alloys

Since the introduction of gas turbines in the 1930's, the efficiency of turbine engines has been improved considerably by the development of turbine blade materials. Early improvements were brought about by the introduction and optimization of solid solution and γ' strengthened nickel-base superalloys. The most important trend in the development of nickel-base superalloys has been the increase in volume fraction of strengthening γ' particles and the temperature in which they dissolve in the γ matrix. But it was recognized that fracture of such polycrystalline materials at high temperature was generally initiated at grain boundaries lying transverse to the applied stress. Versnyder and Guard (1960) were the first to solve this problem by introducing longitudinal grain structure by directional solidification. During their experimental work with Mar M200 they observed the following facts which are clear from Figure-2.1.

1) The fracture resistance as indicated by rupture ductility and time to the end of the second stage of creep is greatest for a longitudinal structure and less for equiaxed and transverse structures.

2) The creep resistance of longitudinal and transverse grain structures in the

early part of the curve is similar.

3) The equiaxed grain structure has higher resistance to creep deformation but lower resistance to fracture than columnar structure.

Increasing the rupture life by minimizing transverse grain boundaries did not yield results up to expectations. It had been observed that solid parts behave quite satisfactorily in the directionally solidified condition,whereas hollow parts of the type used in advanced air cooled engines sometimes experience longitudinal grain boundary cracking during casting or during bi-axial stress test. The main reason was thought to be the presence of second phase particles. This problem was tackled by the addition of 1.5-3.5 wt. pct. Hf to directionally solidified Mar M200 to strengthen the grain boundaries. Kear et al. (1967) explained the effect of Hf addition on transverse grain boundary failure and ductility. By adding Hf they found that the creep properties were improved due to strengthening of longitudinal grain boundaries. The chemical composition and the material properties of the material under consideration in the present work are given in Table-2.3 and 2.4 respectively.

2.5 Strengthening Mechanisms in Superalloys

It is now accepted that γ' strengthening is the most important feature of advanced nickel-base superalloys. The particles act as a barrier to the motion of dislocations through the matrix and the flow can not occur until a critical, or threshold, stress that enables the barrier to be surmounted, has been exceeded. There are three mechanisms by which dislocations can overcome these obstacles and separate threshold stress can be associated with each of them. Only those processes having threshold stress less than the applied stress can be activated and the fastest of these will be the dominant deformation mode. The three mechanisms which have been identified are ;

1) Bowing between particles.

2) Cutting of particles.

3) Dislocation climb over particles.

The detailed treatment of the athermal processes, particle cutting and bowing as described by Brown and Ham (1971) are fairly generally accepted and give critical shear stresses for these processes.

a) Bowing between particles.

Here it is envisaged that dislocations remain in their glide planes and can penetrate an array of particles by an Orowan bowing mechanism when a critical stress τ_c exceeded where

$$\tau_c = A\,(\mu b / 2\pi\lambda)\,\ln(\lambda / r_0) \qquad (2.6)$$

where $A = 1/2\,((2-\upsilon)/(1-\upsilon))$, λ is the particle spacing and υ is Poisson's ratio.

(b) Cutting of particles

As the matrix dislocation passes through an ordered precipitate, like γ', it creates disorder which increases the energy of the system by the antiphase-boundary energy γ. Brown and Ham showed that for the passage of a single dislocation

$$\tau_c = \left(\frac{\gamma^2}{b}\right)^{\frac{3}{2}} [\,2af / \pi\Gamma\,]^{\frac{1}{2}} \qquad (2.7)$$

where f is the precipitate volume fraction, a is the particle diameter and Γ is the dislocation line tension. However, pairs of dislocations can pass through particles with a lower stress where the second annihilates the antiphase boundary created by the first. Three cases have been identified by Brown and Ham :

i) When the dislocation pairs are straight, i. e. $a < \pi\,\Gamma\,f / 2\gamma$, then the particles have little influence on the flow stress.

ii) When the first dislocation bows but the second remains straight, i. e. $\pi\,\Gamma\,f / 2\gamma < a < 2\Gamma / \gamma$, then

$$\tau_c = \gamma / 2b\,[\,(2\,a\,f\,\gamma / \pi\,\Gamma)^{1/2} - f\,] \qquad (2.8)$$

iii) When both dislocations are contoured ($a > 2\Gamma / \gamma$) then

$$\tau_c = \gamma / 2b \left[(4f/\pi)^{1/2} - f \right] \qquad (2.9)$$

(c) Climb over particles

In this case when a gliding dislocation is arrested at an array of particles its delay is only temporary if it can by-pass these obstacles by extending part, or all of the dislocations by climbing out of the glide planes to avoid the particles. Brown (1982) described the climb process as localized climb and general climb. In a localized climb most of the dislocations remain in the glide plane and a small segment profiles the particle while in a general climb all of the dislocations move out of the glide plane. These lead to two different threshold stresses.

$$\tau_{c1} = \sigma_b / \sqrt{2} \quad \text{(for localized climb)} \qquad (2.10)$$

$$\tau_{gc} = f^{\frac{3}{2}} / 2^{\frac{5}{4}} \sigma_b \quad \text{(for general climb)} \qquad (2.11)$$

where σ_b is the Orowan bowing stress.

It is argued that the localized climb can occur more rapidly because it involves less mass transport and will be the dominant climb mechanism when activated. However, general climb has a lower threshold and may cause lower rates when localized climb is suppressed.

2.6 Mechanical Behaviour of Superalloys

Pure metals and many of the single phase alloys are characterized by an extensive constant creep-rate regime followed by a much shorter tertiary creep regime. However, for multiphase alloys such as the nickel-base superalloys, the constant creep rate is rarely observed. Kear and Pearcy (1967), while estimating the tensile and creep properties of a single crystal of nickel-base superalloy Mar-M200, observed the failure by intergranular fracture particularly along those grain

boundaries oriented transverse to the major stress axis. A sharp decrease in yield stress in a temperature range of 1400 to 1800 ^{o}F was noticed, while yield stress hardly altered in a range of 70 to 1400 ^{o}F. Miles and Mclean (1977) investigated the effect of fibre orientation, to the axis of solidification, on creep rupture life of (Co,Cr) (Co , Cr)$_7$ C3 directionally solidified eutectic. They observed that there was a systematic deterioration in creep properties as the angle of fibre orientation increases from 0 to 90 ^{0}. Creep ductility was increased both with increasing the angle of fibre orientation and with decreasing stress, but the stress exponent remained constant at 5.5± 1. Figures 2.2 and 2.3 show the effect of angle of orientation on the rupture time and the ductility. Even though the time required for the dislocation to overcome an individual obstacle depends only weakly on stress, the dislocation velocity can depend exponentially on the applied stress. It comes about because as the stress increases, each particle which is overcome by climb allows a rapidly increasing number of its neighbours to be bypassed by the Orowan mechanism (Shewfelt and Brown (1977)). They developed a theory of dispersion-hardened single crystal as a function of temperature and strain rate. The creep behaviour of a series of alloys based on In 597 has been studied at 800 ^{0}C by Gibbons and Hopkins (1984). Their results showed the consistent pattern of increasing creep resistance with increasing volume fraction of the γ' precipitates, although the effect was more significant in coarse grained materials. Increasing the volume fraction of γ' precipitates increases the friction stress σ_0 and ultimately increases the creep resistance. In a coarse grained structure the dislocations have more chances to climb the γ' precipitates (obstacles). By increasing the γ' precipitates these chances are reduced. On the other hand, no significant change has been found in σ_0 in a medium and fine grained structure with change in volume fraction of γ' precipitates.

The creep and rupture behaviour of a single crystal nickel-base superalloy NASIR 100 was investigated at temperature 925 ^{0}C and 1000 ^{0}C by Nathal and

Ebert (1985). They noticed the power-law dependence on applied stress for the steady state creep rate, time to failure, time to onset of secondary creep and time to onset of tertiary creep. At 1000 ^{0}C, the γ–γ' lamellar structure was found to be fully developed in the primary stage. Strain enhanced plate thickening appeared to be the cause of onset of tertiary creep and final fracture occurred after necking by the initiation of cracks at micropores. Sunderrajan (1985) considered the combined effect of precipitate coarsening, strain induced loss of coherency and cavitation ,to explain the intergranular creep fracture of UDIMET 700. His findings showed both the time to fracture, t_f, and the Monkman Grant constant, $\dot{\epsilon}_s\, t_f$, were reduced significantly in the presence of various forms of damage. Recently Quested and Osgerby (1986) compared the mechanical properties of conventionally cast, directionally solidified and single crystal superalloys. They concluded that directional solidification improves the low cycle fatigue resistance and the creep ductility when tested parallel to the solidification direction, compared with conventionally cast materials. Directionally solidified materials show advantages in thin sections and are less sensitive to the effects of impurities compared with conventional castings. The main reason is that the modulus of elasticity in solidification direction is lower compared with the modulus of elasticity in the other directions. This causes the thermal stresses to be lower in that direction. Again the porosity levels are lower in DS castings as compared with the CC castings. These factors are responsible for the higher strength in solidification direction. Single crystal alloys, when given appropriate heat treatment show an improvement in rupture life compared with DS castings.

2.7 Friction Stress in Superalloys

For most pure metals and single phase alloys, n, the creep index is usually in the range of 4-6 and activation energy Q_c is equal to the activation energy for self diffusion (e.g. Ni-20 Cr, n = 4.6 and Q_c = 69 Kcal mol^{-1}). However, with two

phase alloys the values of n and Qc , in general, vary substantially than those for pure metals and single phase alloys (e.g. In 738 LC, n = 14 to 20 and Qc = 900 kJ mol^{-1}). These anomalously high values of n and Q_c are accounted for in terms of stress and temperature dependence on friction stress σ_0. For pure metals, single phase alloys and two phase alloys steady creep rate varies with stress and temperature as suggested by Williams and Wilshire (1973),

$$\dot{\varepsilon}_s = (\sigma - \sigma_0)^4 \exp (-Q_c^* / RT) \qquad (2.12)$$

The values of n is then determined by the magnitude of stress dependence of the friction stress σ_0

Burt et al. (1979) suggested that the magnitude of σ_0 depends not only on stress and temperature but also on size and distribution of particles in the alloy. Due to the loss of creep resistance associated with particle coarsening, acceleration in creep rate occurs during tertiary creep as observed in Ni 105. A significant improvement in creep life can be obtained by periodically reheat treating the material to restore the original γ' particle distribution. An inherent friction stress (σ_{oin}) which plays an important role during the primary stage can be obtained by extrapolation of secondary σ_0 data to zero applied stress as suggested by Evans and Harrison (1979). The stresses at which the diffusion creep begins to dominate, can also be obtained by an extrapolation procedure. With increasing temperature the (σ_{0in}) term decreases and approaches zero at the temperature where γ' precipitates goes in the solution. Evans and Knowles (1980) further confirmed the strong dependence of σ_0 on the dispersion parameter, r / λ, where r is the particle radius and λ the surface to surface particle separation. The equation for σ_0 obtained by them is given by :

$$\sigma_0 = \frac{8 \Gamma r}{3 \lambda b} \left\{ r^2 + \left[\frac{4 \Gamma}{\sigma b} \sin^{-1} \left(\frac{\sigma b \lambda}{8 \Gamma} \right) \right]^2 \right\}^{-1/2} \qquad (2.13)$$

where b is the Berger's vector, Γ the dislocation line energy and σ the applied stress.

Creep resistance of any alloy strengthened by precipitates or second phase particles can be obtained by successful analysis of individual components of the friction stress as shown by Stevens and Flewitt (1981). They observed the creep strain rate proportional to the third power of effective stress. At low applied stress the creep rate was observed to be lower as compared with the creep rate at higher applied stress. With In 738 they found the values of exponent of applied stress to be 6.1 and 9.6 at lower applied stress and higher applied stress , respectively.

From the literature mentioned above, several authors have proposed the causes of progressive increase in creep rate due to steady decline in friction stress σ_0. But, Dyson and Mclean (1983) explained how the coarsening of γ' is unable to account for tertiary creep in these alloys and predicts the opposite behaviour to the previous observation that particle coarsening causes a progressive increase in creep rate due to steady decline in σ_0. According to their findings an inelastic strain is far more important than time in determining the extent of acceleration of strain rate. Tertiary creep rate is produced by at least two competing strain softening damage micromechanisms. One is fracture damage by cavitation and cracking while the other is caused by the accumulation of dislocations.

With the same concept of inelastic strain responsible for increase in creep rate during tertiary regime, Henderson and Mclean (1983) observed that σ_0,

a) decreases slightly with increasing γ' cuboid size,

b) it is sensitive to initial applied stress with the stress range studied,

c) decreases slightly with increasing temperature,

d) remains fairly constant during creep and decreases more in an alloy with finer γ' particles than in the alloys with larger, more stable cuboids,

e) is associated with the threshold stress for local climb in the alloy studied.

In particle strengthened superalloys, particles act as obstacles to dislocation

motion that may be overcome by a variety of competing processes, each of which has an identifiable threshold stress which must be exceeded before it is operative. Mclean (1985), Henderson and Mclean (1985) through their successive work proved that strain induced loss of coherency should make it easier for the matrix dislocation to climb. The data collected by them showed that creep strain leads to a much higher density of interface dislocations than results from the loss of coherency by particle coarsening during simple ageing. Thus creep strain, at least when plasticity is controlled by dislocation climb around γ' particles, leads to a significant change in the structure of the particle / matrix interface that may contribute to the deformation characteristics. The transition from coherent to incoherent particles takes place when the particle exceeds a critical radius below which it can not support a dislocation loop at its interface. The accumulation of such misfit dislocations is accelerated by plastic deformation and thus the nature of the γ–γ' interface changes much more rapidly due to accumulated creep strain than to particle size. As the incoherent boundaries are more efficient sources and sinks of vacancies they may provide a faster diffusion path than the coherent surfaces. This could enhance the climb process by making mass transport more rapid. The overall effect is that the recovery rate will be enhanced. This concept of recovery creep explains the early onset of tertiary stage. Han and Chaturvedi (1987) studied the effect of friction stress on creep deformation of In 718 alloy. They established the value of effective stress exponent, n_e , between 1.2 and 5.9. They confirmed that these values were attributed to the transformation of diffusional creep to power-law creep when the temperature and applied stress was increased.

2.8 Fracture of Superalloys

Simple wrought superalloys such as Nimonic 80A and other cast superalloys at low stresses are governed by the failure mechanism of nucleation, growth and

linkage of voids at grain boundaries. But more advanced wrought and cast superalloys at higher stress levels have suggested that creep failure occurs by the initiation of cracking at the edge of the specimen or component and its rapid propagation through the section along transverse grain boundaries.

In directionally solidified alloys, since the transverse grain boundaries are eliminated, cracks are constrained to propagate through, rather than between, grains. The cracks nucleate in a variety of ways depending on the detailed microstructure. For example, (a) small cracks segments can be associated with transverse components of longitudinal grain boundaries (either at a surface or within the specimen) and (b) wedge cracks starting at intermediate carbides extended into the bulk alloy. Experimental results on In 738LC directionally solidified alloy suggested that there are insufficient potential cracks to allow interaction by linkage and failure must occur by a single crack slowly propagating across the specimen section as shown in Figure-2.4 and 2.5 by Mclean (1983).

2.9 Multiaxial Stress State in Superalloys

However, before these materials can be used confidently in practical applications, much work is needed to provide design information and to develop relevant design methods. To satisfy design requirements, creep analysis has to be carried out under multiaxial stress conditions experimentally and theoretically. Pandey et al. (1985) examined the smooth and circumferentially notched bars, with a Bridgman notch geometry, of IN X-750 at 700 ^{0}C. Their results indicated that the material was notch strengthened on the basis of net section stress $\sigma_{nom.}$ However, when the fracture life-times were plotted as a function of Bridgman effective stress, σ_{eff}, all data points fell approximately on one line. The notch rupture ductility in notched specimens was found to have a lower value than in smooth ones at all stresses. Sugimoto et al. (1985) examined the effects of crystallographic orientation and thickness of specimen on notch tensile creep strength of single crystals of

UDIMET 520 at 700, 850 and 900 ^{0}C. They observed that the notch tensile creep strength of thin specimens depends on crystallographic orientations, not only in the tensile direction but also in nominal direction of the specimens. The thick notched specimens were found to exhibit great creep resistance regardless of the crystallographic orientations.

Directionally solidified and single crystal alloys are highly anisotropic in their creep properties, and it is this aspect which is more critical in design. Johnson (1977) developed general equations for secondary creep of transversely isotropic materials. His equations are characterized by three material constants . Two constants can be obtained by uniaxial creep tests in two directions mainly in the fibre direction and in a direction transverse to fibres. A third constant can be obtained by shear creep test in a direction parallel to the fibres. The details of his analysis are explained in Appendix-B

2.10 Conclusions

Though much work has been done in order to understand the behaviour of the stress distribution across the notch throat of isotropic materials, still more information is needed to fulfill design requirements. Hayhurst and coworkers (1977) explained the notch strengthening and weakening phenomenon based on a finite element model, but they have analysed very few notch geometries, which does not help when slit type of notch geometries are incorporated. Ellison and Wu (1983) analysed various notch geometries, varying from Bridgman notch to the slit type notch. In their analysis they restricted the geometrical parameters such as b / a and a / R ratio. Data obtained by these authors can not be generalized for creep design. Hence, a step is taken to generate more data based on the finite element model and compare the same with experimental data. In the present work, several notch geometries are analysed and 304-H stainless steel is selected for the uniaxial and

multiaxial experimental analysis. The data on 2-1/4 Cr Mo steel are collected from the literature. A comparison has been made between 2-1/ 4 Cr Mo steel and 304-H stainless steel. A major difference has been pointed out between their rupture ductility under multiaxial stress state using a finite element numerical analysis and metallographic analysis in Chapter-5.

It is observed that not much work has been done on creep under multiaxial stress state conditions on directionally solidified or single crystal alloys which are anisotropic in nature. On the analytical side, there is no literature available which can provide an exact indication of stress state in complicated structures. Coupling of experimental creep data with numerical prediction can lead to better understanding of the behaviour of these alloys in service conditions. Therefore it has been decided to carry out a series of creep tests on smooth and notched bars at $900 \pm 4\ ^{0}C$ of directionally solidified Mar M002 alloy. It was also decided to develop a finite element program which can be used to assess the stress distribution across a notch throat of the geometries under consideration.

TABLE-2.1

Material Properties of 304-H Stainless Steel at 760 ^{0}C

Young's Modulus	Ultimate Stress	Yield Stress	Failure Strain	Reduction in Area
E (GPa)	σ_{uts} (MPa)	σ_y (MPa)	ε_f (%)	A_f (%)
151	202	166	80	84

TABLE-2.2

Material Properties of 2-1/4 Cr Mo Steel at 538 ^{0} C

Young's Modulus	Ultimate Stress	Yield Stress	Failure Strain	Reduction in Area
E (GPa)	σ_{uts} (MPa)	σ_y (MPa)	ε_f (%)	A_f (%)
166	320	166	34	80

TABLE-2.3

Chemical Composition of DS Mar M002

	C	Si	Mn	S	Al	Ba	Co	Cr	Cu	Fe
Max	0.17	0.20	0.20	0.01	5.75	0.02	11.0	10.0	0.10	0.50
Min	0.13	0.00	0.00	0.00	5.25	0.01	9.00	8.00	0.00	0.00
	Hf	Mo	Ta	Ti	V	W	Zr	Mg		
Max	1.70	0.50	2.75	1.75	0.10	11.0	0.08	0.003		
Min	0.80	0.00	2.25	1.25	0.00	9.00	0.03	0.00		

Heat Treatment - 16 hours at 870 ^{0}C - Air cooled

TABLE-2.4

The elastic properties from Rolls Royce Plc. Ltd are as follows

$$E_2/E_1 = 1.33, \quad \upsilon_1 = 0.394, \quad \upsilon_2 = 0.143 \text{ and } \frac{G_{12}}{E_1} = 0.718$$

Material properties of DS Mar M002 at 900 ^{0} C

Young's Modulus	Ultimate Stress	Yield Stress	Failure Strain	Reduction in area
E (GPa)	σ_{uts} (MPa)	σ_y (MPa)	ε_f (%)	Af (%)
87	712	121	26	38

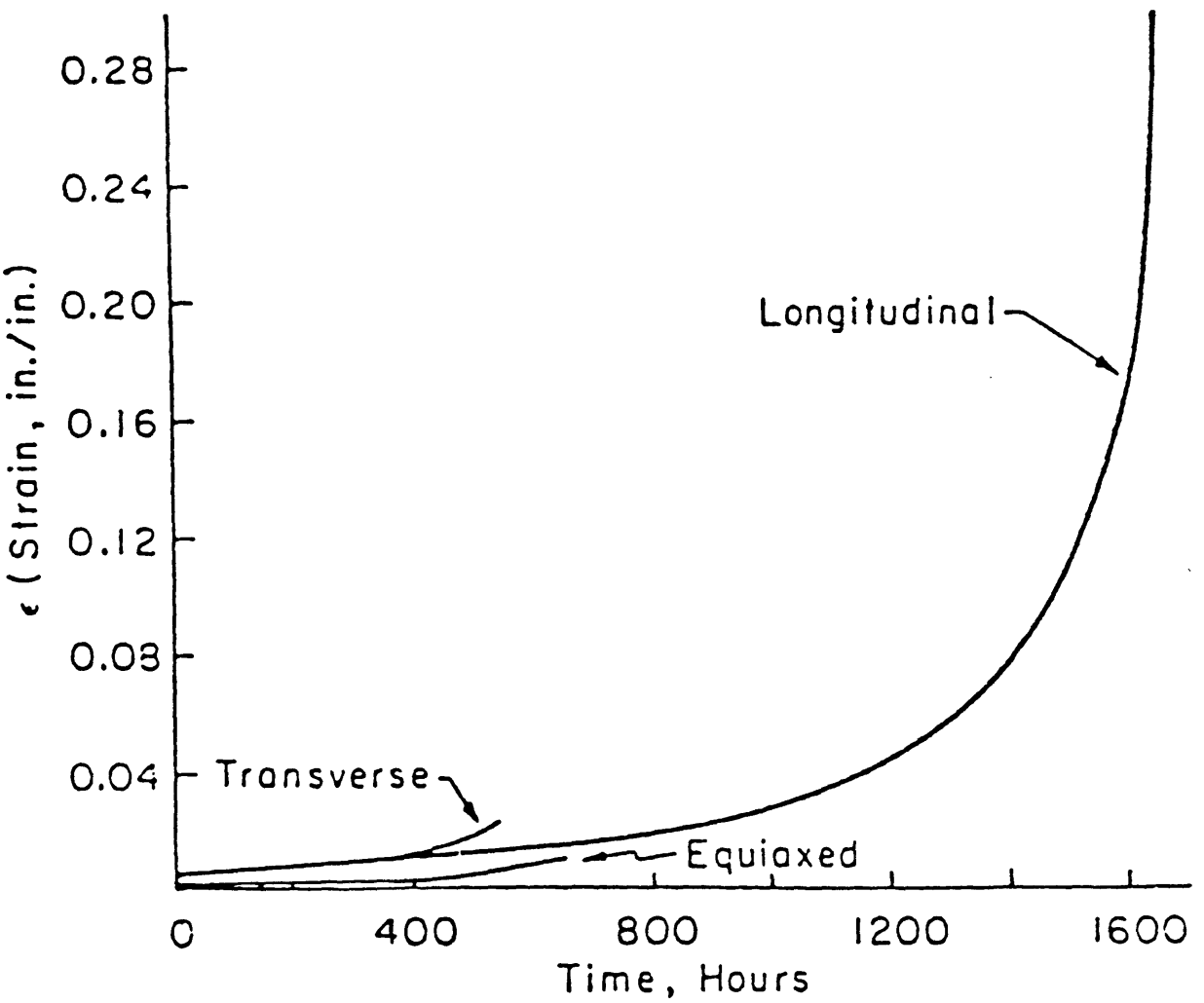


Figure 2.1 : Comparison of minimum strain rate for different structures

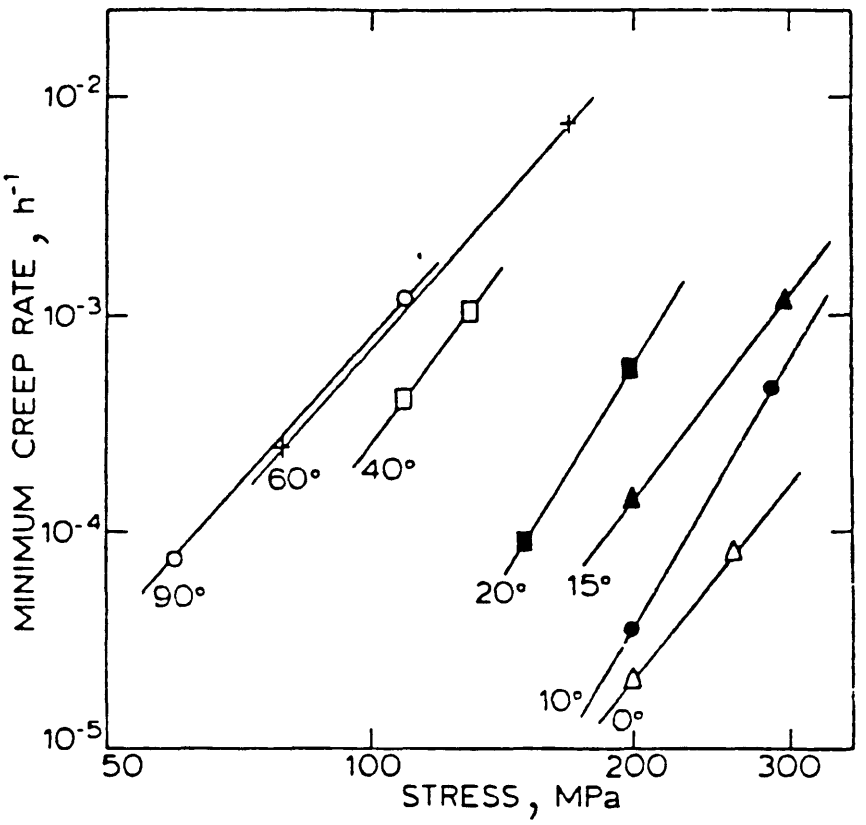


Figure 2.2 : Variation of minimum creep rate with stress for different angle of fibre orientation

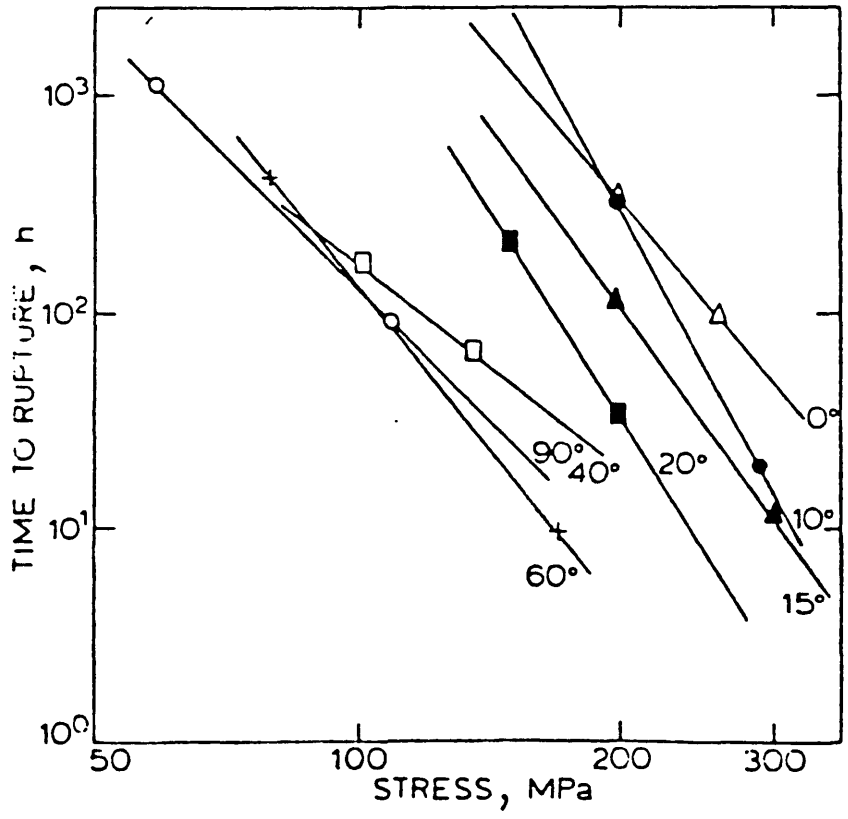


Figure 2.3 : Variation of rupture time with stress for different angle of fibre orientation

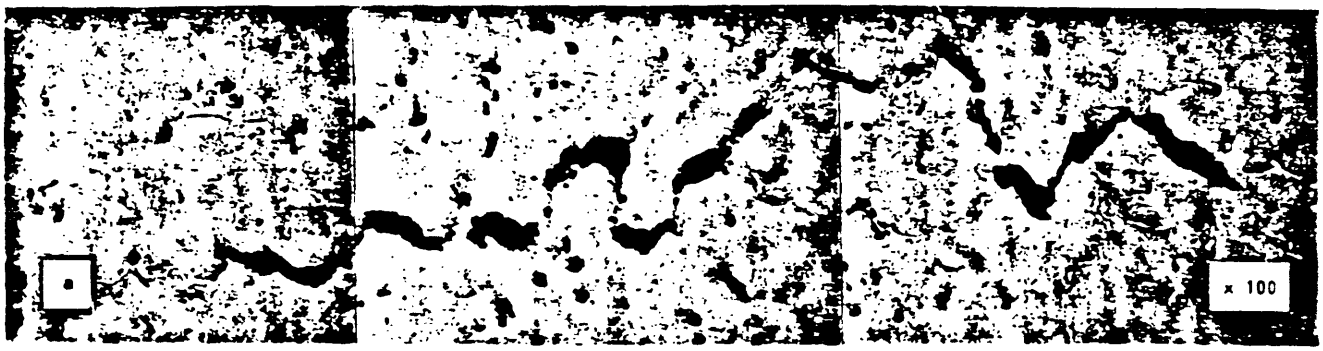
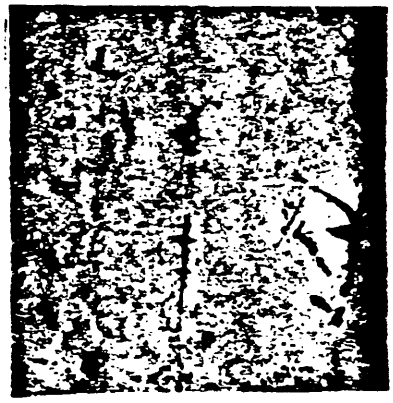


Figure 2.4 : Nucleation of voids and coalescence in Conventionally cast IN738LC



a) transverse segments of grain boundary



b) interdendritic carbides





Figure 2.5 : Example of a crack initiation at carbides and growth through the grains in directionally solidified IN738LC

CHAPTER-3

CREEP STRESS ANALYSIS

3. Isotropic Analysis

In this section a brief description of the finite element method for an isotropic material, used by Al-Faddagh (1983), is given. His program was found to have a few drawbacks. Therefore, in the present work, important steps have been taken to modify the boundary conditions and convergence criterion (Chapter-5). The strain-stress relationship for an isotropic materials is given as :

$$\varepsilon_{11} = \frac{1}{E}[\sigma_{11} - \upsilon(\sigma_{22} + \sigma_{33})]$$

$$\varepsilon_{22} = \frac{1}{E}[-\upsilon\sigma_{11} + \sigma_{22} - \upsilon\sigma_{33}] \qquad (3.1)$$

$$\varepsilon_{33} = \frac{1}{E}[-\upsilon\sigma_{11} - \upsilon\sigma_{22} + \sigma_{33}]$$

$$\gamma = \frac{\tau}{G}$$

The relationship between stress and strain is :

$$[\sigma] = [D][\varepsilon] \qquad (3.2)$$

where [σ] and [ε] are vectors of stresses and strains. [D] is the elastic property matrix defined by :

$$[D] = \frac{E^*}{1-\upsilon^{2*}} \begin{bmatrix} 1 & \upsilon^* & \upsilon^* & 0 \\ \upsilon^* & 1 & \upsilon^* & 0 \\ \upsilon^* & \upsilon^* & 1 & 0 \\ 0 & 0 & 0 & \frac{1}{2}(1-\upsilon^*) \end{bmatrix} \qquad (3.3)$$

where E * and υ*, being the Young's modulus and Poisson's ratio, modified as for plane strain conditions :

$$E^* = \frac{E}{1-\upsilon^2} \quad ; \quad \upsilon^* = \frac{\upsilon}{1-\upsilon} \tag{3.4}$$

To assemble the overall stiffness matrix, [K], for an axisymmetric body, the conditions for equilibrium must be satisfied, so that :

$$[K][\delta] = [F] \tag{3.5}$$

where [δ] is the overall vector for displacement components, and [F] is the overall vector for the externally applied forces.

3.1. Non-Linear Finite Element Analysis

The non-linearity is introduced through making the overall stiffness matrix [K] in equation (3.5) variable. A new condition for equilibrium after each iteration has to be satisfied until steady-state is reached. This is made possible by making the elements representing the elastic properties in matrix [K] dependent on the local state of strain or stress ; therefore, equation (3.5) is written as :

$$[K(\delta)][\delta] = [F] \tag{3.6}$$

when $\delta = \delta_0$, the elastic solution is obtained. Convergence to steady-state is achieved when the displacement components after the successive iterations differ by only a small amount :

$$\frac{\Sigma_i \{ |\Delta u_i| + |\Delta v_i| \}}{\Sigma_i \{ |u_i| + |v_i| \}} \leq \lambda \tag{3.7}$$

when Δu_i and Δv_i are the changes in the computed displacements between the successive iterations. The tolerance, λ, can take values of 10^{-2} to 10^{-8}, depending on the accuracy required. The method of solution in the elastic region is based on using the displacement as a nodal point variable ; therefore, the elastic modulus has to be expressed as a function of the local state of strain during the successive iterations needed to achieve steady state.

Most materials are not fully isotropic when they undergo plastic deformation. Many materials are anisotropic in nature. The finite element program quoted in Al-Faddagh (1983) had to be modified in order to accommodate anisotropy. The details of the formulation of effective stress and strain equations for the material used in this work are given in the following sections.

3.2 Anisotropy of Materials

Materials in which grains are initially oriented at random, and which are therefore isotropic, become anisotropic during plastic deformation. An interesting and important type of polycrystalline anisotropy occurs when the material possesses an axis of symmetry, in the sense that all rays at right angles to this axis are equivalent. Anisotropy of this kind is found in rolled and extruded bars. Directionally solidified superalloys fall into the same category. Single crystal alloys form another family of anisotropic materials in which properties in all three directions are different. Apart from metals there exist several non-metallic materials which are highly anisotropic in their behaviour, e.g. timber, reinforced polymers etc. Due to the modes of failure being complex and dependent on numerous variables, the development of a consistent, reliable design criterion has been difficult. There are several theories now in existence. But most of these predict the multiaxial failure characteristics from uniaxial tests in different directions. Since it is often difficult to achieve, experimentally, a particular failure criterion, a general theory is necessary. Several anisotropic failure criteria have been suggested in the literature (Hill (1948), Fisher (1949), Hu (1956), Marin (1956), Griffith and Baldwin (1962), Hoffman (1967), Franklin (1968), Hosford (1985), Kobayashi (1985)) using the following assumptions.

The main assumptions made in the development of effective stress and strain equations and subsequently in the finite element program are as follows ;

(1) The material is transversely isotropic.

(2) The axes of orthotropy coincide with the principal axes.

(3) There are no volume changes during creep.

3.3 Present Anisotropic Effective Stress and Strain Equations

With the assumptions made above, the stress-strain relationship for anisotropic materials in terms of effective elastic constants can be written as ;

$$\varepsilon_{11} = \frac{\sigma_{11}}{E_1} - \upsilon_{21}\frac{\sigma_{22}}{E_2} - \upsilon_{31}\frac{\sigma_{33}}{E_3}$$

$$\varepsilon_{22} = -\upsilon_{12}\frac{\sigma_{11}}{E_1} + \frac{\sigma_{22}}{E_2} - \upsilon_{32}\frac{\sigma_{33}}{E_3} \qquad (3.8)$$

$$\varepsilon_{33} = -\upsilon_{13}\frac{\sigma_{11}}{E_1} - \upsilon_{23}\frac{\sigma_{22}}{E_2} + \frac{\sigma_{33}}{E_3}$$

$$\gamma_{12} = \frac{\tau_{12}}{G_{12}}$$

where 1,2,3 represents the axial , radial , and hoop direction. When $E_1 = E_2 = E_3$ and $\upsilon_{12} = \upsilon_{21} = \upsilon_{31} = \upsilon_{32} = \upsilon_{13} = \upsilon_{23}$ then equation (3.8) reduces to the equation (3.1).The material property matrix of equations (3.8) $\{[\varepsilon] = [M][\sigma]\}$ is given by

$$[M] = \begin{bmatrix} \frac{1}{E_1} & -\frac{\upsilon_{21}}{E_2} & -\frac{\upsilon_{31}}{E_3} & 0 \\ -\frac{\upsilon_{12}}{E_1} & \frac{1}{E_2} & -\frac{\upsilon_{32}}{E_3} & 0 \\ -\frac{\upsilon_{13}}{E_1} & -\frac{\upsilon_{23}}{E_2} & \frac{1}{E_3} & 0 \\ 0 & 0 & 0 & \frac{1}{G_{12}} \end{bmatrix}$$

As the material is assumed to be transversely isotropic, the moduli of elasticity in radial and hoop directions are the same, that is, $E_2 = E_3$.To ensure that the strain energy is a single valued function of the strain , the material matrix of equations (3.8) must be symmetric. That means

$$\frac{\upsilon_{21}}{E_2} = \frac{\upsilon_{12}}{E_1} \;,\; \frac{\upsilon_{31}}{E_3} = \frac{\upsilon_{13}}{E_1} \text{ and } \frac{\upsilon_{32}}{E_3} = \frac{\upsilon_{23}}{E_2} \qquad (3.9)$$

As $E_2 = E_3$, $\upsilon_{23} = \upsilon_{32}$

and υ_{12} is assumed to be equal to υ_{13}

Therefore equations (3.8) can be written as,

$$\varepsilon_{11} = \frac{\sigma_{11}}{E_1} - \upsilon_{12}\frac{\sigma_{22}}{E_1} - \upsilon_{12}\frac{\sigma_{33}}{E_1}$$

$$\varepsilon_{22} = -\upsilon_{12}\frac{\sigma_{11}}{E_1} + \frac{\sigma_{22}}{E_2} - \upsilon_{23}\frac{\sigma_{33}}{E_2} \qquad (3.10)$$

$$\varepsilon_{33} = -\upsilon_{12}\frac{\sigma_{11}}{E_1} - \upsilon_{23}\frac{\sigma_{22}}{E_2} + \frac{\sigma_{33}}{E_2}$$

$$\gamma_{12} = \frac{\tau_{12}}{G_{12}}$$

Now the volumetric strain is written as ,

$$\varepsilon_{vol} = \varepsilon_{11} + \varepsilon_{22} + \varepsilon_{33} \qquad (3.11)$$

and for incompressibility is zero.That is

$$(1-2\upsilon_{12})\frac{\sigma_{11}}{E_1} + (1-\upsilon_{21}-\upsilon_{23})\frac{\sigma_{22}}{E_2} + (1-\upsilon_{21}-\upsilon_{23})\frac{\sigma_{33}}{E_3} = 0 \qquad (3.12)$$

The coefficients of σ_{11} , σ_{22} and σ_{33} should each be equal to zero.
Therefore

$$1-2\upsilon_{12} = 0 \quad \text{or} \quad \upsilon_{12} = 0.5$$

and $1-\upsilon_{21}-\upsilon_{23} = 0$

From equation (3.9)

$$\upsilon_{21} = \upsilon_{12}\frac{E_2}{E_1} \quad \text{or} \quad \upsilon_{21} = 0.5\frac{E_2}{E_1} \quad \text{and} \quad \upsilon_{23} = 1-0.5\frac{E_2}{E_1}$$

Substituting the values of υ_{21} and υ_{23} in equation (3.8) we have

$$\varepsilon_{11} = \frac{\sigma_{11}}{E_1} - \frac{1}{2}\frac{\sigma_{22}}{E_1} - \frac{1}{2}\frac{\sigma_{33}}{E_1}$$

$$\varepsilon_{22} = -\frac{1}{2}\frac{\sigma_{11}}{E_1} + \frac{\sigma_{22}}{E_2} - \left(1 - \frac{1}{2}\frac{E_2}{E_1}\right)\frac{\sigma_{33}}{E_2} \qquad (3.13)$$

$$\varepsilon_{33} = -\frac{1}{2}\frac{\sigma_{11}}{E_1} - \left(1 - \frac{1}{2}\frac{E_2}{E_1}\right)\frac{\sigma_{22}}{E_2} + \frac{\sigma_{33}}{E_2}$$

$$\gamma_{12} = \frac{\tau_{12}}{G_{12}}$$

Now substituting

$$\frac{2E_1 - E_2}{E_2} = \beta$$

equation (3.13) takes the form of,

$$\varepsilon_{11} = \frac{1}{2E_1}\left[2\sigma_{11} - \sigma_{22} - \sigma_{33}\right]$$

$$\varepsilon_{22} = \frac{1}{2E_1}\left[-\sigma_{11} + (1+\beta)\,\sigma_{22} - \beta\,\sigma_{33}\right] \qquad (3.14)$$

$$\varepsilon_{33} = \frac{1}{2E_1}\left[-\sigma_{11} - \beta\,\sigma_{22} + (1+\beta)\,\sigma_{33}\right]$$

$$\gamma_{12} = \frac{\tau_{12}}{G_{12}}$$

In the case of a rigid plastic material, an increase in strain is not necessarily associated with the corresponding increase in stress, but only with a constant but finite value of stress. The principal stress directions and principal strain or strain rate directions are coincident. Thus from the Levy-Mises rule for rigid plastic materials, the stress- strain relationship can be expressed as,

$$d\varepsilon^p_{11} = \frac{d\lambda}{2}(2\sigma_{11} - \sigma_{22} - \sigma_{33})$$

$$d\varepsilon^p_{22} = \frac{d\lambda}{2}(-\sigma_{11} + (1+\beta)\sigma_{22} - \beta\sigma_{33}) \qquad (3.15)$$

$$d\varepsilon^p_{33} = \frac{d\lambda}{2}(-\sigma_{11} - \beta\sigma_{22} + (1+\beta)\sigma_{33})$$

$$d\gamma^p_{12} = (1+2\beta)\tau_{12}\, d\lambda$$

where $d\lambda$ is a constant linking stress and strain in the plastic range.

The incremental plastic work done per unit volume is given by

$$dw^p = \sigma_{11}\, d\varepsilon^p_{11} + \sigma_{22}\, d\varepsilon^p_{22} + \sigma_{33}\, d\varepsilon^p_{33} + 2\,\tau_{12}\, d\varepsilon^p_{12} \qquad (3.16)$$

or

$$dw^p = \frac{d\lambda}{2}\{2\sigma^2_{11} + (1+\beta)\sigma^2_{22} + (1+\beta)\sigma^2_{33} - 2\sigma_{11}\sigma_{22} - 2\beta\sigma_{22}\sigma_{33} - 2\sigma_{11}\sigma_{33} + 2(1+2\beta)\tau^2_{12}\} \qquad (3.17)$$

The plastic work done is expressed as

$$dw^p = \sigma^2_{eff}\, d\lambda \qquad (3.18)$$

Therefore,

$$\sigma^2_{eff} = \frac{1}{2}\{(\sigma_{11} - \sigma_{22})^2 + \beta(\sigma_{22} - \sigma_{33})^2 + (\sigma_{33} - \sigma_{11})^2 + 2(1+2\beta)\tau^2_{12}\} \qquad (3.19)$$

or,

$$\sigma_{eff} = \frac{1}{\sqrt{2}} \{ (\sigma_{11} - \sigma_{22})^2 + \beta (\sigma_{22} - \sigma_{33})^2 + (\sigma_{33} - \sigma_{11})^2 + 2 (1+2\beta) \tau_{12}^2 \}^{1/2} \quad (3.20)$$

and from equation (3.16) we can write

$$(\sigma_{11} - \sigma_{22}) = \frac{(\beta \, d\varepsilon^p_{11} - d\varepsilon^p_{22})}{\frac{d\lambda}{2} (1+2\beta)}$$

$$(\sigma_{22} - \sigma_{33}) = \frac{(d\varepsilon^p_{22} - d\varepsilon^p_{33})}{\frac{d\lambda}{2} (1+2\beta)} \quad (3.21)$$

$$(\sigma_{33} - \sigma_{11}) = \frac{(d\varepsilon^p_{33} - \beta \, d\varepsilon^p_{11})}{\frac{d\lambda}{2} (1+2\beta)}$$

$$\tau_{12} = \frac{d\gamma^p_{12}}{d\lambda \, (1+2\beta)}$$

The effective strain can be expressed as

$$\varepsilon_{eff} = d\lambda \, \sigma_{eff} \quad (3.22)$$

and

$$\varepsilon_{eff} = \frac{d\lambda}{\sqrt{2}} \{ (\sigma_{11} - \sigma_{22})^2 + \beta (\sigma_{22} - \sigma_{33})^2 + (\sigma_{33} - \sigma_{11})^2 + 2 \, (1+2\beta) \, \tau_{12}^2 \}^{1/2} \quad (3.23)$$

Representing the small change in the strain increment, $d\varepsilon_p$, as ε and using equations (3.21) to define $(\sigma_{11} - \sigma_{22})$, $(\sigma_{22} - \sigma_{33})$, $(\sigma_{33} - \sigma_{11})$ and τ_{12} we obtain

$$\varepsilon_{eff} = \frac{\sqrt{2}}{(1+2\beta)} \left[(\beta \, \varepsilon_{11} - \varepsilon_{22})^2 + \beta \, (\varepsilon_{22} - \varepsilon_{33})^2 + (\varepsilon_{33} - \beta \, \varepsilon_{11})^2 + 2(1+2\beta) \, \varepsilon_{12}^2 \right]^{1/2} \quad (3.24)$$

3.4 FINITE ELEMENT ANALYSIS

3.4.1 The Finite Element Formulation for Linear Elasticity

In the present finite element formulation attention is concentrated on the simplest types of element, namely ones triangular in shape over which the strains or strain rates are assumed to be constant. Such elements are often referred to as Constant Strain Triangles. An advantage of using triangular elements is that they can be made to fit any shape of domain boundary, provided the boundary can be represented with sufficient accuracy by a series of short straight lines.

Figure-3.1, shows the typical triangular finite element, numbered m, in the axial-radial plane, r and z being local co-ordinates parallel to global co-ordinates R and Z. The element has three nodes, i, j and k, located at each corner. The radial and axial displacement components are assumed to vary linearly over the typical element, so that

$$u = C_1 + C_2\, r + C_3\, z \tag{3.25}$$

$$w = C_4 + C_5\, r + C_6\, z \tag{3.26}$$

where the six constants may be found in terms of the six nodal displacements from

$$C_1 = u_i \;;\; [\, C_2 \;\; C_3 \,]^T = \frac{1}{2\Delta_m} [\, d \,] [\, u_i \; u_j \; u_k \,]^T \tag{3.27}$$

$$C_4 = w_i \;;\; [\, C_5 \;\; C_6 \,]^T = \frac{1}{2\Delta_m} [\, d \,] [\, w_i \; w_j \; w_k \,]^T \tag{3.28}$$

where

$$[\, d \,] = \begin{bmatrix} b_i & b_j & b_k \\ a_i & a_j & a_k \end{bmatrix}$$

$$\Delta_m = \frac{1}{2} (a_k b_j - a_j b_k)$$

is the area of the element. Hence, most of the non-zero strains are constant over the element and

$$\varepsilon_{rr} = \frac{du}{dr} = c_2 \quad ; \quad \varepsilon_{zz} = \frac{dw}{dz} = c_6$$

$$\varepsilon_{rz} = \frac{du}{dz} + \frac{dw}{dr} = c_3 + c_6 \qquad (3.29)$$

$$\varepsilon_{\theta\theta} = \frac{u}{R} = \frac{\bar{u}}{\bar{R}_m}$$

where $\bar{u}$ and $\bar{R}_m$ are the mean values over the element of the radial displacement and radial distance from the axis of symmetry.

$$\bar{u} = \frac{(u_i + u_j + u_k)}{3} \quad ; \quad \bar{R}_m = \frac{(R_i + R_j + R_k)}{3}$$

Combining equations (3.27) to (3.29), the element strain components can be expressed in terms of nodal point displacements by

$$[\varepsilon] = [\varepsilon_{rr}\ \varepsilon_{zz}\ \varepsilon_{\theta\theta}]^T = \frac{1}{2\Delta_m}[B][\delta]^T \qquad (3.30)$$

Where

$$[\delta]_m = [\,u_i\ w_i\ u_j\ w_j\ u_k\ w_k\,]^T$$

$$B = \begin{bmatrix} b_i & 0 & b_j & 0 & b_k & 0 \\ 0 & a_i & 0 & a_j & 0 & a_k \\ \frac{2\Delta_m}{3\bar{R}_m} & 0 & \frac{2\Delta_m}{3\bar{R}_m} & 0 & \frac{2\Delta_m}{3\bar{R}_m} & 0 \\ a_i & b_i & a_j & b_j & a_k & b_k \end{bmatrix}$$

The relationship between the element stresses and strains can be derived from Hooke's law as

$$[\sigma] = \left[\sigma_{rr}\ \sigma_{zz}\ \sigma_{\theta\theta}\ \sigma_{rz}\right]^T = [D][\varepsilon] \qquad (3.31)$$

where the elastic property matrix, obtained by solving equation (3.10) and replacing Poisson's ratio in the axial direction by υ_1 and perpendicular to the axial direction by υ_2, is given by

$$D = \frac{E_1}{(1+\upsilon_1)(1-\upsilon_1 - 2n'\upsilon_2^2)} \times$$

$$\begin{bmatrix} n'(1-n'\upsilon_2^2) & n'\upsilon_2(1+\upsilon_1) & n'(\upsilon_1+n'\upsilon_2^2) & 0 \\ n'\upsilon_2(1+\upsilon_1) & (1-\upsilon_1)^2 & n'\upsilon_2(1+\upsilon_1) & 0 \\ n'(\upsilon_1+n'\upsilon_2^2) & n'\upsilon_2(1+\upsilon_1) & n'(1-n'\upsilon_2^2) & 0 \\ 0 & 0 & 0 & m'(1+\upsilon_1)(1-\upsilon_1-2n'\upsilon_2^2) \end{bmatrix}$$

where $n' = E_2 / E_1$; $m' = G_{12} / E_1$

Equilibrium conditions for the entire mesh of elements can be obtained by requiring the total potential energy, ψ, to be stationary for small changes in the displacements , Fenner (1975). Hence

$$d\psi = 2\pi \Sigma \bar{R}_m \Delta_m [\sigma]^T d[\varepsilon] - [F]^T d[\delta] = 0 \qquad (3.32)$$

where [δ] is a vector containing all the nodal point displacement components, while [F] contains the corresponding forces, uniformly distributed around the circumference through the nodes at which they are applied. Introducing equations (3.30) & (3.31) this result becomes

$$2\pi \Sigma_m \frac{\bar{R}_m}{4\Delta_m} [B]^T [D][B][\delta]_m = \Sigma_m [k]_m [\delta]_m$$
$$= [K][\delta] = [F] \qquad (3.33)$$

where $[k]_m$ are element stiffness matrices, which are assembled to form the overall stiffness matrix.

3.5 Treatment of Non-Linear Problems

In general, non-linearities in material behaviour, such as creep and plastic deformation, which cause the effective elastic properties E and υ to vary with, for example, time or the local state of strain, can be dealt with in different ways. One approach is to solve a series of linear problems corresponding to small increments of the relevant independent variables, such as time or loading. An advantage of this approach is that solutions are obtained not only at the final time required but also at a number of intermediate times. The main disadvantage is that if the time increment is made too large, the computed solutions will diverge from their true values. On the other hand, if the time increment is made very small, the amount of computing required becomes excessive as a large number of equations in the form of equation (3.33) are required.

A second approach, and the one which is used here, is to treat the elastic properties as variables, thereby making the [D] matrix for each element, its stiffness matrix, and the overall stiffness matrix into variables. Thus equation (3.33) is no longer linear. Nevertheless, it is possible to solve it using the iterative Gauss-Seidel technique, provided the elastic properties and stiffness matrices are updated during the iterative process. Although the amount of computing involved in a typical non-linear solution of this type is more than that required for the corresponding linear solution, it is generally greater by a factor of some two or three. Therefore, the non-linear stiffness approach is more economical than the incremental time step approach, and it is generally much easier to ensure correct convergence of the solution. On the other hand, the many intermediate solutions associated with the incremental approach are not available, the partially converged results of intermediate iterations having no physical significance.

Since the present finite element formulation uses displacements as the nodal point variables, the elastic modulus needs to be expressed as a function of the local state of strain. The relationship between the apparent modulus of elasticity and the local state of strain is given below.

The constitutive relation used is given by :

$$\varepsilon_{eff} = C\,\sigma_{eff}^{n}\,f(t) \tag{3.34}$$

which may be inverted to give :

$$\sigma_{eff} = \left[\frac{\varepsilon_{eff}}{C\,f(t)}\right]^{\frac{1}{n}} \tag{3.35}$$

An apparent or effective modulus, E' , can be defined, such that :

$$E' = \sigma_{eff} / \varepsilon_{eff} \tag{3.36}$$

Substituting in equation (3.35) gives :

$$E' = \frac{1}{\varepsilon_{eff}}\left(\frac{\varepsilon_{eff}}{C\,f(t)}\right)^{\frac{1}{n}} = E_0\left(\frac{\varepsilon_{eff}}{\varepsilon_{eff(0)}}\right)^{\frac{1}{n}-1} \tag{3.37}$$

where E_0 is the effective modulus at some convenient reference strain, $\varepsilon_{eff(0)}$. If $n > 1$, E' is a function of strain, where σ_{eff} and ε_{eff} are given by equation (3.20) and (3.24) respectively.

The elastic constants which are used in the program are obtained from Rolls Royce Plc. for the DS Mar M002 material. These constants are taken from Chapter-2.

$$E_2 / E_1 = 1.33 \quad , \quad \upsilon_1 = 0.394 \quad , \upsilon_2 = 0.143 \quad \text{and} \quad G_{12} / E_1 = 0.718$$

A difficulty is expressed with the present finite element formulation when the material is incompressible. Setting $\upsilon_1 = 0.5$ the convergence rate was found to be slow. Therefore for non-linear analysis, the Poisson's ratio, υ_1 is assumed to be 0.45 which is close enough to incompressibility . The poisson's ratio υ_2 is obtained from the incompressibility condition and given as 0.305. The general procedure for non-linear analysis can be summariesd in the following steps.

1) Taking the elastic properties to be constant everywhere, The overall stiffness matrix is assembled using equation (3.33).

2)The elastic stresses and strains are calculated using the Gauss-Seidel iterative technique

2) New moduli E', which vary from element to element are computed using equations (3.30) and (3.37). A modified [K] matrix is reassembled.

3) A few cycles of Gauss-Seidel are carried out which are termed inner iterations. In the present analysis 10 inner iterations are carried out after each outer iteration. If a small number is used the amount of computing required becomes excessive. If a large number is used the solution does not converge to a correct value.Therefore an optimum value of inner iterations is used.

4) From the partially converged displacement solution, new moduli E' are determined as in step (2).

5) Steps (2) and (3) are repeated until satisfactory convergence is achieved. These iterations are termed outer iterations.

Convergence is achieved when the difference between the load calculated on the top end and load calculated on the lower end of the geometry considered, is less than 2%. This can be written as

$$\frac{F1 - F2}{F1} \leq 0.02$$

where F1 = Load on the top end

F2 = Load on the lower end

It was found that the convergence criterion based on a tolerance in the difference between the displacements after successive iterations could not hold good for slit-type notch geometries. Often it was observed that though the prescribed tolerance was achieved, the load on the top and bottom of the bar was not fully balanced. To overcome this difficulty the present convergence criterion is adopted. From experience, in all the notch geometries including slit-type sharp geometries maximum error between the top and bottom load was observed to be less or equal to 2%.

3.6 Comparison With an Analytical Solution

In order to check the numerical solution , an example of a thick-walled cylinder subjected to an internal pressure is selected. An isotropic analysis is carried out using the program for anisotropic analysis. The stresses across the wall are checked against the

stresses calculated in Al-Faddagh(1983). Good correlation is found between the two solutions. For an anisotropic check the analytical solution obtained by Pai (1967) is used. The analytical solution gives the non-dimensionalised stresses as

$$S_r = \frac{\sigma_r}{P} = -K\,(X^{-2q} - 1)$$

$$S_\theta = \frac{\sigma_\theta}{P} = K\,[\,(\frac{2}{n} - 1)\,X^{-2q} + 1\,] \qquad (3.38)$$

$$S_z = \frac{\sigma_z}{P} = K\,[\,(\frac{1}{n} - 1)\,X^{-2q} + 1\,]$$

$$S_e = \frac{\sigma_e}{P} = K\,\frac{1}{n}\,(1 + \frac{1}{m})\,X^{-2q}$$

The normalised hoop strain rate is given by

$$\frac{\varepsilon_\theta}{B p^n} = \frac{\sqrt{3}}{2} A^n\,[\frac{2}{n} K\,]^n\,X^{-2} \qquad (3.39)$$

Using the present anisotropic effective stress & strain equations the strain rate is obtained as

$$\frac{\varepsilon_\theta}{B\,p^n} = \frac{1}{2}\,(\frac{1+\beta}{2})^{\frac{n+1}{2}}\,[\frac{2}{n} K\,]^n\,X^{-2} \qquad (3.40)$$

where n is the creep index, B is the material constant, m is the constant refering to anisotropy in the range $0.5 < m < 2$ to maintain the convexity of the yield locus,and

$$A = (\frac{1}{2} + \frac{1}{2m})$$

$$K = \frac{1}{[\,(\frac{r_i}{r_o})^{\frac{-2}{n}} - 1\,]}\,, \quad X = \frac{r}{r_o} \quad \text{and} \quad q = \frac{1}{n}$$

Figure- 3.2a shows the finite element mesh for the thick-walled cylinder problem. A uniform pressure, P , is applied on the internal surface of the cylinder. The cylinder is prevented from moving in the vertical direction by imposing the constraints at the top and

bottom end as shown in the figure.Thus, only radial movement is allowed. Stresses through the wall of the cylinder were calculated using the finite element program, for n = 1 and n = 6, and were compared with the analytical solution in Figure- 3.2b.

A closed end cylinder is further analysed to confirm the conclusions drawn by Pai (1967). For this case a long cylinder of thickness to length ratio 12, keeping other dimensions the same, is selected. Constant axial stress, which is applied on the cylinder top end when the uniform pressure, P , of unity was applied inside the cylinder, was calculated. The finite element mesh for this problem is shown in Figure 3.3a. It is concluded that the plane strain solution and closed end solution are strictly equivalent as shown in Figure-3.3b for n = 6. In a closed end condition the cylinder is subjected to a constant stress on the top end. Under the plastic condition constant stress causes a cylinder to elongate in the axial direction by a fixed amount. Thus the final end condition is identical to the plane strain condition.

The effect of anisotropy on the stress distribution in a thick-walled cylinder under creep conditions was studied by Bhatnagar et al. (1986). In their analysis, they observed that materials which are stiffer in the radial direction than in the axial direction maintain lower values of effective stress compared with the isotropic case as shown in Figure-3.4. From equations (3.38) it is found that the individual stresses i. e. σ_{rr}, $\sigma_{\theta\theta}$, σ_{zz} are similar to the isotropic stresses but, the effective stress is influenced by the anisotropy as it contains the anisotropy factor, m . From equation 3.39 it is clear that the material anisotropy is found to have a significant effect on the creep rate behaviour of a thick-walled cylinder. The factor A^n represents the ratio of the creep strain rate for an orthotropic cylinder compared with an isotropic cylinder for which m=1, and thus A =1. A slight change in , m , greatly affects the factor A as it is raised to the power n. Similarly from equation (3.40) the strain rates in the hoop and radial direction are found to have been influenced by the anisotropy. For $\beta = 1$, an equation reduces to a isotropic case . For $\beta < 1$, the present case the strain rate is found to be less than the isotropic case. This is the reason why the anisotropic effective stress is lower than the isotropic effective stress.

3.7 Conclusions

In this chapter the development of an anisotropic effective stress and strain equations based on anisotropic yield criterion is given in detail. Using these equations a finite element program is developed. Some case studies were carried out to confirm the solution obtained from the program. It was found that the numerical solutions were in good agreement with the analytical solutions. A cylinder which has lower creep rate in the radial and hoop direction than the axial direction can possess higher creep life than the isotropic cylinder. This fact is confirmed from the effective stress distribution which shows that the anisotropic effective stress is lower than the isotropic effective stress.

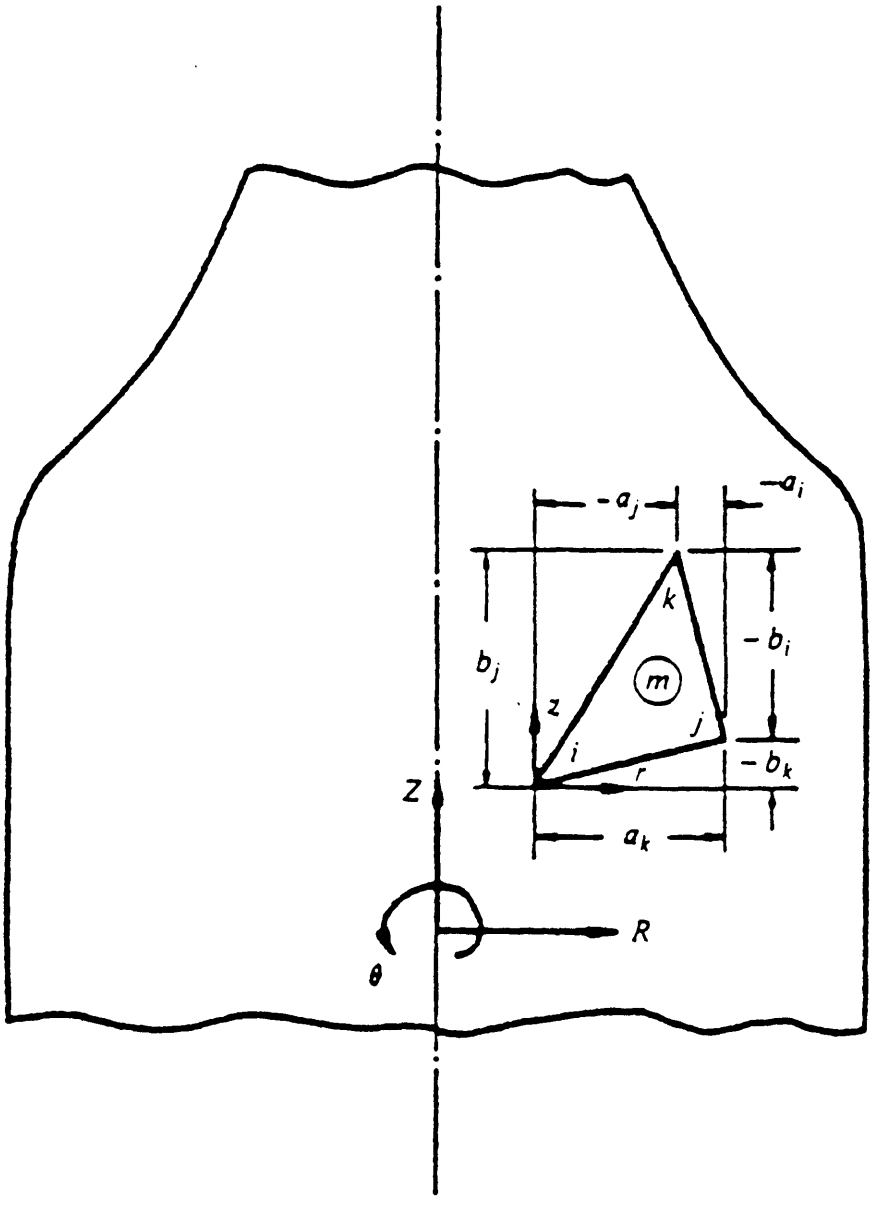


Figure - 3.1 : Triangular finite element in a two- dimentional solution domain

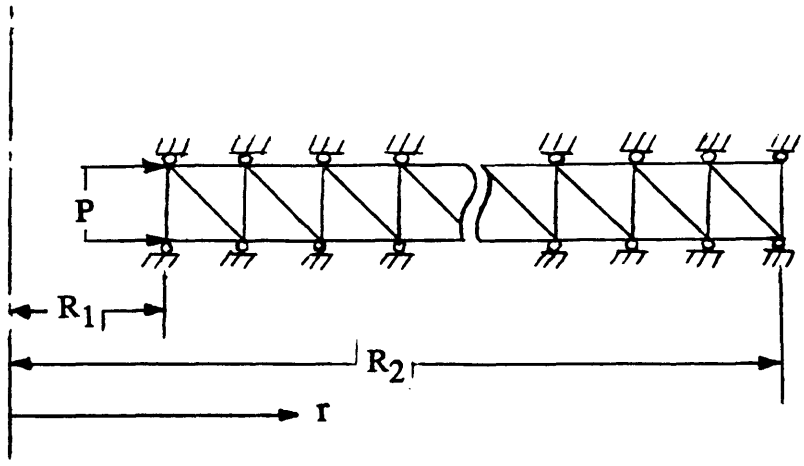


Figure 3.2a : Simple finite element mesh for thick-walled cylinder problem : $R_2 = 2R_1$

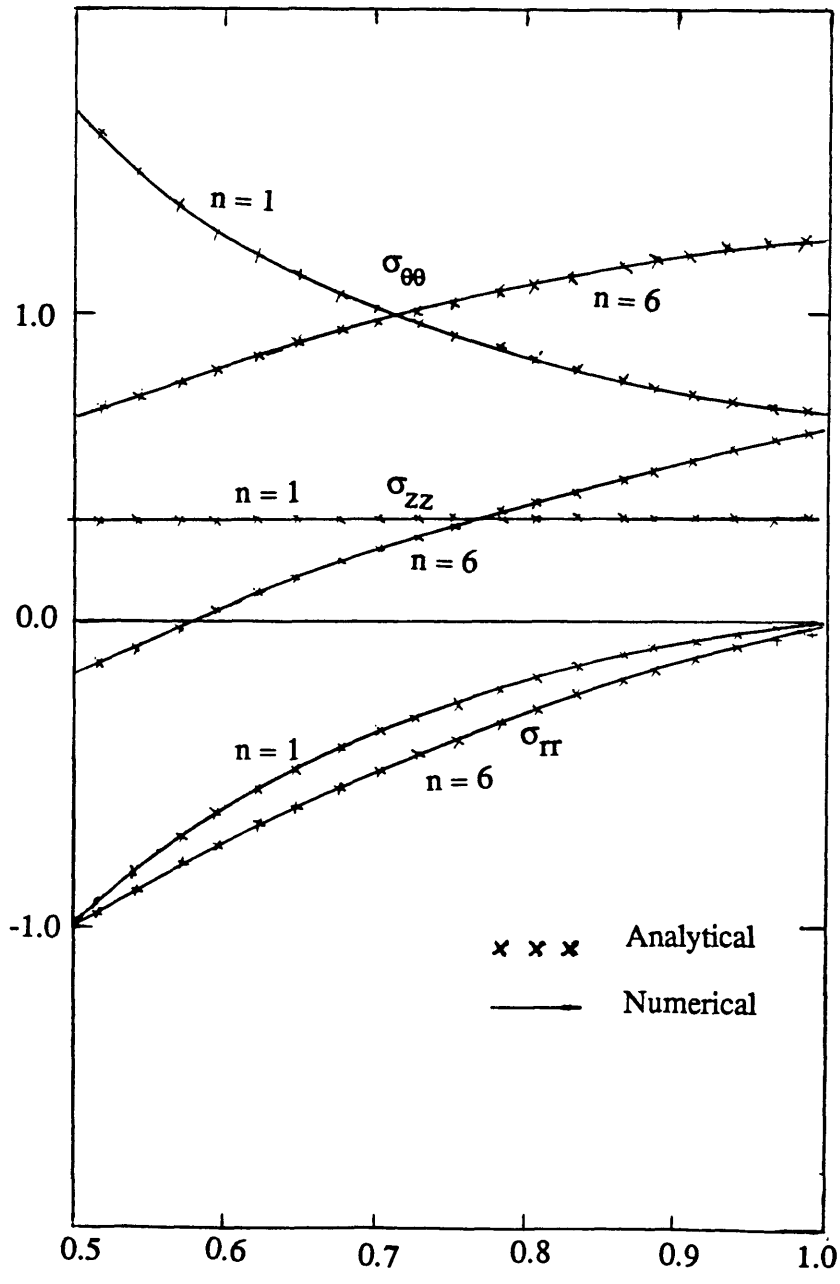


Figure 3.2b : Comparision of numerical and analytical stress distribution across a thick - walled cylinder

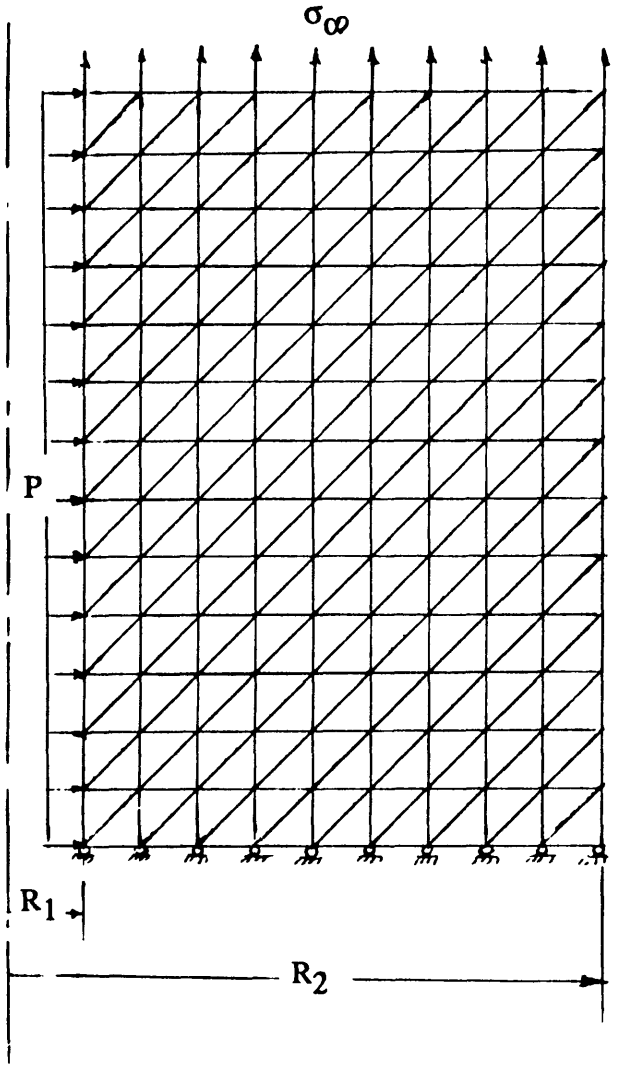


Figure 3.3 a : Finite element mesh for a long cylinder closed end problem

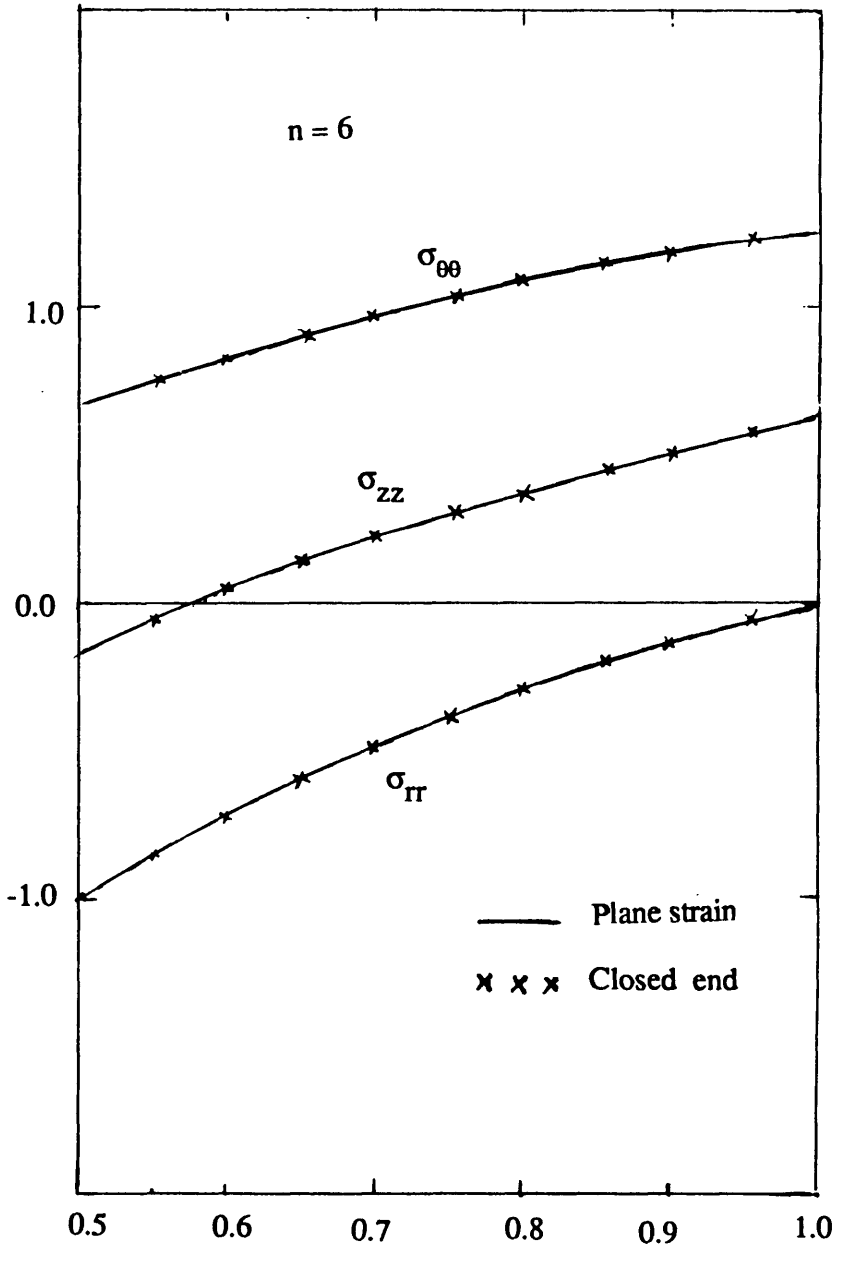


Figure 3.3 b : Comparision of stresses in plane strain and closed end problem

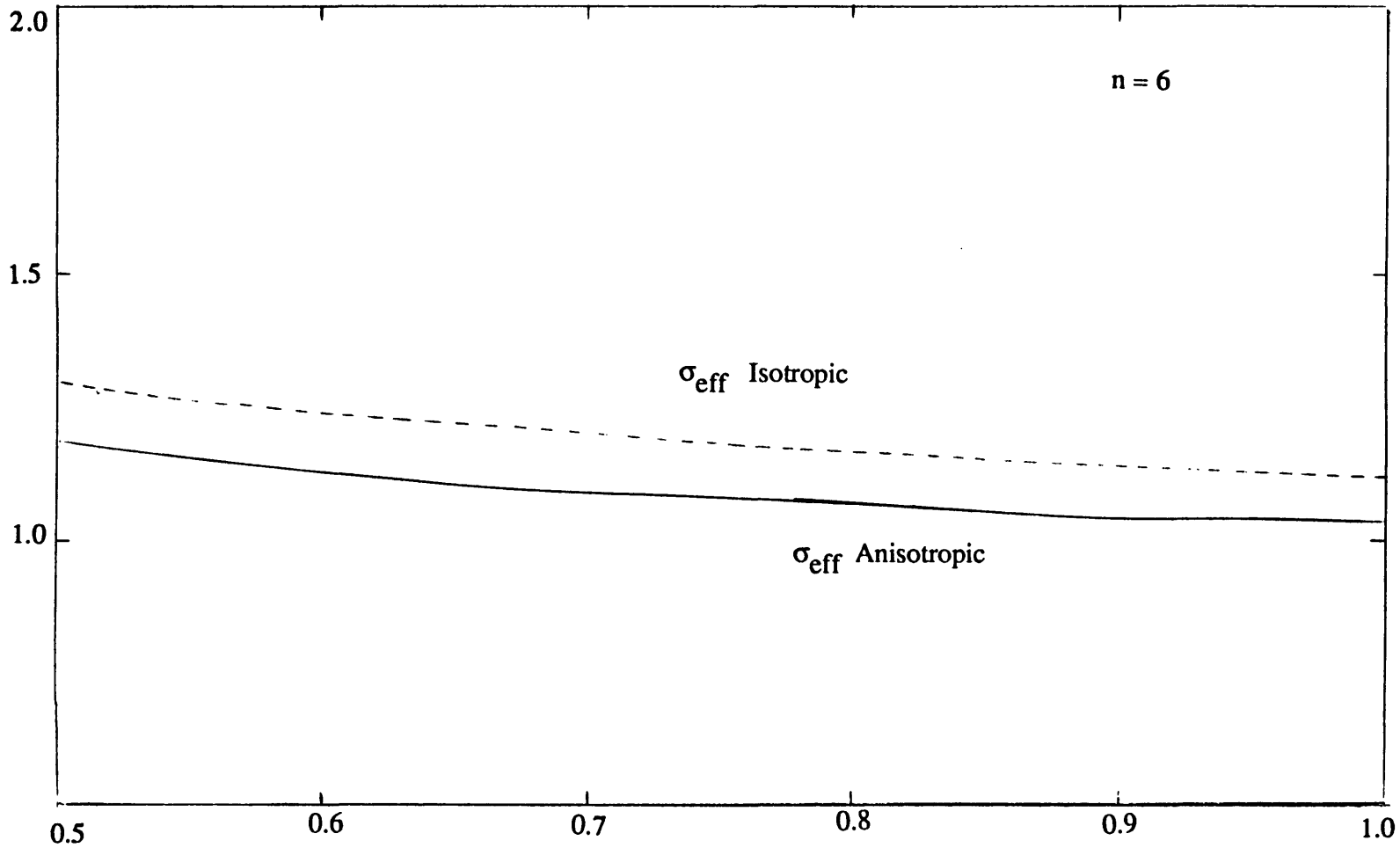


Figure 3.4 : Comparision of Isotropic and Anisotropic effective stress distribution across a thick-walled cylinder

CHAPTER-4

SPECIMENS AND EQUIPMENT

4. Introduction

The experimental work described in this thesis was carried out at Imperial College and the National Physical Laboratory. Uniaxial tests on plain specimens and multiaxial tests on notched specimens of 304-H stainless steel were carried out in constant load tensile creep machines at Imperial College. Uniaxial tests on plain specimens of DS MAR M002 were carried out at NPL in constant load and constant stress tensile testing machines, while multiaxial tests on notched specimens were carried out at Imperial College and NPL. Three tests were performed on DS MAR M002 notched specimens to measure diametral strain using the facilities available at NPL. The details of the machines are described in the following sections.

4.1 Creep Testing at Imperial College

4.1.1 Constant Load Creep Machines

The machine comprises the following parts.

1) A lever with a dead weight with leverage ratio 1:10 ;

2) A set of shackles to hold pull rods machined from heat resistant steel ;

3) A set of pull rods machined from Ni 115 ;

4) Adapters to screw the specimen in position, machined from CC MAR M002 ;

5) A furnace which slides on the guide ways ;

6) A load cell ;

7) A set of extensometers and attachment to hold an LVDT ;

8) An electronic unit to measure the extension of a specimen from LVDT during a test.

Figure 4.1 shows the general arrangement of the machines at Imperial College.

4.1.2 Experimental Procedure

Before starting an experiment the dimensions of the specimen were measured on a shadowgraph. The transducer was calibrated using a drum micrometer. Next, the lever was balanced by moving the position of a balancing weight with the upper pull rod, the specimen and the extensometer in position. A suitable counterweight was added on the scale pan to bring the lever to horizontal position. Further the bottom pull rod was placed in position with the specimen and the whole loading train was completed. Three thermocouples were tied to the specimen at a suitable distance along the gauge length to check a uniform temperature distribution throughout the gauge length during a test. The thermocouples were checked against the room temperature on the potentiometer before the extensometers were attached to the specimen.

4.1.3 Cold Loading

The purpose of cold loading was to check the bending of the specimen and the linearity of a transducer. Output from the transducer was connected to an x-y recorder. First a 10 lb. weight was added on the pan and the output from the transducer was recorded on the recorder. Next a series of weights were added in steps of 10 lb. and each time the output from the transducer was recorded. A specimen was taken to ensure that the total weight on the pan did not cause the yield stress of the material to be exceeded. The specimen was then unloaded, repeating the same procedure to check for repeatability in the output of the transducer. Thus the bending of the specimen and the linearity of the transducer were checked before heating up the test. Then the furnace was lowered, keeping the specimen position exactly in the centre of the furnace. The ends of the furnace were packed with the Kaowool ceramic fibers and loading-unloading was repeated to check the free movement of the whole assembly. Once it was found to be satisfactory, the machine was switched on.

4.1.4 Hot Loading

After switching on , the furnace controller was adjusted to acheive the required temperature. Thermocouple readings were read on the potentiometer and the gradient, if

any, was adjusted by adjusting the controller knobs. Next the required amount of weights were added on a scale pan which gave the required stress on the specimen. The signal from the transducer was recorded using a chart recorder. The first 10-12 minutes were monitored to ensure that movement of the transducer was satisfactory. Thereafter further recording was continued and signal were read continuously until failure occurred.

4.2 Creep Testing at NPL

The creep tests at NPL were undertaken in accordance with the test and calibration procedure specified in the " Creep Laboratory Manual " (Loveday 1985). The manual covers testing guidelines to be followed in order to comply with criteria satisfying the NAMAS accreditation of the creep laboratory, showing that the tests comply with the British Standard and to provide traceability back to the primary standards.

4.2.1 Constant Load Creep Machines at NPL

The constant load creep machines at NPL comprise similar parts to those described in section 4.1. The only difference is that these machines are equipped with the automatic beam levelling arrangement which maintains the lever in an approximately level attitude during both during calibration and testing, in order to achieve the requirements of BS 1610 grade A or A1. Specifications of these Machines are given below ;

Make	: Mayes
Capacity	: 20KN
Lever Ratio	: 1:10

4.2.2 Constant Stress Creep Machines at NPL

Most of the physical laws describing the creep behaviour of a material relate the creep strain rate to an applied stress. Thus to verify these laws for highly ductile materials, constant stress creep testing machines have been developed. The commonest method for achieving constant stress conditions in tension or compression, is to adjust the load applied to the specimen in proportion to the deformation, by varying the lever ratio on single lever creep machines using an approximately profiled cam. Using the same

principle of constant volume deformation for a particular gauge length (50 mm) the constant stress machines at NPL have been developed. The specifications of these machines are given below ;

Make	: Mayes
Capacity	: 30KN
Lever Ratio	: 1 : 15

Figure 4.2 shows the general arrangement of both types of machines. The detailed procedure of setting up the test on these machines is mentioned in NPL report DMA (c) 29 , August 1985.

4.2.3 Diametral Strain Measurement

Special extensometer has been designed at NPL to measure the diametral strain on the Bridgman Type notched specimens. The extensometer comprises two 120^0 Vee'd knife edges, of Nimonic 80 A, which are diametrically opposed on the notched region of the specimen as shown in Figure-4.3. The outer knife edge is supported by two rods which pass concentrically through two tubes which are attached to the inner knife edge. The rods and tubes are made of alumina, which, being a material with a low coefficient of thermal expansion , minimizes errors due to fluctuations in the furnace temperature. The tubes are attached to an Invar frame which carries two super-linear variable capacitance transducers. The spring loaded measuring plungers of the transducers contact metal caps secured to the ends of the alumina rods. These caps serve both as measuring anvils and as a means of providing shoulders for a phospher bronze leaf spring which holds the knife edges against the specimen. The spring tension is adjusted by movement of a central knife-edge fulcrum. The schematic arrangement is shown in Figure 4.4. The change in specimen diameter is calculated from the average of the two transducer readings. The actual reading being multiplied by a factor of 0.866 i. e. (sin 60), since the angled knife-edges mechanically magnify the true diametral displacements. This is explained in Figure-4.5. The whole unit is suspended about its balance point from an Invar cantilever fixed to the top of the furnace. Adjustment being provided in the vertical

plane for levelling the unit when setting up. The complete design and development of this arrangement is quoted in Furse and Loveday (1981)

4.3 Schematic Geometries and Manufacture

Mainly two types of specimen were used for generating experimental data. One was a plain specimen and the other was the notched specimen. The 25 mm. gauge length specimens were used for the tests at a constant load and 50 mm. gauge length specimens were used for the tests at a constant stress . Figure-4.4 shows the overall dimensions of the plain and notched specimens. Notched specimens of 25 mm gauge length were used to generate creep data under triaxial state of stress.

4.3.1 Specimen Manufacture

All specimens were manufactured with great care as the creep phenomenon is sensitive to any type of discontinuity in the geometry of the specimen. Care was taken to maintain the uniform diameter along the gauge length within the accepted tolerance mentioned in BS 3500. The different operations of the manufacturing procedure are described below.

Operation-1

Cut and face blanks to length on a conventional lathe and drill centres in each end to the same depth.

Operation-2

Rough machine outside diameter to thread size plus 1mm on diameter.

Operation-3

Rough machine centre section to below the core diameter of the thread and finish thread diameter.

Operation-4

Machine the thread to 0.75 mm. below the normal effective diameter by reducing cut depths on the leading flank. At this stage, the specimen is removed from the machine and replaced the opposite way round

Operation-5.

Rough machine outside to thread size plus 1mm. on diameter

Operation-6

Finish machine thread diameter

Operation-7

Machine thread to 0.075 mm. below normal effective diameter by reducing cut -depths on the leading flank.

Operation-8

Finish machine center in two equal cuts.

The machining operations to manufacture blank circumferentially-notched tensile specimens are the same. Further the notches are turned by using the correct profile tool. Once the machining operations are completed on the lathe, final finish is given by polishing the specimens over the gauge length.

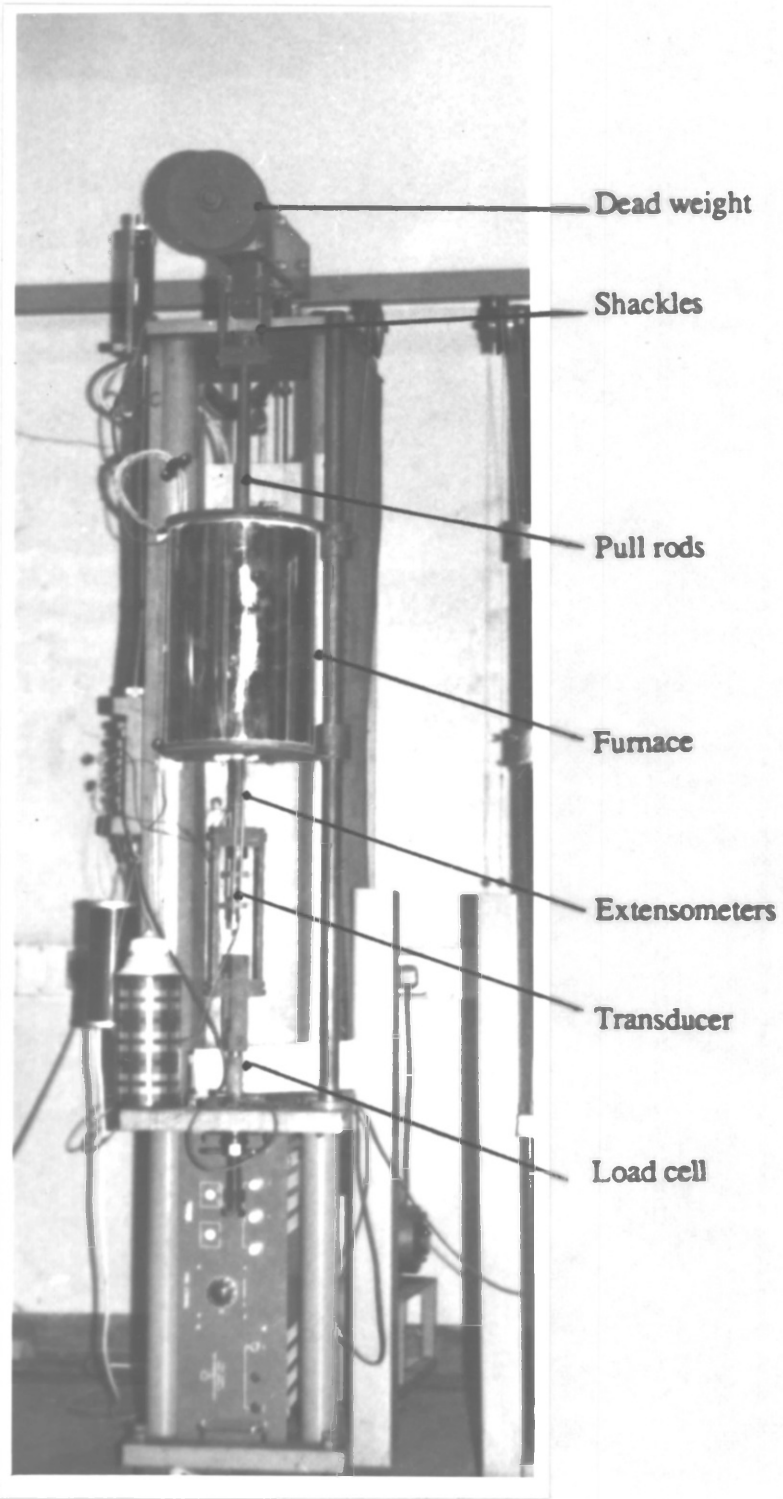
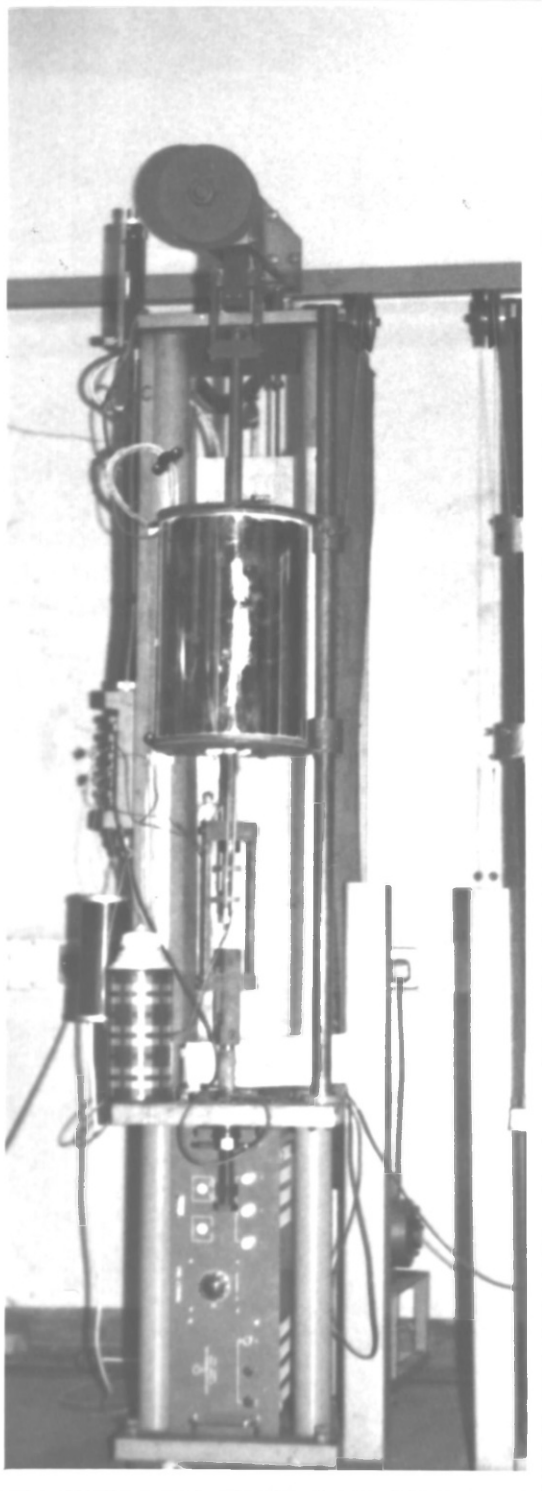


Figure 4.1 : Uniaxial creep testing machine at Imperial College



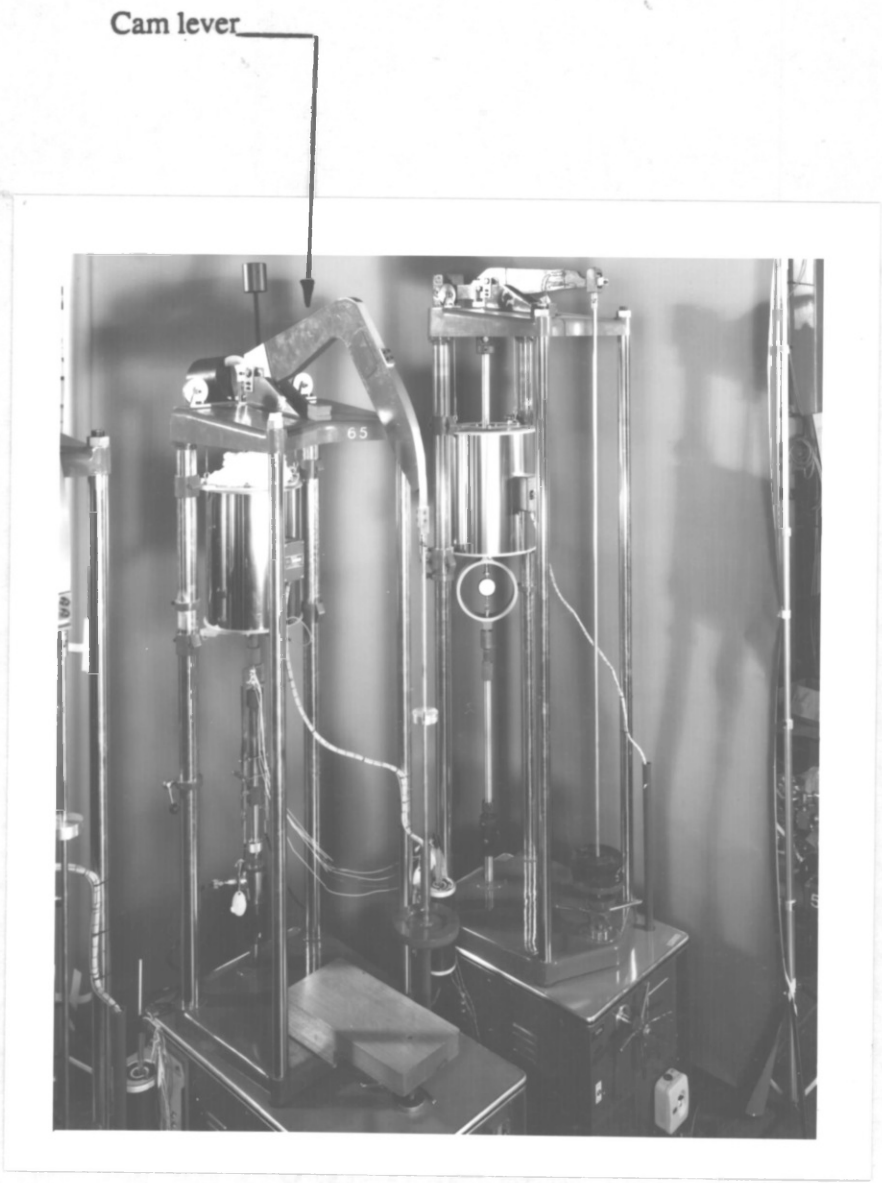


Figure 4.2 : Uniaxial Constant stress and Constant load creep testing machine at NPL


65

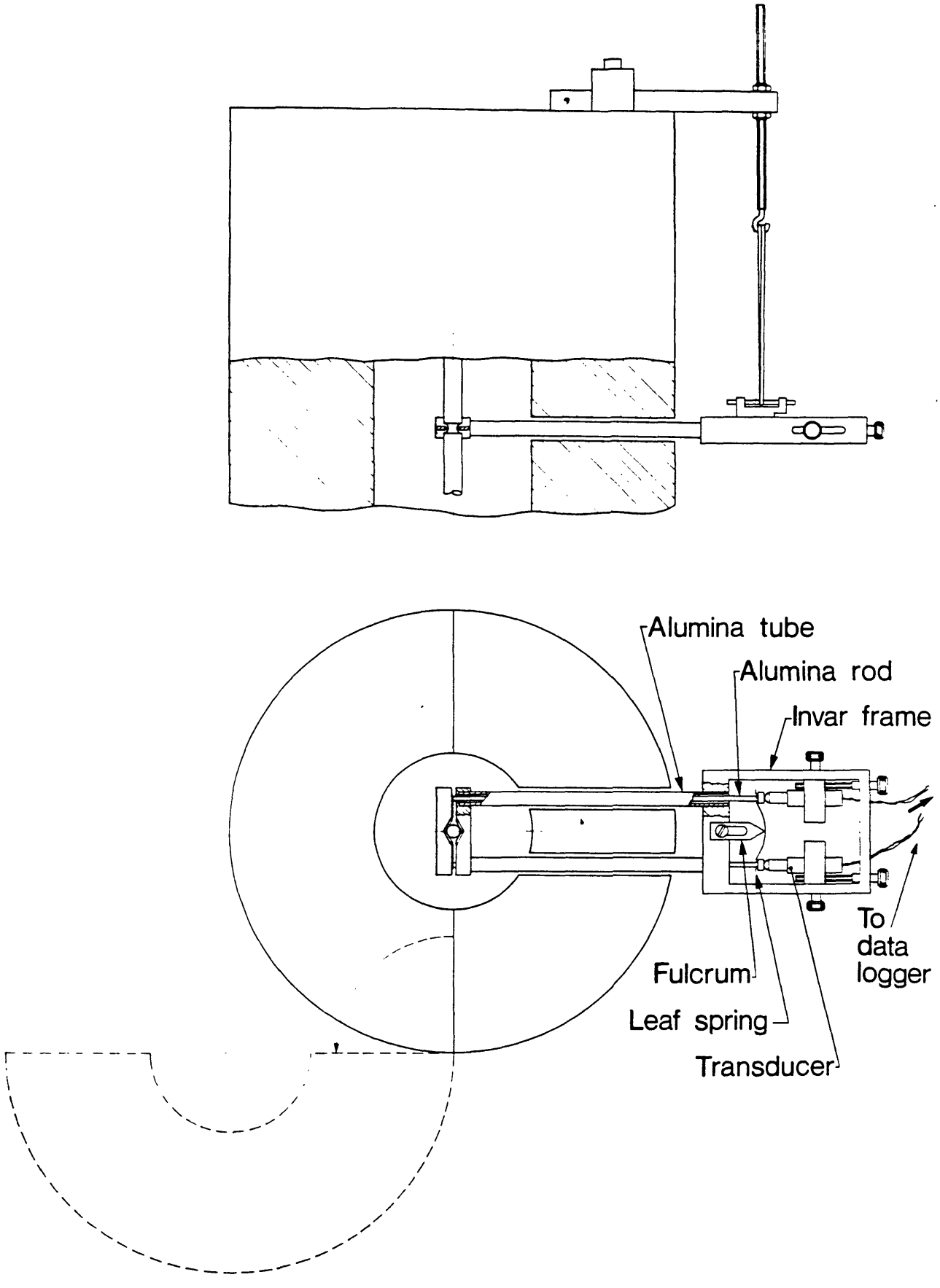
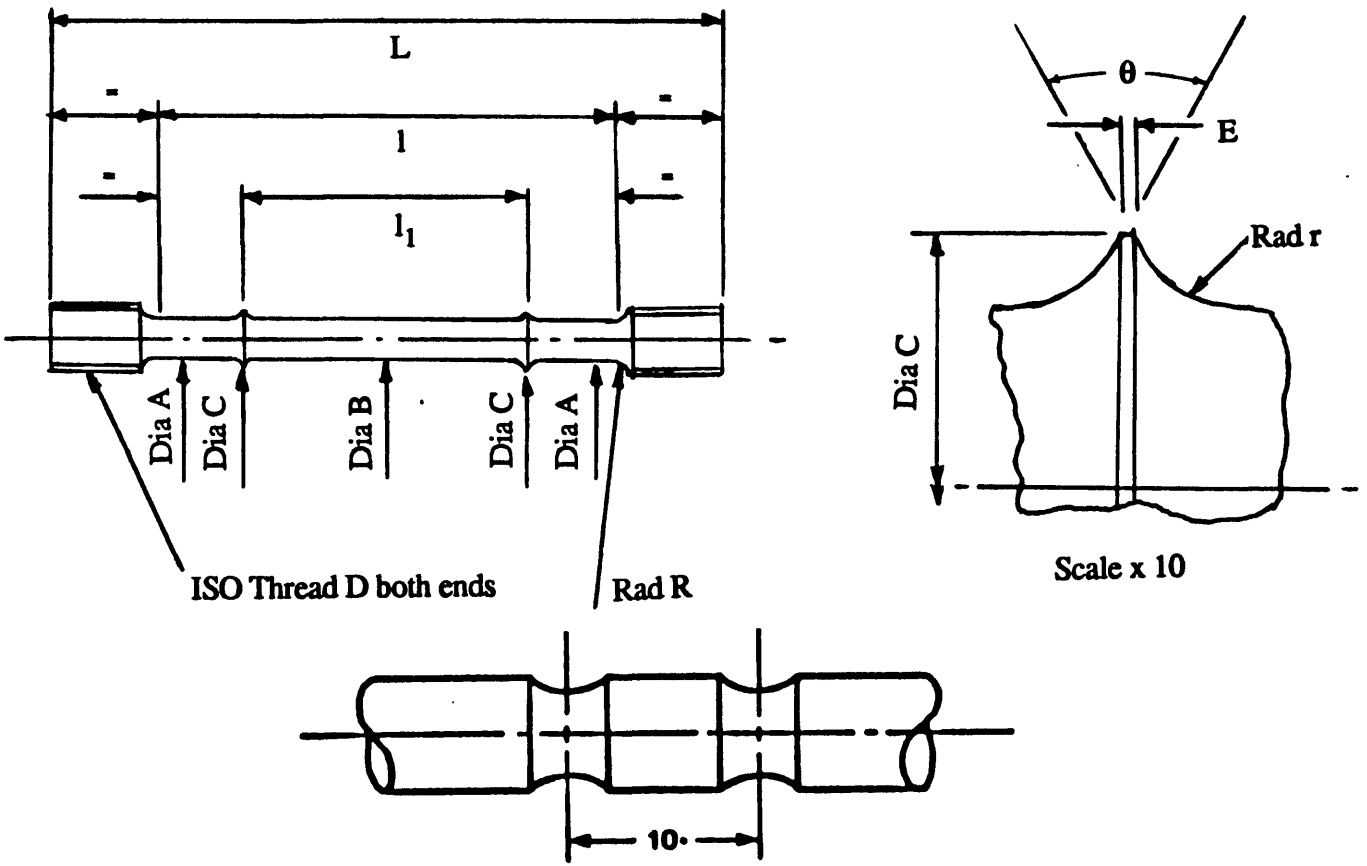


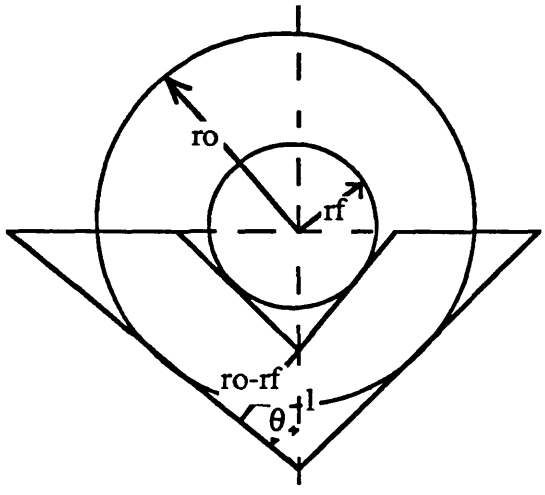
Figure 4.3 : Arrangement for the dimetral strain measurement at NPL



Dimensions in mm

Type	A	B	C	D	E	L	l	l_1	R	r	θ
Uniaxial	6.53	6.50	12.04	M12 x 1.75	0.2	70.0	36.0	25.4	2.5	1.25	60^0
Bridgeman	9.75	9.5	12.04	M12 x 1.75	0.2	70.0	36.0	25.4	5.0	1.25	60^0

Figure 4.4 : Dimensions of the Uniaxial and Multiaxial test specimens



ro = Initial Radius

rf = Final Radius

$$\varepsilon\theta = (ro - rf / ro)$$

$$= 1 \sin \theta / ro$$

$$= 1 \sin 60 / ro$$

Figure 4.5 : Correction of diametral strain.

CHAPTER-5

EXPERIMENTAL RESULTS AND ANALYSIS FOR ISOTROPIC MATERIALS

5. Introduction

In this chapter different notch geometries are analysed using the finite element program. The main purpose of numerical analysis is to obtain various stresses which are responsible for the failure of components under multiaxial stress conditions across a notch throat. These stresses are then used to predict the behaviour of a material using different theoretical models. In the present study the materials used are 304-H stainless steel and 2-1/4 Cr Mo steel for comparison. The experimental rupture data were collected on 304-H stainless steel at 760 ± 2 ^{0}C, and the data on 2-1/4 Cr Mo steel at 538 ±2 ^{0}C were obtained from the literature. Experimental data are further correlated with a constant ductility model obtained through numerical solutions and different void growth models. Finally, metallography is carried out on different broken notched specimens and microscopic damage is used to correlate with the stress state across a notch throat.

5.1 Experimental results (Isotropic)

This section comprises the experimental results on 304-H stainless steel. Creep tests were carried out on plain and notched bars of 304-H stainless steel at 760 ±2 ^{0}C. Results on 304 -H stainless steel are compared with 2-1/4 Cr Mo steel. The uniaxial creep data and notched bar data on 2-1/4 Cr Mo steel is obtained from Al-Faddagh (1983).

5.1.1 Uniaxial Constant Load Creep Tests

A series of tests were carried out on plain bars in order to determine the material constants. Nominal stress applied varied from 110 MPa to 56 Mpa and a life of 20 to 2200 hrs. was obtained. Standard creep curves are presented in Figure-5.1(a) and 5.1(b). The results are tabulated in Table-5.1. A stress versus rupture time relationship is plotted on a log-log scale as shown in Figure-5.2, and stress versus minimum strain rate is

plotted on log-log scale as shown in Figure-5.3.

The material constants obtained from Figure-5.3 are as follows,

a) Creep index n = 8.10

and

b) Creep constant C = 3.98 E $^{-18}$ [1/ (Mpa)^{n} hr]

Stress versus rupture time relationship is compared with data available in the literature, at two different temperatures, 593 ^{0}C and 815 ^{0}C, Garofalo (1959). It is observed that present data are in good agreement with the data available as shown in Figure-5.4

5.1.2 Uniaxial Constant Stress Creep Tests

Uniaxial constant stress creep data on 2-1/4 Cr Mo steel at 538 ^{0}C are obtained from Al-Faddagh (1983).

5.1.2 1 Prediction of Constant Load Creep Curve From Constant Stress Creep Curve (Time Hardening)

Assume the constant stress creep law

$$\varepsilon = C \sigma^{n} F(t) \tag{5.1}$$

Therefore for time hardening

$$\dot{\varepsilon} = C \sigma^{n} F'(t) \tag{5.2}$$

For constant load

$$d\varepsilon = C \left(\frac{P}{A}\right)^{n} F'(t)\, dt \tag{5.3}$$

For constant volume deformation $A = A_0 L_0 / L$

Therefore

$$d\varepsilon = C \left[\frac{P L}{A_0 L_0}\right]^{n} F'(t)\, dt \tag{5.4}$$

But $L = L0 (1 + \varepsilon)$

Therefore

$$\int d\varepsilon = \int C \left[\frac{P(1+\varepsilon)}{A_0} \right]^n F'(t)\, dt \qquad (5.5)$$

Integrating the equation (5.5)

$$\frac{(1+\varepsilon)^{-n+1}}{(1-n)} = C \sigma_0^n F(t) + \text{constant} \qquad (5.6)$$

At $t = 0$, $\varepsilon = 0$. Therefore we have

$$\left(\frac{1}{n-1} \right) \left[1 - \frac{1}{(1+\varepsilon)^{n-1}} \right] = C \sigma_0^n F(t) = \varepsilon_0 \qquad (5.7)$$

where, ε is the strain accumulated in constant load test at time t and ε_0 is the strain accumulated at time t in constant stress test

$$\varepsilon_0 = \left(\frac{1}{n-1} \right) \left[1 - \frac{1}{(1+\varepsilon)^{n-1}} \right] \qquad (5.8)$$

5.1.2.2 Prediction of Constant Load Creep Curve From Constant Stress Creep Curve (Strain Hardening)

For strain hardening

$$\varepsilon = C \sigma^n t^m \qquad (5.9)$$

Therefore strain rate is expressed as

$$\dot{\varepsilon} = C^{\frac{1}{m}} m \sigma^{\frac{n}{m}} \varepsilon^{1-\frac{1}{m}} \qquad (5.10)$$

or

$$\frac{d\varepsilon}{\varepsilon^{1-\frac{1}{m}}} = C^{\frac{1}{m}} m \left(\frac{P}{A_0} \right)^{\frac{n}{m}} \int (1+\varepsilon)\, dt \qquad (5.11)$$

Integrating the equation (5.11) we have

$$\frac{1}{m}\left[\int \frac{d\varepsilon}{(1+\varepsilon)^{\frac{n}{m}}\varepsilon^{(1-\frac{1}{m})}} - \text{constant}\right]^{m} = \varepsilon_0 \qquad (5.12)$$

Expanding $(1+\varepsilon)^{-n/m}$ for $\varepsilon << 1$ we have

$$\int_0^{\varepsilon}\left[1-\frac{n}{m}\varepsilon+\frac{n}{m}\left(\frac{n}{m}-1\right)\frac{\varepsilon^2}{2}+\text{--------}\right]\varepsilon^{-1+\frac{1}{m}}d\varepsilon = C\left(\frac{P}{A_0}\right)^{\frac{n}{m}}t + \text{constant} \qquad (5.13)$$

At $t = 0$, $\varepsilon = 0$. Therefore we have

$$\varepsilon\left[1-\frac{n}{m}\left(\frac{\varepsilon}{m+1}\right)+\frac{n}{m}\left(\frac{n}{m}-1\right)\frac{\varepsilon^2}{2(2m+1)}\text{------}\right]^{m} = C\left(\frac{P}{A_0}\right)^{n}t^{m} = \varepsilon_0 \qquad (5.14)$$

The constant load creep curves are predicted from the constant stress creep curves using the equations (5.8) and (5.14). The comparison between the experimental constant load creep curve and predicted constant load creep curve is shown in Figure-5.5. It is found that in the secondary creep region both the experimental and predicted curves show a good agreement. But in the tertiary region the predicted curve shows the lower creep strain rate. This can be due to the necking observed in the constant load tests in the early stages.

5.1.3 Multiaxial Constant Load Creep Tests

Notched bars, having the same throat diameter as the plain bars, were machined to give a constant b / a ratio of 1.46 and different a / R ratios as shown in Table-5.2. These specimens were creep tested in a constant load uniaxial creep testing machine at 760 ± 2 ^{0}C. All tests were carried out at a constant nominal stress, across a notch throat, of 90 MPa.

5.2 Data Analysis

Data obtained from notched bar creep tests are analysed to explain the notch strengthening behaviour of this material. A notch strengthening ratio is the ratio of rupture life of a notched bar to the rupture life of a plain bar subjected to the same nominal stress, σ_{nom}. This ratio, t_{no} / t_{un}, is plotted against a / R ratio in Figure-5.6. The experimental data on 2-1/4 Cr Mo steel are plotted in Figure-5.7

The final dimensions after fracture are measured by joining the two halves together on a shadowgraph, and the reduction in area is calculated for all the notch geometries. Figure-5.8 shows the comparison of original a / R ratio with the final a / R ratio in Reduction in area for 2-1/4 Cr Mo steel is compared with reduction in area for 304-H stainless steel in Figure-5.9 From the data collected at the specified temperature, it is found that although the uniaxial ductility, measured in terms of reduction in area, is almost the same, multiaxial ductility in these steels differs considerably. The reduction in area of notched bars is then normalized with respect to the reduction in area of a plain bar, subjected to a same nominal stress as the notched bars and plotted in Figure-5.10 along with the two void growth models mentioned before. Strain to fracture under multiaxial stress is calculated from simplified form of Cocks and Ashby's void growth model given by,

$$\varepsilon_f = \frac{\alpha}{(n+1)} \log_n \left[\frac{1}{(n+1)f_i} \right] \qquad (5.15)$$

This strain to fracture in terms of reduction of area is plotted for different values of 2l in Figure-5.11 and 5.12 for 304 -H stainless steel and 2-1/4 Cr Mo steel respectively. Reduction of area for different notch geometries is superimposed as shown by dotted lines in respective figures. Further, an approximate value of f_i is calculated from these plots and fed into equation 5.15 replacing α by α_0. Thus the uniaxial strain to fracture is calculated. The respective values for 304-H stainless steel and 2-1/4 Cr Mo steel are 180 and 214. Normalized reduction of area is recalculated using these values of uniaxial ductility and plotted in Figure-5.10 as shown by dotted lines.

5.3 Numerical Analysis

A finite element program available in Al-Faddagh (1983), is used for numerical analysis. This program was found to have two drawbacks ;

a) the convergence rate to get a steady state solution was slow,

b) the convergence criterion given by,

$$\frac{\Sigma_i \{ | \Delta u_i | + | \Delta v_i | \}}{\Sigma_i \{ | u_i | + | v_i | \}} \leq \lambda \qquad (5.16)$$

where λ varies from 10^{-3} to 10^{-8} depending on the nature of the problem.The above convergence criterion could not hold good for very sharp and slit type notch geometries. The reason is that, because of the slow convergence rate the solution obtained based on the above criterion could be far from the actual solution, even though the tolerance specified was achieved.

In the present work some modifications have been made in the program to overcome the above difficulties. Convergence is accelerated by imposing displacement boundary conditions rather than stress boundary conditions. In almost all finite element programs which are used for stress analysis the displacements are unknown variable. First the displacements are calculated at all the nodal points from which the strains are calculated and ultimately the stresses. The unknown value has to be continuous across the interface of the adjacent elements for the fast convergence of the present finite element method. By imposing the displacement boundary conditions the displacements are well defined all over the domain and thus the continuity of unknown displacements is assured. Since the value of the displacements is prescribed the stiffness matrix is modified and made more diagonally dominant, which gives the optimum condition for convergence. This is the reason why the convergence rate accelerates by imposing the displacement boundary conditions rather than stress boundary conditions. At the same time, the convergence criterion adopted is based on the balance of load between the top and bottom end of a notched bar under analysis. The mathematical form of this criterion is already

mentioned in Chapter-3 .

A range of notch geometries is chosen from Bridgman type notch to a slit type notch in order to study the effect of constraint on stress state across a notch throat.

5.4 Mesh Generation

As the problem considered here is axisymmetric, only one quarter of cross sectional plane is used for analysis. An automatic mesh generation program similar to that described in Segerlind (1978) is used to generate a triangular mesh pattern. The main requirement of constant strain triangle finite element program is to have the triangles of equal angles as far as possible, in order to achieve best conditions for convergence. An aspect ratio between any two sides of a triangle should not be greater than 2. Therefore care is taken to avoid an obtuse angle at any nodal point of a triangle in a mesh. Special attention is given at the notch root as the elements are very small. A reasonable element size is obtained at the notch root by refining the mesh several times. Figure-5.13 shows the general nomenclature of a notched bar and Figure-5.14 shows some of the mesh patterns obtained for the analysis.

5.5 Stress Variation Across A Notch Throat

The material constants used in the program were obtained from the uniaxial creep data for 304-H stainless steel, and are given by ;

$E_0 = 141$ Mpa and $\upsilon = 0.45$

where E_0 = Reference modulus of elasticity

υ = Poisson's ratio

Stresses in each element across the notch throat are obtained. Because of the oscillations in the stress values in two adjacent elements (1&2, 3&4, e.t.c.) the average stress is calculated from the stresses in these two elements. This average stress is then normalized with respect to the stress at the remote end of a bar , σ_∞. The distance of this point from the centre line of a bar is normalized with respect to the radius of a bar " a "

across the notch throat. Thus the normalized stresses across the notch throat are plotted against the normalized radial distance " r / a ".

A skeletal point is defined as, the point (across the throat of a notched bar) at which the stress is supposed to remain constant throughout a creep history. The skeletal point is observed in all the notch geometries studied for $n \geq 3$ as shown in Figure-5.15. From the stress distributions a skeletal point is found to exist in a localized portion of a notch throat. This point may not be exactly constant, but the stresses at this point can be used as a best approximation to characterize the behaviour of the components under multiaxial loading conditions.† This skeletal point approach is extensively used in the literature to predict the life of the complicated structures subjected to creep. In the present work the same approach is adopted to correlate numerical data with the experimental data. The materials tested and analysed obey the effective stress failure criterion and are thus termed as, σ_{eff}, materials. Hydrostatic stress , σ_{mean}, is responsible for causing the voids to grow. Therefore it is important to have a knowledge of these stresses in order to understand the failure pattern of the components subjected to multiaxial stresses under creep conditions. To examine the effect of constraint on the stress state three notch geometries, b / a = 1.46 and a / R = 1.67,9.30,21.60 are selected for analysis. These notch geometries represent low, medium and high constraint. Examples of variation of different stresses across a notch throat of these notch geometries are presented, and compared with the results obtained from ASAS-NL package available at Atkins Pvt. Ltd., Lowe (1987) in Figures-5.16-5.18. The results are found to be in good agreement. Further similar stresses are calculated for different values of creep index, n, by using the present finite element program. These results are presented in Figures-5.19-5.21.

To understand the effect of geometrical parameters such as the b / a ratio or notch depth, stress variations across a notch throat are obtained for different values of b / a ratio. Again maximum principal stress, effective stress, hydrostatic stress and triaxiality factor,$\sigma^*_{mean} / \sigma^*_{eff}$, at a skeletal point are plotted in Figures-5.22-5.25 against a / R ratio for different values of b / a ratio. Detailed analysis is carried out for the notch

† The presence of a skeletal point may not be valid during tertiary creep when damage accumulation is involved

geometries of b / a = 1.46 and a / R ratio ranging from 1.67 up to 50 . The normalized stresses at the skeletal point are shown in Figure-5.26 for different values of a / R. The constraint factor, $\sigma_{nom} / \sigma^*_{eff}$ at a skeletal point is plotted against notch depth for different a / R ratios in Figure-5.27. A slip line field solution obtained by Bridgman (1952) for a necked cylinder bar is plotted on the same figure.

The Bridgman slip line field solution is obtained from the following equation

$$\frac{\sigma_{nom}}{\sigma_{eff}} = \left(1+\frac{2R}{a}\right) \log_n \left(1+\frac{a}{2R}\right) \qquad (5.17)$$

A constant ductility model used to predict theoretically the notch strengthening effect is obtained from the equation,

$$t_{no} / t_{un} = (\sigma_{nom} / \sigma^*_{eff})^n \qquad (5.18)$$

The void growth models suggested by Rice and Tracey (1969) and Cocks and Ashby (1980) are represented by the following equations,

$$\frac{\varepsilon_{no}}{\varepsilon_{un}} = \frac{1.64}{\exp\left(\frac{3\sigma_{mean}}{2\sigma_{eff}}\right)} \quad \text{(Rice and Tracey)} \qquad (5.19)$$

$$\frac{\varepsilon_{no}}{\varepsilon_{un}} = \frac{\mathrm{Sinh}\left[\frac{2(n-1/2)}{3(n+1/2)}\right]}{\mathrm{Sinh}\left[\frac{2(n-1/2)}{(n+1/2)}\frac{\sigma_{mean}}{\sigma_{eff}}\right]} \quad \text{(Cocks and Ashby)}$$

(5.20)

The experimental data on 304-H stainless steel are compared with the constant ductility model given by equation (5.18) and the other two void growth models given by equations (5.19) and (5.20) in Figure-5.6. The experimental data on 2-1/4 Cr Mo steel plotted are compared with similar models in Figure-5.7

5.6 Comparison of Numerical and Experimental Deformation Rate

To examine the validity of the experimental results, the experimental deformation

rate obtained for the notched bars are compared with the theoretical deformation rates. From the deformation versus time plot, the deformation rates for selected notch geometries were obtained. A suitable value of reference stress , σ_0, calculated from the uniaxial data, was fed into the numerical analysis. Numerical analysis was carried for 304-H stainless steel and 2-1/4 Cr Mo steel. The results are tabulated in Table-5.3. It is observed that the theoretical deformation rate is always higher than the experimental deformation rate. This indicates that the overall deformation in these steels is affected by necking.

5.7 Metallographic Analysis

Metallographic analysis was carried out mainly to study the progress of a damage across the notch throat as the triaxiality increases. Two notch geometries,a) shallow a / R = 2.6, and b) sharp a / R = 21.6 were selected for the analysis. The broken specimens were cut longitudinally along the centre line within a tolerance of ±0.1 mm.. Sectioned specimens were then polished and etched several times to give the best possible details of the damage. The etchent used for 304-H stainless steel was Marble's reagent and for 2-1/4 Cr Mo steel was 2% nital. Figure-5.28 shows the failure of the blunt notch of 304-H stainless steel. It is seen that the damage has spread throughout the notch throat indicating that the failure is governed by the global phenomenon. Figure-5.29 shows the failure of the sharp notch of 304-H stainless steel. The damage in this case is in the form of cracks traversing through the grains in the vicinity of the notch root where the skeletal effective stress exists. This damage thereafter spreads towards the notch root surface and away from the notch root towards the centre of the notch (Tvegard (1984)). Similar findings are reported by Hayhurst et al. (1984) in 316 stainless steel. Thus the failure in this case is a local event as described by Wu et al.(1985). Figure-5.30 shows the failure of the blunt notch of 2-1/4 Cr Mo steel and Figure-5.31 shows the failure of the sharp notch of 2-1/4 Cr Mo steel. In both the notch geometries there is no indication of the damage. But large deformation of the grains suggests the failure is mainly due to necking. Figure-5.32

shows the cavities becoming stabilized due to diffusion in the 304-H stainless steel. These cavities seem to occur nucleated randomly along the grain boundaries. On the other hand cavities do not occur in 2-1/4 Cr Mo steel. Figure-5.33 shows the difference in the failure mechanism of these steels.

5.7.1 Quantitative Metallography of 304-H Stainless Steel

The spacing of the voids in 304-H stainless steel calculated from the void growth model presented in Figure-5.11 is in the range of 10-20 μm. The value of f_i occurring in equation 5.15 is calculated for different notch geometries using the stresses at the skeletal point from the finite element calculations. The average value of f_i obtained is 4×10^{-6}. Using the average value of f_i and the spacing of 20 μm, the value of initial radius is calculated which is around 0.04 μm. The initial radius is also calculated from the equation

$$r_i = 2\gamma / \sigma_1 \qquad (5.21)$$

where γ is the surface energy $= 2.0\ J\ m^{-2}$

σ_1 the nominal stress across the notch throat = 90 Mpa

The value of r_i obtained is approximately equal to 0.04 μm. The value of initial radius calculated is in good agreement with the value obtained from the void growth model. From Figure-5.32 it is observed that the voids grow by diffusion initially. Once they are stabilized they grow by power-law creep, and thus the final failure is due to the growth and coalescence as shown in Figure-5.28 and 5.29. The average spacing at the failure calculated from Figures 5.28 and 5.29 is equal to 130 μm..The average grain size is 140 μm. The average spacing at the time of failure is slightly less than the average grain size. The difference in the original spacing and the final spacing can be explained in the following way.

According to Cocks and Ashby (1980) void growth model cavities are distributed uniformly along the grain boundary and failure occurs when they grow and join each other. In the present analysis it can be seen that voids are distributed uniformly in random groups. Once the voids in each group are stabilized by diffusion they grow by power-law. The cavities in one group grow and combine to form big holes which act as a

individual cavity. Failure occurs when these holes continue to grow and join each other. These groups of holes when joined separate two grains from each-other. Thus the spacing calculated after the final failure can not be equal to the initial spacing.

5.8 Discussion

5.8.1 Discussion of Experimental Results

Creep rupture data on 304-H stainless steel shows very little primary and tertiary creep but a pronounced and long secondary creep as shown in Figures 5.1(a) and 5.1(b). The data compared with the data in the literature shows a good agreement in Figure-5.4. As shown in Figure-5.5 the predicted constant load creep curve is in good agreement in the secondary region but underestimating in the tertiary region. The reason is that necking commences in the constant load test much earlier in life. But in constant stress test necking occurs just before the failure. Thus in the secondary region the curves show a good agreement. Figure-5.6, life in 304-H stainless steel increases with a / R ratio up to the value of 9.30. Later the life decreases steeply as a / R ratio increases. On the other hand life in 2-1/4 Cr Mo steel increases and attains the same value as 304-H stainless steel up to the a / R value of 6.0. After that it drops slightly and remains constant for the rest of the a / R values. This suggests that both steels show notch strengthening up to a certain value of a / R . After that 304-H stainless steel shows less notch strengthening. This gives an indication of change in mode of fracture in 304-H stainless steel while 2-1/4 Cr Mo steel does not show any indication of notch sensitivity. A constant ductility model which does not account for the effect of hydrostatic stress represents the upper bound solution to the notch strengthening. On the other hand void growth models which account for the effect of hydrostatic stress show the lower bound to the notch strengthening in the present situation. Under triaxial stress condition the deformation is governed by effective stress. Once the voids are initiated, they grow under the combined effect of effective stress and hydrostatic stress. The hydrostatic stress assists the voids to grow faster and thus helps to reduce the life. As experimental data lie between the two

models, it clearly shows that failure in both the steels is due to the combined effect of effective stress and the hydrostatic stress. This fact is explained in Figures-5.6 and 5.7 for 304-H stainless steel and 2-1/4 Cr Mo steel, respectively. From Figure-5.8 it can be seen that the original notch dimensions have been reduced. In other words the notch has become blunt. Thus the triaxiality effect is less which results in an increase in the life of a component.

Reduction in area in 304-H stainless steel drops from 75 % of its uniaxial value to 21 % as the notch sharpness increases. On the contrary, reduction in area in 2-1/4 Cr Mo steel shows a negligible change from its uniaxial value as shown in Figure-5.9. Normalized reduction in area, as defined by the reduction in area of a notched bar to the reduction in area of a unnotched bar, does not agree with the void growth models as shown in Figure-5.10. This explains the necking instability in the uniaxial tensile test. Due to necking, stresses across the bar are no longer constant, but a triaxial state of stress prevails. This causes the uniaxial ductility to drop depending on the amount of necking. Several authors have reported this phenomenon in literature. Tvegard (1984) reported a reduction in logarithmic axial strain from 1.84 to 1.17. It is observed that normalized reduction in area for 304-H stainless steel falls between the two void growth models, but the normalized reduction in area for 2-1/4 Cr Mo steel does not agree with both the models. This indicates that failure mechanism in 2-1/4 Cr Mo steel is quite different from that of 304-H stainless steel.

5.8.2 Discussion of Numerical Results

From figures-5.16 - 5.18 it is noted that the present solution is in good agreement with the solution obtained from the ASAS-NL program . From Figures-5.19 to 5.21 it is observed that steady state distribution across the blunt notch with a / R equal to 1.67 is much more uniform compared with the medium and sharp notch geometries with a / R equal to 9.30 and 21.60 respectively. In the sharp notch, maximum principal stress and hydrostatic stress are found to be localized near the notch root. A skeletal point is found to be well established in all the notch geometries studied. Stresses at this skeletal point are

then used to characterize the general behaviour of a notch throat. An interesting fact is that the skeletal point shifts towards the notch root as the notch sharpness increased. For example, the position of the effective stress skeletal point in the case of a / R equal to 1.67 is 0.57, a / R equal to 9.30 is 0.80 and a / R equal to 21.60 is 0.91. This indicates that the damage is much more likely to be concentrated near the notch root as notch sharpness increases.

From Figures-5.23 and 5.24 it is clear that both maximum principal stress and hydrostatic stress increase with increase in a / R ratio, i. e. notch sharpness and b / a ratio, or notch depth. On the other hand, effective stress decreases up to a certain value of a / R ratio, i. e. 9.30, and then becomes constant as shown in Figure-5.22. The overall effect is that the triaxiality factor or the ratio, $\sigma^*_{mean} / \sigma^*_{eff}$, increases with increase in notch sharpness as well as notch depth as shown in Figure-5.25. In 304-H stainless steel mode of fracture changes from global to local failure as notch sharpness increases. In a local failure mode the damage is localized near the notch root. An increase in triaxiality factor may assist the damage to grow faster and thus affect the mode of fracture. Similar conclusions can be drawn from Figure-5.26 which shows the stresses at the skeletal point for different notch geometries.

In Figure-5.27, ratio of $\sigma_{nom} / \sigma^*_{eff}$ increases with increase in a / R ratio up to a particular value and then becomes constant. This ratio defined as a constraint factor by Bridgman represents the degree of constraint in the notch root and is projected in the same figure. The constraint factor obtained by Bridgman overestimates the values obtained in the present analysis up to the a / R ratio of 10 and underestimates the value for a / R ratio of 20. The Bridgman solution is applicable to the blunt notches (low triaxiality) where the effective stress is almost uniform. The equation is least important when the total reduction in area is very small Hill (1950). For the blunt notch (a / R =1) the error between the finite element solution and the Bridgman solution is around 6 %. But with increase in the notch sharpness there is no close agreement between the two solutions. This fact can be explained by the limitations of the applicability of the equation suggested

by Bridgman for a constraint factor.

5.8.3 Discussion of Metallographic Analysis

From Figures-5.28 and 5.29 it is confirmed that the final failure in 304-H stainless steel is due to void growth. This fact is supported by the quantitative metallography carried out in Section 5.7.1 for 304-H stainless steel. From Figures-5.30 and 5.31, it is clear that 2-1/4 Cr Mo steel does not show any indication of the voids, but in 304-H stainless steel voids first grow by diffusion. Once they are stabilized they grow by power-law under the influence of hydrostatic stress and effective stress. The coalescence of these voids causes the final failure. This fact is proved from the final spacings of the voids which is slightly less than the average grain size. However, in both the steels failure is intergranular. But , in 2-1/4 Cr Mo steel, as failure is mainly due to necking, it is less intergranular and from inside to outside as shown in Figure-5.33. Damage in 304-H stainless steel near the notch root increases as notch sharpness increases. For example, the area in the vicinity of a sharp notch is severely damaged due to cracking along the grain boundaries. Damage has been found to be localized in the notch root. Away from the notch root, inside, the damage is very small. In the case of a blunt notch, there is no indication of a localized damage in the form of cracks. The damage is spread throughout the notch region as similar to the damage predicted by Hayhurst et al. (1984) in the case of 316 stainless steel. This explains the phenomenon of global failure in a blunt notch and local failure in a sharp notch as suggested by Wu et al. (1984). For a sharp notch the skeletal point exists near to the notch root. The damage can be assumed to start in the region near to the skeletal point. Thereafter it propagates towards the centre and simultaneously towards the notch surface (Tvegard (1984)). Thus the failure is always localized near the notch root. In the case of 2-1/4 Cr Mo steel, it is observed that there is no indication of the damage either in the blunt or sharp notch. Grains near the notch root are found to be elongated. From the above facts it is confirmed that the failure of 2-1/4 Cr Mo steel is mainly due to necking. The main difference in the failure mode in these steels is explained in Figure-5.32. This can explain why ductility remains constant after a

certain value even though notch sharpness is increased.

Average grain size measured in 304-H stainless steel is found to be 140μm while in 2-1/4 Cr Mo steel it is around 70 μm. From Cocks and Ashby (1980) void growth model the strain to failure can be written as ;

$$\varepsilon_f = \dot{\varepsilon}_s \, t_f + 0.2\, l / d \qquad (5.21)$$

Normally $\varepsilon_f = \dot{\varepsilon}_s \, t_f$ but, in multiaxial stress condition the term 0.2 l / d, can be of the order as $\dot{\varepsilon}_s \, t_f$. Therefore ε_f can become sensitive to grain size. For a larger grain size, under high triaxiality the measured ductility and the predicted ductility can be of the same order. For a small grain size, the measured ductility can be much higher than the predicted ductility. That means triaxiality is more dangerous for larger grain size. This can be the fact why stainless steel becomes more notch sensitive as notch sharpness increases. The same ideas are reported by Davis and Manjoine (1967) in their investigations with different steels.

5.9 Conclusions

The main conclusions from this chapter are summarized as follows;

1)Even though the uniaxial ductility in the two steels investigated is the same, multiaxial ductility is quite different.

2) Failure of 304-H stainless steel is due to the growth of voids and their coalescence. The damage in the blunt notch is found to be distributed throughout the notch throat region. The damage in the sharp notch is found to be localized in the notch root region. Thus the failure in the blunt notches is a global event while the failure in the sharp notches is a local event. The failure of 2-1/4 Cr Mo steel is mainly by necking.

3) Failure in 304-H stainless steel is more intergranular and is from outside to inside, while failure in 2-1/4 Cr Mo steel is less intergranular and is from inside to outside.

4) The redistribution time calculated from the finite element program ASAS-NL has been found to be very short. As the stresses get settled early , the redistribution time does not contribute to the total life of the component.

TABLE - 5.1

Uniaxial Creep Data For 304-H Stainless Steel

Stress (MPa)	Minimum Creep Rate ε_s (h^{-1})	Rupture Time t_f (hours)	Failure Strain ε_f (%)	Reduction in Area A_f (%)
110	7.7624×10^{-3}	20	38	70.62
89	2.4547×10^{-3}	72	58	55.00
79	1.3489×10^{-3}	172	70	65.00
70	5.8884×10^{-4}	650	70	72.00
65	2.5704×10^{-4}	1150	70	73.00
56	1.0965×10^{-4}	1800	68	68.30

TABLE - 5.2

Different notch geometries used in the numerical analysis

b / a	a / R	2b	2a	2R
1.46	1.67	9.50	6.50	3.892
1.46	2.60	9.50	6.50	2.490
1.46	4.00	9.50	6.50	1.625
1.46	5.00	9.50	6.50	1.300
1.46	6.00	9.50	6.50	1.086
1.46	9.30	9.50	6.50	0.698
1.46	13.00	9.50	6.50	0.500
1.46	17.00	9.50	6.50	0.382
1.46	21.60	9.50	6.50	0.309
1.46	28.00	9.50	6.50	0.232

TABLE-5.3

Comparison of theoretical and experimental deformation rate for 304-H stainless steel

a / R	Theoretical deformation rate δs ($mm\ h^{-1}$)	Experimental deformation rate δs ($mm\ h^{-1}$)
1.67	7.175×10^{-3}	5.43×10^{-3}
4.60	8.000×10^{-3}	2.77×10^{-3}
6.00	6.400×10^{-3}	2.00×10^{-3}
21.60	5.400×10^{-3}	1.04×10^{-3}

Comparison of theoretical and experimental deformation rate for 2¼ Cr Mo Steel

a / R	Theoretical deformation rate δ average ($mm\ h^{-1}$)	Experimental deformation rate δ average ($mm\ h^{-1}$)
1.67	12.00×10^{-2}	7.036×10^{-3}
4.60	6.80×10^{-2}	1.960×10^{-3}
9.30	4.80×10^{-2}	2.272×10^{-3}
21.60	3.60×10^{-2}	2.000×10^{-3}

-

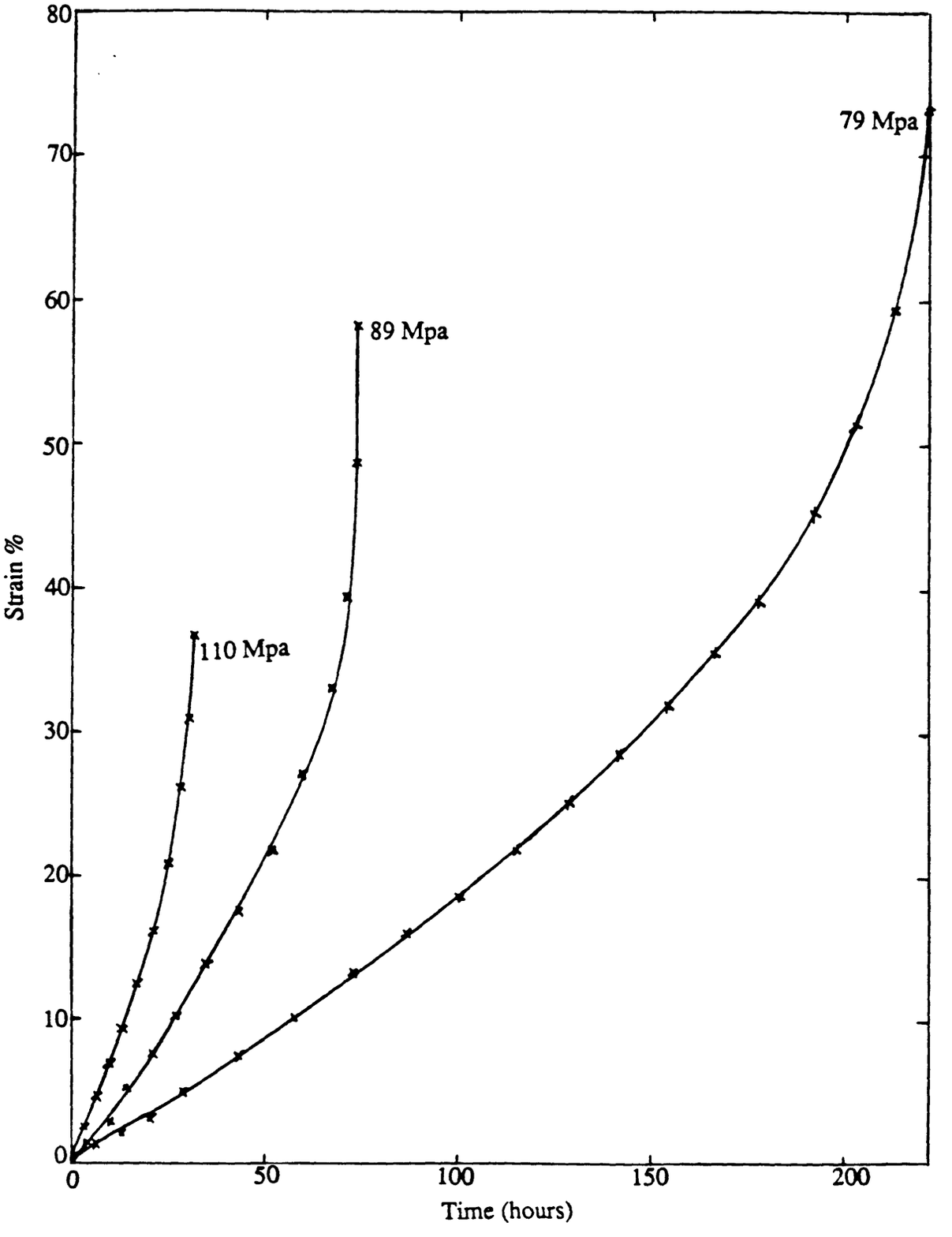


Figure - 5.1a : Uniaxial constant load creep data for 304-H stainless steel at 760 ±2 ^{0}C

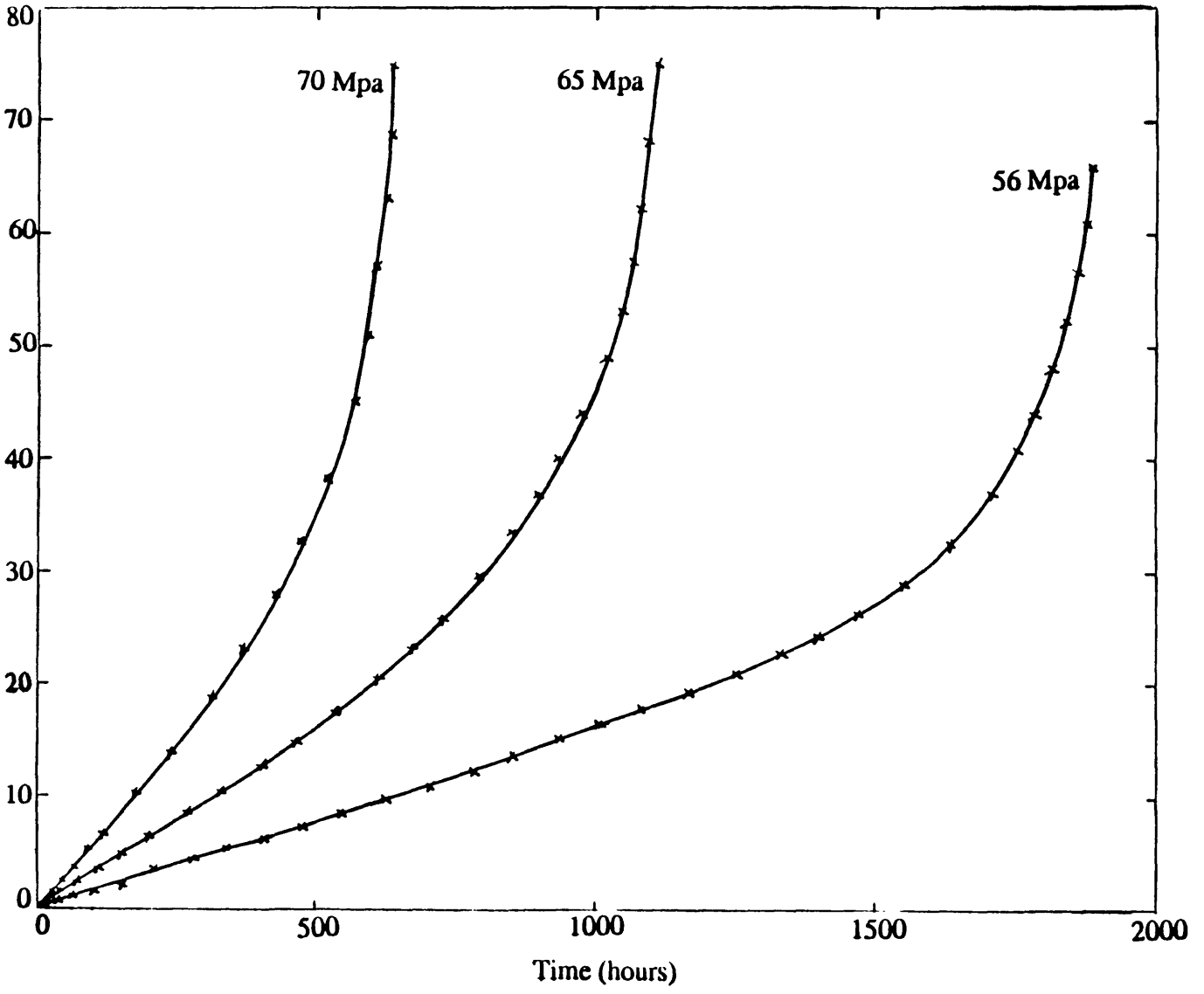


Figure - 5.1b : Uniaxial constant load creep data for 304-H stainless steel at 760 $\pm 2^{0}$C

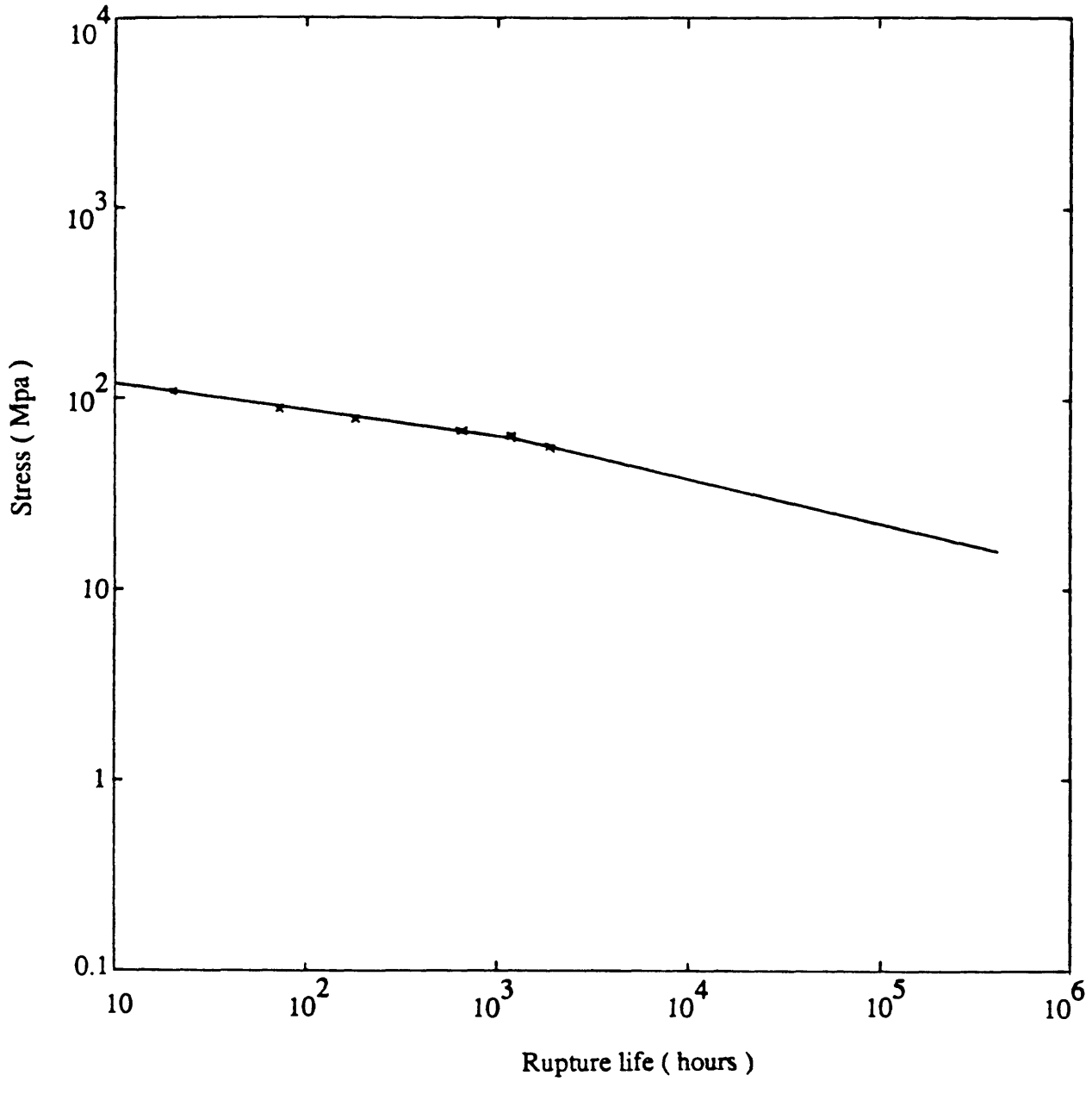


Figure - 5.2 : Log-Log plot of nominal stress versus time to fracture for 304-H stainless steel

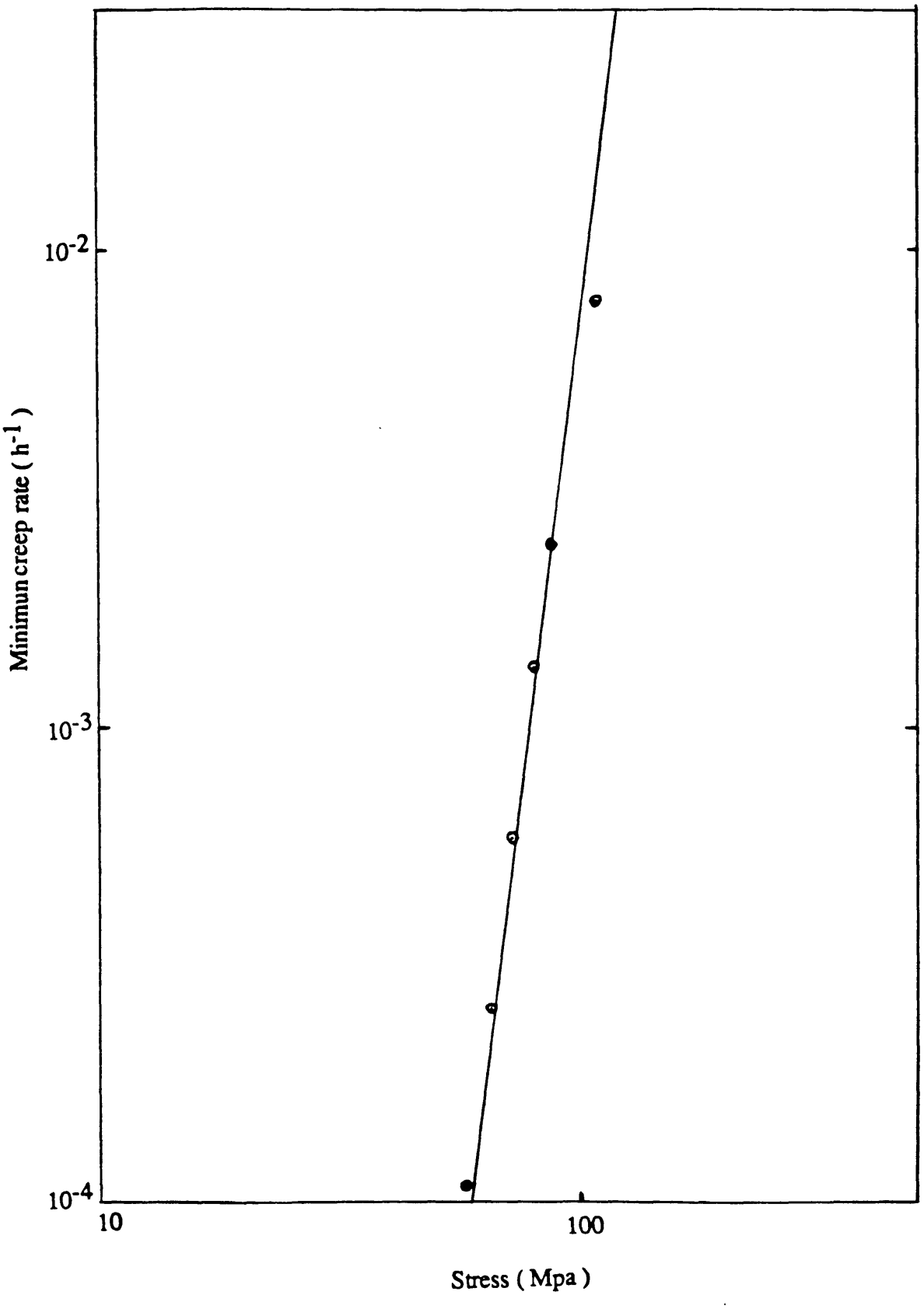


Figure - 5.3 : Log-Log plot of minimum creep rate versus stress for 304-H stainless steel

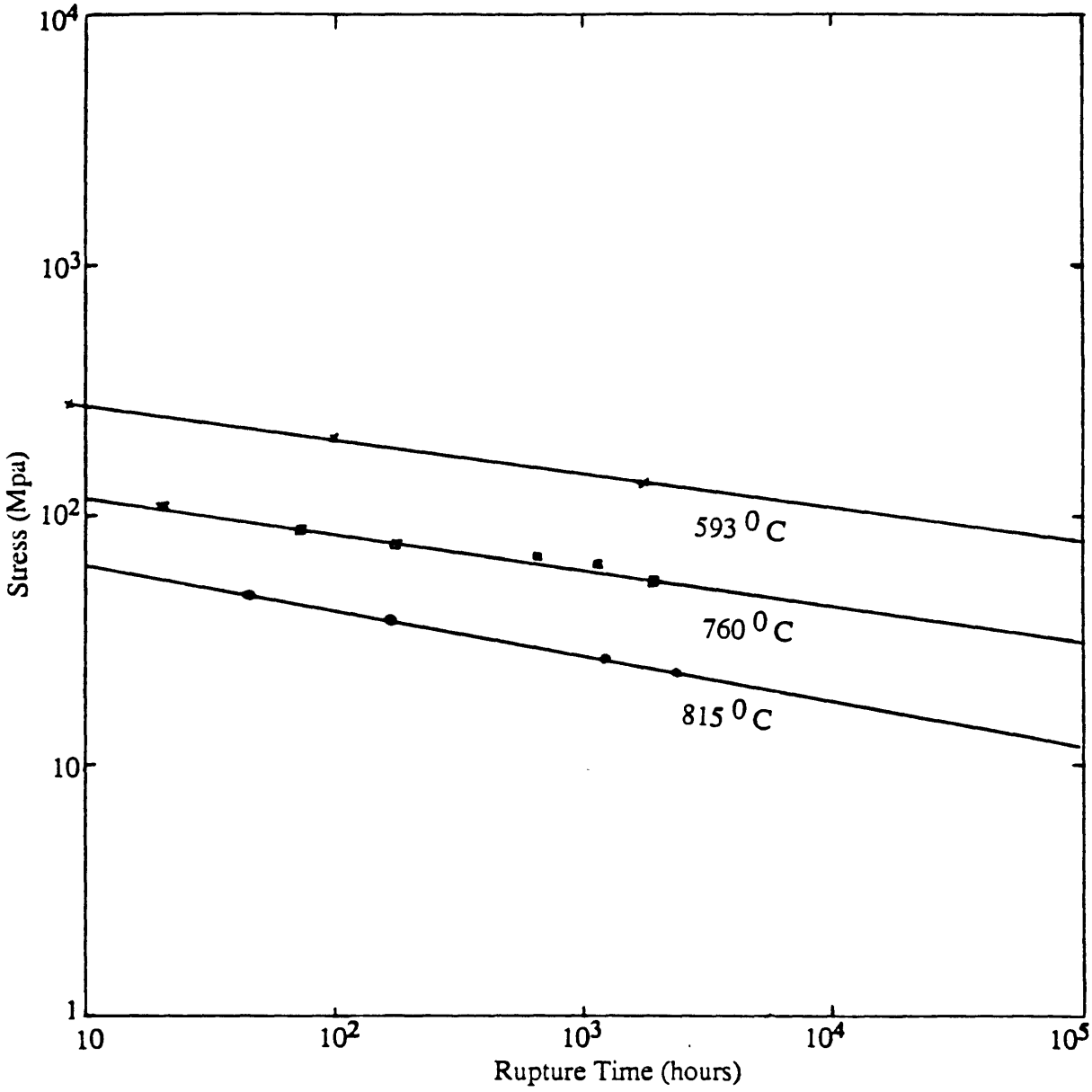


Figure - 5.4 : Comparison of creep rupture data at different temperatures

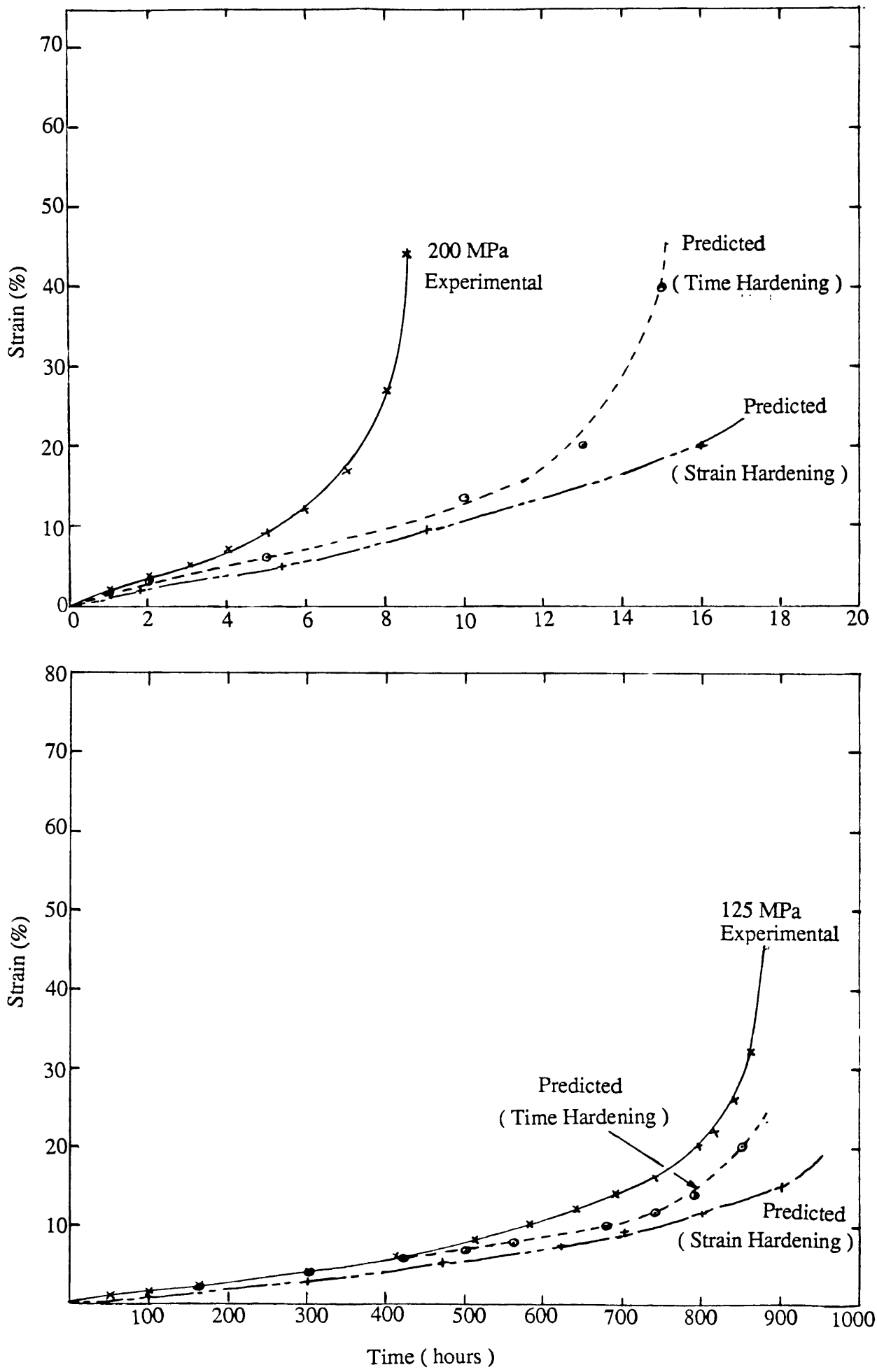


Figure 5.5: Comparison of experimental constant load creep curve with the predicted constant load curve from constant stress curve 2-1/4 Cr Mo steel

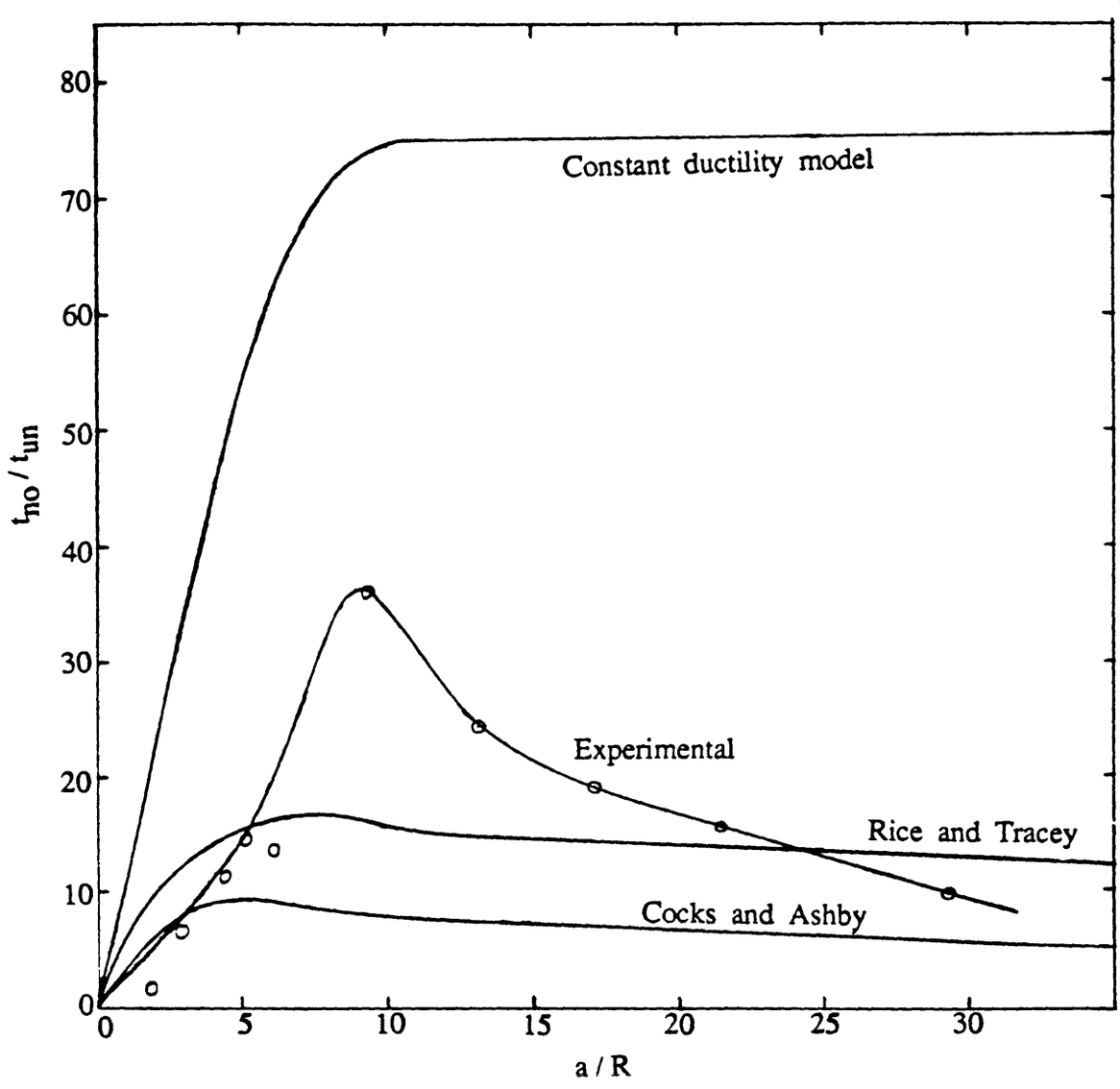


Figure - 5.6 : Comparison of experimental data with different theoretical models for 304-H stainless steel

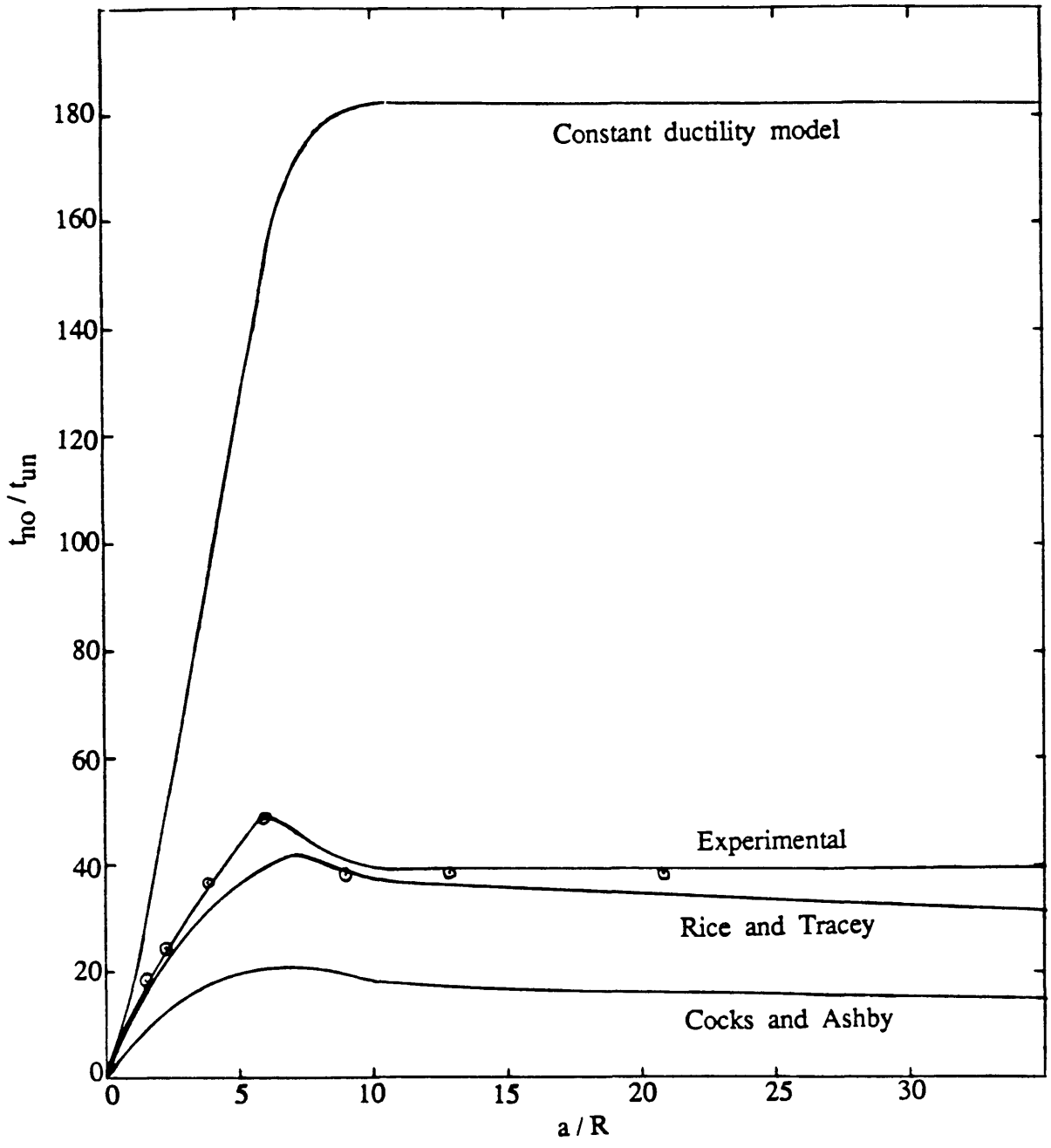


Figure 5.7 : Comparison of experimental data with different theoretical models for 2-1/4 Cr Mo steel

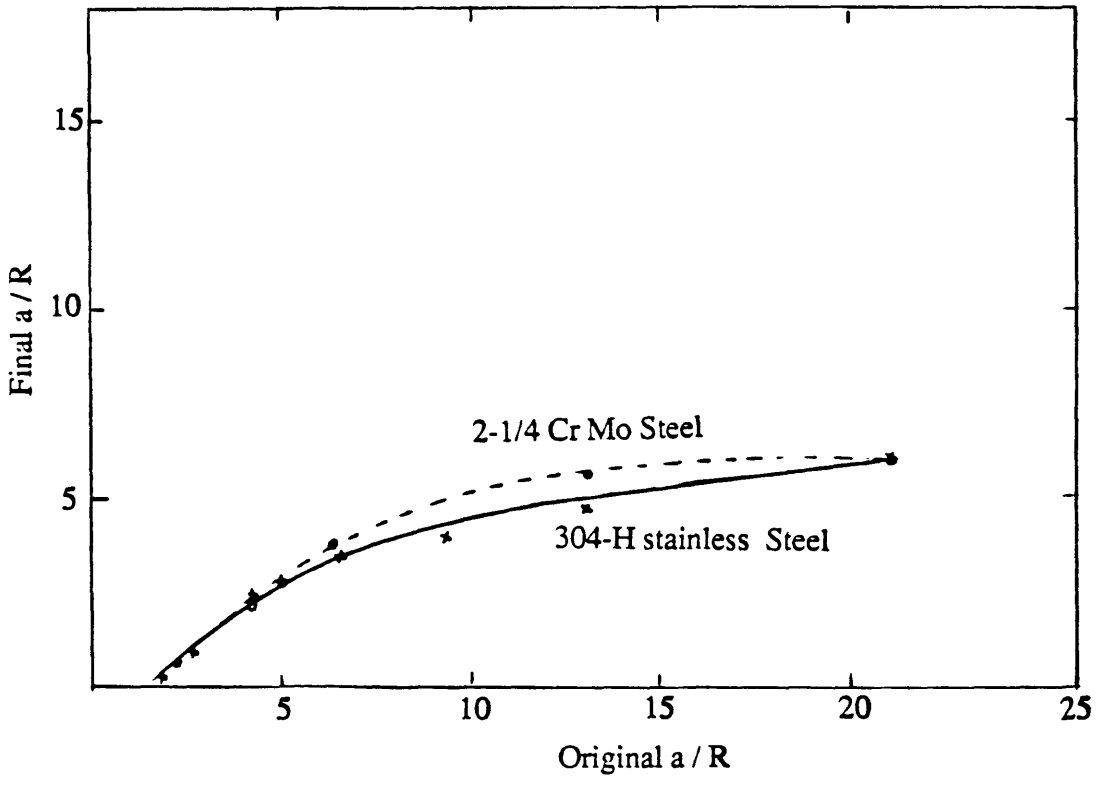


Figure - 5.8 : Comparison of final a / R ratio with original a / R ratio

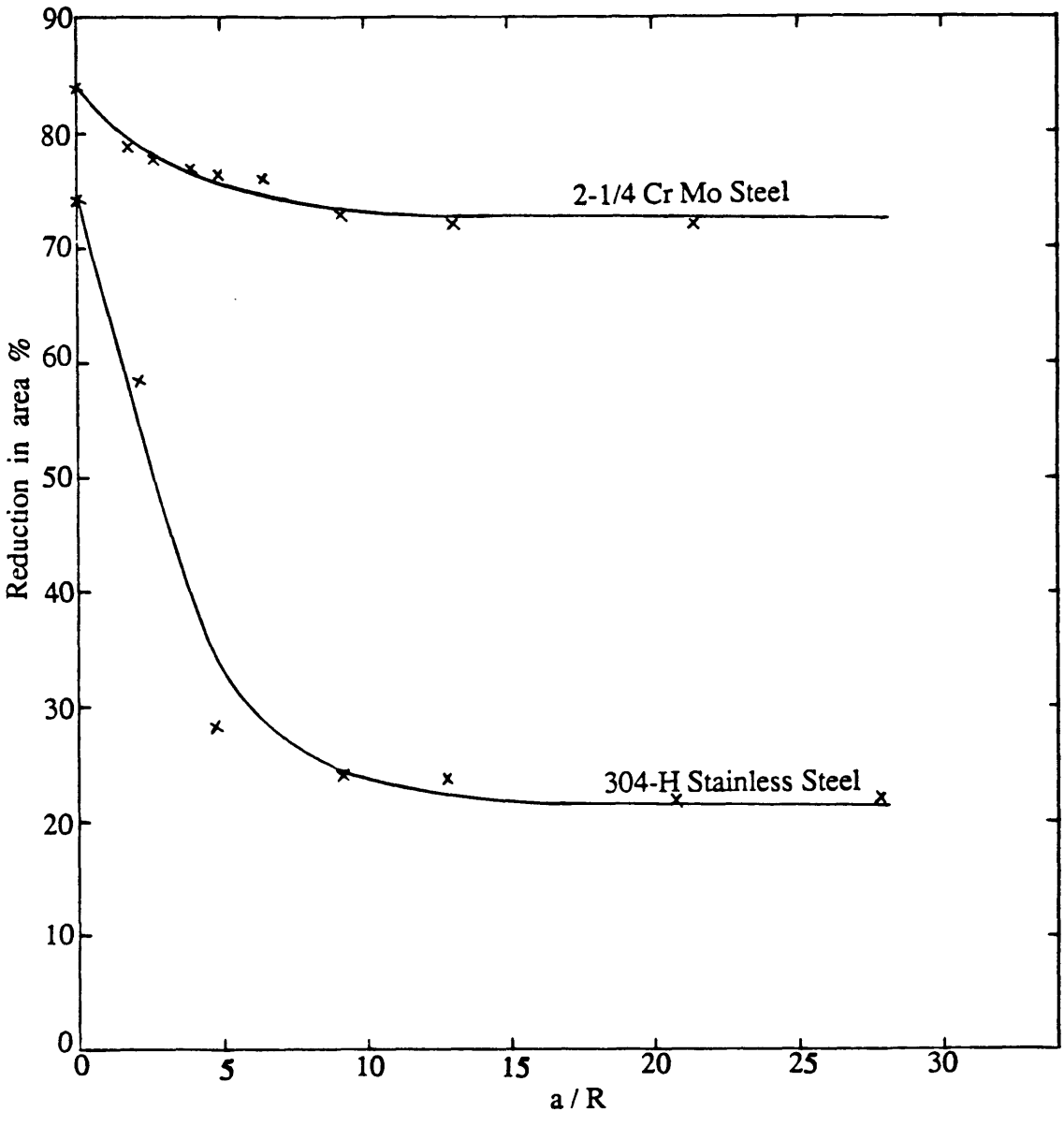


Figure - 5.9 : Comparison of reduction of area of 304-H stainless steel and 2-1/4 Cr Mo steel for different a / R ratio

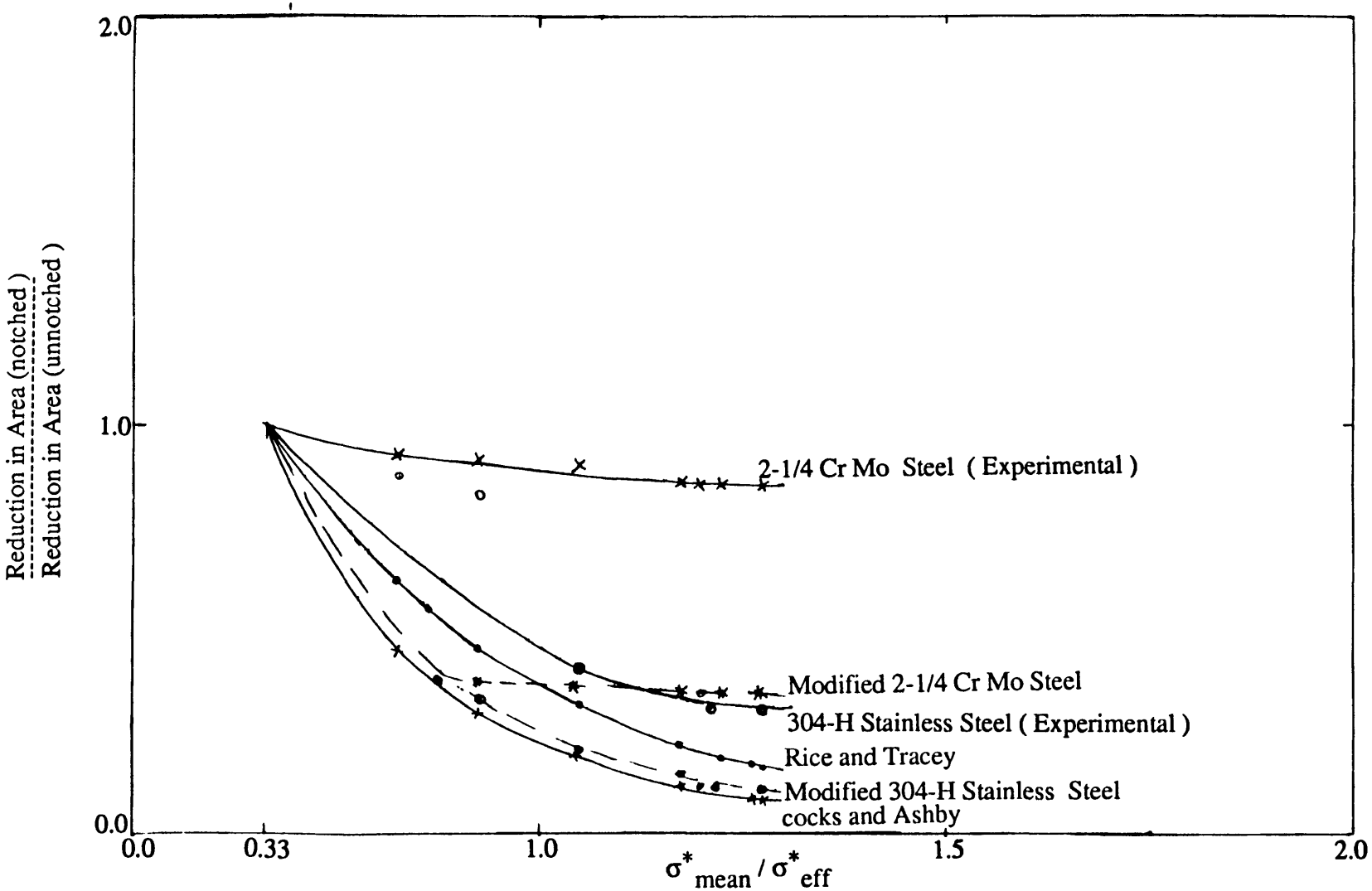


Figure 5.10 : Variation of normalised reduction in area with triaxiality

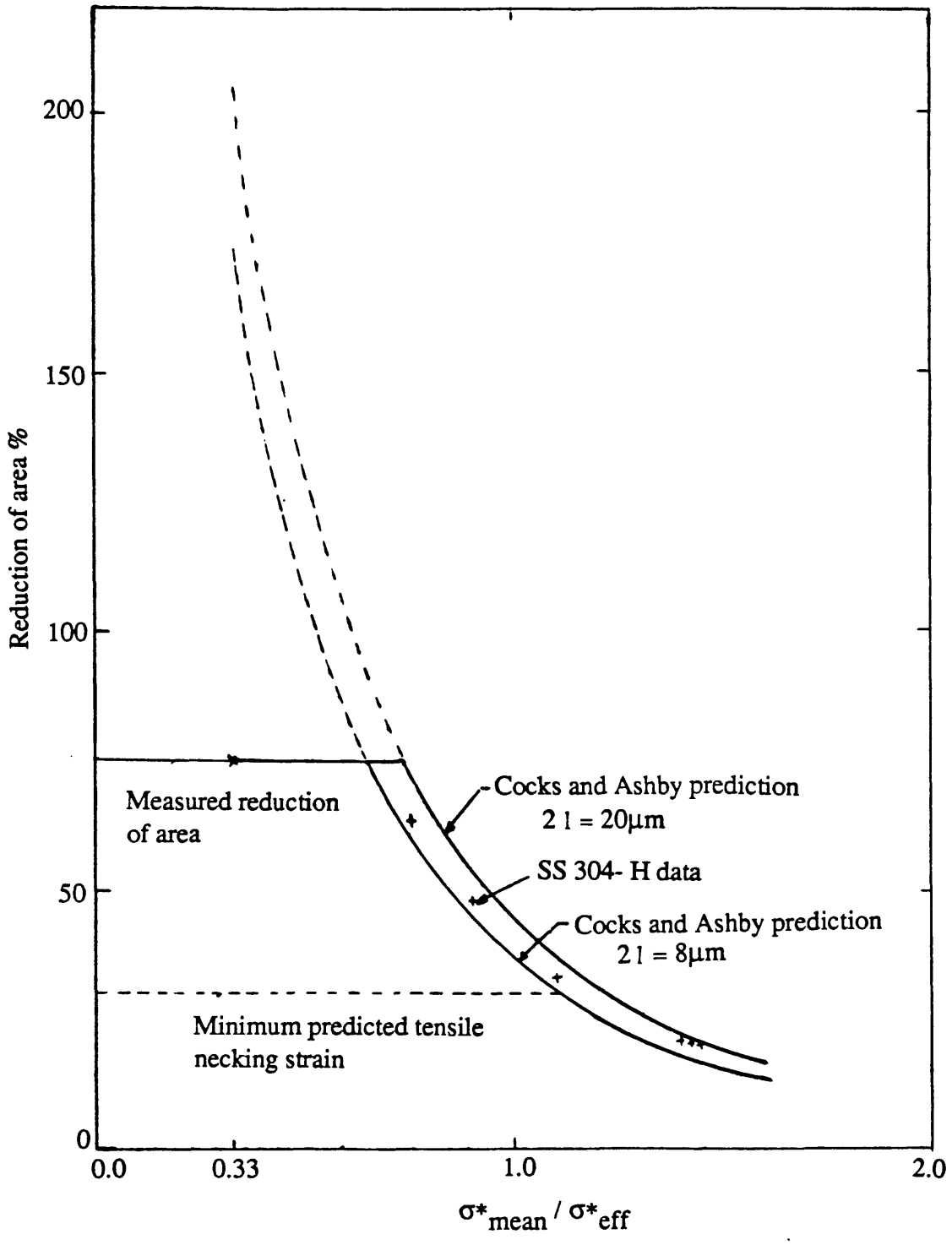


Figure 5.11 : Representation of reduction of area by a void growth model 304-H stainless steel

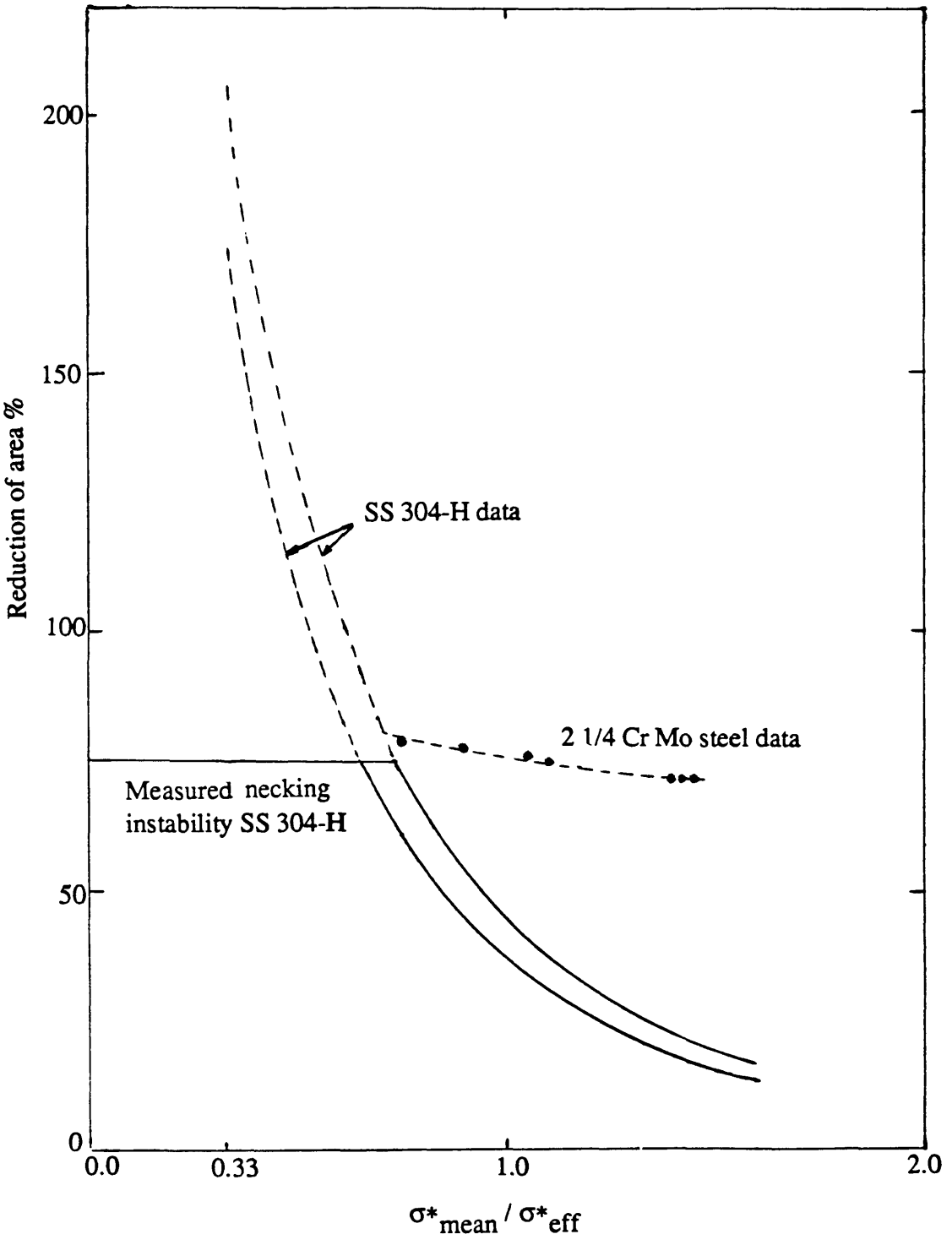


Figure 5.12 : Representation of reduction of area by a void growth model 2-1/4 Cr Mo steel

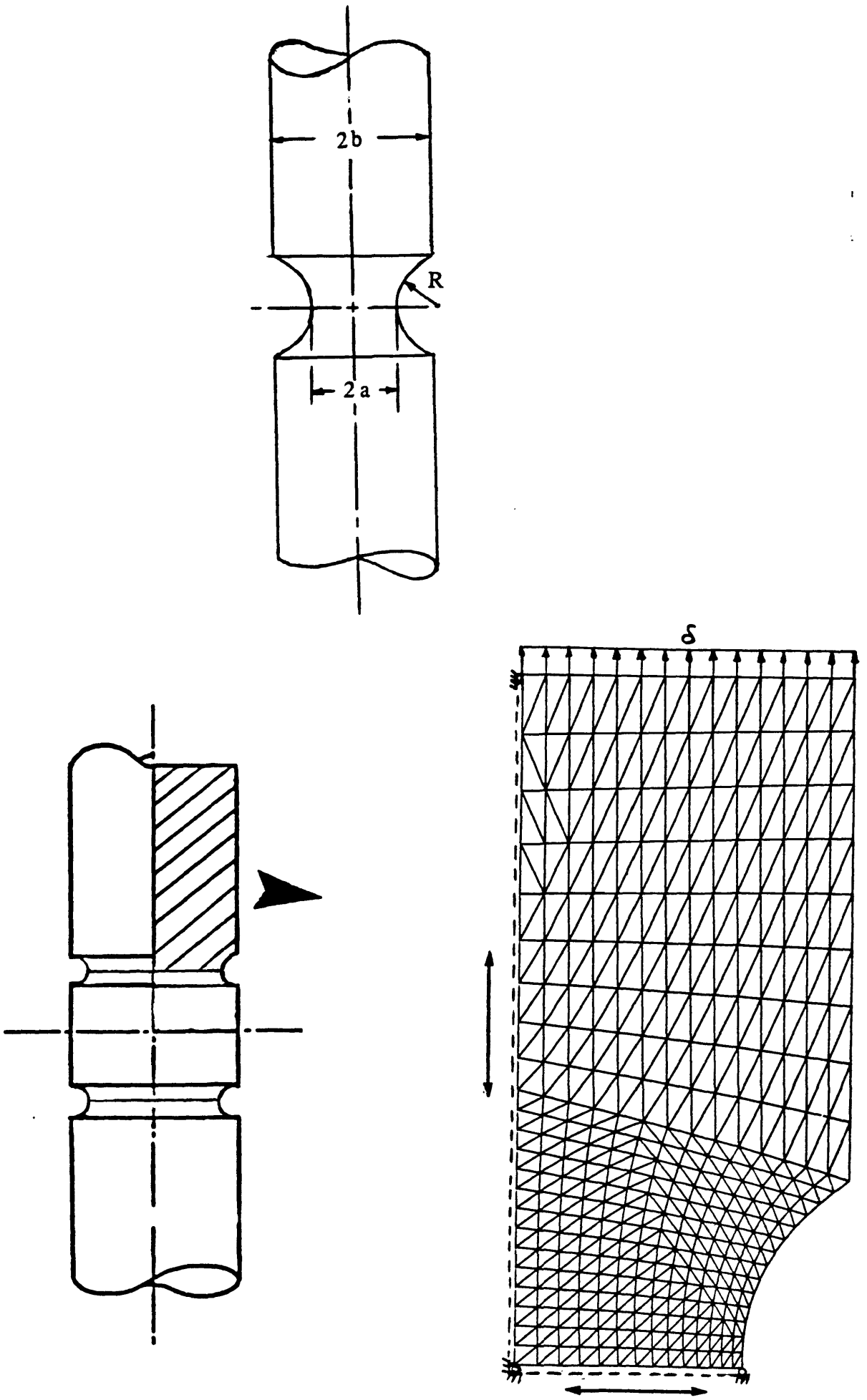


Figure 5.13: General nomenclature of a notched bar

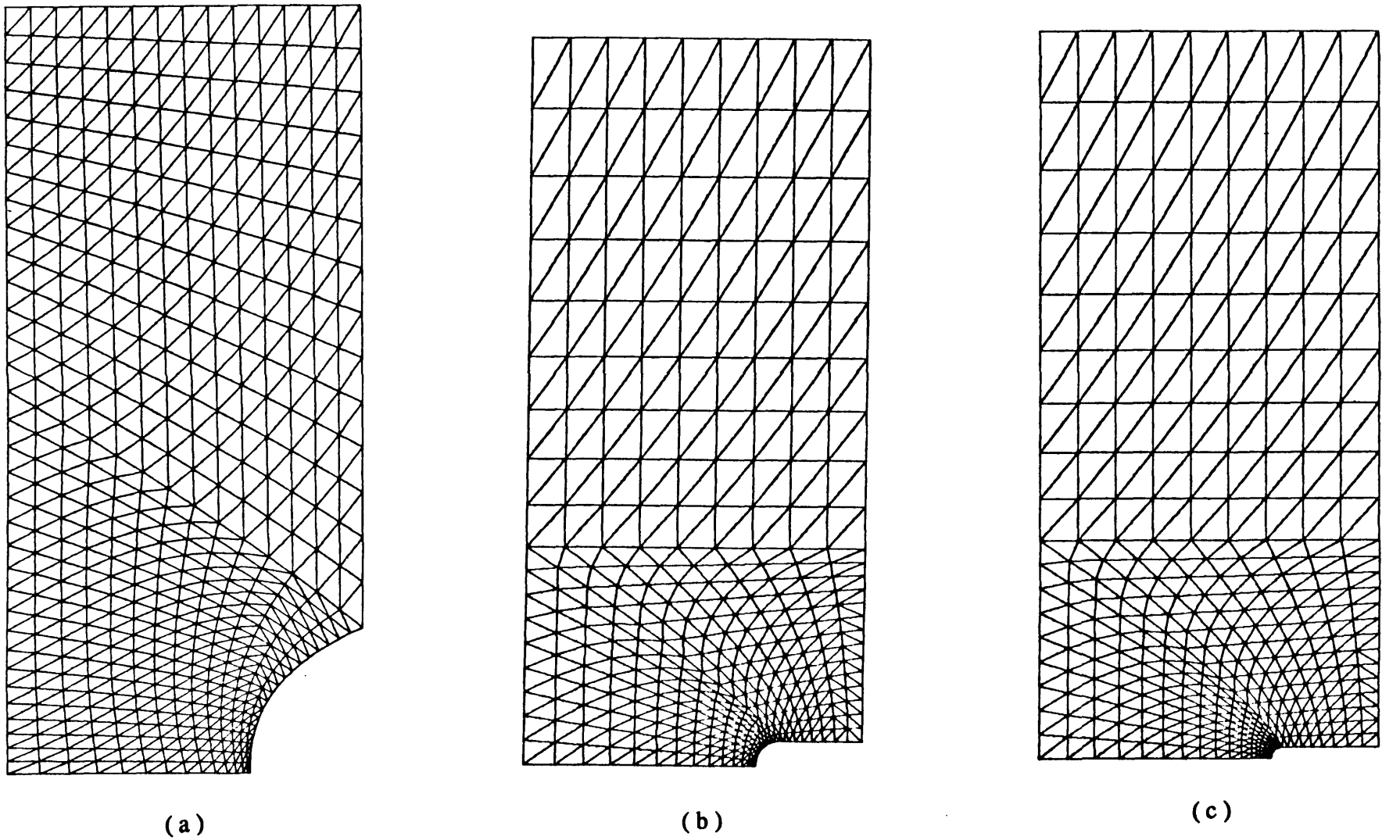


Figure 5.14: Finite element mesh for b / a = 1.46 ; (a) a / R = 1.67, (b) a / R = 9.30, (c) a / R = 21.6

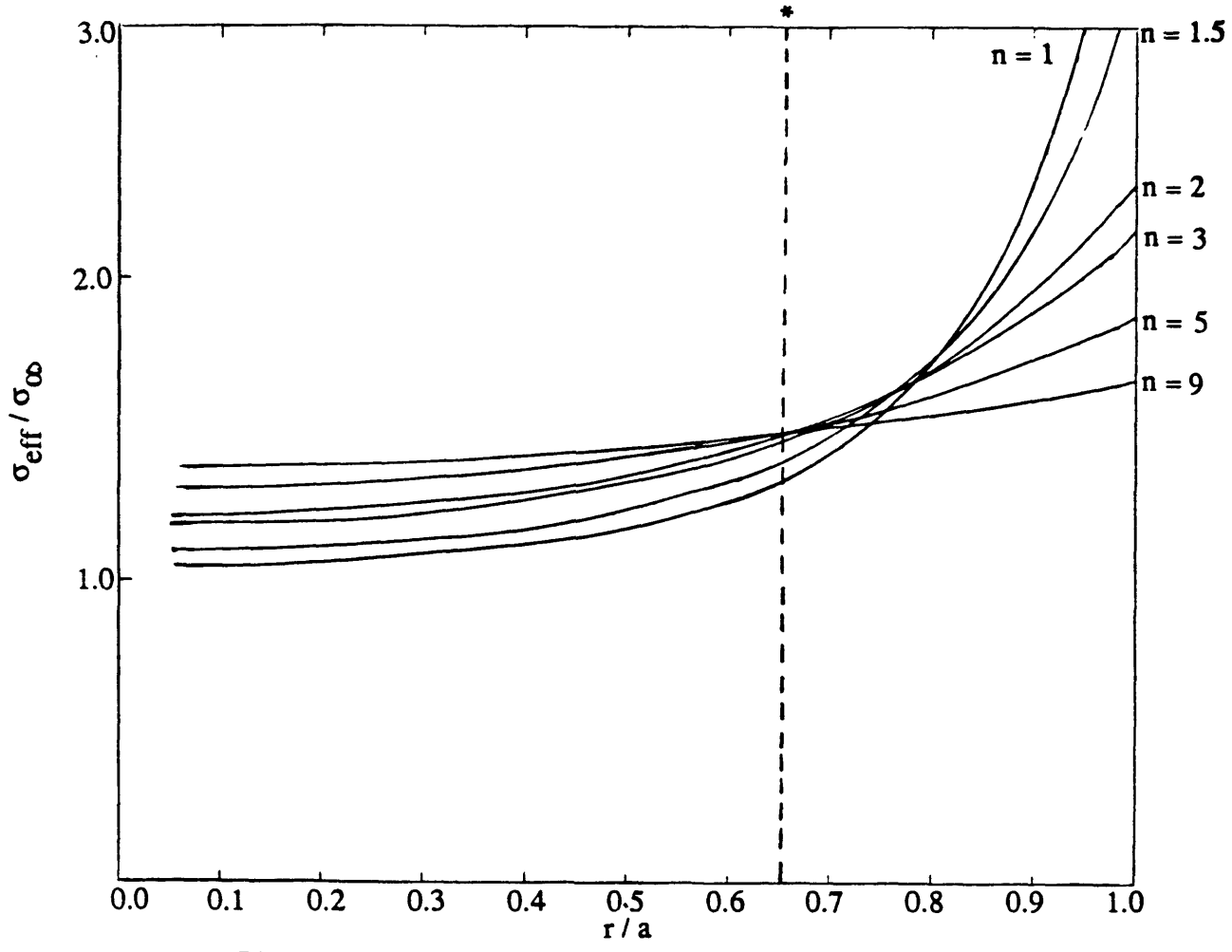
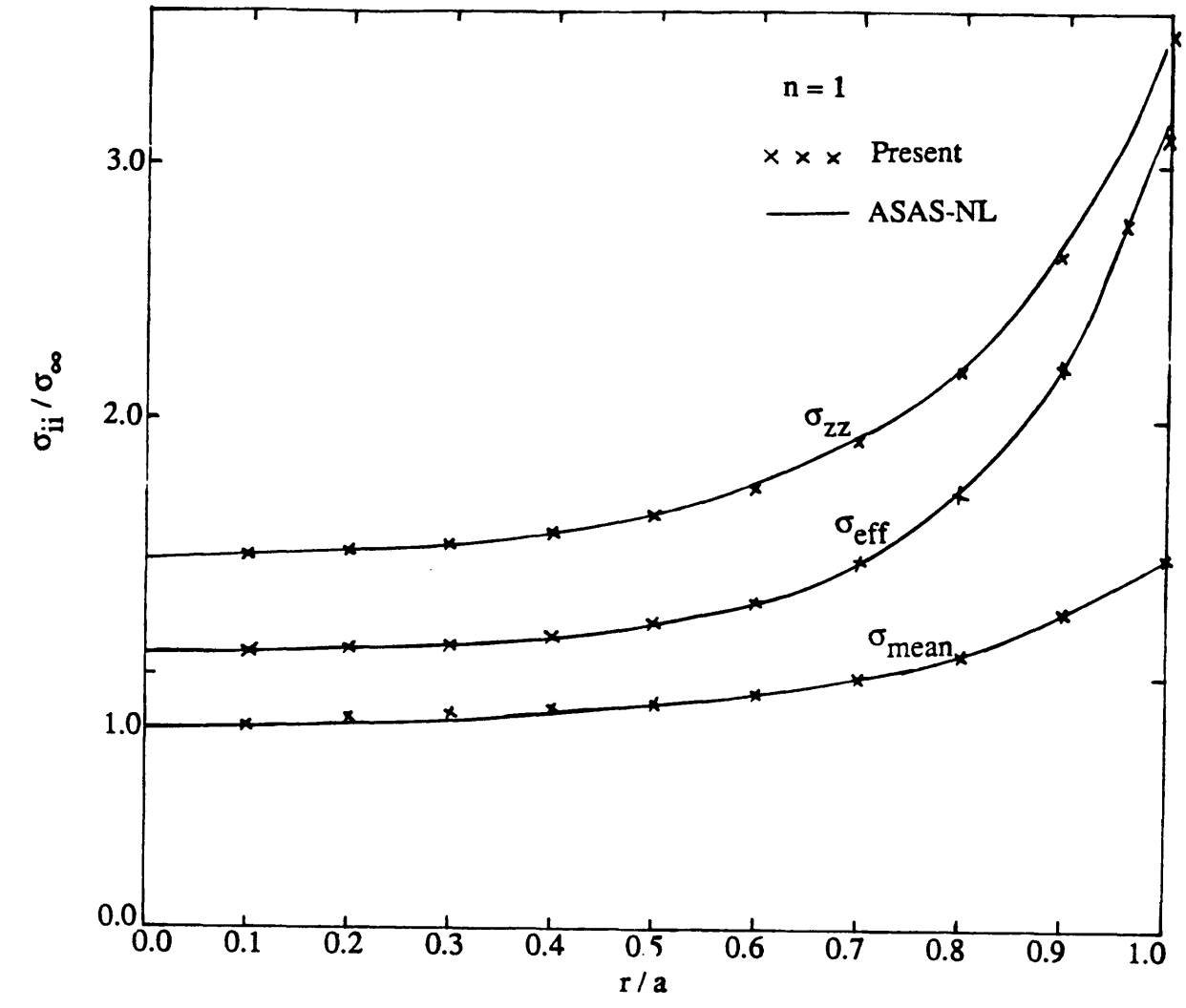


Figure 5.15: Establishment of a skeletal point for $n \geq 3$

b / a = 1.46, a / R = 2.00



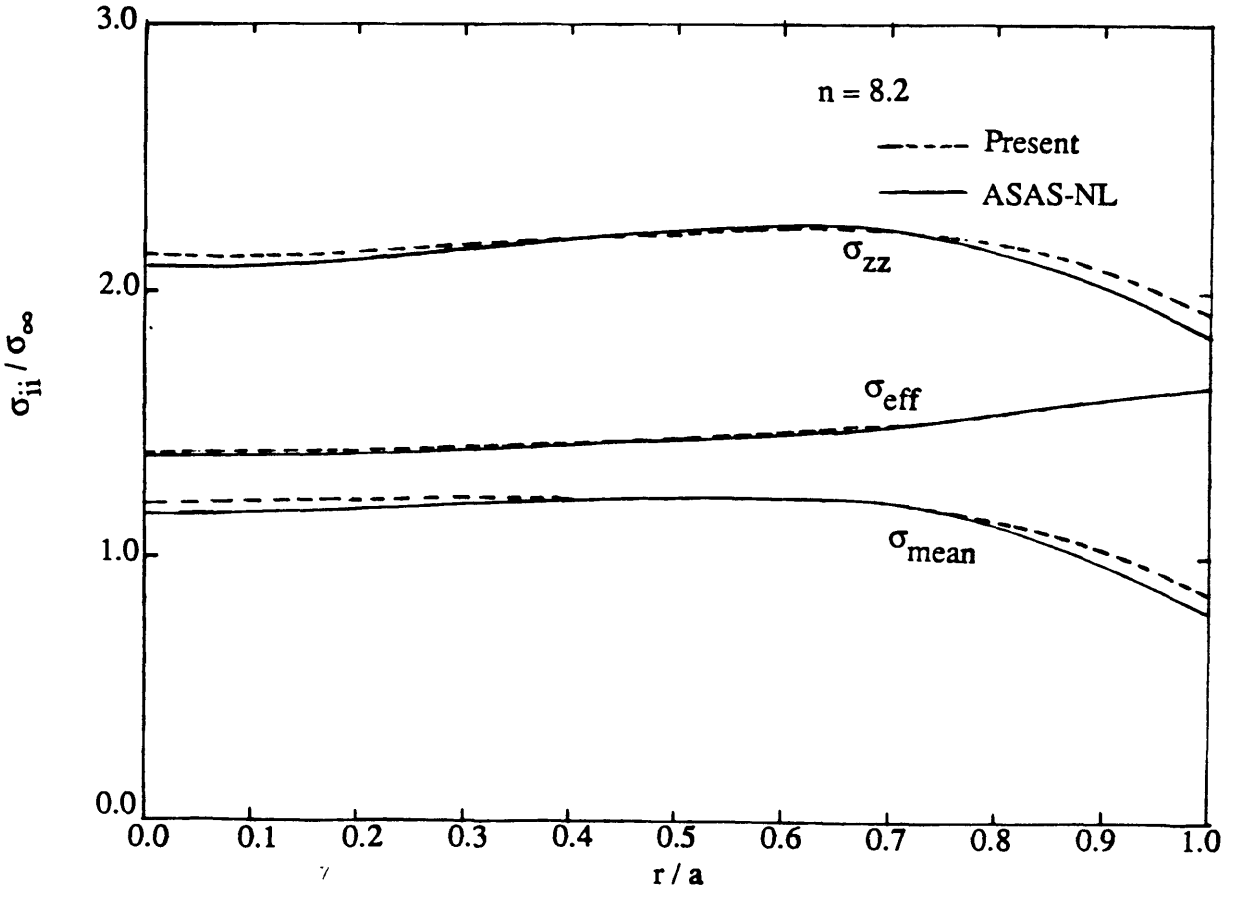
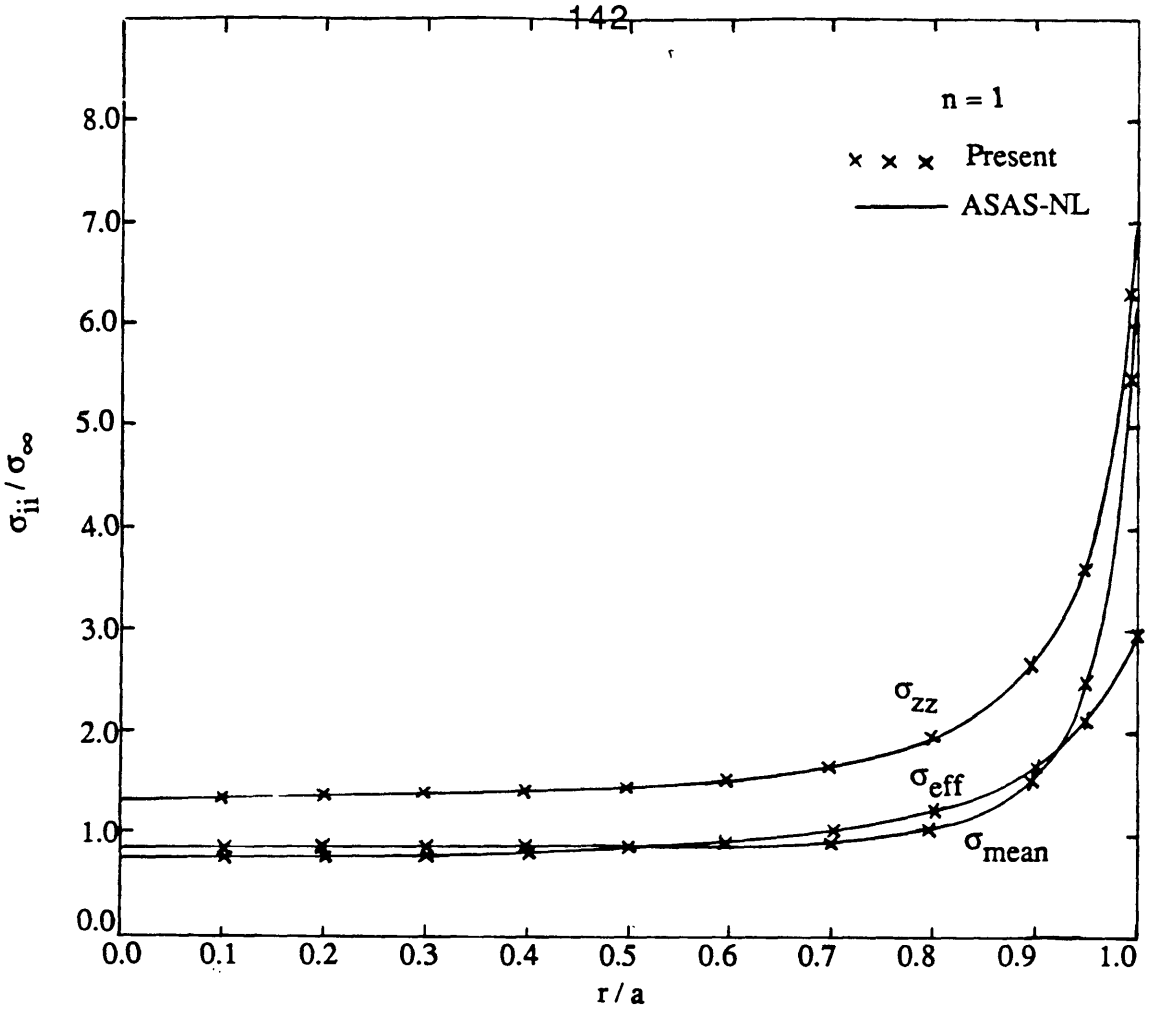


Figure 5.16 : Comparison of stresses across a notch throat from the present work and ASAS-NL program, b /a = 1.46 , a / R = 1.67



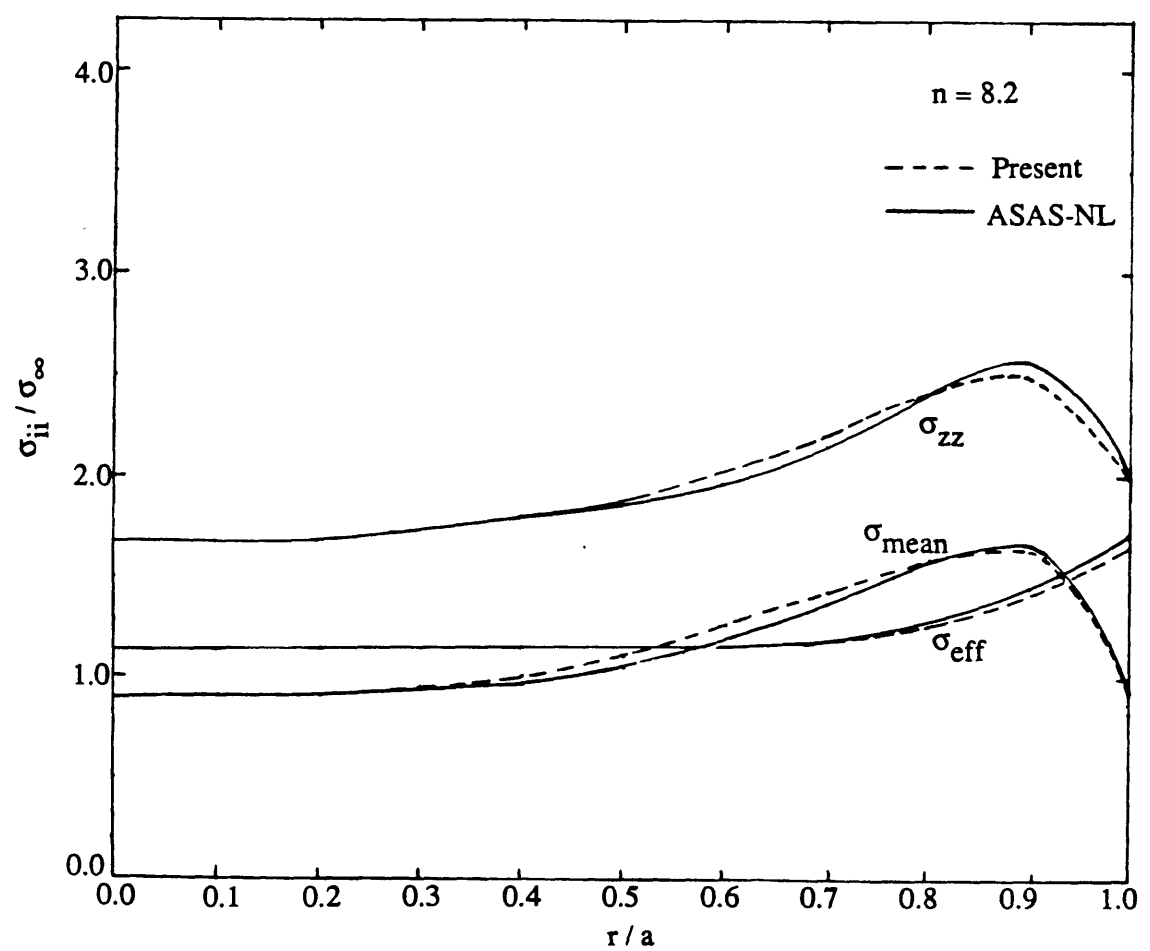


Figure 5.17 : Comparison of stresses across a notch throat from the present work and ASAS-NL program, b / a = 1.46, a / R = 9.30

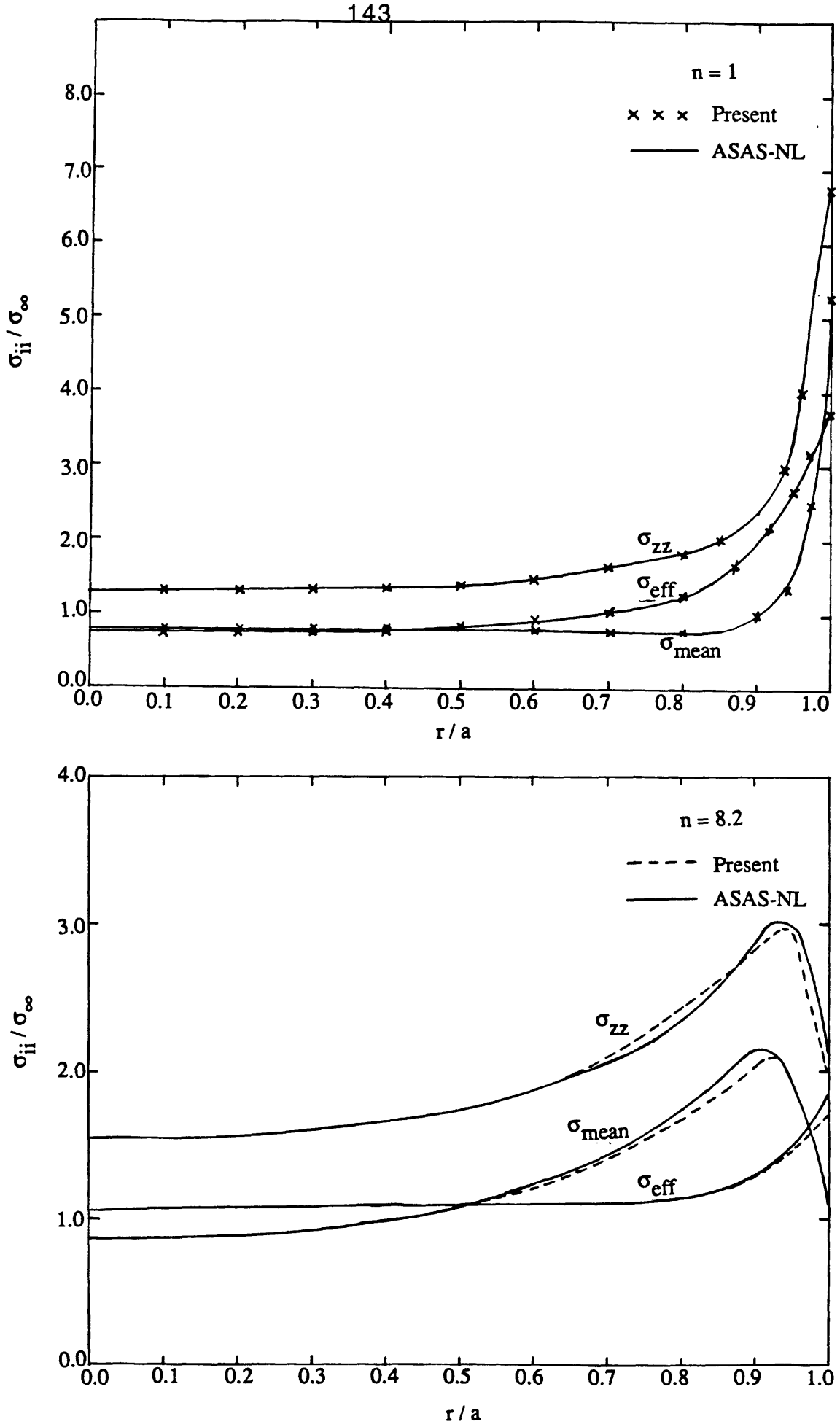


Figure 5.18 : Comparison of stresses across a notch throat from the present work and ASAS-NL program, b / a = 1.46, a / R = 21.60

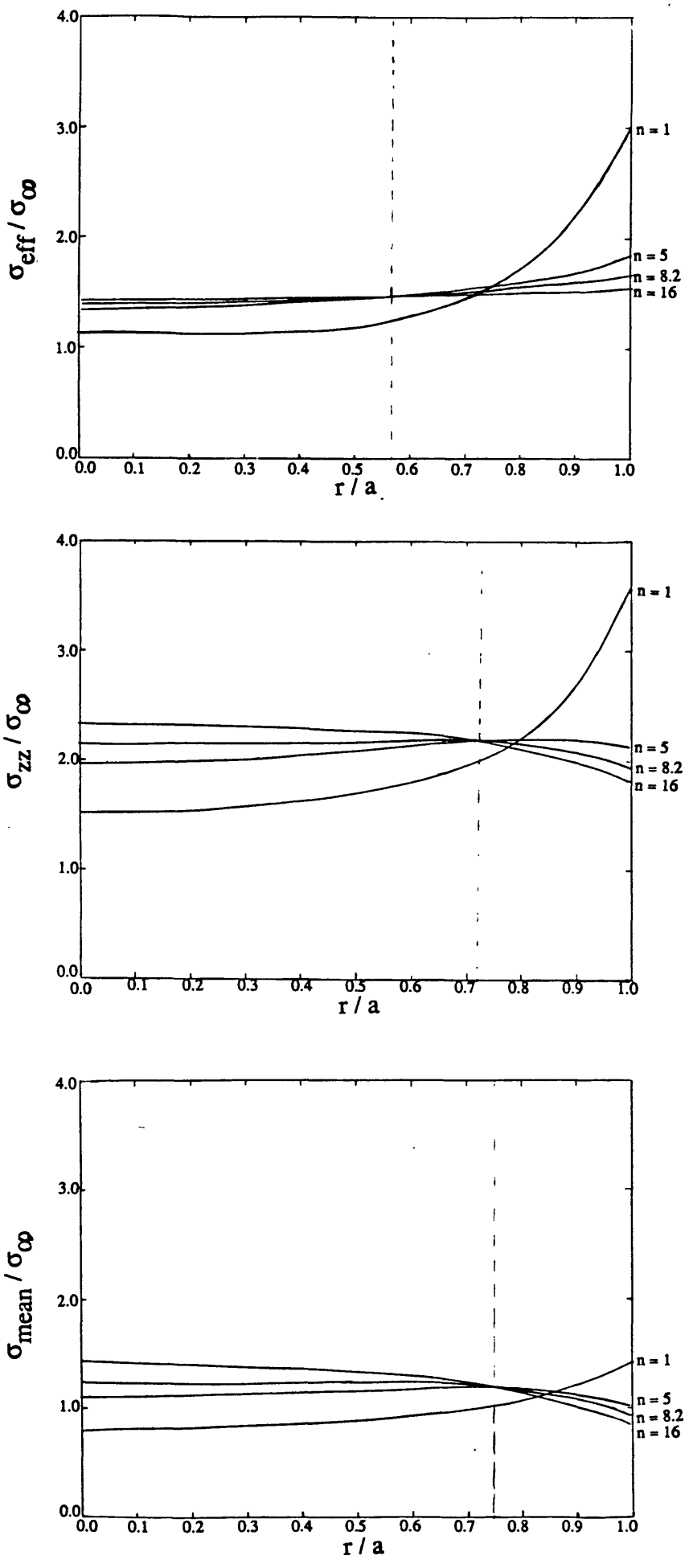


Figure 5.19 : Variation of stresses across a notch throat, b / a = 1.46, a / R = 1.67

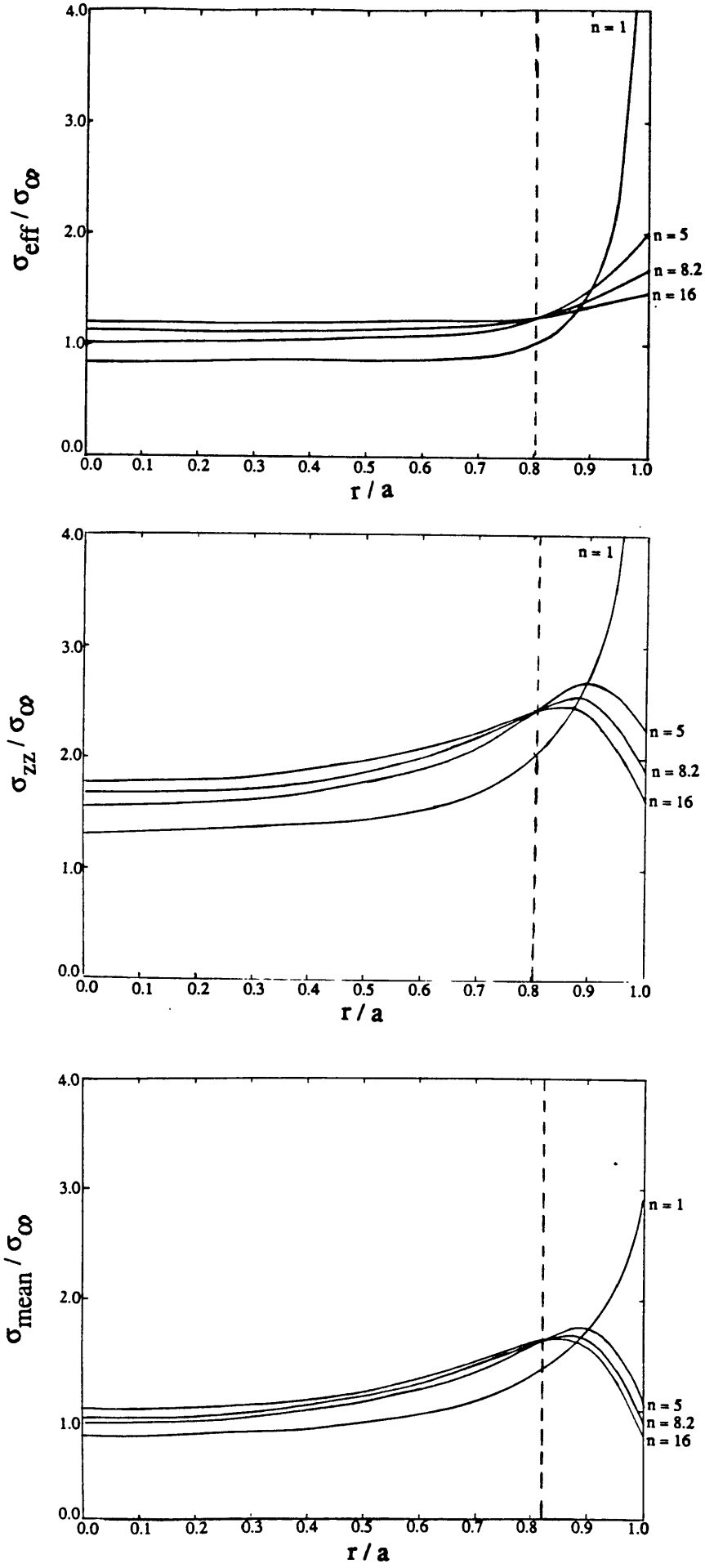


Figure 5.20 : Variation of stresses across a notch throat, b / a = 1.46, a / R = 9.30

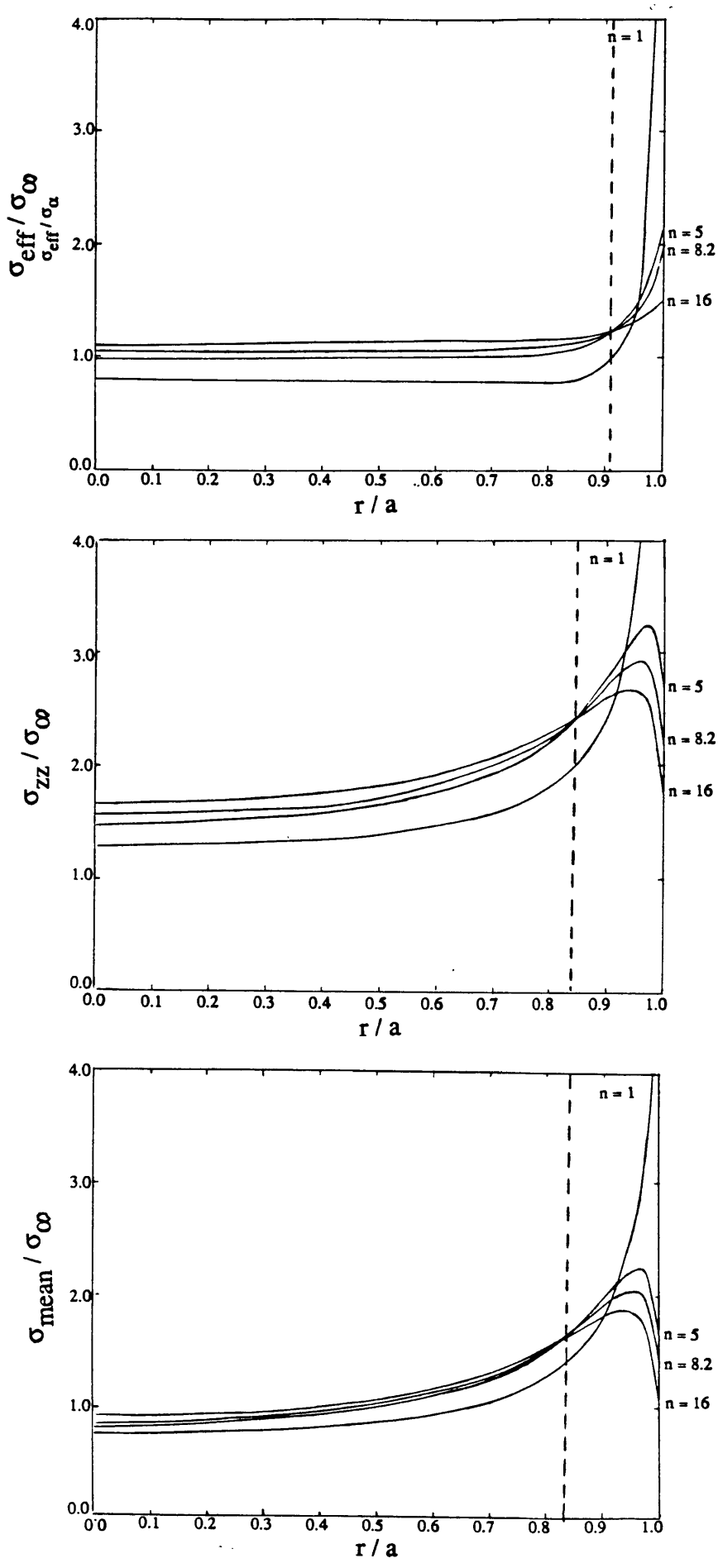


Figure 5.21 : Variation of stresses across a notch throat, b / a = 1.46, a / R = 21.60

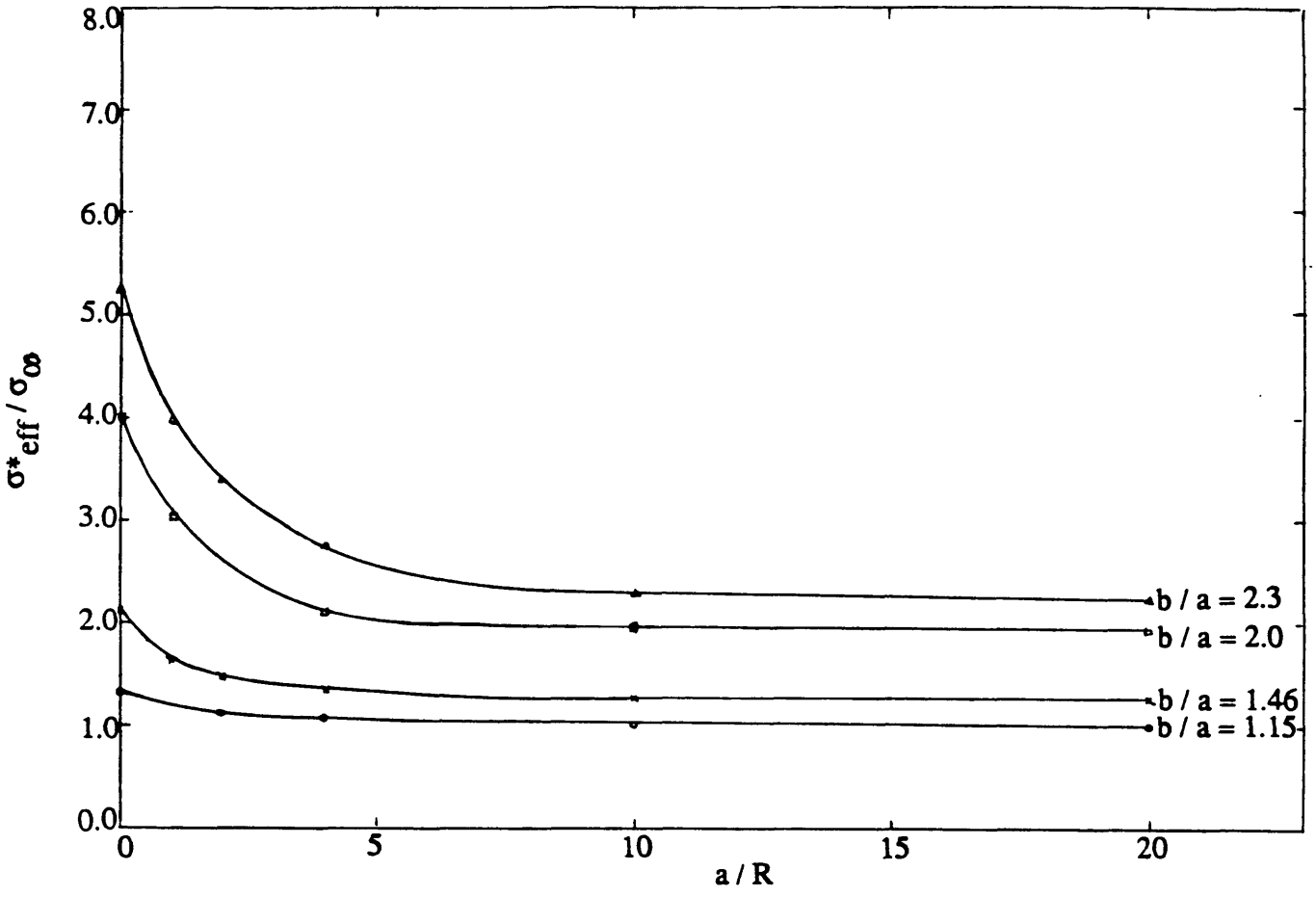


Figure 5.22 : Variation of effective stress at a skeletal point with a / R for different b / a ratio

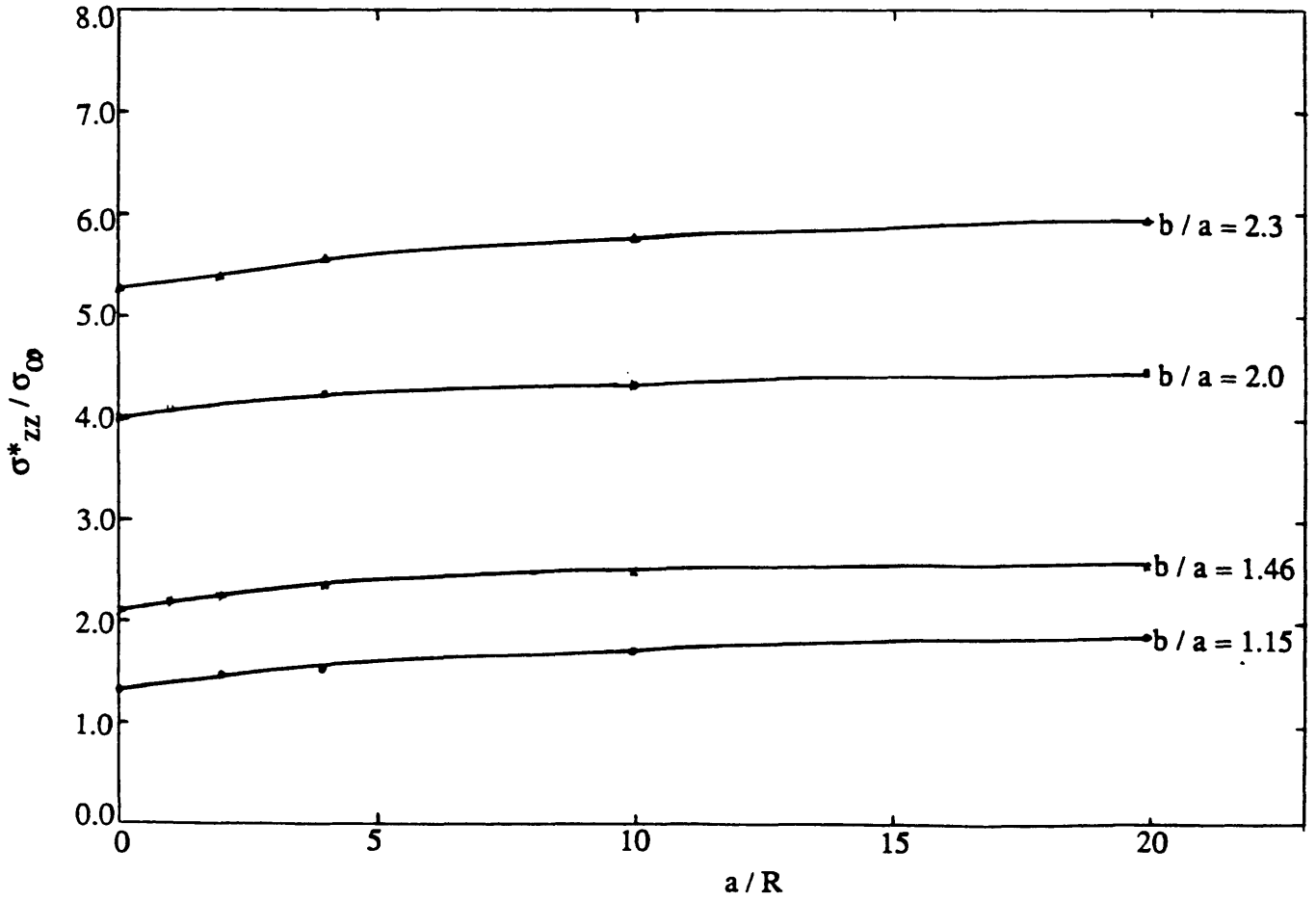


Figure 5.23 : Variation of maximum principal stress at a skeletal point with a / R for different b / a ratio

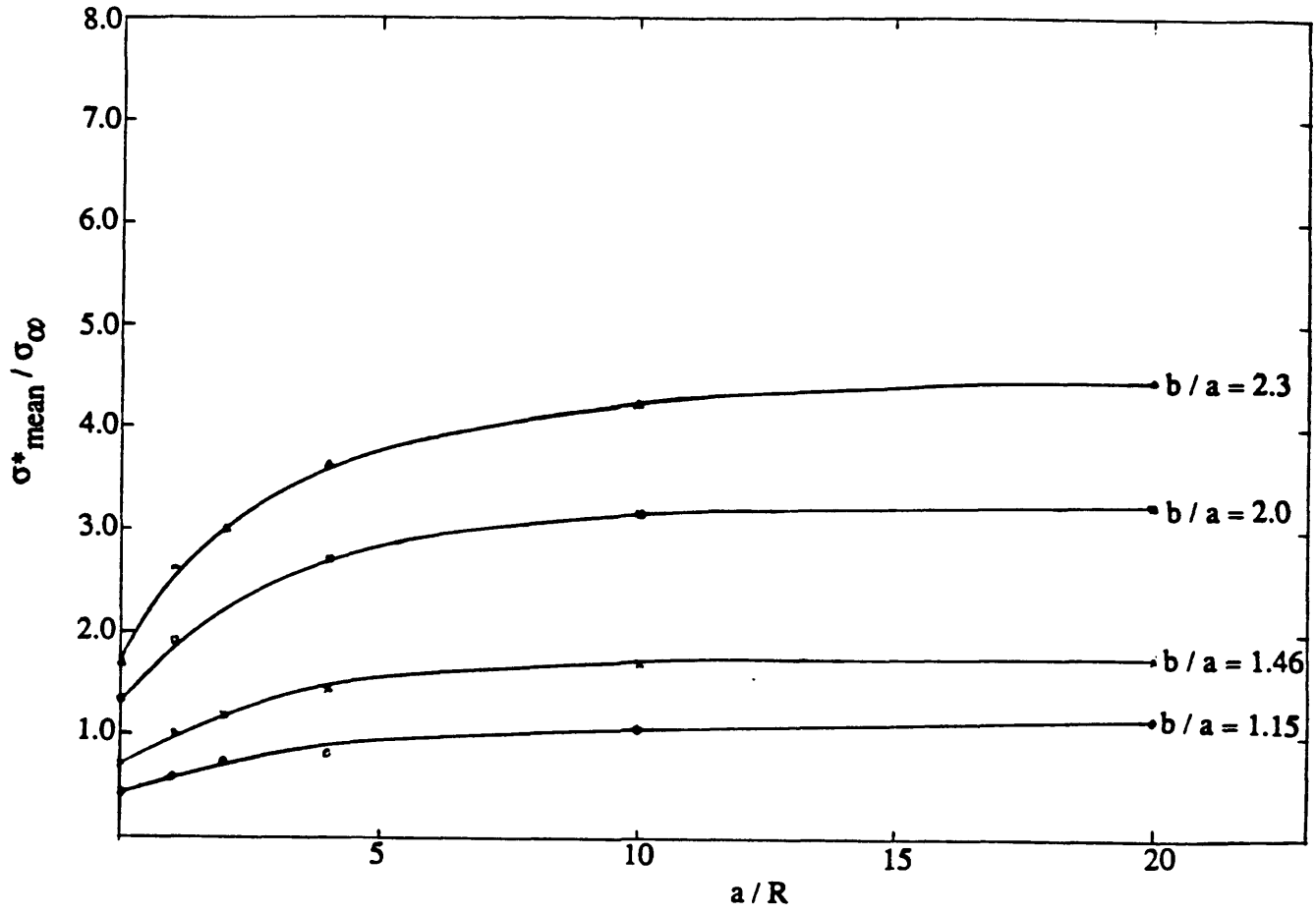


Figure - 5.24 : Variation of hydrostatic stress at a skeletal point with a / R for different b / a ratio

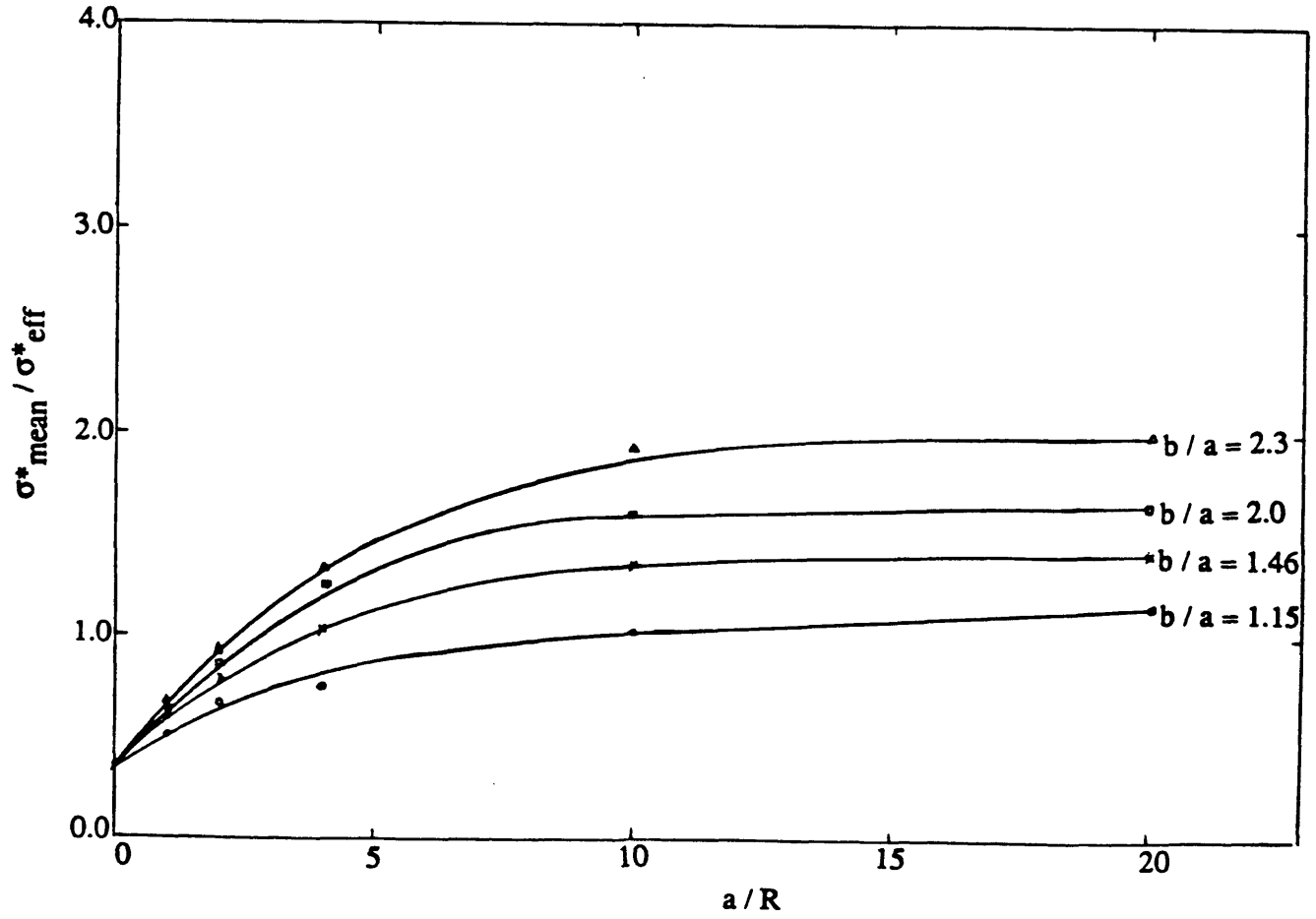


Figure 5.25 : Variation of a triaxiality factor at a skeletal point with a / R for different b / a ratio

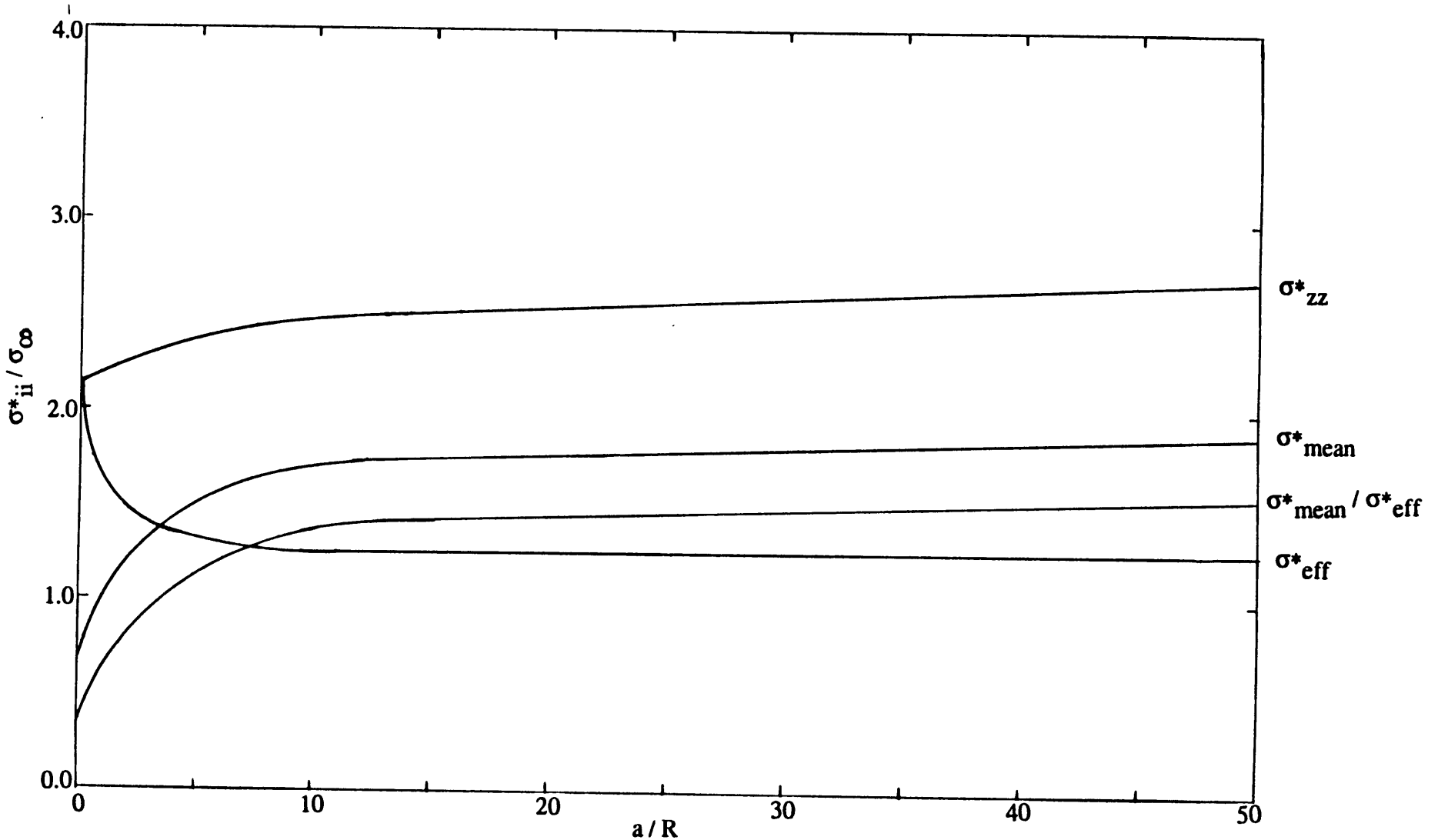


Figure 5.26 : Variation of normalised stresses at a skeletal point with a / R ratio for b / a = 1.46

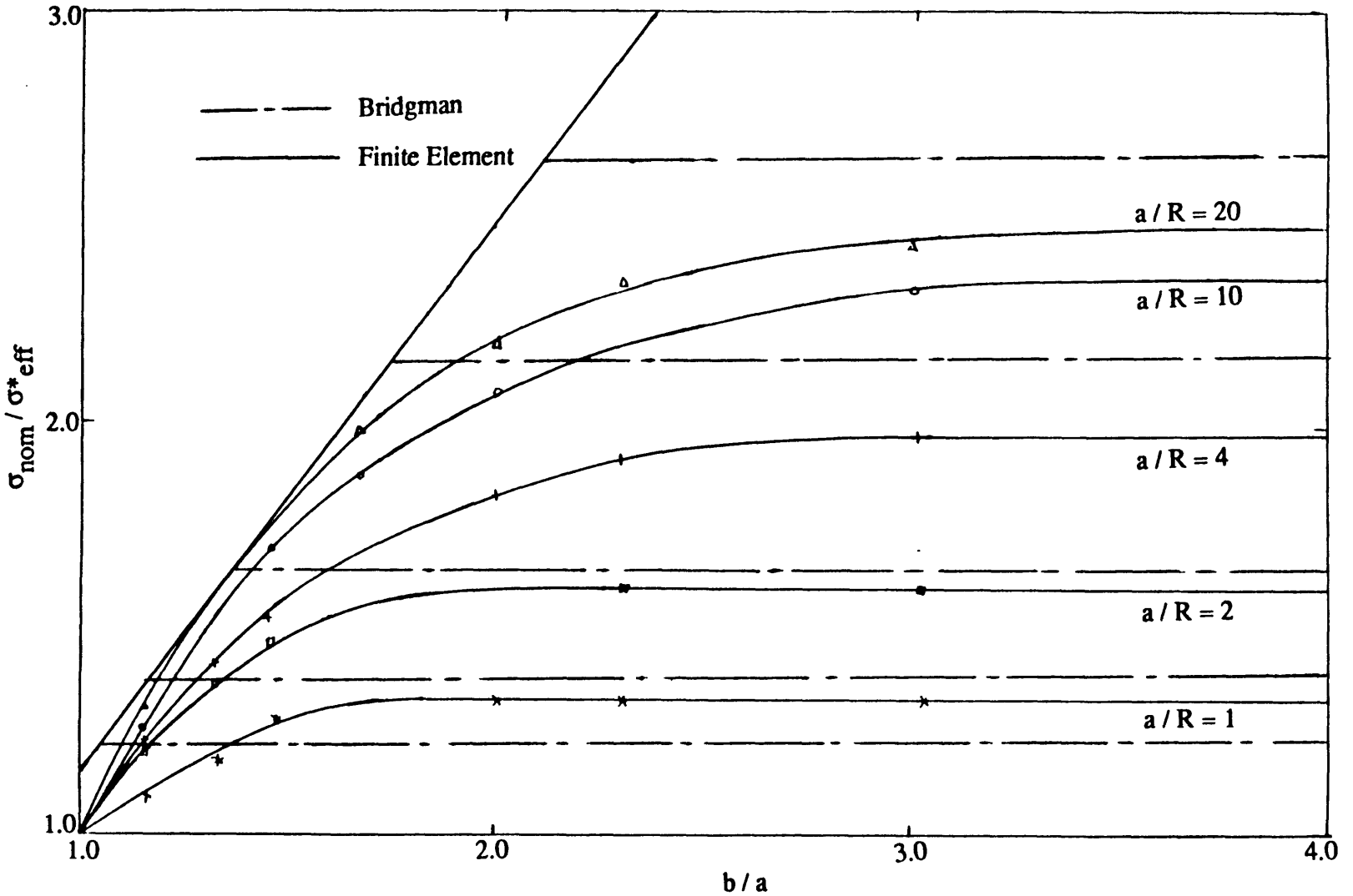
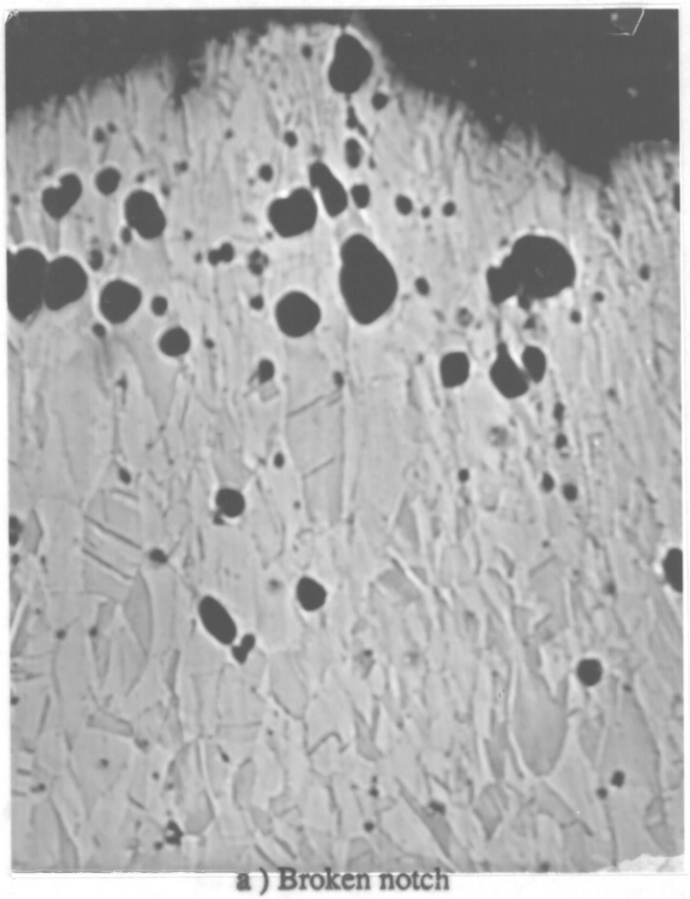
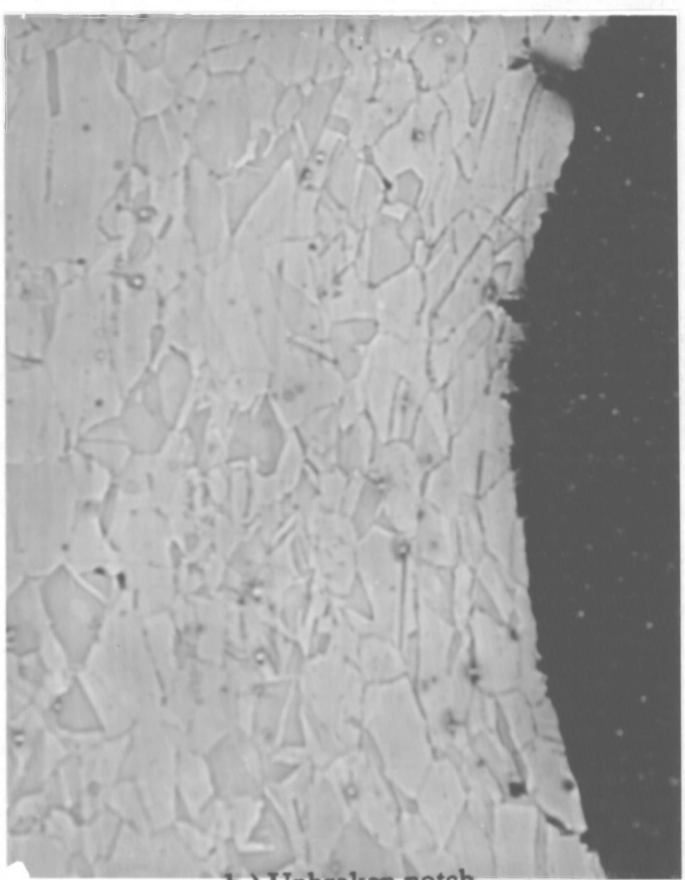


Figure 5.27 : Variation of a constraint factor at a skeletal point with b / a ratio for different a / R ratio

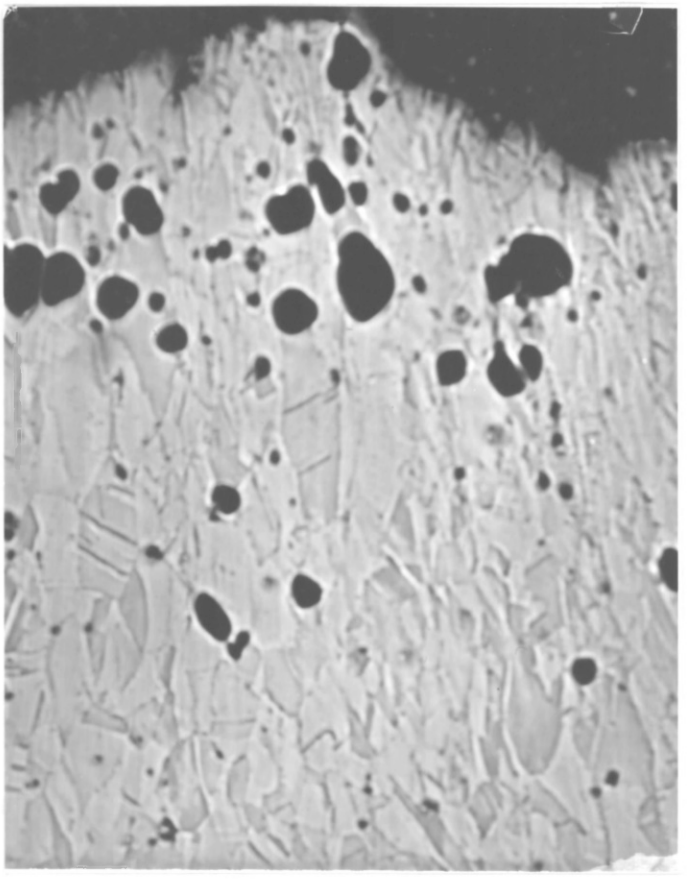


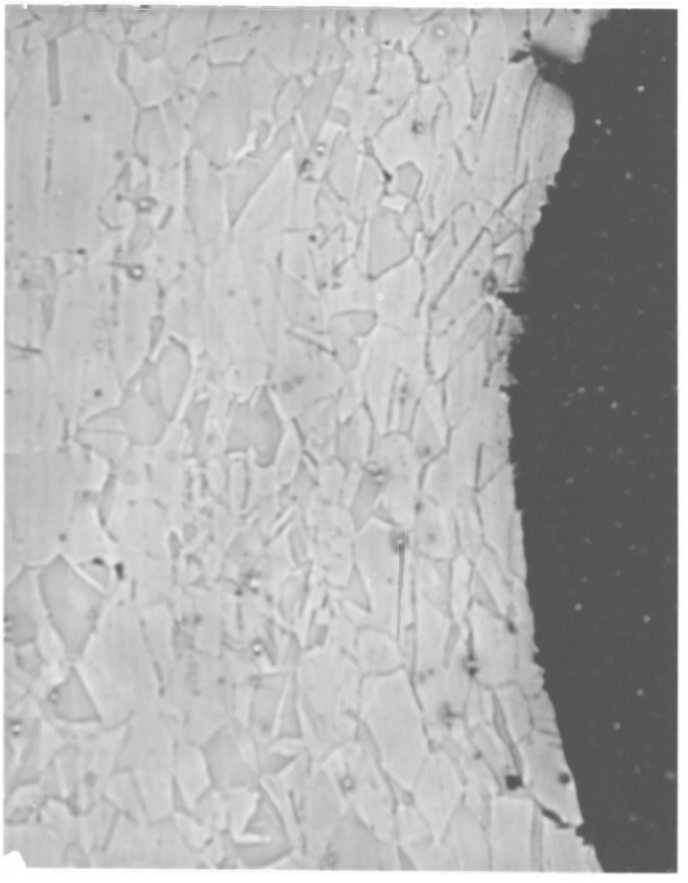
a) Broken notch

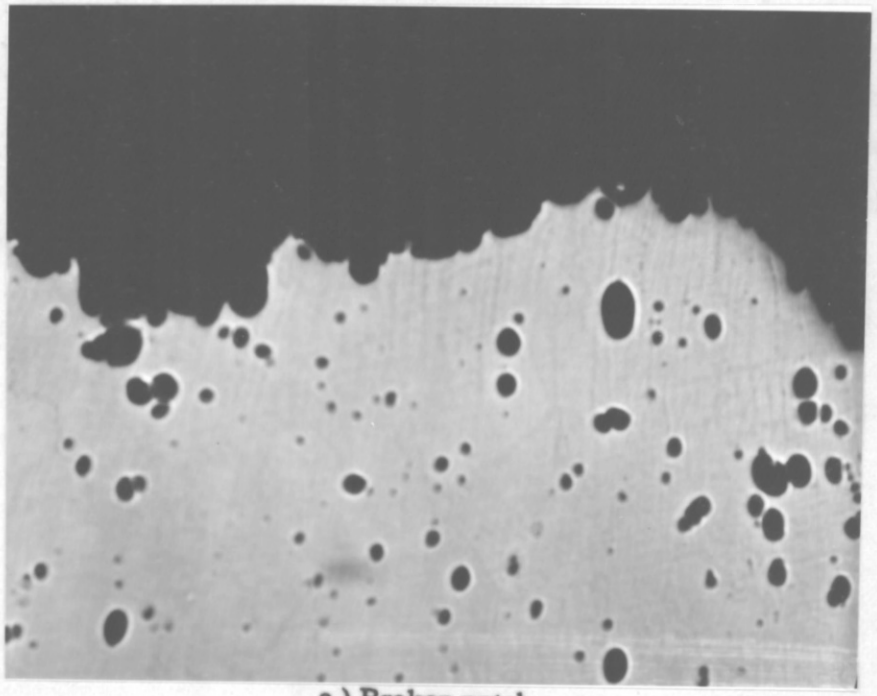


b) Unbroken notch

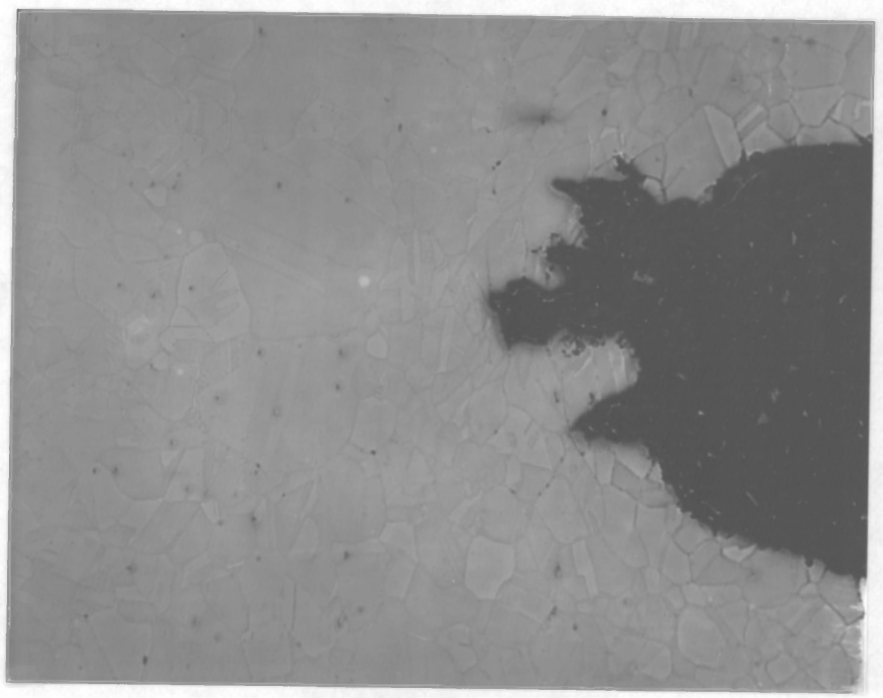
Figure 5.28 : Failure of a blunt notch of 304-H stainless steel





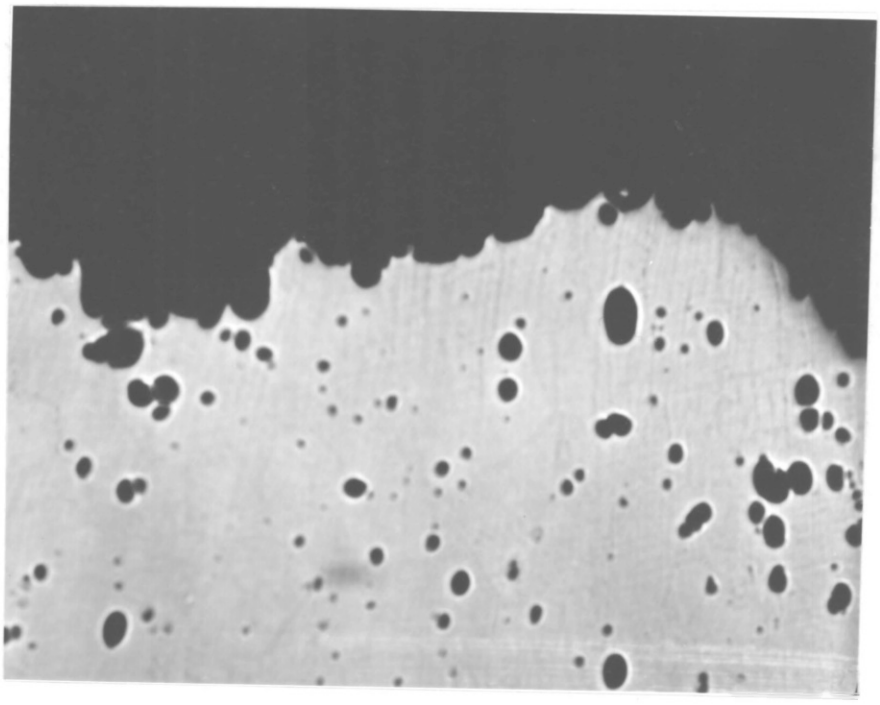


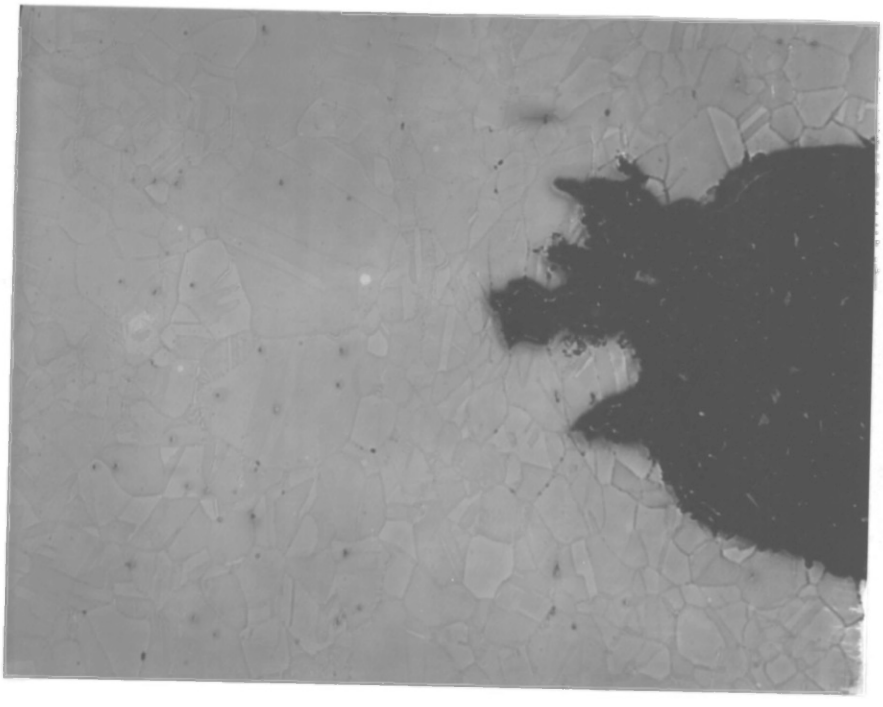
a) Broken notch

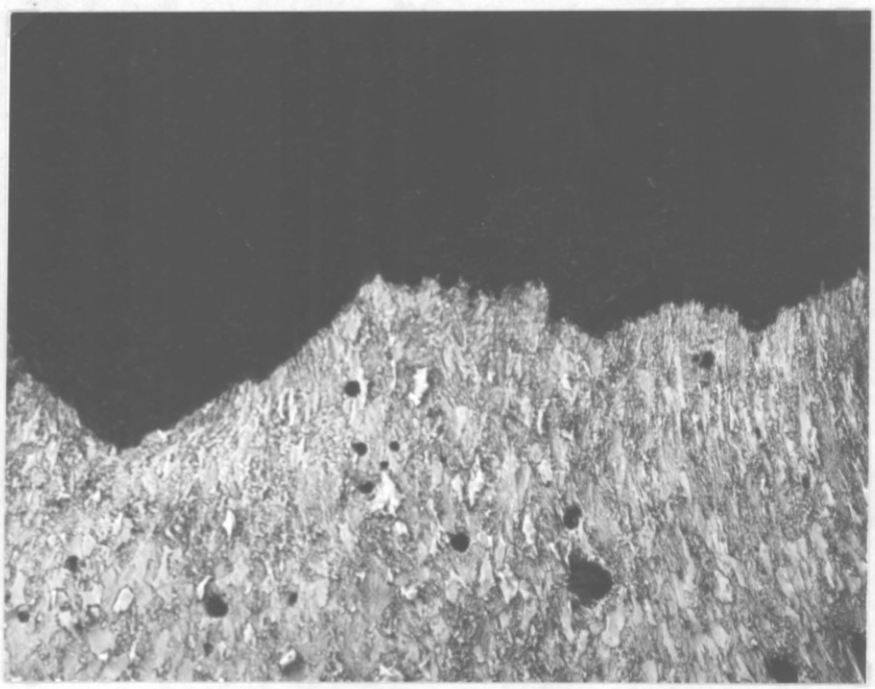


b) Unbroken notch

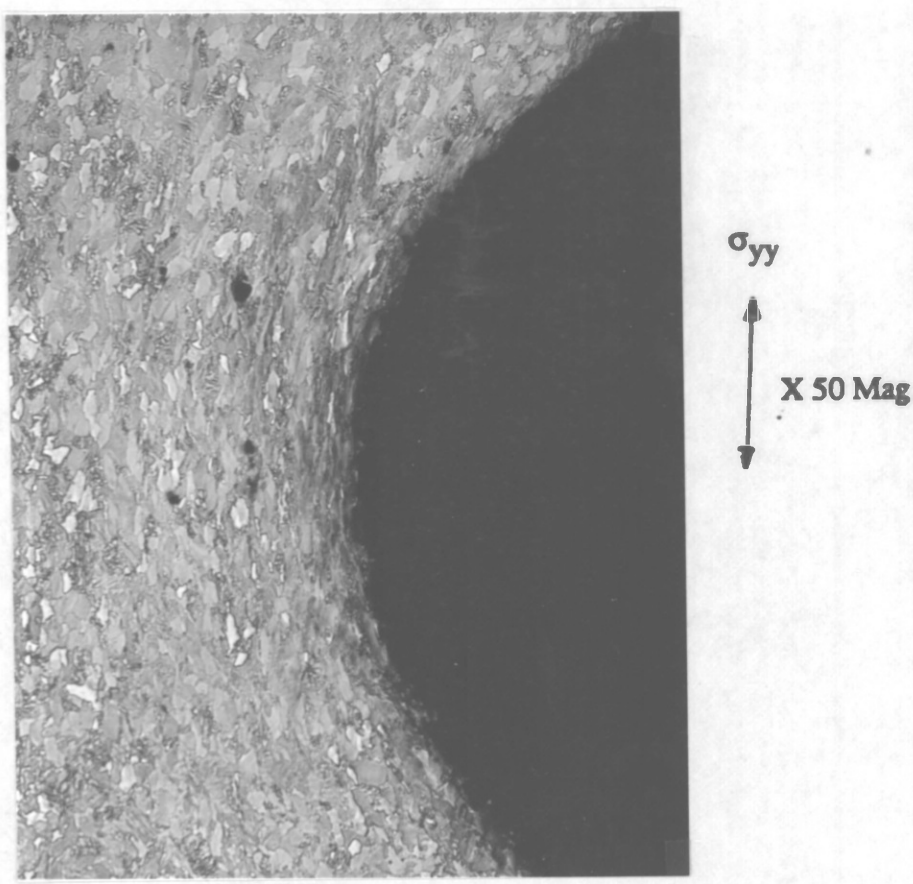
Figure 5.29 : Failure of a sharp notch of 304-H stainless steel





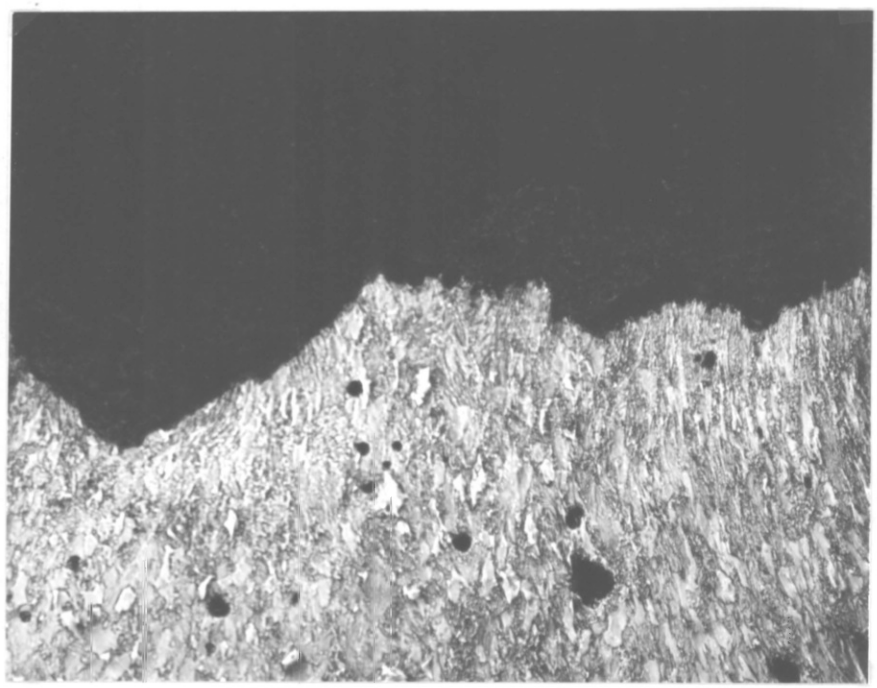


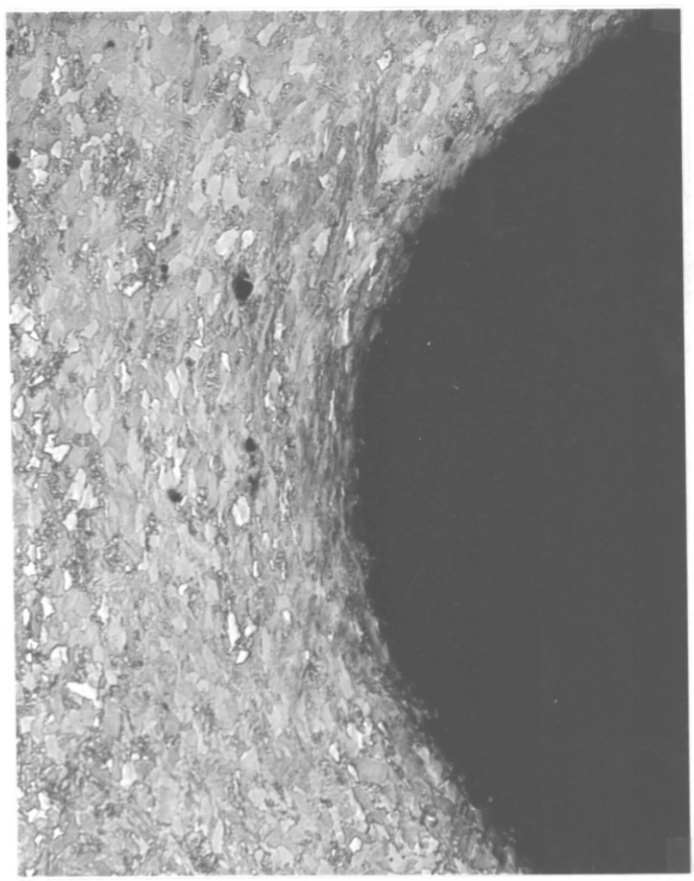
a) Broken notch

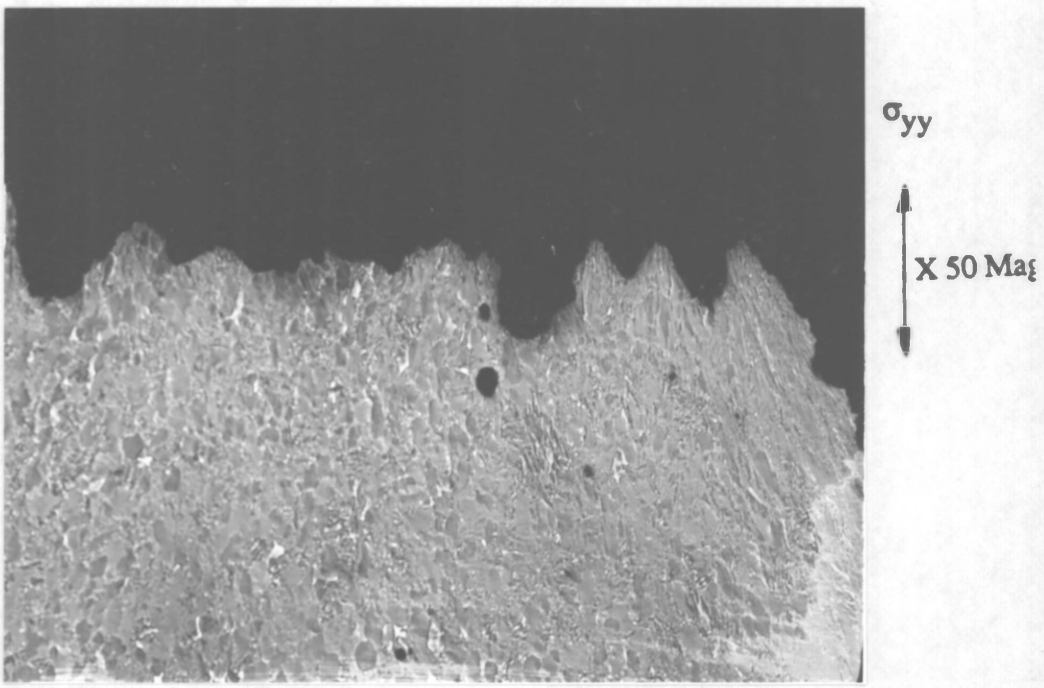


b) Unbroken notch

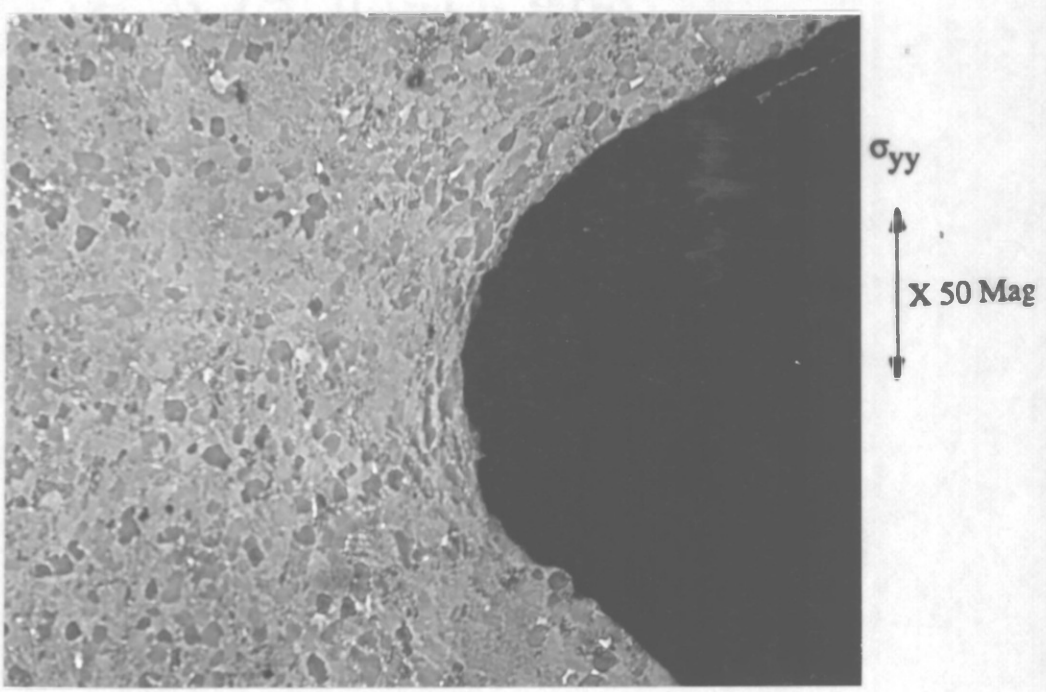
Figure 5.30 : Failure of a blunt notch of 2-1/4 Cr Mo steel





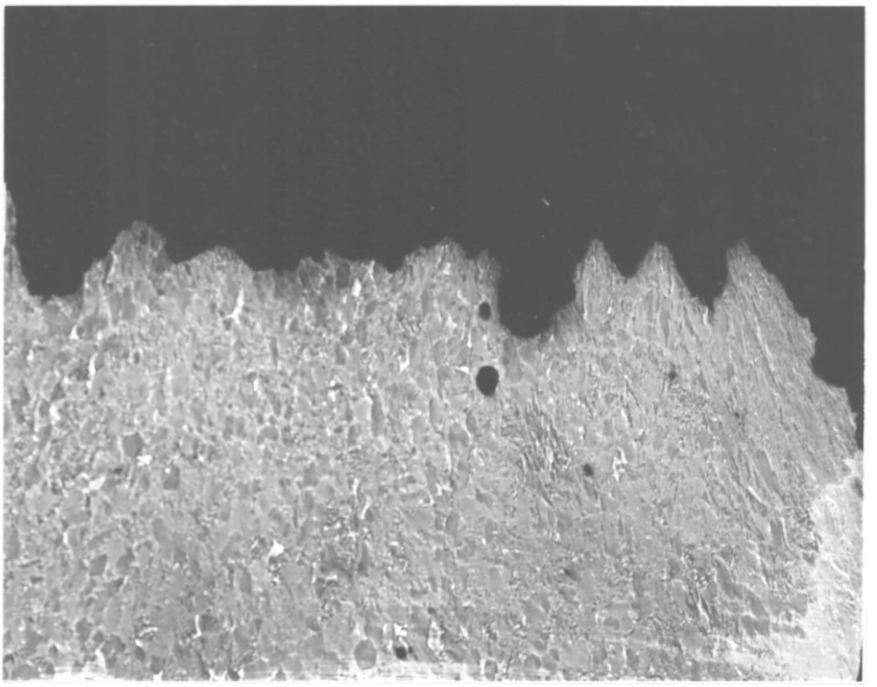


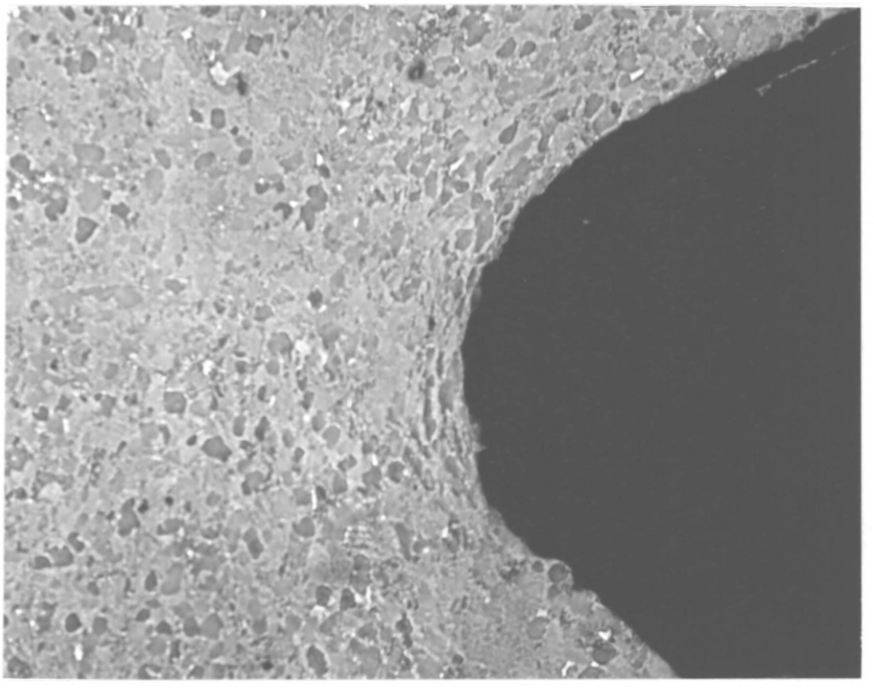
a) Broken notch

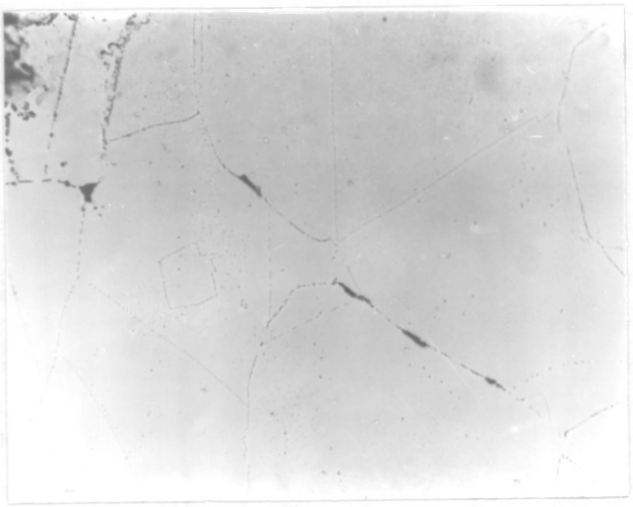


b) Unbroken notch

Figure 5.31 : Failure of a Sharp notch of 2-1/4 Cr Mo steel

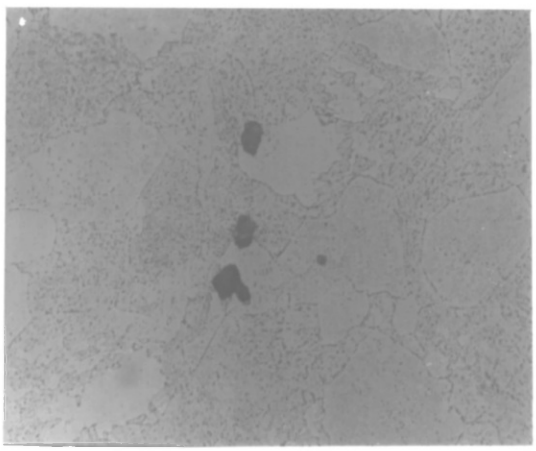






X 500 Mag

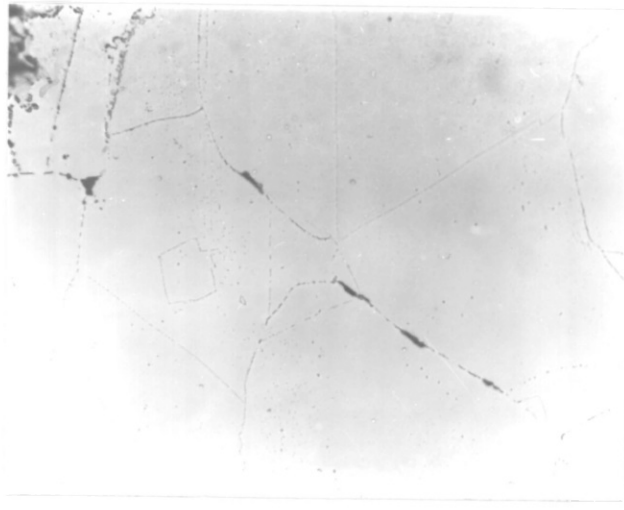
304-H stainless steel

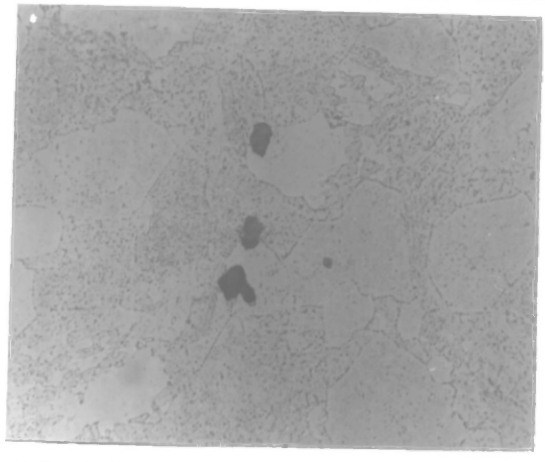


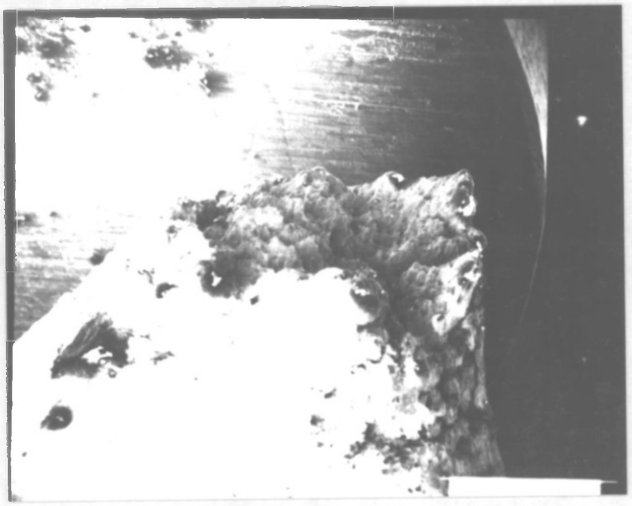
X 500 Mag

2-1/4 Cr Mo steel

Figure 5.32 : Failure in 304-H stainless steel and 2-1/4 Cr Mo steel

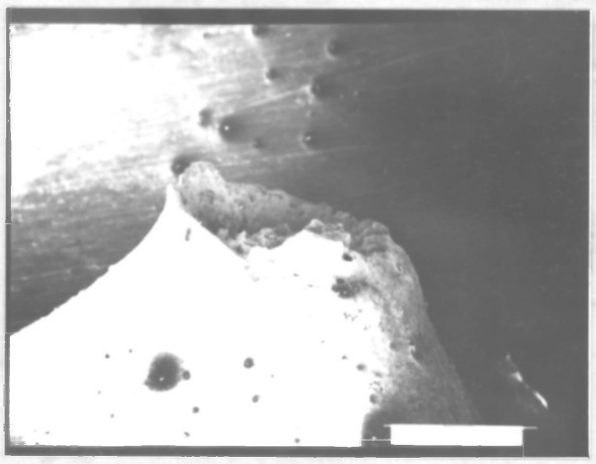






X 15 Mag

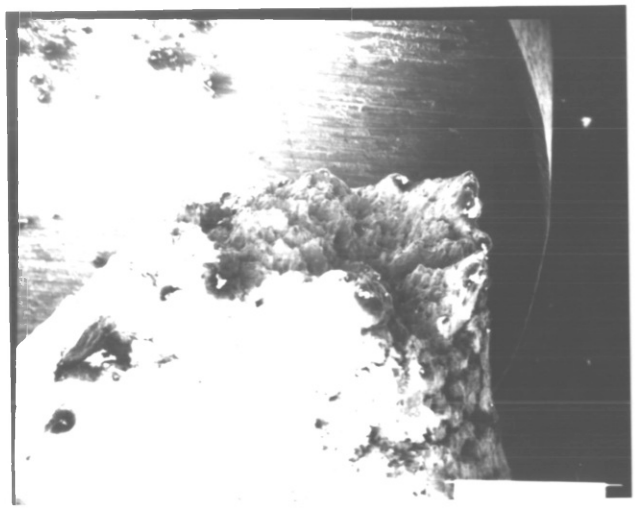
a) 304-H Stainless steel (otside to inside)

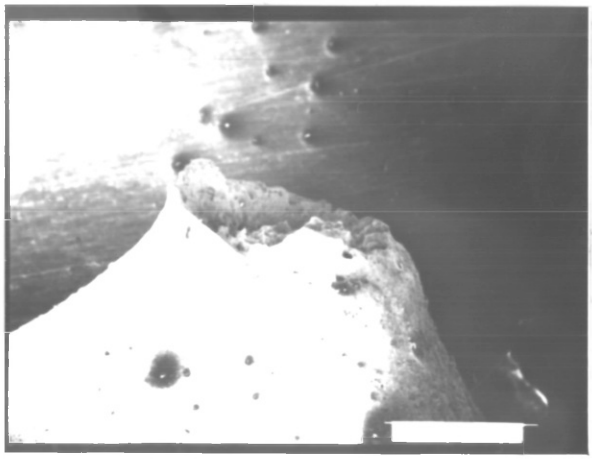


X 15 Mag

b) 2-1/4 Cr Mo steel (inside to outside)

Figure-5.33: Final failure of a notched bar b / a = 1.46, a / R = 1.67





CHAPTER-6

RESULTS AND ANALYSIS OF DS MAR M002 EXPERIMENTS

6. Introduction

Several materials exhibit anisotropy either due to their structural pattern or orientation of grains in particular directions. Because of anisotropic behaviour it is difficult to characterize the failure mode, as pointed out in Chapter-3. As the material used in the present study is directionally solidified, all grains are assumed to be aligned in the direction of solidification, and because of the granular pattern it is anisotropic in nature. In this chapter an attempt is made to understand the behaviour of this material under multiaxial stress conditions through the numerical and experimental techniques. A notched bar technique is used to simulate a multiaxial stress state. The uniaxial constant load and constant stress creep data were collected at 900±4 ^{0}C. The material constants obtained are then used in the mathematical model. The theoretical deformation rate in the axial direction and radial direction are calculated and compared with the experimental deformation rate. A metallographic analysis is carried out on selected notch geometries to study the microscopic features of failure.

6.1 Experimental Results DS (Mar M002)

Experiments were carried out on plain specimens at constant load and constant stress. A comparison between the constant load and constant stress behaviour is made in terms of minimum strain rate. Simultaneously the tests were carried out on the notched bar specimens in constant load creep testing machines at Imperial College. Notched bar data are plotted in terms of notch strengthening ratio. All tests were carried out at 900±4 ^{0}C.

6.1.1 Uniaxial Constant Load Creep Tests

Creep tests on plain bar specimens were carried out at NPL using the standard

constant load creep testing machines described in Chapter-4. The nominal stress was selected from 400 to 200 MPa. which gave the rupture lives between 25.5 to 2660 hours. The results of these tests are summarized in Table-6.1, and the strain-time curves are shown in Figures-6.1 (a) and 6.1(b). The creep curves for all the specimens exhibited very little primary and secondary region, but a relatively long and very pronounced tertiary region. In all the tests, the ductility in terms of final failure strain varies from 20% to 31%. The ductility in terms of reduction in area varies from 40% to 50%. In order to find the material constants, C and n, occurring in the Norton's law, log-log plot of stress versus minimum strain rate is plotted in Figure-6.2. Creep rupture data are plotted in Figure-6.3 as a log of stress versus log of rupture time. The material constants are given as :

a) The creep index, n= 8.2

and

b) The creep constant, $C = 7.1 \times 10^{-24}$ [$1/ (MPa)^n$ hr]

6.1.2 Uniaxial Constant Stress Creep Tests

Constant stress tests on plain bar specimens were carried out at NPL in the standard cam type constant stress creep machines described in Chapter-4. Due to the limitations in the strain measurement on these machines all tests were terminated before final failure. The strain versus time curves are plotted in Figure-6.4. The comparison of the constant load and constant stress creep curve at 350 MPa. is shown in Figure-6.5, and the minimum strain rate is plotted in Figure-6.2. The minimum strain rate is tabulated in Table-6.2

The comparison of experimental creep curves at constant load and predicted curves using equations (5.8) and (5.14) is shown in Figure-6.6. A good agreement is found between the two when the time hardening law is used. With the strain hardening law the life predicted from constant stress data is higher than the experimental life. This suggests that a constant load creep curve can be obtained from the constant stress curve with good accuracy when the time hardening law is used.

6.1.3 Multiaxial Constant Load Creep Tests

Notched bar tests were carried out to examine the behaviour of this material under multiaxial stress state. The notch geometries tested are tabulated in Table-6.3. The triaxiality is varied by varying the notch root radius keeping other dimensions constant. All tests were carried out at the nominal stress of 350 MPa. The displacement versus time curves for some of the geometries are plotted in Figure-6.7 and 6.8. It is observed that they exhibit a similar shape to the constant load tests carried out on unnotched bars.The notched bar experimental results are plotted in Figure-6.9 in terms of the notch strengthening ratio which is described in the previous chapter. The reduction in area versus a / R ratio is plotted in Figure-6.10. The final a / R ratio after the failure versus the original a / R ratio is plotted in Figure-6.11. The notched bar creep data are tabulated in Table-6.4. The results are discussed in Section-6.5.

6.1.4 Diametral Strain Measurement on Notched Bars

Most of the creep data on notched bars are generated from the axial strain measurements. Very few data are available on diametral strain measurement. Diametral strain measurement is studied in order to understand the creep behaviour of a notched specimen in the radial direction. In this work three notched specimens were tested at NPL. Strain versus time curves are plotted in Figure-6.12. It can be seen that all curves show primary, secondary and a long tertiary region.

6.2 Numerical Analysis

From the previous chapter it is clear that extensive work has been done to understand the stress distribution in circumferentially notched bars for isotropic materials. In the literature there is no such information available on stress distribution across a notch throat for anisotropic (transversely isotropic) materials. Therefore the main aim of this work was the development of suitable multiaxial effective stress and strain equations with an anisotropy in the axial direction. Step by step formulation of these equations is presented in Chapter-3. An incorporated finite element program using the same

equations, is used to calculate the steady state stresses across a notch throat. From the experimental creep data available on plain bars in the axial and radial direction, the value of , β, occurring in the equation (3.20) is calculated for different values of n, assuming a strain rate in the axial direction twice of that in the radial direction. The calculation procedure for a constant, β, is described in Appendix-C. Material properties used in the analysis are given in Chapter-2. The values of material properties are ;

$$E_2 / E_1 = 1.33 ; \; E_1 / G_{12} = 1.04 ; \; \upsilon_{12} = 0.45 \; ; \; \upsilon_{23} = 0.305$$

As mentioned before in Chapter-3, the value of $\upsilon_{12} = 0.5$. But it was found that by using the value of 0.5 the computing time increased considerably. Therefore a suitable value of 0.45 which is close to the incompressibility condition is chosen for the analysis. Stresses across a notch throat are normalised with respect to the stress at a remote end, σ_∞. The normalised stresses are then plotted against the normalised distance, r / a, across the notch throat.

6.2.1 Stress Variation Across a Notch Throat

Notch geometries with different triaxiality ratios are analysed. Figure-6.13 illustrates the mesh patterns of some of the notch geometries. The same procedure as that described in the previous chapter for mesh generation is used. Stresses obtained across a notch throat are normalised with respect to the stress at the remote end and plotted against a normalised distance, r / a. The three stresses which are mainly responsible for the creep deformation and final failure are maximum principal stress, effective stress , and hydrostatic stress. These stresses are studied in detail. Notch geometries which illustrate a gradually increasing constraint in Figure-6.9 are selected for the analysis. Figures-6.14-6.16 show the comparison of the elastic and steady state stresses calculated using the present finite element program and MARC package available at ZENTCH Pvt. Ltd. (1987). Figures-6.17-6.20 illustrate the variation of the stresses for different values of creep index, n, for different notch geometries. The stress distribution away from the notch root plane is studied carefully. The effective stress is observed to be maximum away from the notch root plane as shown in Figure-6.21. The stress in each black and

white portion represents an average stress. Thus the maximum stress is found to be in the portion 5. The maximum principal stress and the hydrostatic stress are found to be higher in the plane of the notch root. Assuming that the effective stress governs the deformation from the stress distribution across a notch throat, the average effective stress in different planes is calculated as described in Appendix-D. The average effective stress in the notch root plane is found to be always lower than the average effective stress away from the notch root plane. It is assumed that the maximum average effective stress is responsible for the overall deformation of the notch root region. The experimental diametral displacement rate is compared with the uniaxial data using the maximum average effective stress in Figure-6.2.The theoretical diametral displacement rate calculated using the finite element program for different a / R ratios is compared with the experimental displacement rate in Figure-6.22. All the calculations were carried out for n equal to 8.2. The reason for selecting a value of 8.2 for theoretical calculations is explained in Section-6.5. Good agreement is found between the theoretical and experimental displacement rates. The numerical values of experimental diametral strain rates and theoretical effective stress are tabulated in Table-6.5

Figure-6.23 shows the variation of maximum average effective stress in the plane away from the notch root , average effective stress in the plane of the notch root and the effective stress at the skeletal point in the notch root plane. Figure 6.24 shows the variation of the stresses at the skeletal point in the notch root plane. The constant ductility model based on the maximum average effective stress away from the notch root plane, and the constant ductility model based on the effective stress at a skeletal point in the notch root plane, are shown in Figure-6.9. The Rice and Tracey and Cocks and Ashby void growth models are further used to compare the experimental multiaxial ductility with predicted ductility as shown in Figure-6.25

6.3 Comparison of Isotropic and Anisotropic Stresses Across a Notch Throat

Two notch geometries with b / a = 1.46 and a / R ratio equal to 1.67 and 21.60 are

selected for the comparison. As seen from Figure-6.9 these notch geometries represent low and high constraint respectively. Normalised maximum principal stress , effective stress and hydrostatic stress across a notch throat are compared. Figures-6.26-6.27 show the comparison of maximum principal stress, radial stress and hoop stress. Figures-6.28-6.30 show the comparison of maximum principal stress, effective stress and hydrostatic stress in the isotropic and anisotropic materials for n = 1 and Figures-6.31-6.33 show the comparison for n= 8.2 which represent the elastic and steady state stresses respectively. It is observed that the effective stress in an anisotropic material is always lower than the effective stress in an isotropic material. The maximum principal stress and the hydrostatic stress at the notch root in an anisotropic material are lower or equal to the maximum principal stress and hydrostatic stress at the notch root surface in an isotropic material. The results are discussed in section-6.5

6.4 Metallographic Analysis

Metallographic analysis was carried out on selected specimens after fracture. The notch geometries were selected such that the evolution of damage under different triaxial stress conditions could be studied. A plain bar specimen subjected to the same nominal stress as the notched bars was selected for the metallographic analysis. All specimens were slit longitudinally within a tolerance of ± 0.1 mm. The specimens were then mounted in a bakelite, polished and etched several times using Marble's reagent. Progressively sharper notches covering experimental range are examined. Figure-6.34 shows the micrograph of the plain specimen, after creep failure, which was subjected to 350 MPa. Small edge cracks are observed which are shown by an arrow. Figure-6.35 shows the failure of the broken notch and Figure-6.36 shows the damage in the unbroken notch of a / R equal to 4.60. In this notch, the damage is observed to originate and propagate away from the notch root at an angle approximately 50-55 ^{0} to the axis of the solidification direction. Figure-6.37 shows the broken notch and the damage along the longitudinal grain boundaries, while Figure-6.38 shows the unbroken notch of a / R

equal to 13.0. In this case also, the damage is observed to originate away from the notch root approximately at the same angle (50 -55^0) to the solidification direction. The grain boundary split, near the notch root, has been found to be caused by high constraint. Figure-6.39 shows the broken notch and the unbroken notch of a / R equal to 21.60. Figure-6.40 shows the magnified view of the unbroken notch. Similar features of grain boundary splitting are observed in this case but the damage originate from the corner, because of high stress concentration factor caused by machining.

6.5 Results and Discussion

6.5.1 Discussion of Experimental Results

From the constant load strain versus time curves (Figure-6.1a and 6.1b) it is clear that the material shows a very little primary and secondary regions and a prolonged tertiary region. This is exactly the behaviour of superalloys and the cause of this behaviour can be found in the literature cited in Chapter-3. Ductility in terms of final strain to failure is observed to be between 20 % to 31 % while ductility in terms of reduction in area is observed to be between 40 % to 50 %. The higher ductility in terms of reduction in area is mainly due to necking. From the log-log plot of minimum strain rate versus stress (Figure-6.2) two values of , n , can be calculated. For the low stress region the value of, n ,is observed to be 6.1, and for high stress region the value of, n, is observed to be 15.0. The average value of , n , is found to be around 8.2. For the theoretical calculations the average value is chosen. The reason is that, though the stresses relax once a steady state has been reached some regions of the notch throat can be subjected to a stress equivalent to a nominal stress. As the average value can represent the behaviour of the notch throat between the range of steady state stress to the nominal stress, it is found to be reasonable to use the average value. The minimum strain rate under the constant stress tests is lower or slightly higher than the minimum strain rate under constant load tests. As seen from Figure-6.6, the constant load creep curves predicted from the constant stress creep curves using a time hardening law, show a good

agreement with the experimental constant load creep curves. On the other hand, constant load creep curves predicted using strain hardening law, give higher life compared with the curve predicted from the time hardening law. Thus, the time hardening law has been found to be more appropriate for the prediction of the constant load data from the constant stress data. The displacement versus time curves plotted in Figures-6.7 and 6.8 for some of the notch geometries show a similar trend to the constant load creep curve for a plain bar. The theoretical displacement rate is found to be higher than the experimental displacement rate.

From Figure-6.9 it is clear that the material shows notch strengthening. Life is found to be increased up to the a / R value of 9.30. After this a / R value, life is found to be decreased gradually till the material attains the notch strengthening ratio of 21.0 at a / R equal to 44.7. To understand the true nature of the failure , stresses within the whole geometry are calculated using the finite element program. As explained before, it is observed that the maximum effective stress does not occur in the plane of the notch root but has the maximum value away from the notch root. Thus the maximum average effective stress is calculated after studying the stress distribution carefully in the notch region. As most of the deformation is assumed to be taking place in the region of maximum effective stress, this stress is then chosen for the characterization of the general behaviour of the notch. Based on this maximum average effective stress, the notch strengthening ratio, as given by constant ductility model, is calculated and compared with the experimental results in Figure-6.9. Good agreement is found between the experimental and predicted results up to the a / R value of 9.30. After this value of a / R the predicted ductility remains constant. A similar comparison has been made using the effective stress at the skeletal point in the plane of the notch root. It is observed that the life is always higher than the measured value. The average value of hydrostatic stress is calculated in the plane of average maximum effective stress. Thus the ratio of average hydrostatic stress to the average maximum effective stress is calculated. From this ratio the notch strengthening ratio is calculated using the Rice and Tracey, Cocks and Ashby

void growth models. Again, based on the skeletal point stresses in the notch root plane these models are obtained as shown by dotted lines in Figure-6.9. The models based on the skeletal point stresses in the notch root plane predict lower life than the models based on the stresses in the plane of the maximum average effective stress. The reason is that the average effective stress in the plane away from the notch root is higher than the effective stress at the skeletal point in the notch root plane. Thus the ratio of ,$(\sigma_{mean} / \sigma_{eff})_{average}$, away from the notch root plane is lower than the ratio at the skeletal point in the notch root plane. Both models show the deviation from experimental results which indicates that the void growth models used here do not characterize the present material. From Figure-6.25 it is seen that the reduction in area in the case of blunt notches does not agree with the theoretically predicted reduction in area. Thus the failure in this material is not due to the void growth and coalescence as in the equiaxed materials, but by the cracks which originate from the voids at transverse steps in longitudinal grain boundaries and traverse right through the grains.

From Figure-6.10 it is observed that the reduction in area is decreased from 40 % of its uniaxial value to the 4.5 % at a / R equal to 44.7. That is, material exhibits low ductility in terms of reduction in area at high constraint. The failure is due to the nucleation and growth of cavities along the transverse steps of longitudinal grain boundaries, and propagation of the cracks from these voids across the grains. The final a / R ratio as plotted against the original a / R ratio in Figure-6.11 varies linearly and does not vary much from the original a / R ratio. There is no substantial change in the notch profile before the final failure. In an equiaxed or isotropic material the deformation in the notch root region is restricted, mainly due to the constraint of the notch profile. In DS material the deformation is constrained due to the columnar structure of the material and notch constraint. This dual constraint restricts the deformation of the notch root region in DS material as compared with the deformation in an isotropic material.

From Figure-6.12 it is clear that the material exhibits a very short primary and secondary, but a prolonged tertiary creep. The diametral strain is in good agreement with

the uniaxial data as seen in Figure-6.2. This diametral strain is plotted on the basis of the maximum average effective stress away from the notch root. Thus maximum average effective stress can be used for the characterization of the present material.

6.5.2 Discussion of Numerical Results

From the comparison of stresses in Figures-6.14-6.16, it is clear that there is good agreement between the stresses obtained from the present finite element program and the MARC program for elastic conditions. In the case of steady state condition, for the blunt notch, a / R equal to 1.67, the stresses obtained from the MARC program are not fully redistributed. In the case of medium notch, a / R equal to 9.30 and a sharp notch a / R equal to 21.60, effective stress is in good agreement. The maximum principal stress and the hydrostatic stress differ in the notch root region within a tolerance of 10 %. The redistribution time calculated using the MARC program was found to be around 6 hrs. for the notches analysed. As the stresses get redistributed early in the life of the component, the redistribution time does not contribute to the total failure time.

From Figures-6.17-6.20, it is observed that a good skeletal point exists for all the notch geometries. In the blunt notch a steady state effective stress is almost uniform. For the notch of a / R equal to 4.60 and a / R equal to 9.30 the effective stress at the notch root surface is observed to be lower compared with the stress inside near to the notch root. For a / R equal to 21.60 which represents fairly sharp notch geometry the steady state effective stress is observed to be maximum at the notch root surface. For all the notch geometries studied, the elastic maximum principal stress is lower at the notch root surface. Under steady state conditions, apart from a blunt notch, the stresses are highly localized inside near to the notch root. A similar trend is observed in the case of hydrostatic stress. From Figure-6.22 it is clear that the the theoretical diametral displacement rate is in good agreement with the experimental displacement rate. But, from Figures-6.7 and 6.8, it is seen that axial theoretical diaplacement rate differs considerably from the experimental displacement rate. The main reason is that in the theoretical calculations , from the uniaxial data on plain bars in the longitudinal and

transverse directions , the axial creep rate is assumed to be twice that of the creep rate in the radial direction. This may not be the case under multiaxial stress conditions. Depending on the notch sharpness this ratio can vary. Figure-6.23 gives the variation of maximum average effective stress away from the notch root plane, the average effective stress and the effective stress at a skeletal point in the notch root plane. The average value of the effective stress in the plane of the maximum effective stress, is calculated as explained in Appendix-C. The average effective stress in the notch root plane is lower than the maximum average effective stress away from the notch root plane and the effective stress at the skeletal point in the notch root plane. From Figure-6.24 , it can be seen that the effective stress at a skeletal point in the notch root plane decreases from its uniaxial value of 2.13 sharply to certain value of a / R and remains constant for the rest of the a / R values. The maximum principal stress , hydrostatic stress and the ratio of hydrostatic stress to effective stress all show continuous trend.

As mentioned above, the most interesting result of the present analysis is that the effective stress which governs the deformation under multiaxial stress conditions is found to be maximum in the plane away from the notch root, for all the notch geometries studied. The material is stiffer in the radial direction than the axial direction. Under plastic conditions it deforms less in the radial direction than in the axial direction. In the notch root region radial deformation is restricted both due to anisotropic behaviour of the material and the constraint of the notch profile. This causes the notch root to experience less deformation . Thus the maximum deformation occurs away from the notch root, and ultimately the maximum effective stress shifts away from the notch root ωhile in the case of an isotropic material , maximum deformation is confined to the notch root plane and thus maximum effective stress occurs in the notch root plane. The Cocks and Ashby (1980) void growth model does not show good agreement with the experimental reduction in area. This suggests that this void growth model can not be used for the characterization of the present material.

Comparison of isotropic and anisotropic stresses as shown in Figures-6.26-6.33

suggests that anisotropic effective stress is always lower than the isotropic effective stress across a notch root plane. This fact was reported by Bhatnagar et al (1986) who derived the analytical solution for a thick-walled cylinder under internal pressure. They reported that the material which is stiffer in the radial direction than the axial direction has lower effective stress compared with the isotropic material. Other stresses are found to have a value, lower or equal to, the isotropic stresses at the surface of the notch root, but significantly higher near the notch root. It is clear that the stresses near the notch root do not redistribute as quickly as they redistribute in an isotropic materials. The maximum effective stress occurs away from the notch root plane. Thus the deformation is less in the notch root region. This means that the strain rate in the notch root is slower compared with the strain rate in the isotropic materials. The stresses redistribute faster if the strain rate is faster. As the strain rate is slower compared with the isotropic materials, stresses do not redistribute as fast as they redistribute in an isotropic material.

6.5.3 Discussion of Metallographic Analysis

Figure-6.34 shows a micrograph of the plain specimen subjected to the same nominal stress as the notched specimens. The voids first nucleate at the transverse steps of the longitudinal grain boundaries. Once they nucleate they act as a source for small cracks. These cracks further propagate individually and meet each other to form a single crack which propagate through the grain causing a complete failure of a grain. Thus the final failure occurs, due to the failure of grains by a single crack, or due to the loss of strength because of the presence of the several cracks. Edge cracks have been found on the surface of the specimen as shown in Figure-6.34. The broken end shows the presence of small cracks throughout the cross section. From Figures-6.35-6.36, which show the micrograph of the broken and the unbroken notch of a / R equal to 4.60, it has been found that the damage is localised away from the notch root region. A magnified view of the damage indicates that small cracks are traversing at an angle to the notch profile, while in the middle of the notch damage is in the form of cracks perpendicular to the axis of the stress applied. These cracks are found to originate either from carbides, or

from the voids developed at the transverse steps of the longitudinal grain boundaries. The broken end shows the fracture due to the propagation of a single crack which comprises several small cracks at an angle to the notch profile. In the case of the sharp notch geometries as shown in Figures-6.37-6.40, grain boundaries are observed to be split vertically. This may be due to the high triaxiality ratio near to the notch root. In all the notch geometries studied damage is always found to be initiated away from the notch root. This fact is in good agreement with the theoretical prediction of maximum effective stress away from the notch root plane, as the deformation is mainly governed by the effective stress.

Hayhurst et al.(1984) correlated the experimental damage across the notch throat with the numerically predicted damage. They showed that the damage in copper first developes in the plane of the notch root just inside the notch root where the maximum principal stress has its maximum value. The damage then spreads towards the notch root not in the plane of the notch root but away from the notch root plane. In the present material damage developes away from the notch root plane because of the maximum effective stress existing there. Once developed it then spreads in the form of small cracks at an angle to the notch root plane (approximately 50-55 ^{0} to the solidification direction).

From the metallographic analysis, it has been demonstrated that the failure in this material is mainly due to the formation and propagation of a damage in the form of small cracks from the notch root ,where the maximum average effective stress prevails.

6.6 Conclusions

1) Creep curves of constant load, and constant stress uniaxial tests and multiaxial tests on the notched bars, show very little primary and secondary creep but a pronounced and long tertiary creep.

2) The constant load curves predicted from the constant stress curve using time hardening law and strain hardening law, show a good agreement with the experimental creep curve. The curve predicted from strain hardening law gives a higher value of life

compared with the curve predicted from the time hardening law. therefore it is proved that the time hardening law is more appropriate for the prediction of a constant load curve.

3) The comparison of the stresses, across a notch throat, calculated using the present finite element program and MARC program show good agreement for elastic stress distributions. For steady state distributions, the stresses are found to be in good agreement in the case of sharp notch geometry. In the blunt notch geometry the stresses obtained from MARC are found not to be distributed fully. In the medium notch geometry, the effective stress is found to be in good agreement while the maximum principal stress and hydrostatic stress show a difference. This difference can be due to the difference in the size of the elements in the notch root region used in MARC program.

4) The comparison of isotropic and anisotropic stresses show that effective stress in the notch root plane for an anisotropic analysis is always lower than the stress in an isotropic analysis. The effective stress in an anisotropic analysis is found to be higher away from the notch root plane. The position of maximum effective stress is found to be dependent on the notch profile. Other stresses are found to be higher in the notch root plane in both the analyses. The stresses in the notch root in an anisotropic analysis are found to be sufficiently higher compared with the stresses in an isotropic analysis. This indicates that the stresses in an anisotropic analysis do not redistribute as quickly as they redistribute in an isotropic analysis. As the deformation in ductile materials is controlled by the effective stress it is advantageous to use the materials which are stiffer in the radial direction than the axial direction for the high temperature (creep) applications.

5) Good agreement is found between the theoretical , constant ductility model, and experimental notch strengthening ratio up to an a / R ratio of 9.30 for the average value of creep index, using maximum average effective stress away from the notch root plane. Following this life predicted by constant ductility model is found to remain constant while the life obtained experimentally shows the decreasing trend which indicates the change in the failure mode.

6) From the metallographic analysis it is found that the voids first nucleate at the

transverse steps of the longitudinal grain boundaries. Once stabilised, they act as a source for the nucleation of small cracks. These cracks further propagate through the grains . The failure is found to occur when such cracks join each other, or by the loss of strength due to the presence of several such cracks.

7) The damage hasbeen found to be developed away from the notch root plane at an angle approximately $50\text{-}55^0$ to the solidification direction. Compared with the damage predicted by Hayhurst (1984) in 316 SS and the damage initiation studied in 304-H stainless steel in the previous chapter, the damage initiation and propagation in DS material is entirely different. The damage in the stainless steels is found to originate always in the notch root plane where the maximum effective stress exists.

TABLE-6.1

Uniaxial constant load creep data of DS Mar M002 at 900 ^{0}C

Stress (MPa)	Minimum creep rate ε_s (h-1)	Rupture time t_f (hours)	Failure strain ε_f (%)	Reduction in area A_f (%)
200	1.00×10^{-5}	2660.00	36.00	54.00
225	1.80×10^{-5}	1213.00	35.98	52.00
250	3.00×10^{-5}	737.00	31.90	41.50
275	6.80×10^{-5}	471.00	38.20	47.50
295	1.00×10^{-4}	260.00	23.00	47.00
325	1.38×10^{-4}	165.00	23.70	48.00
350	4.71×10^{-4}	73.00	31.00	46.00
400	1.50×10^{-3}	25.50	24.55	45.00

TABLE-6.2

Constant stress uniaxial creep data for DS Mar M002 at 900±4 ^{0}C

Stress (MPa)	Minimum strain rate ε_s (h^{-1})
350	2.60×10^{-4}
325	2.13×10^{-4}
275	9.14×10^{-5}

TABLE-6.3

Different notch geometries used in the numerical analysis

b /a	a / R	2b	2a	2R
1.46	0.50	9.50	6.50	13.040
1.46	1.67	9.50	6.50	3.892
1.46	2.60	9.50	6.50	2.490
1.46	4.60	9.50	6.50	1.625
1.46	6.00	9.50	6.50	1.086
1.46	9.30	9.50	6.50	0.698
1.46	13.00	9.50	6.50	0.500
1.46	21.60	9.50	6.50	0.309
1.46	44.70	9.50	6.50	0.146

TABLE-6.4

Notched bar creep data of DS Mar M002 at 900 ^{0}C

a /R	Rupture time t_f (hours)	Reduction in area A_f (%)
0.50	183.00	31.00
1.67	657.00	26.00
2.60	1095.00	12.00
4.60	1188.00	18.00
6.00	1633.50	11.50
9.30	2228.00	9.50
13.00	1733.00	7.50
21.60	1559.00	6.50
44.70	1238.00	4.50

TABLE-6.5

Diametral strain and average effective stress for different notch geometries

b / a	a / R	Secondary creep rate ε_s (h-1) (Experimental)	Rupture time t_f (hours)	Effective stress notch root (MPa) (Theoretical)	Effective stress maximum (MPa) (Theoretical)
1.46	0.50	1.45 x 10-4	170.00	251.00	300.00
1.46	1.67	4.50 x 10-5	650.00	233.00	275.00
1.46	2.60	2.06 x 10-5	1168.00	216.00	255.00

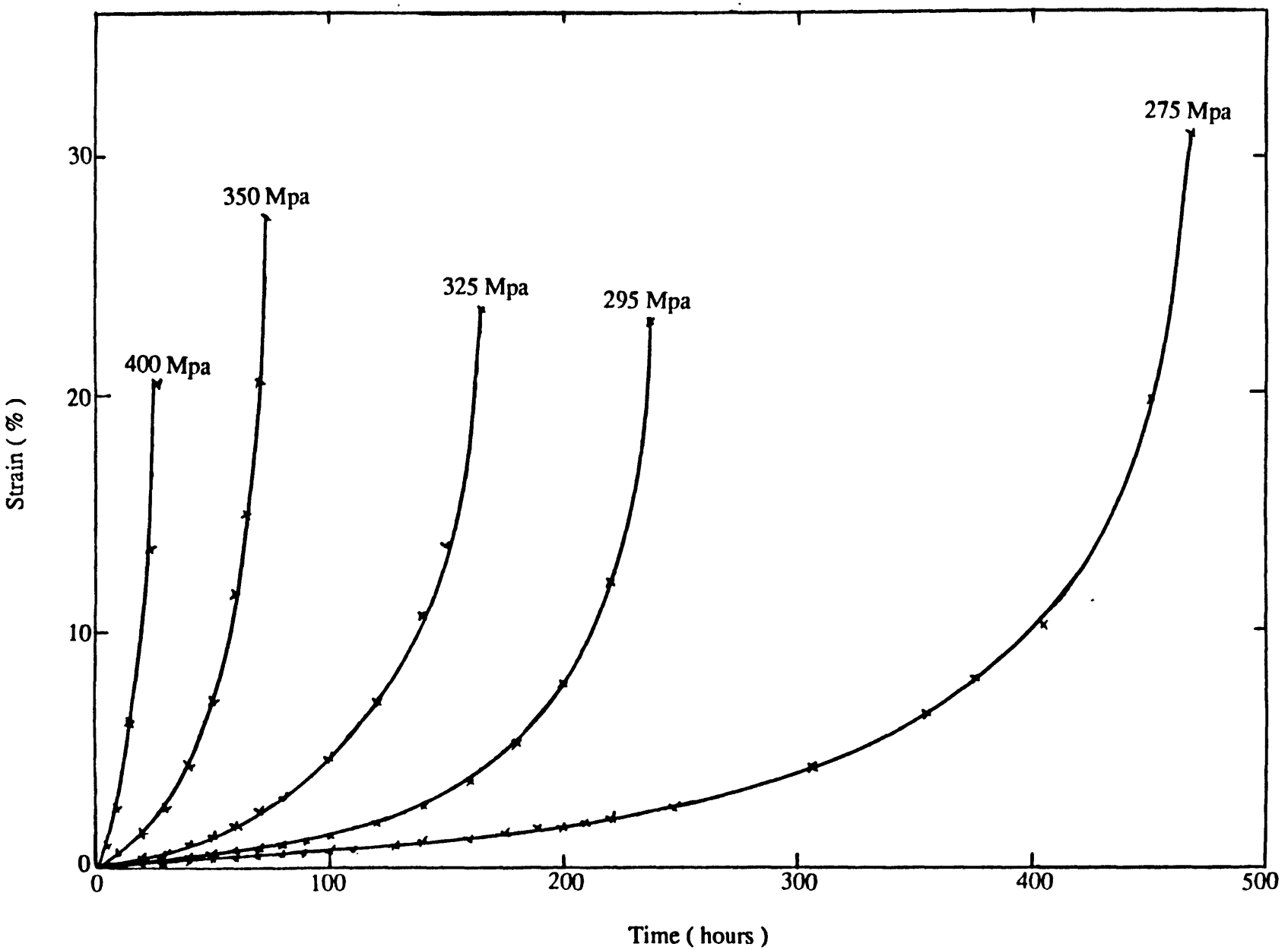


Figure 6.1a : Uniaxial creep data at constant load for DS Mar M002 at 900± 4^{0}C

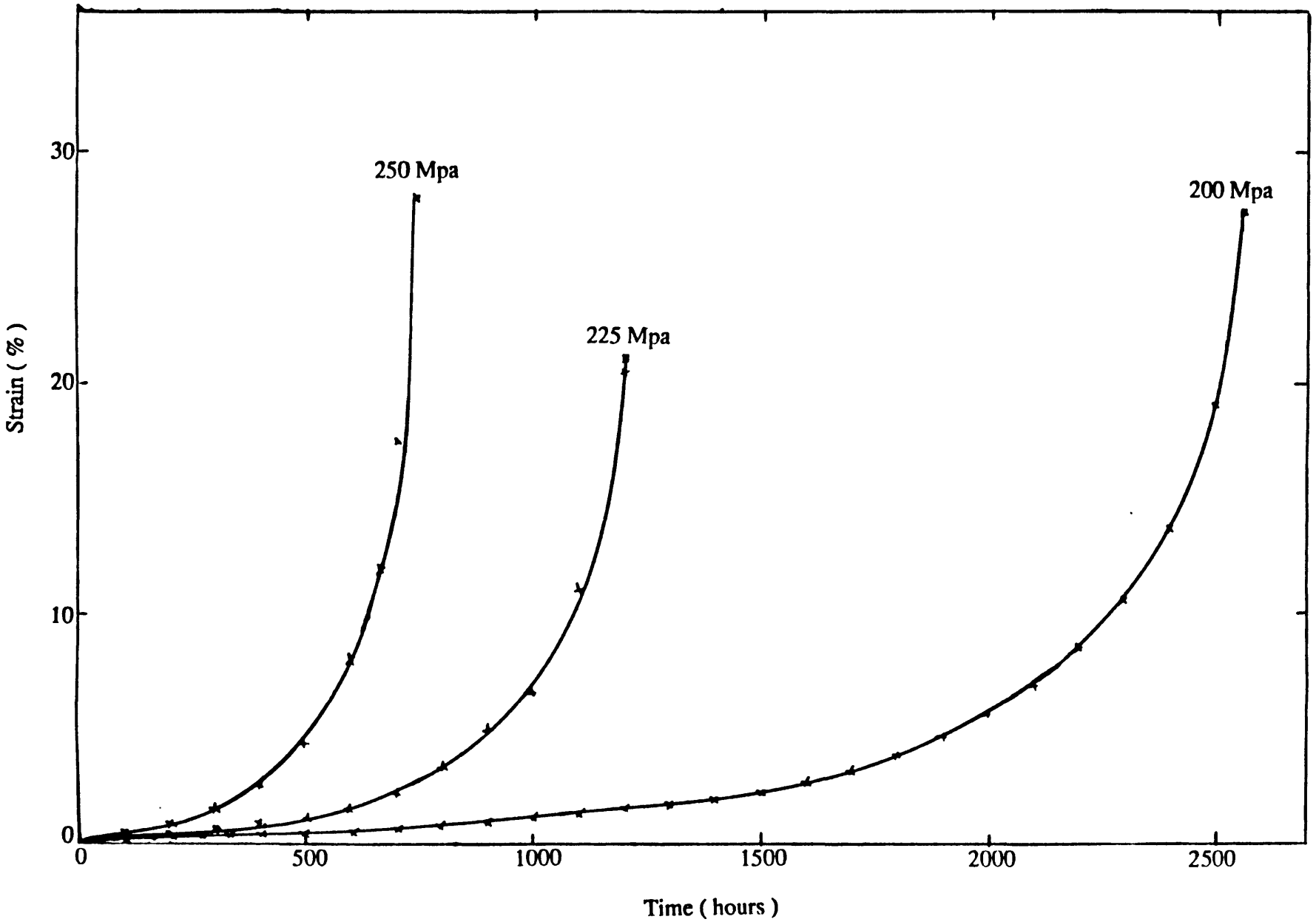


Figure 6.1b : Uniaxial creep data at constant load for DS Mar M002 at 900 ± 4^0C

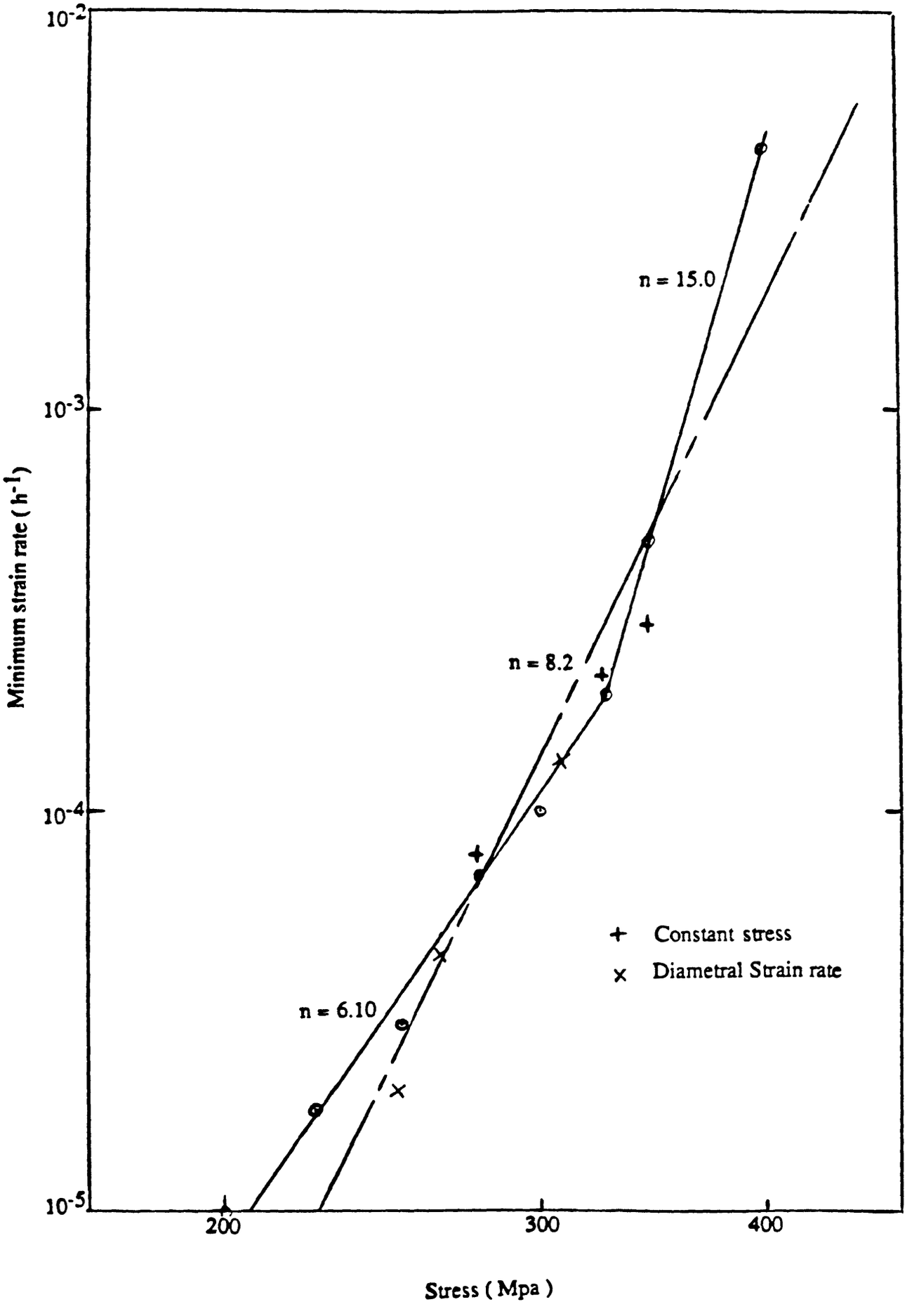


Figure 6.2 : Log-Log plot of minimum strain rate versus stress for DS Mar M002

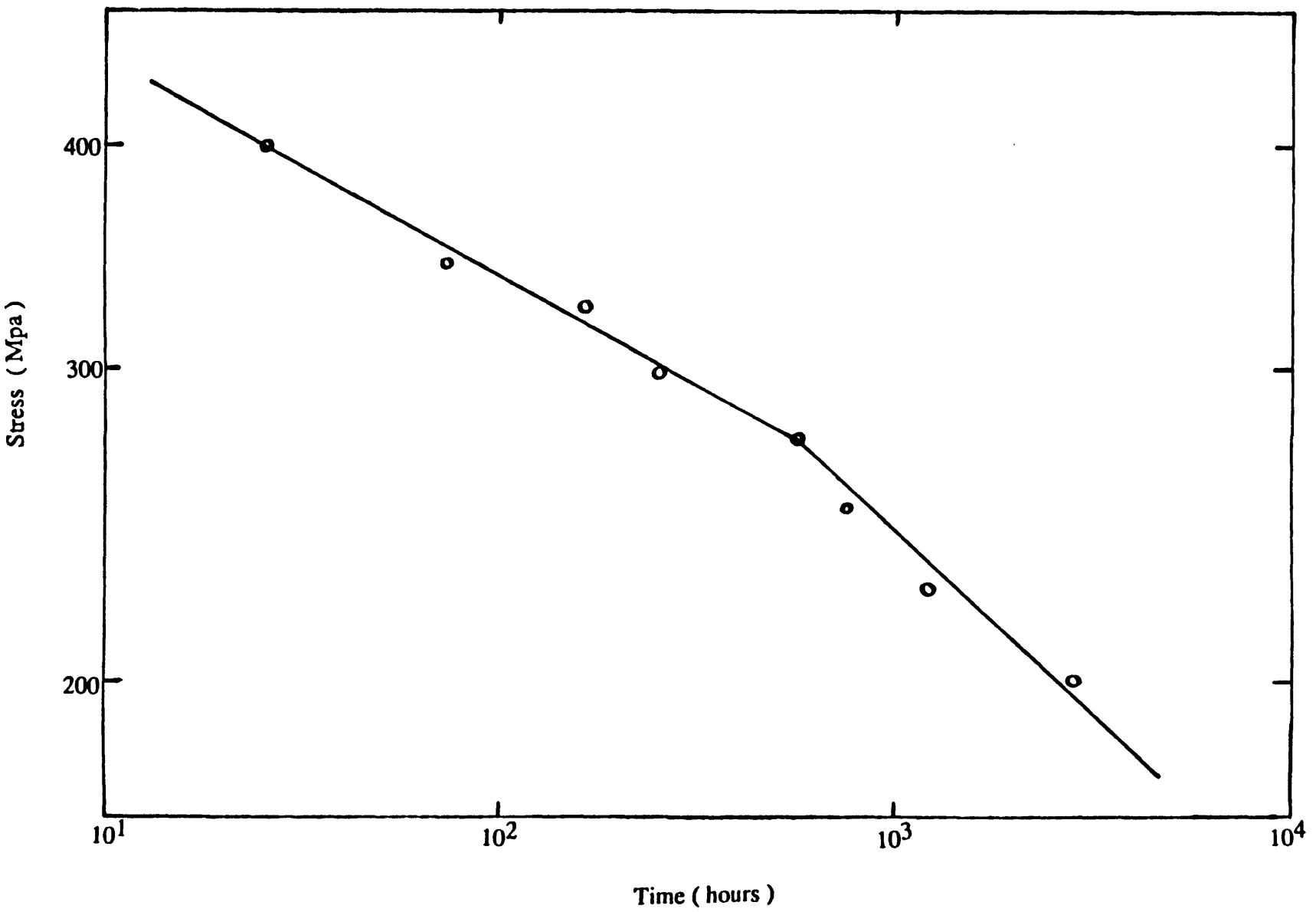


Figure 6.3 : Log-Log plot of stress versus rupture time for DS Mar M002

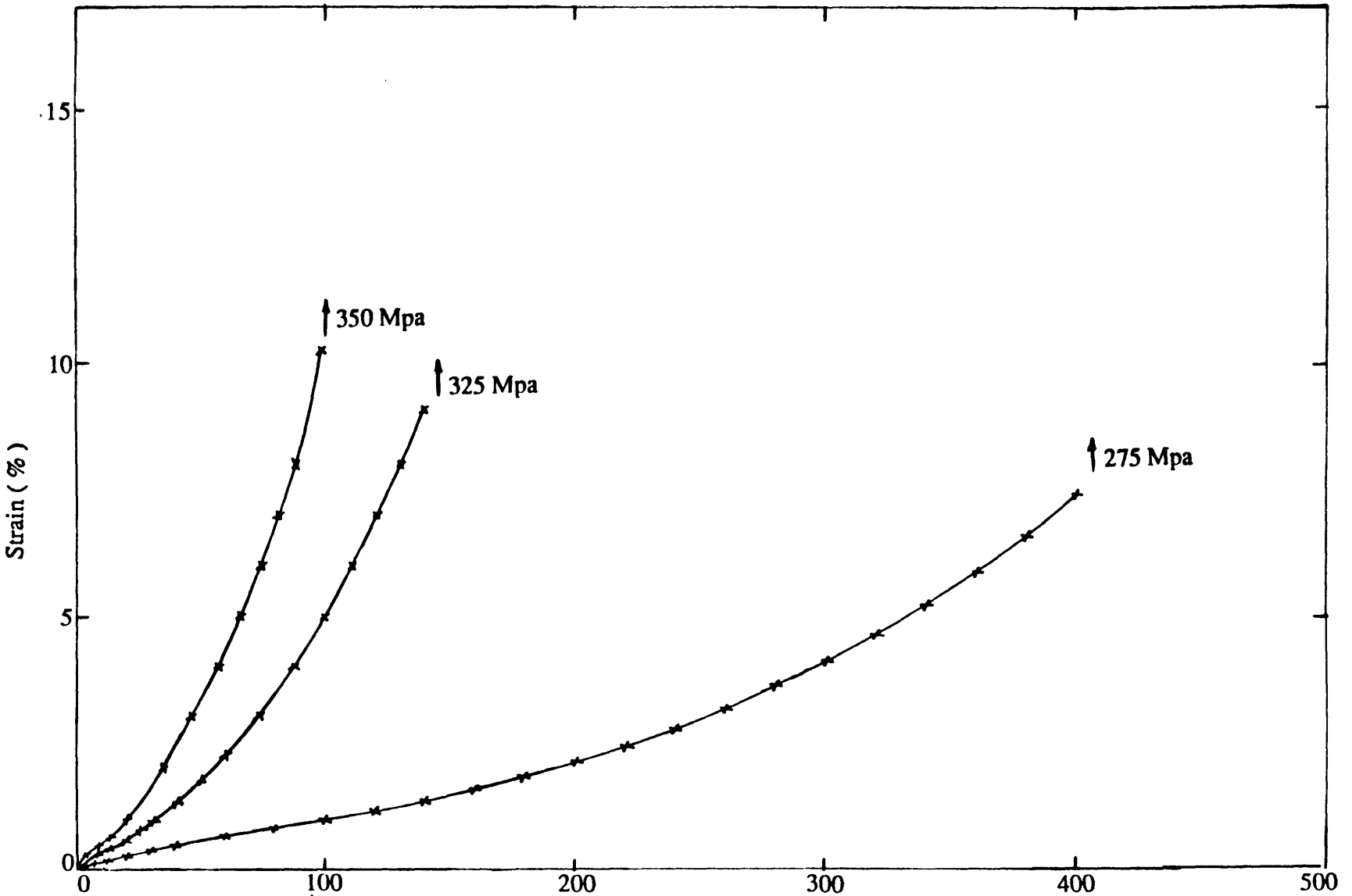


Figure 6.4 : Uniaxial creep data at constant stress for DS MarM002 at 900±4^{0}C

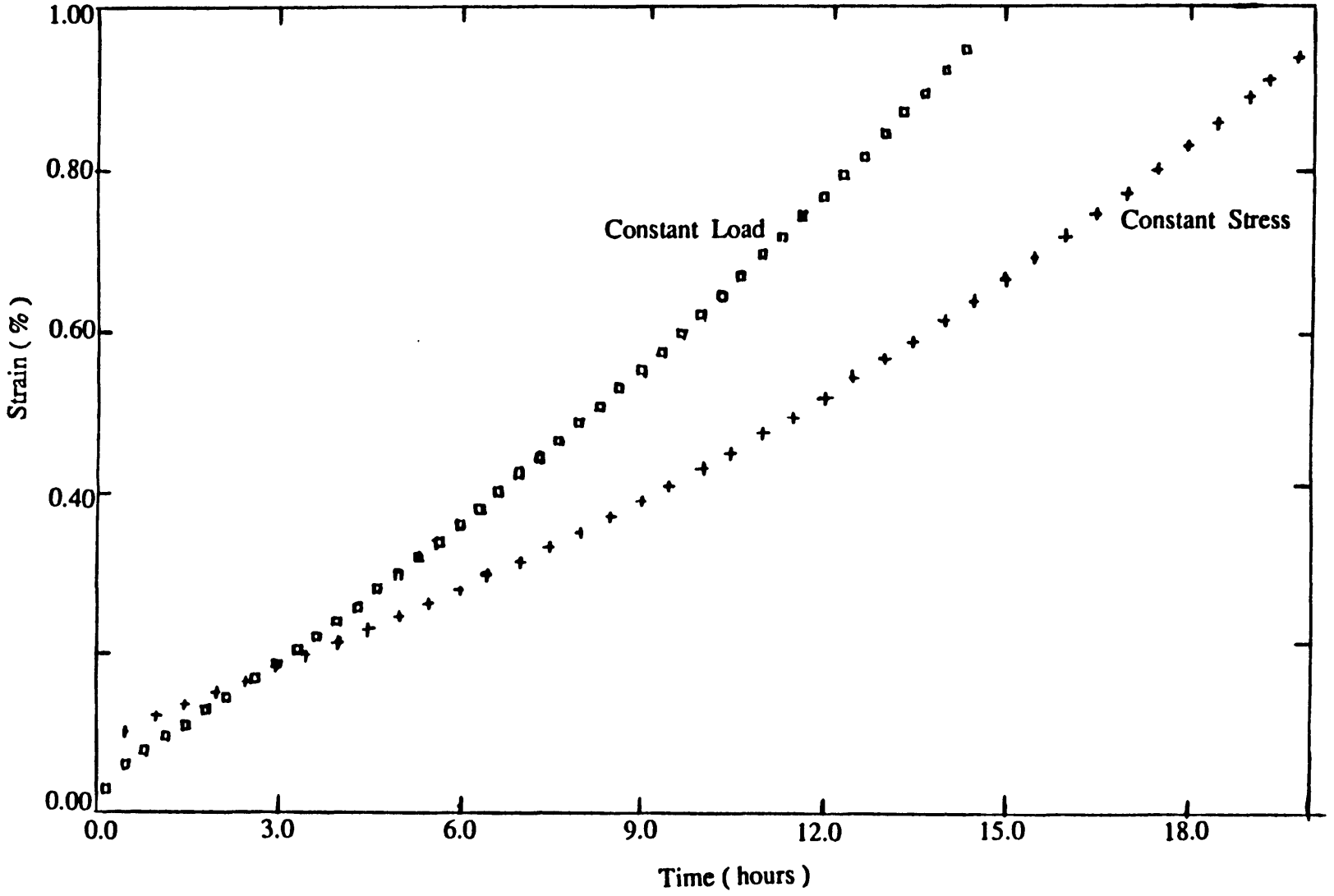


Figure 6.5 : Comparison of constant load and constant stress strain rate at 350 Mpa

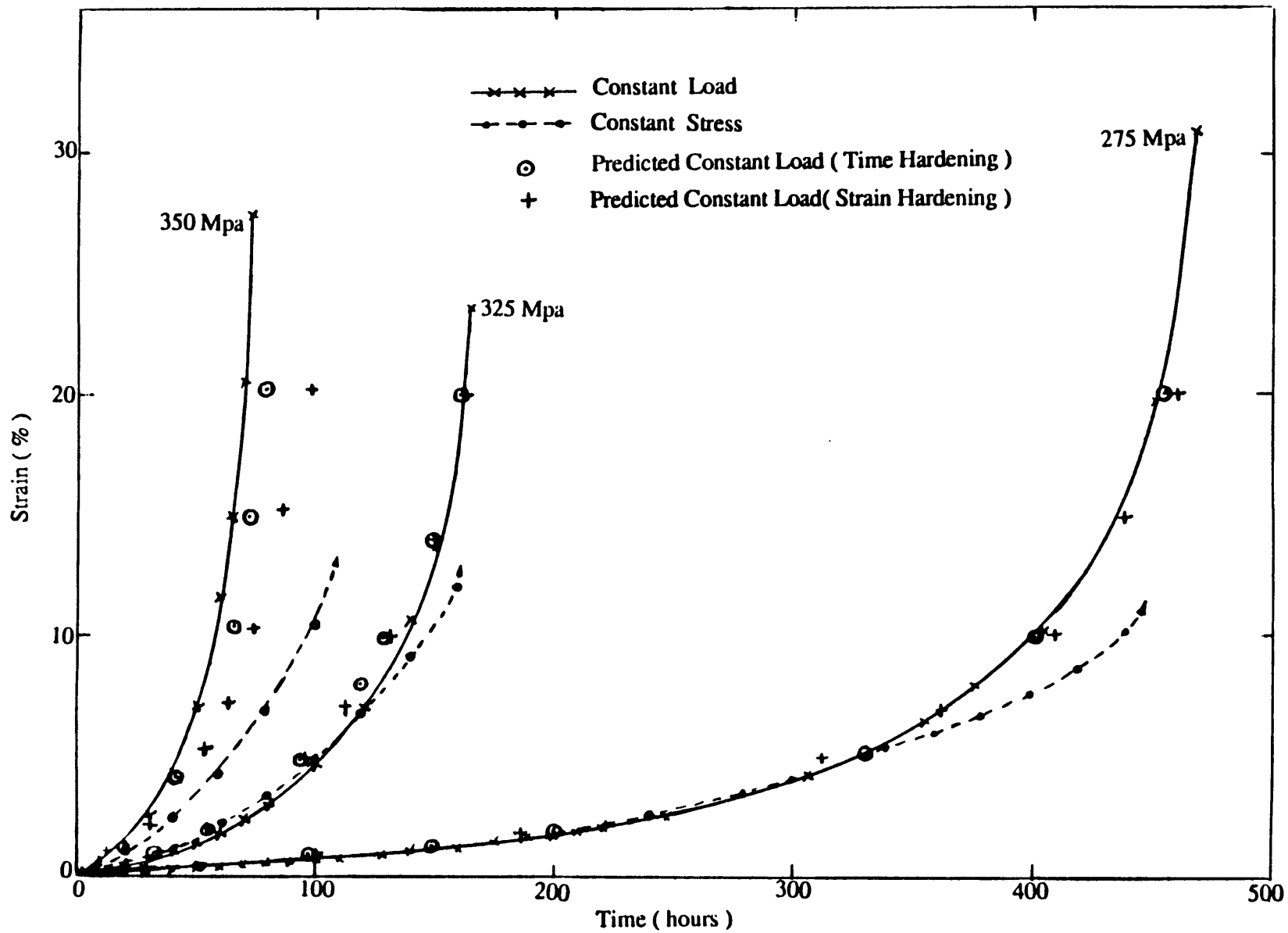


Figure 6.6 : Comparison of experimental constant load, constant stress and predicted constant load creep curves

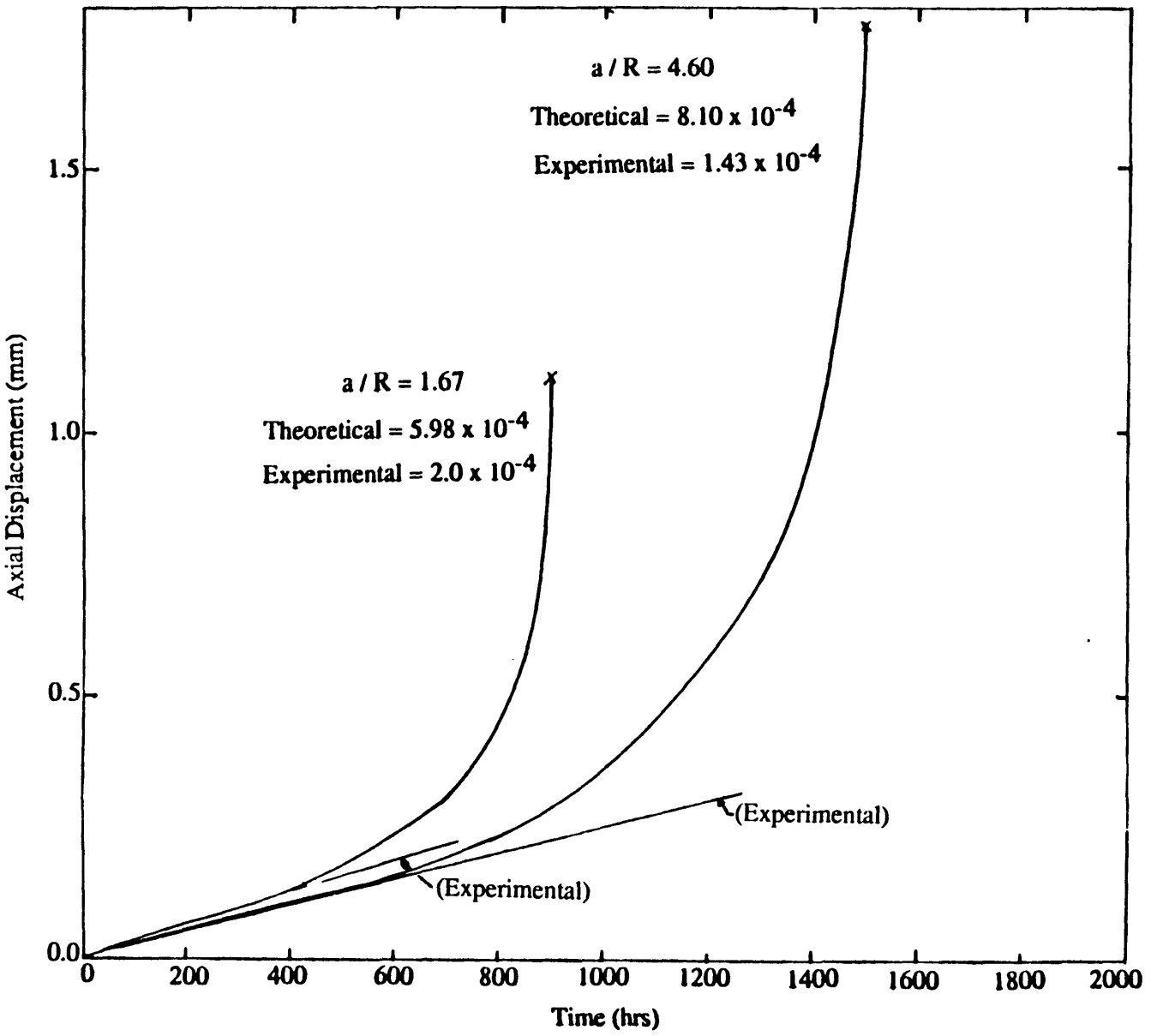


Figure 6.7 : Variation of axial displacement with time for b / a = 1.46,
a) a / R = 1.67, b) a / R = 4.60

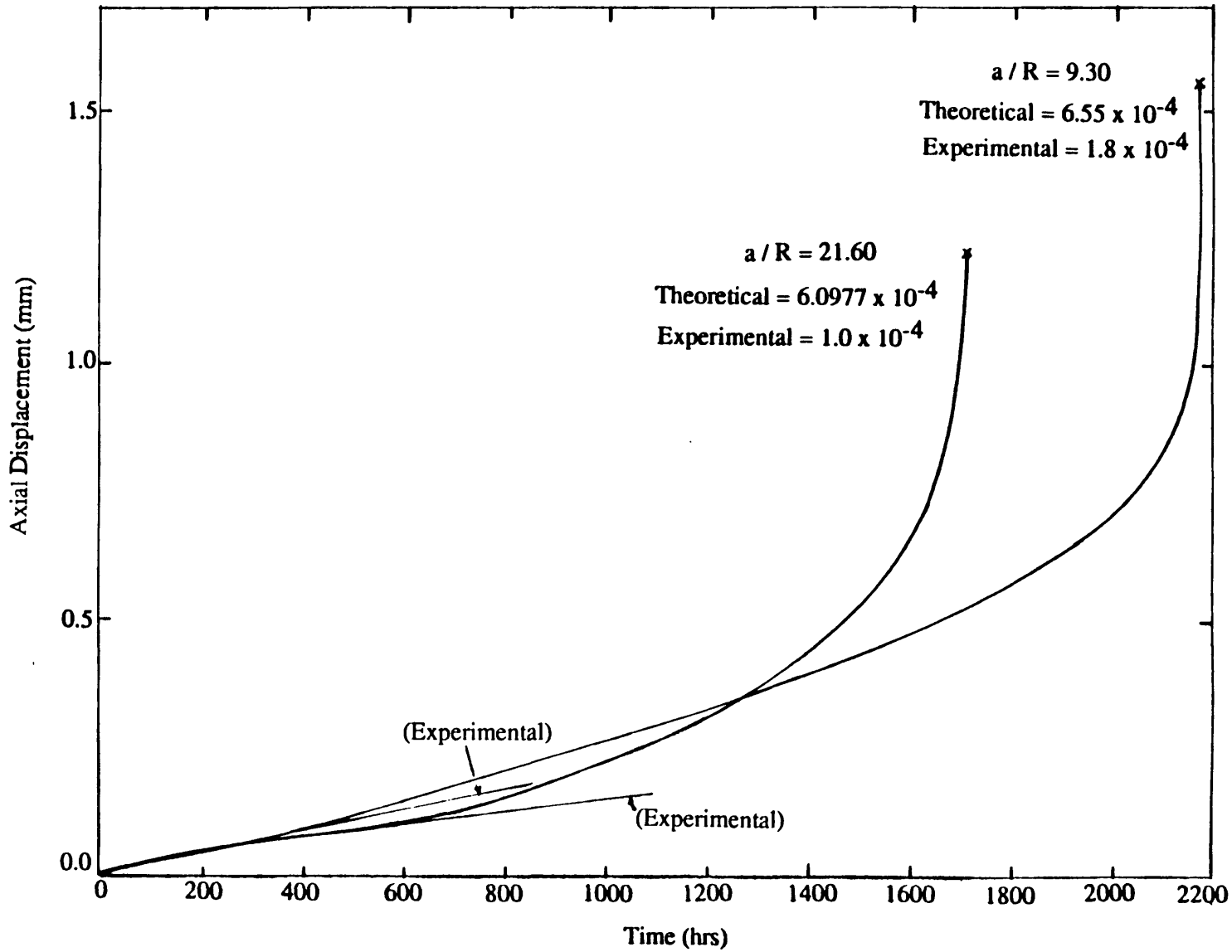


Figure 6.8 : Variation of axial displacement with time for b / a = 1.46,
a) a / R = 9.30, b) a / R = 21.60

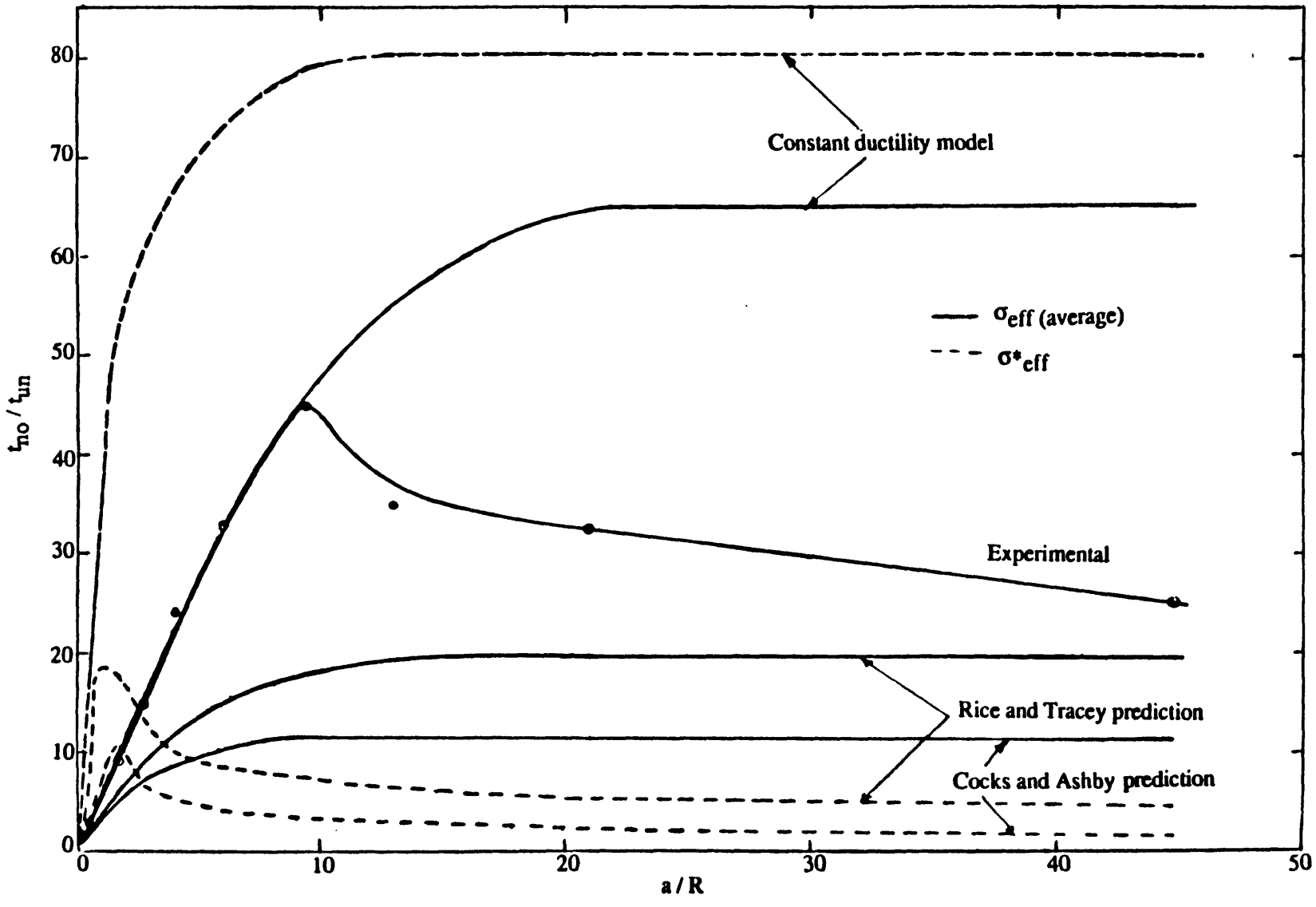


Figure 6.9 : Comparison of notch strengthening ratio with different models

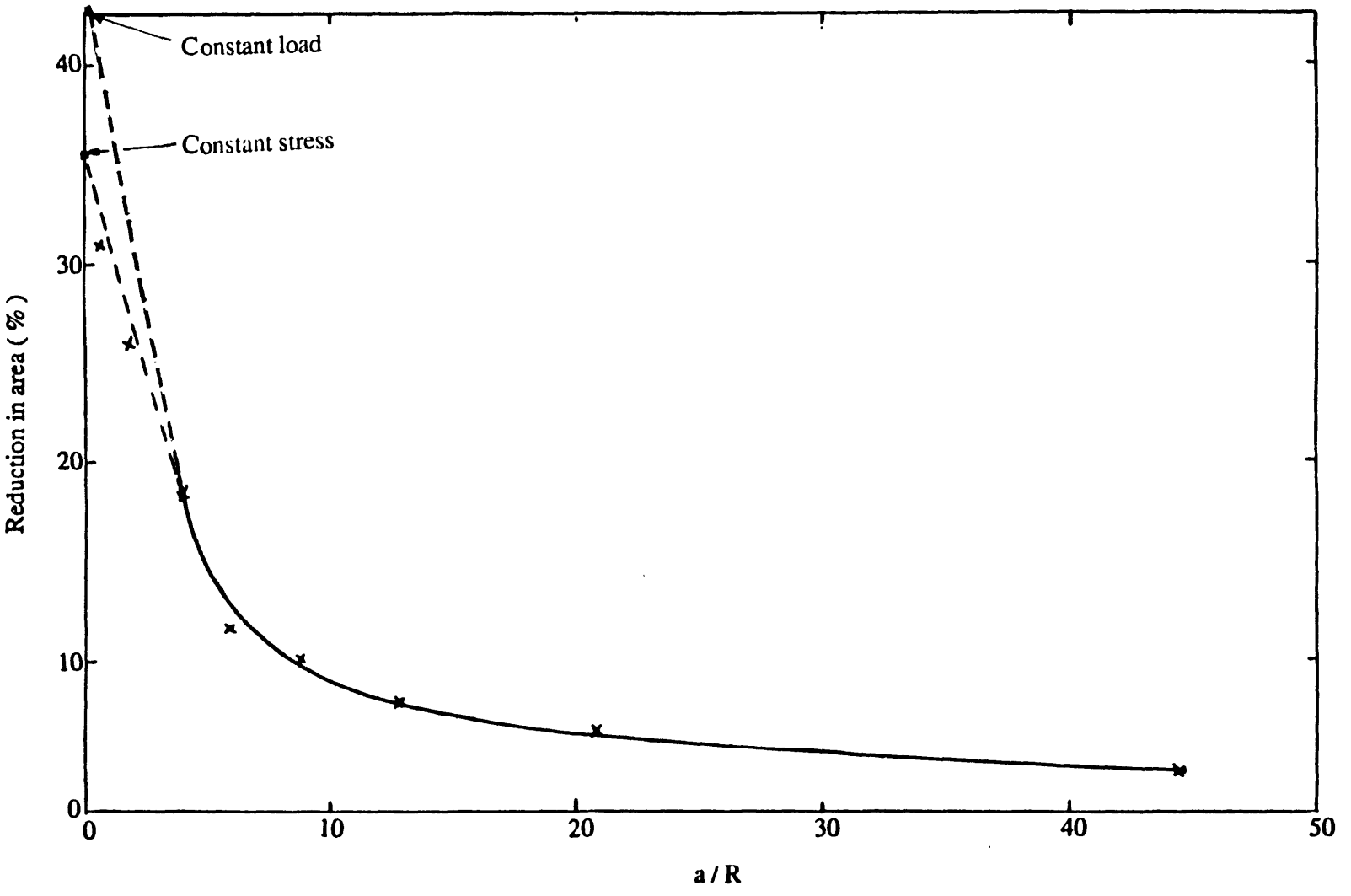


Figure 6.10 : Variation of reduction of area with a / R ratio

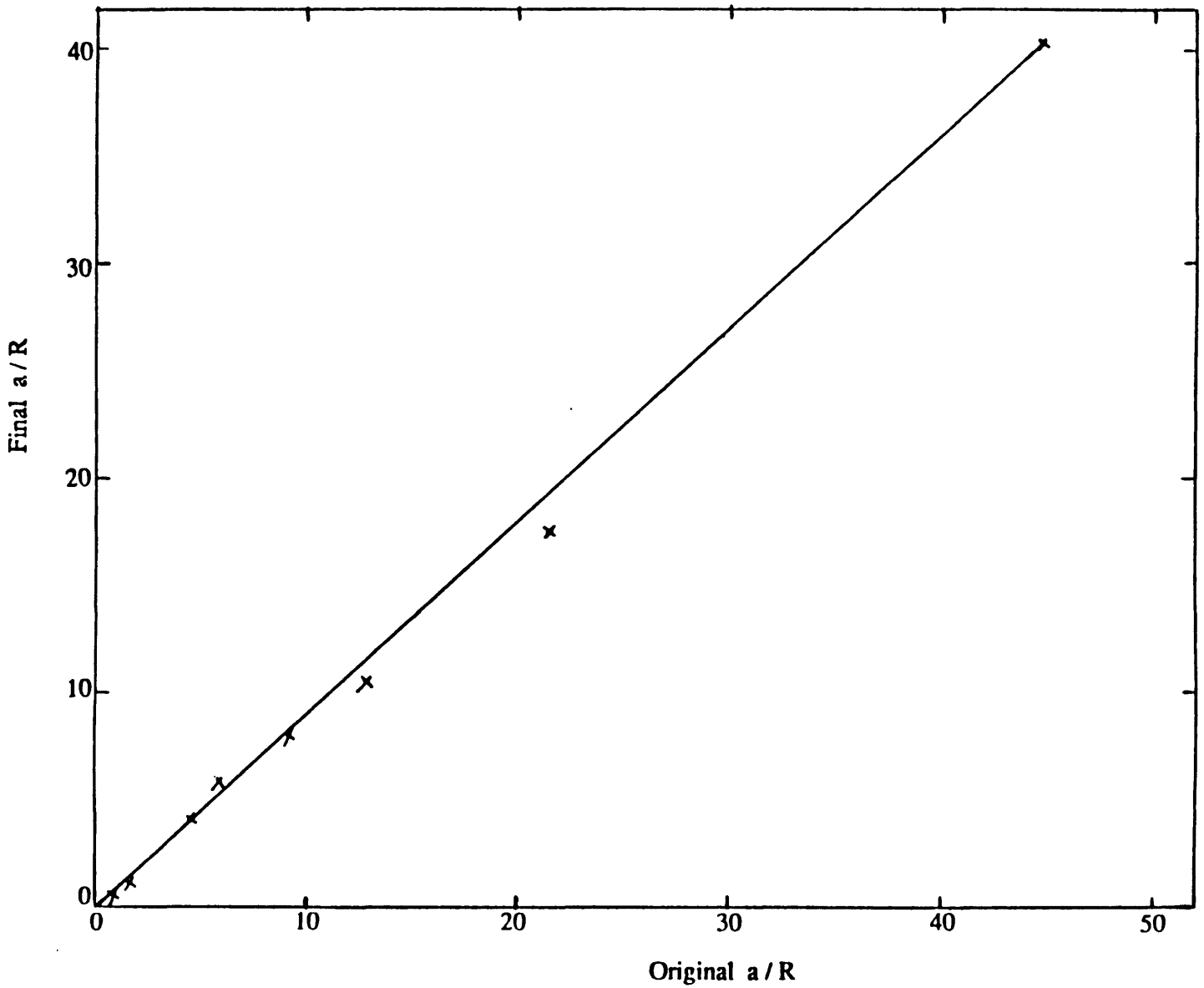


Figure 6.11 · Comparision of final a / R ratio with original a / R ratio

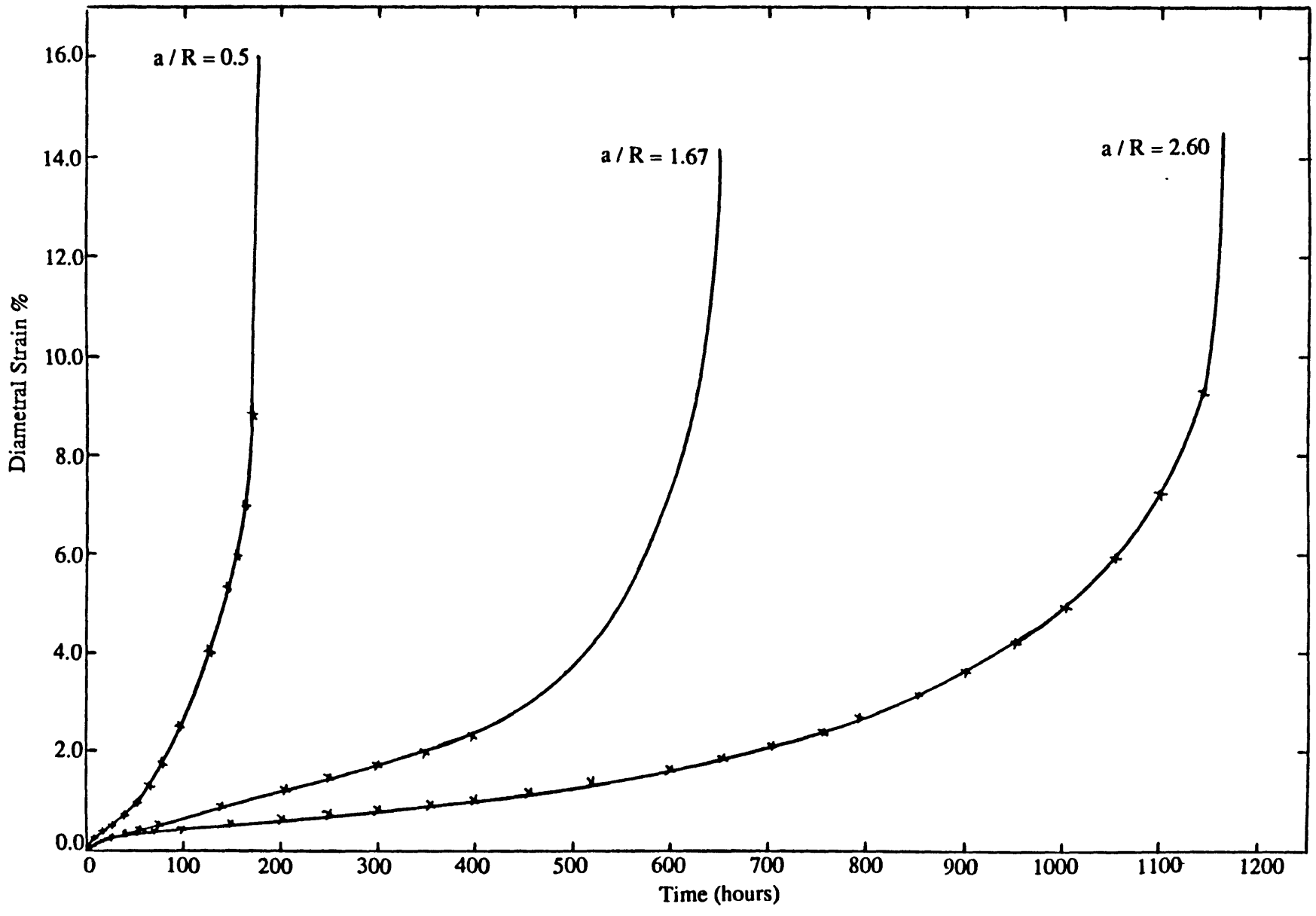


Figure 6.12 : Variation of diametral strain with time for different notch geometries

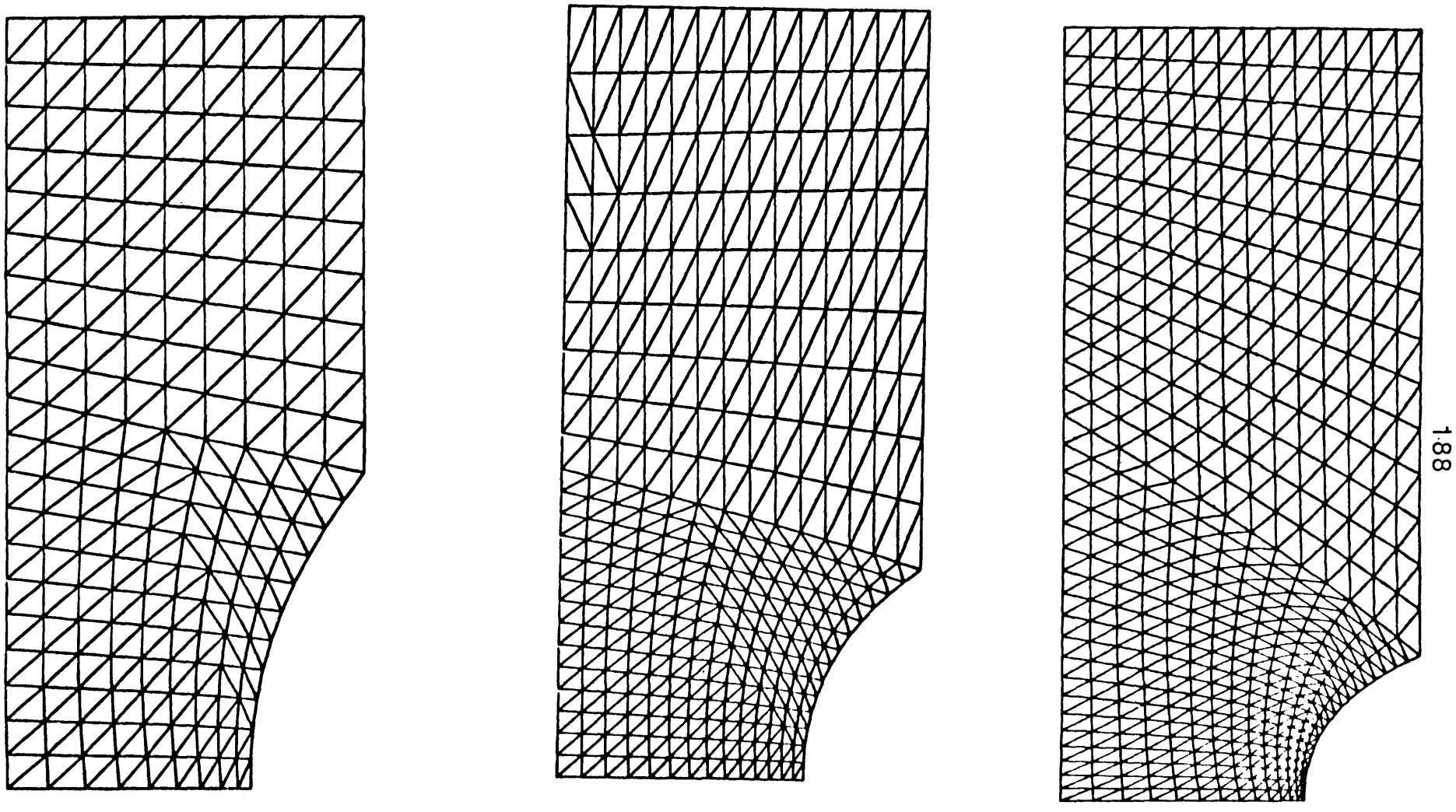
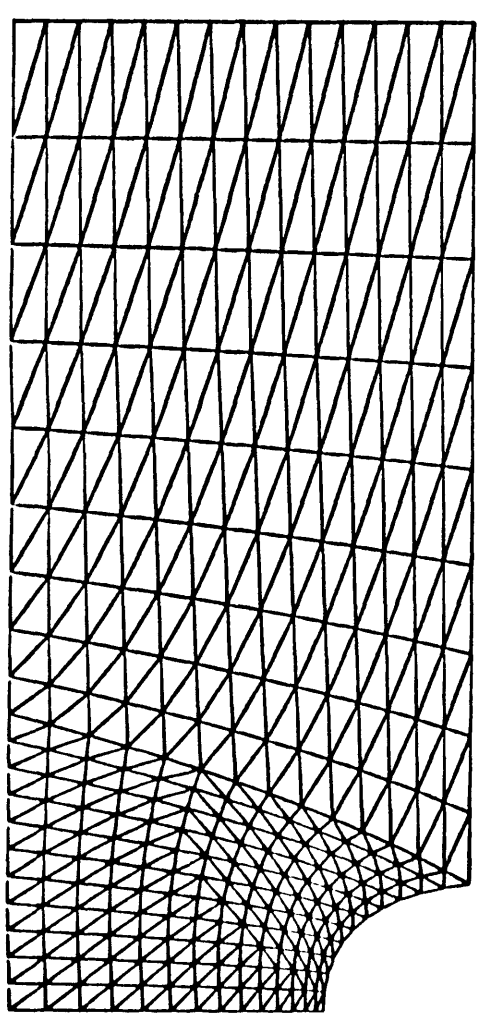
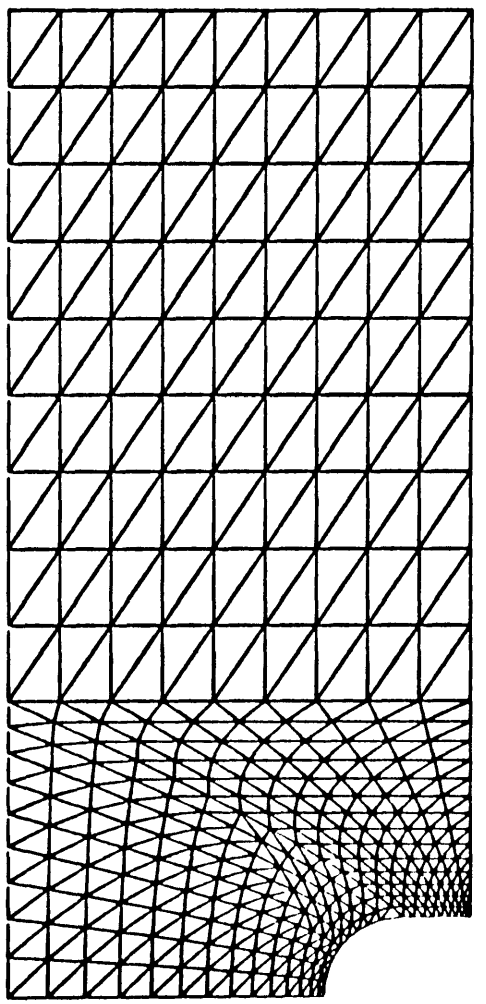


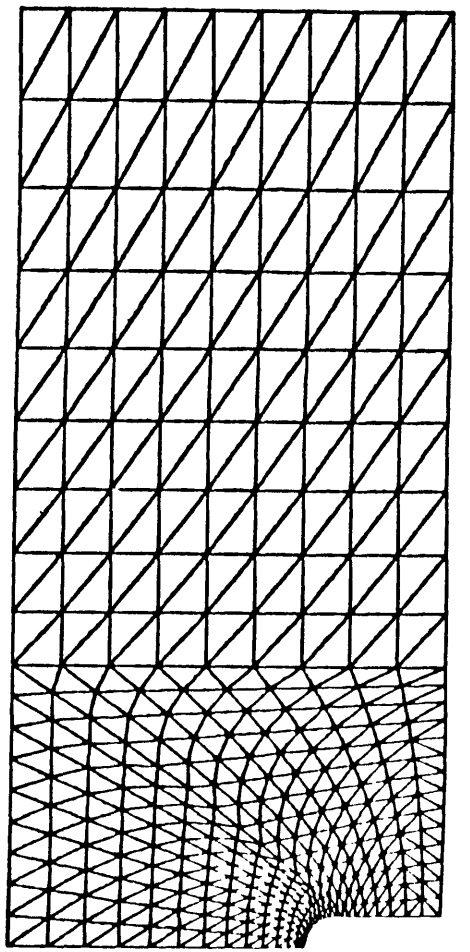
Figure 6.13 a : Finite element mesh for b / a = 1.46, a) a / R = 0.5, b) a / R = 1.0, c) a / R = 1.67



(d)

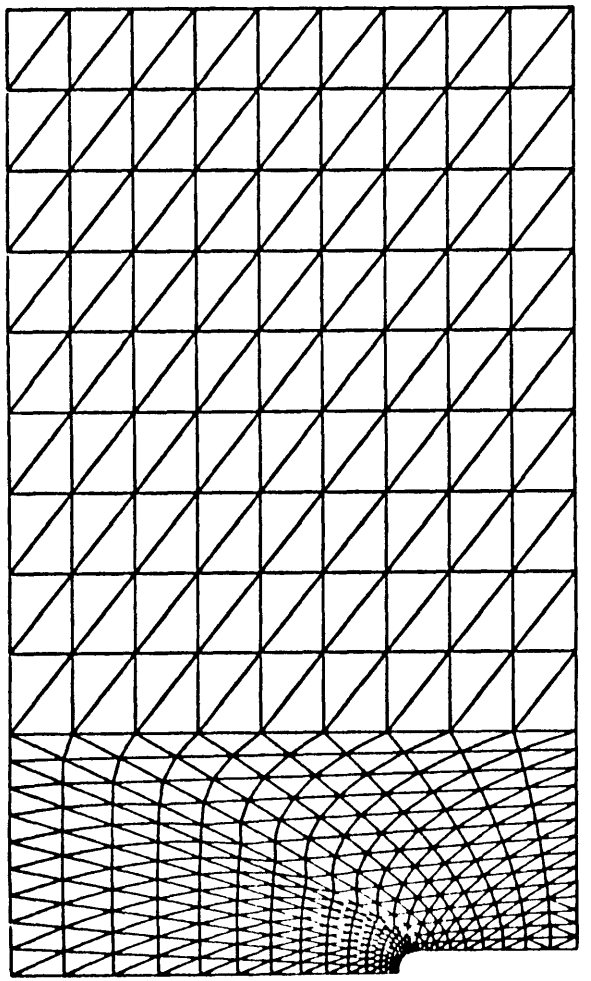


(e)

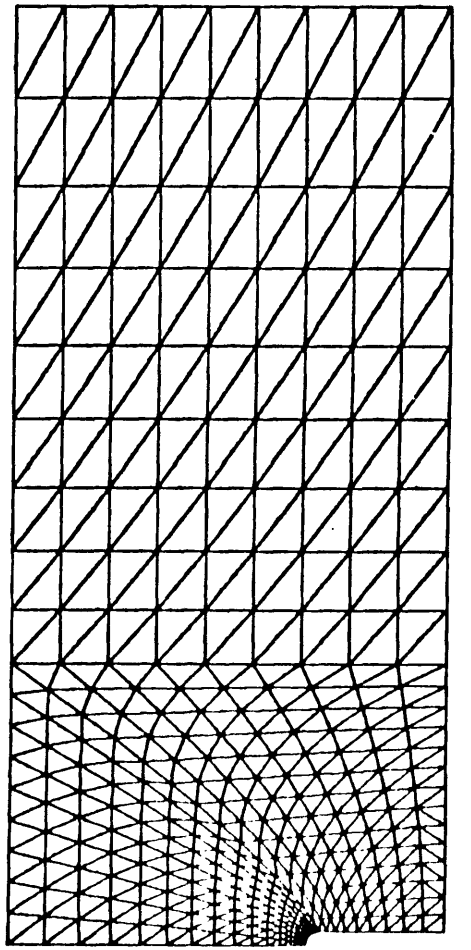


(f)

Figure 6.13 b : Finite element mesh for b / a = 1.46, d) a / R = 2.60, e) a / R = 4.60, f) a / R = 9.30



(g)



(h)

Figure 6.13 c : Finite element mesh for b / a = 1.46, g) a / R = 17.0 , h) a / R = 21.60

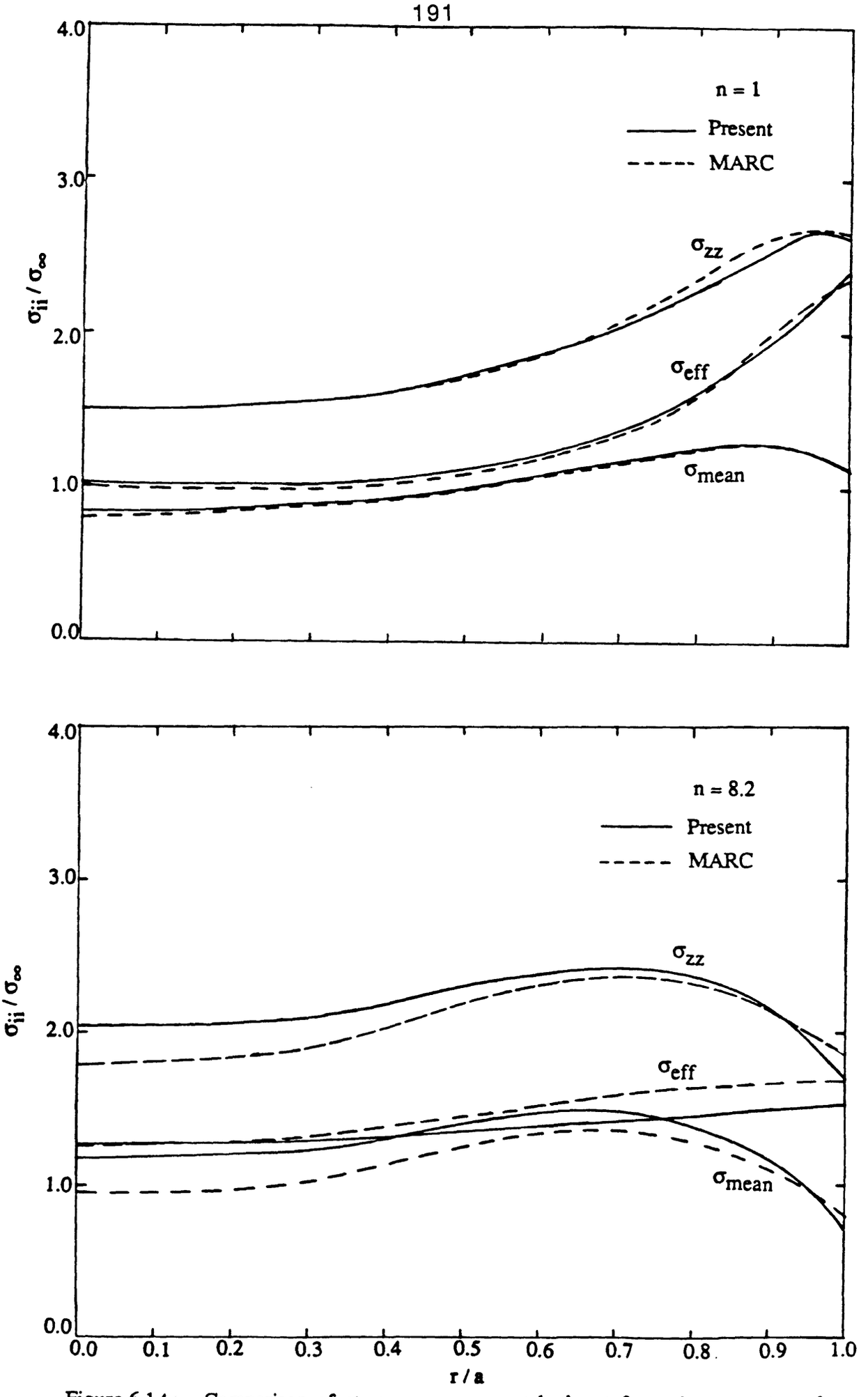


Figure 6.14 : Comparison of stresses across a notch throat from the present work and MARC program b /a = 1.46, a / R = 1.67

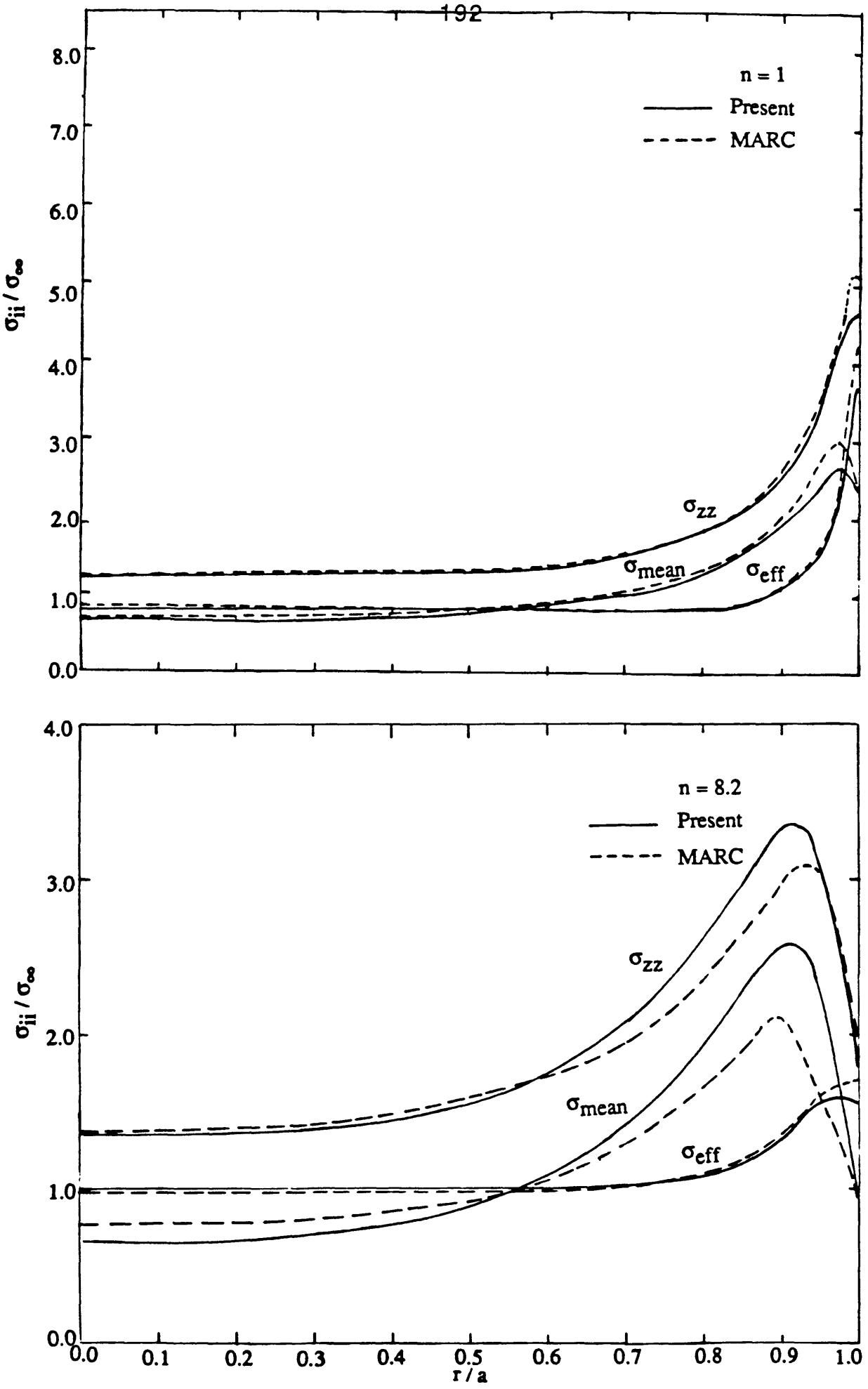


Figure 6.15 : Comparison of stresses across a notch throat from the present work and MARC program b / a = 1.46, a / R = 9.30

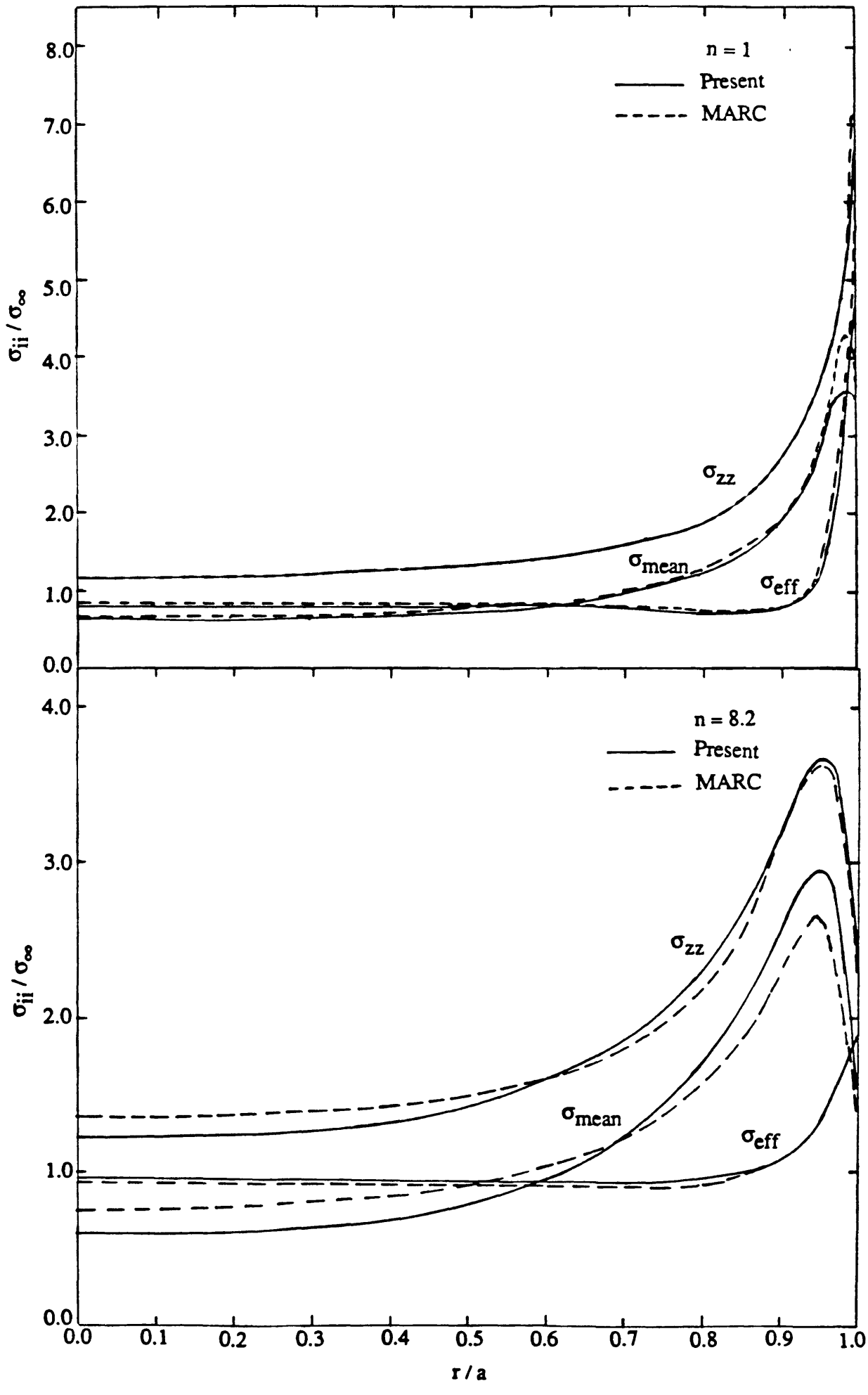


Figure 6.16 : Comparison of stresses across a notch throat from the present work and MARC program b / a = 1.46, a / R = 21.60

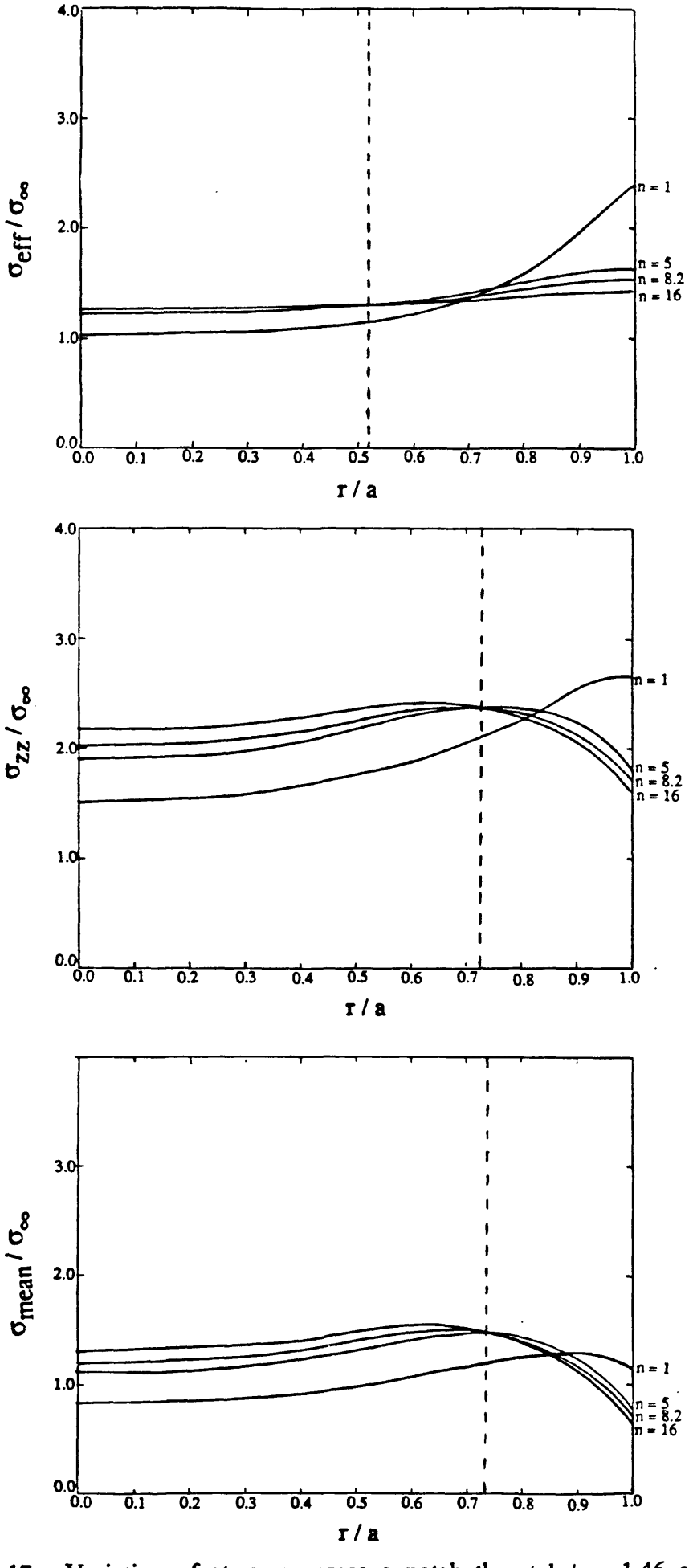


Figure 6.17 : Variation of stresses across a notch throat b / a = 1.46, a / R = 1.67

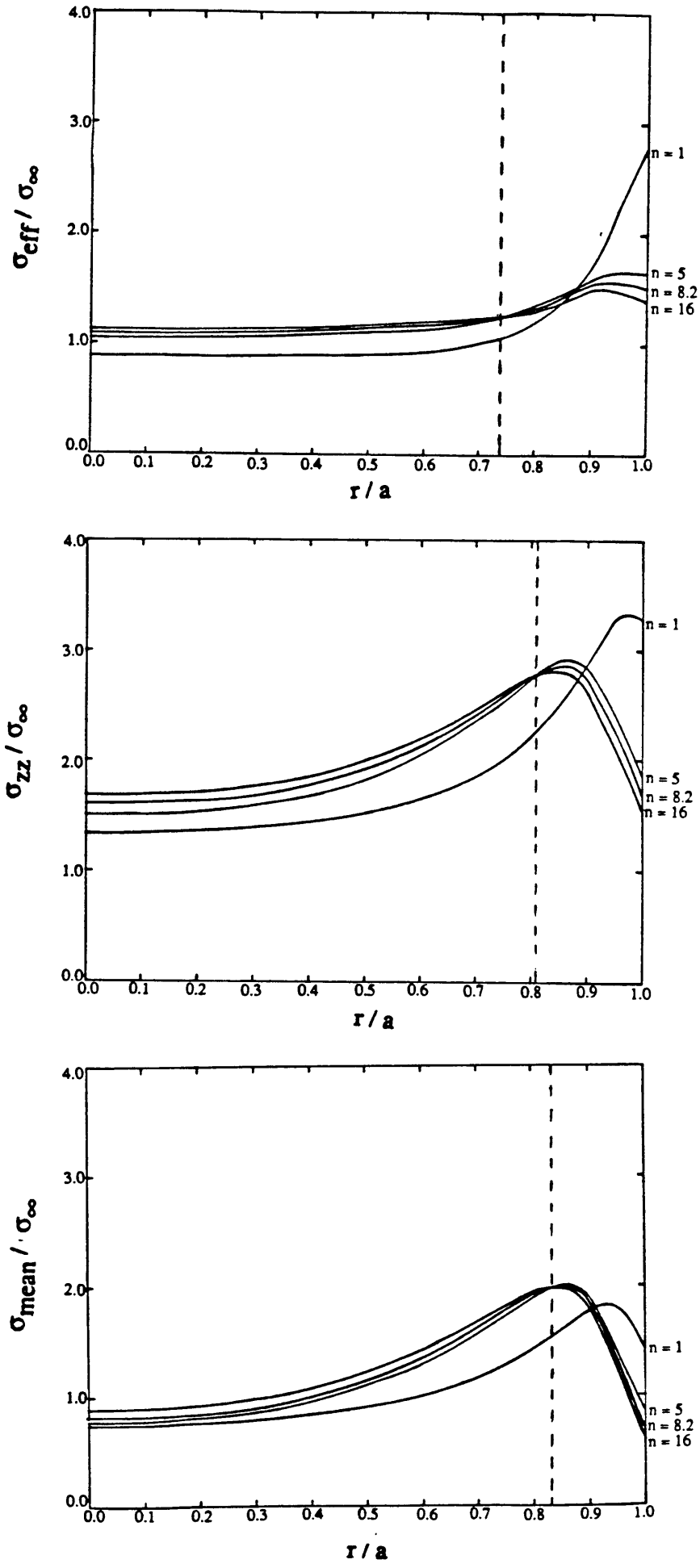


Figure 6.18 : Variation of stresses across a notch throat b / a = 1.46, a / R = 4.60

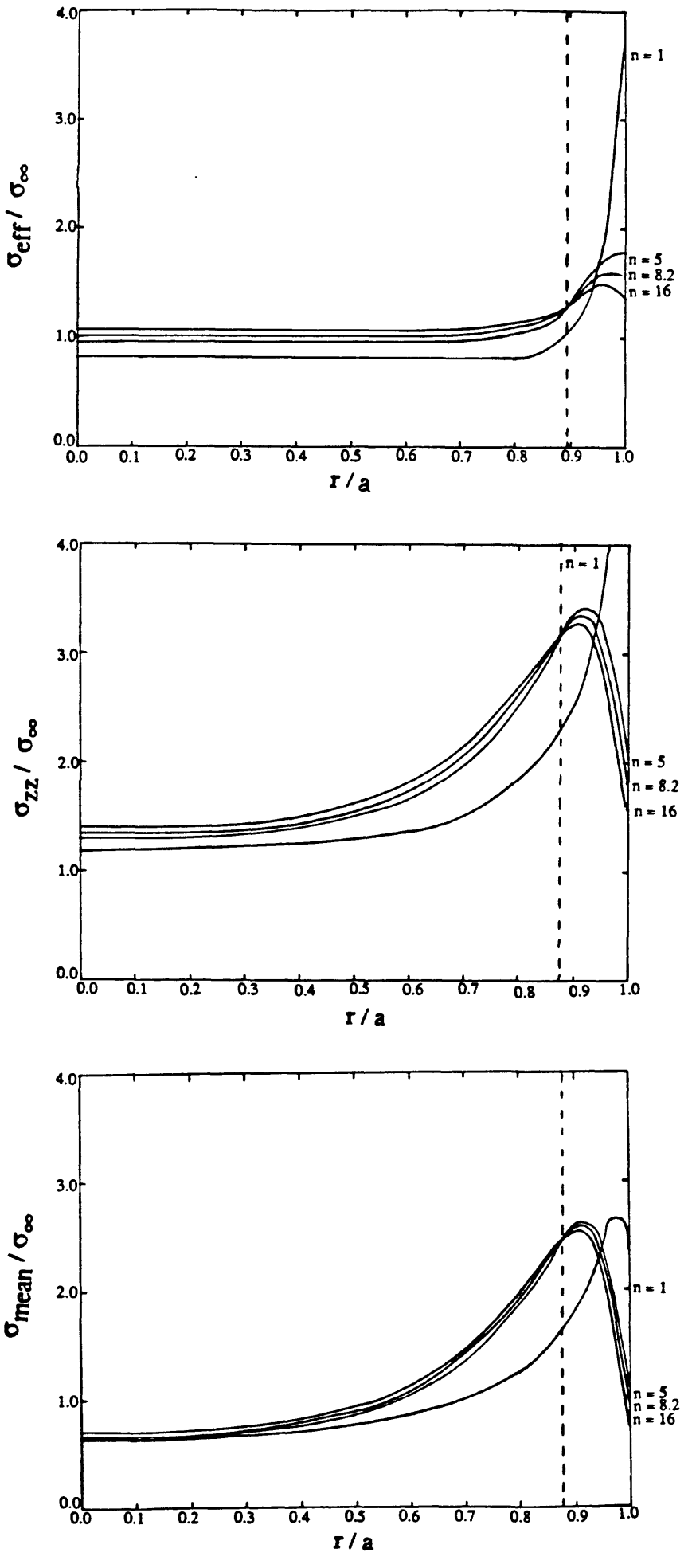


Figure 6.19 : Variation of stresses across a notch throat b / a = 1.46, a / R = 9.30

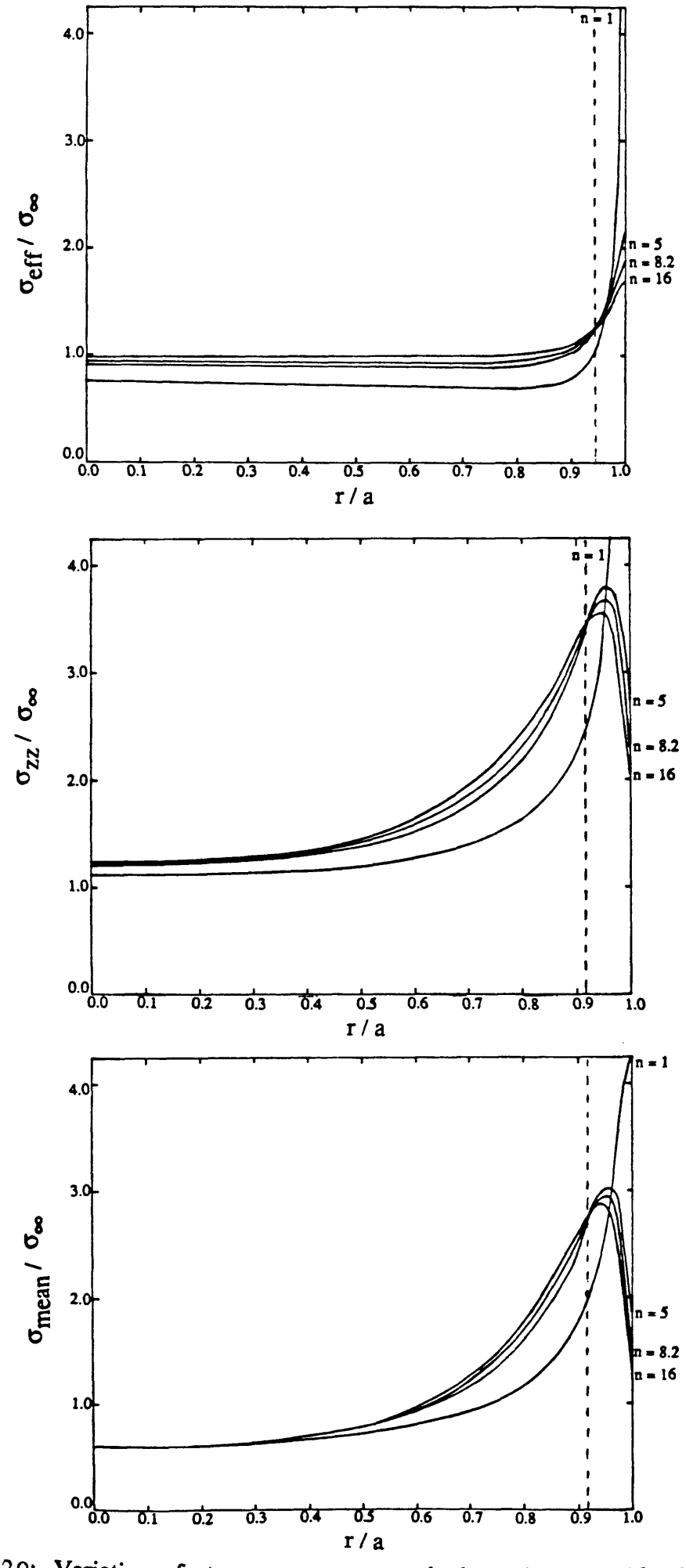


Figure 6.20: Variation of stresses across a notch throat b / a = 1.46, a / R = 21.60

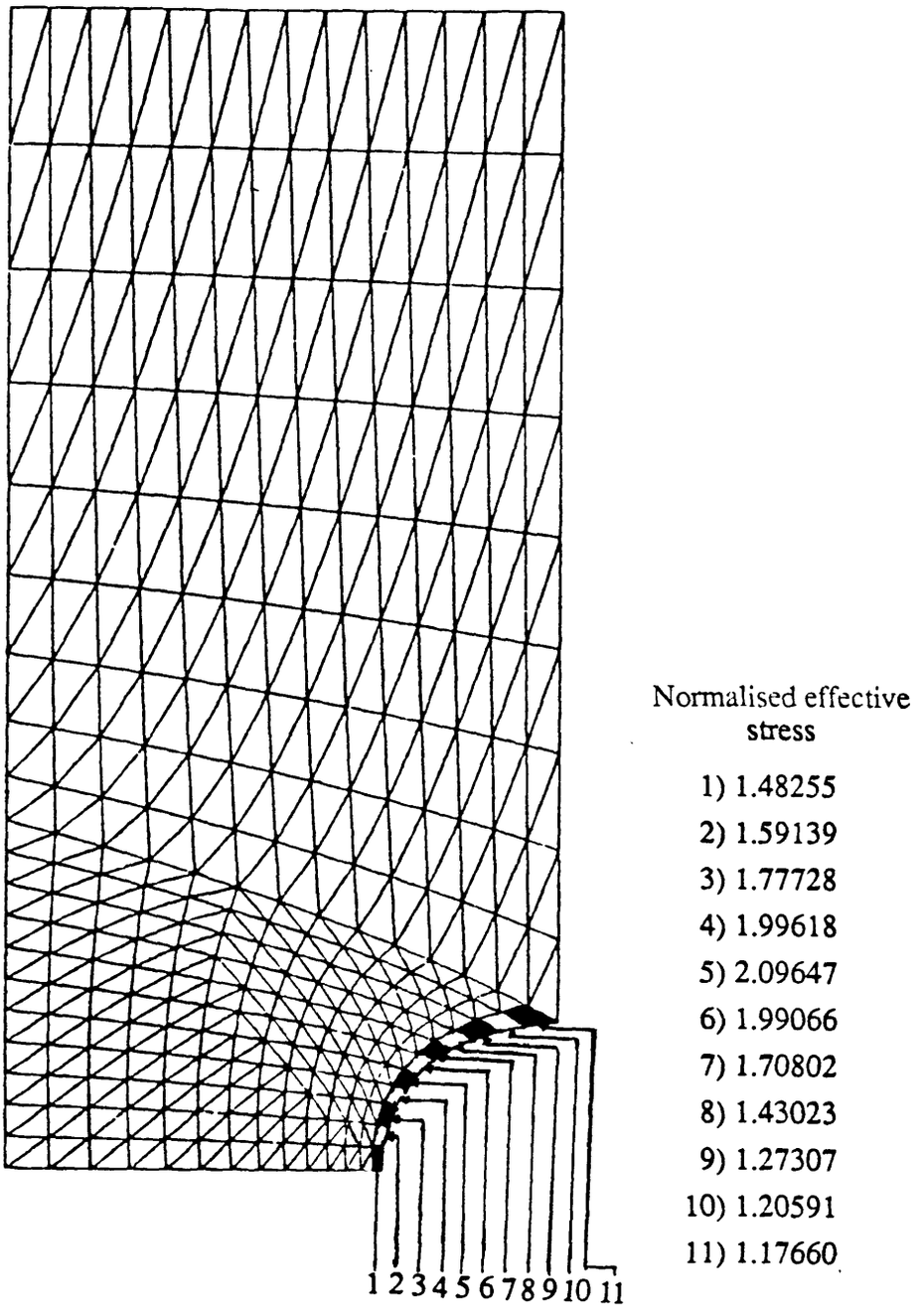


Figure 6.21 : Variation of normalised effective stress along the notch profile for $n = 8.2$, $b / a = 1.46$, $a / R = 2.60$

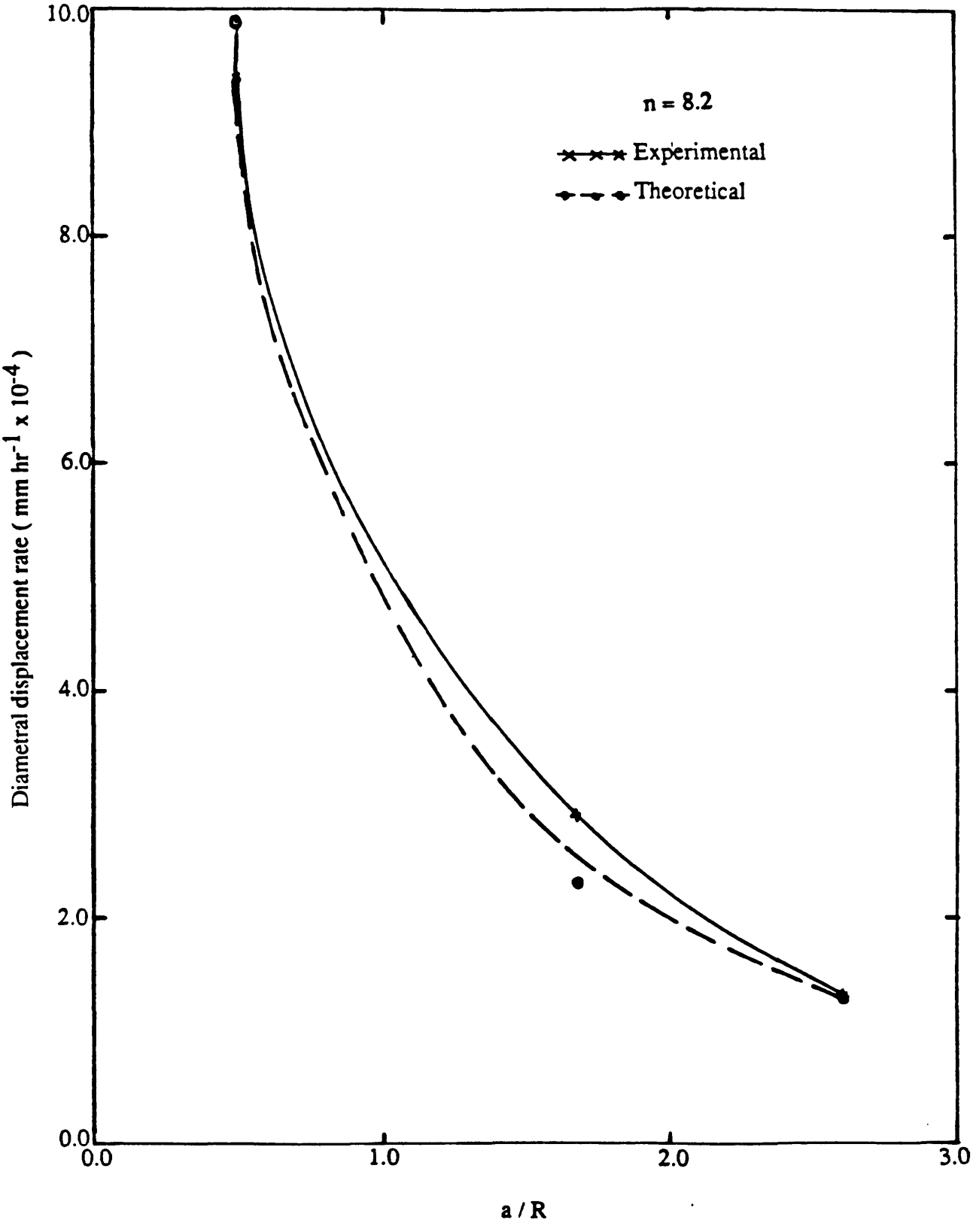


Figure 6.22 : Comparison of theoretical and experimental diametral displacement rate

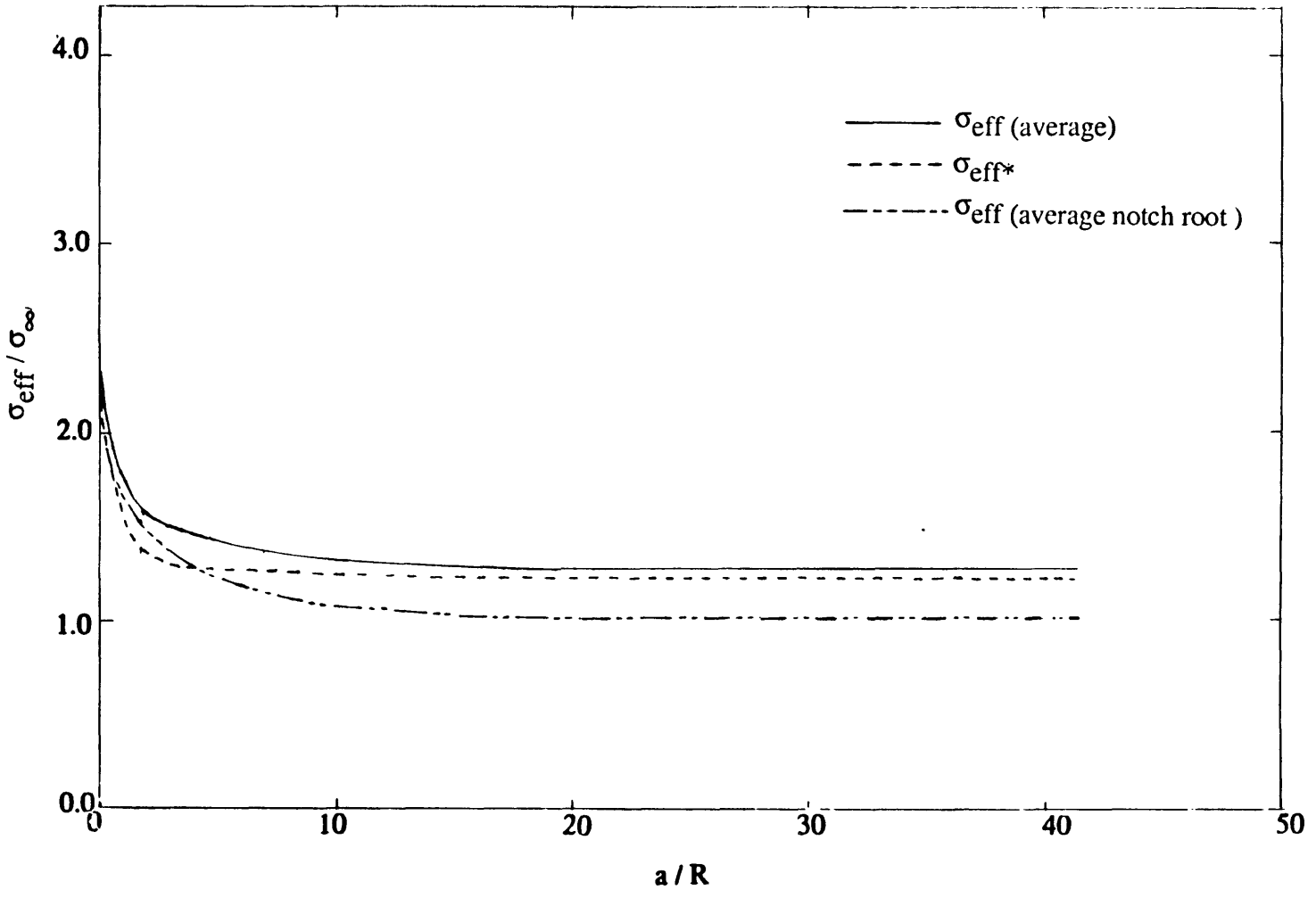


Figure 6.23 : Comparison of maximum average effective stress away from the notch root with the effective stress at the skeletal point and the average effective stress in the notch root plane

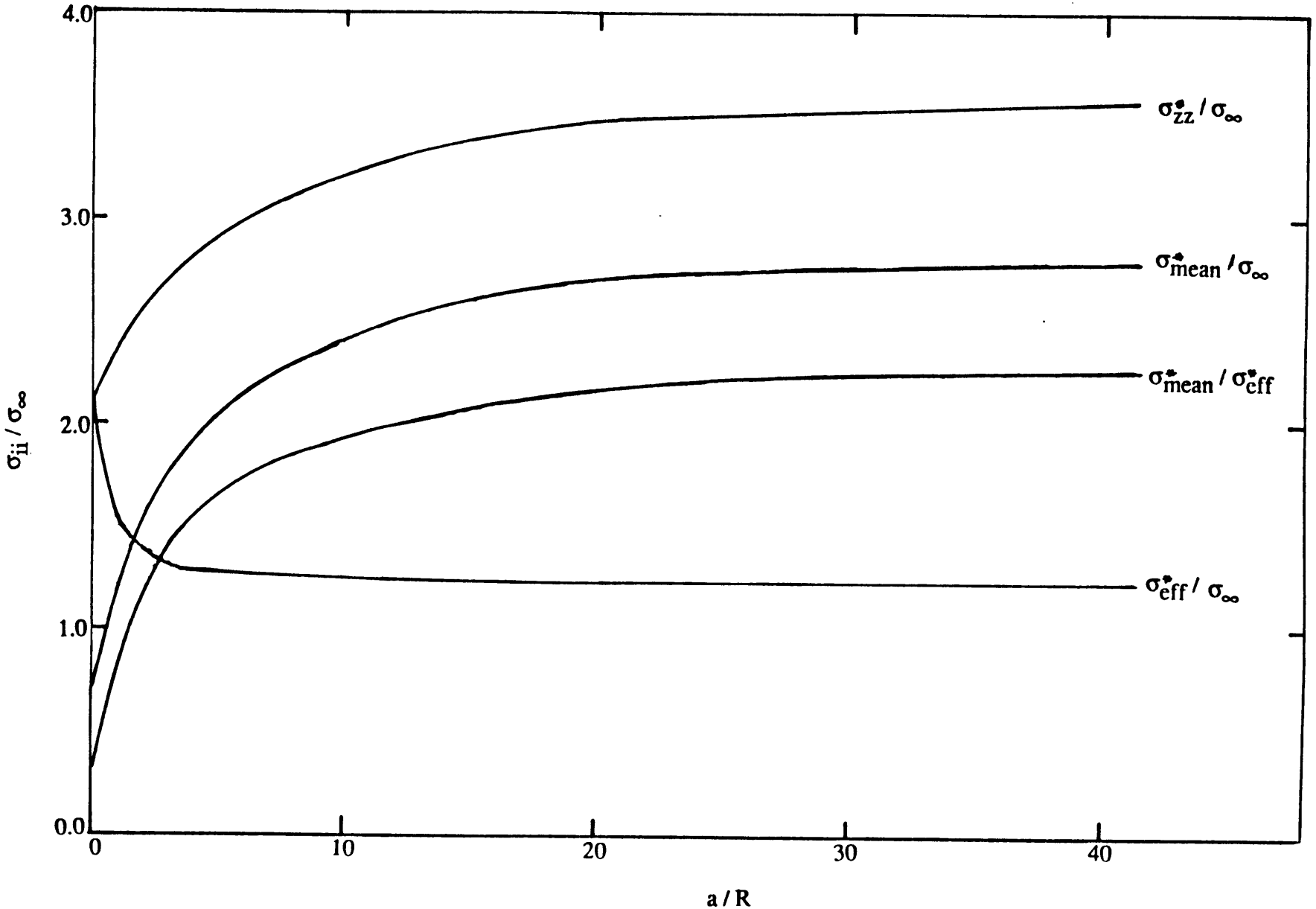


Figure 6.24 : Variation of stresses at a skeletal point across a notch throat

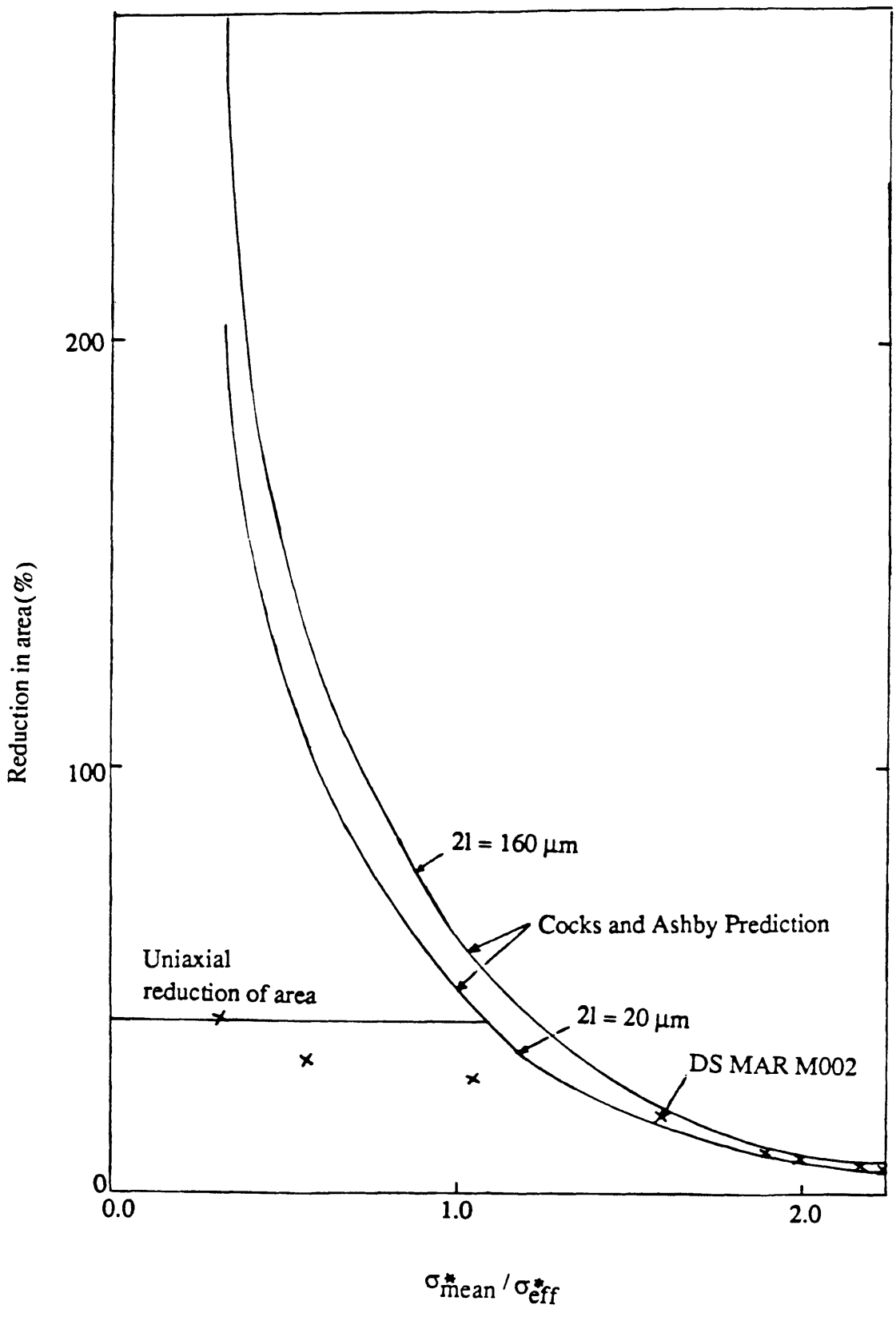


Figure 6.25: Comparison of multiaxial reduction in area with predicted reduction of area

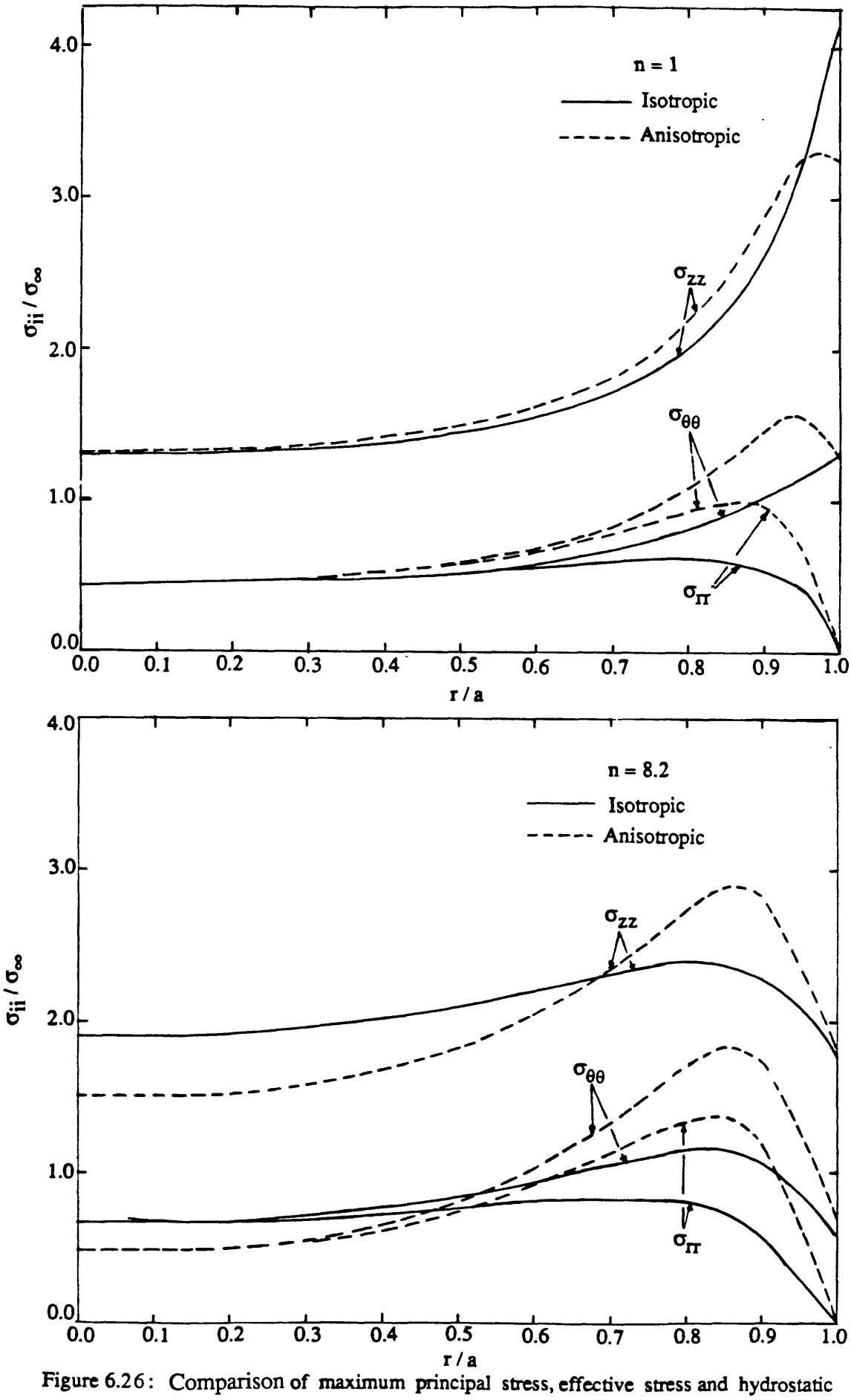


Figure 6.26: Comparison of maximum principal stress, effective stress and hydrostatic stress in an Isotropic and Anisotropic analysis b / a = 1.46, a / R = 1.67

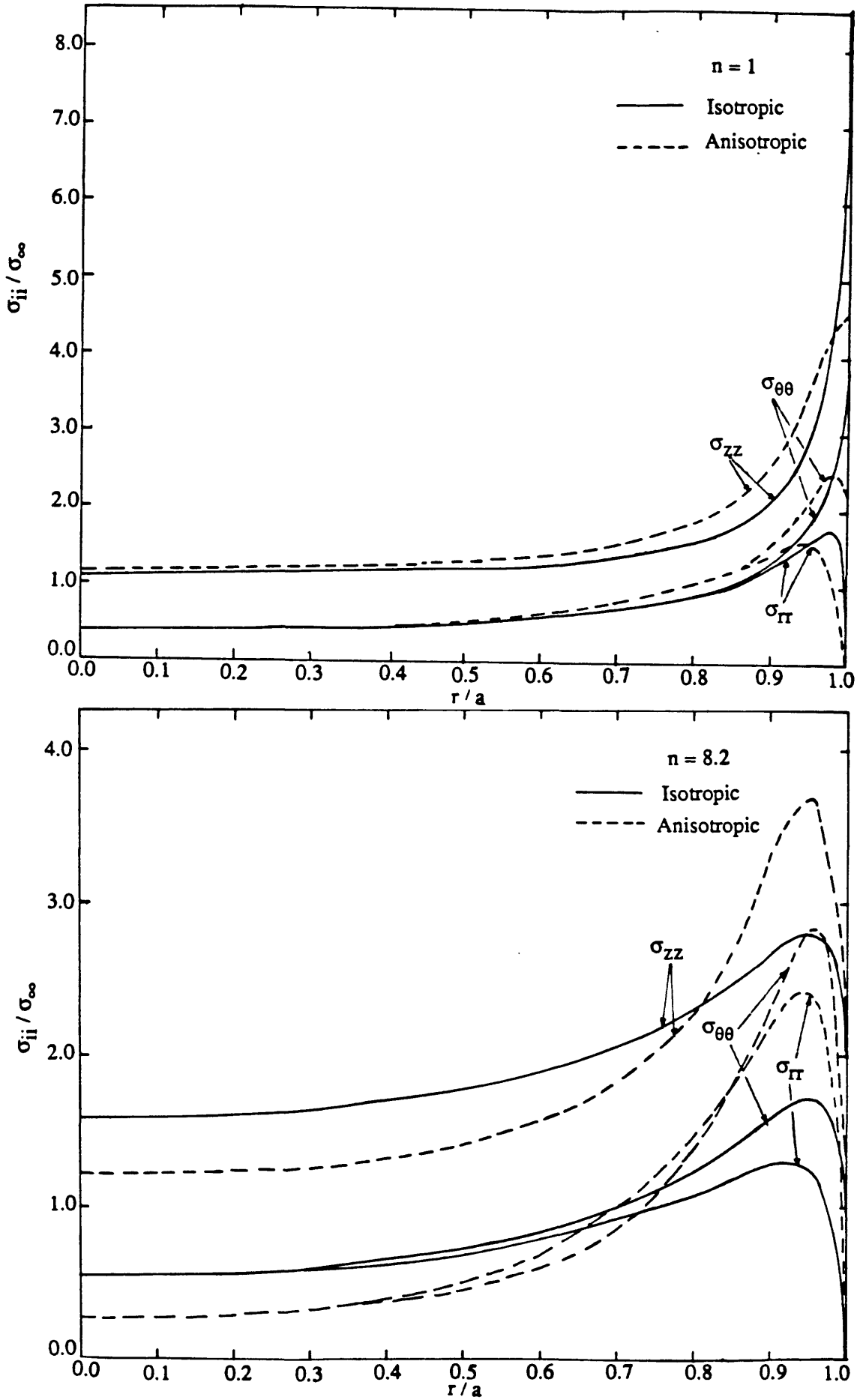


Figure 6.27 : Comparison of maximum principal stress, effective stress and hydrostatic stress in an Isotropic and Anisotropic analysis b / a = 1.46, a / R = 21.60

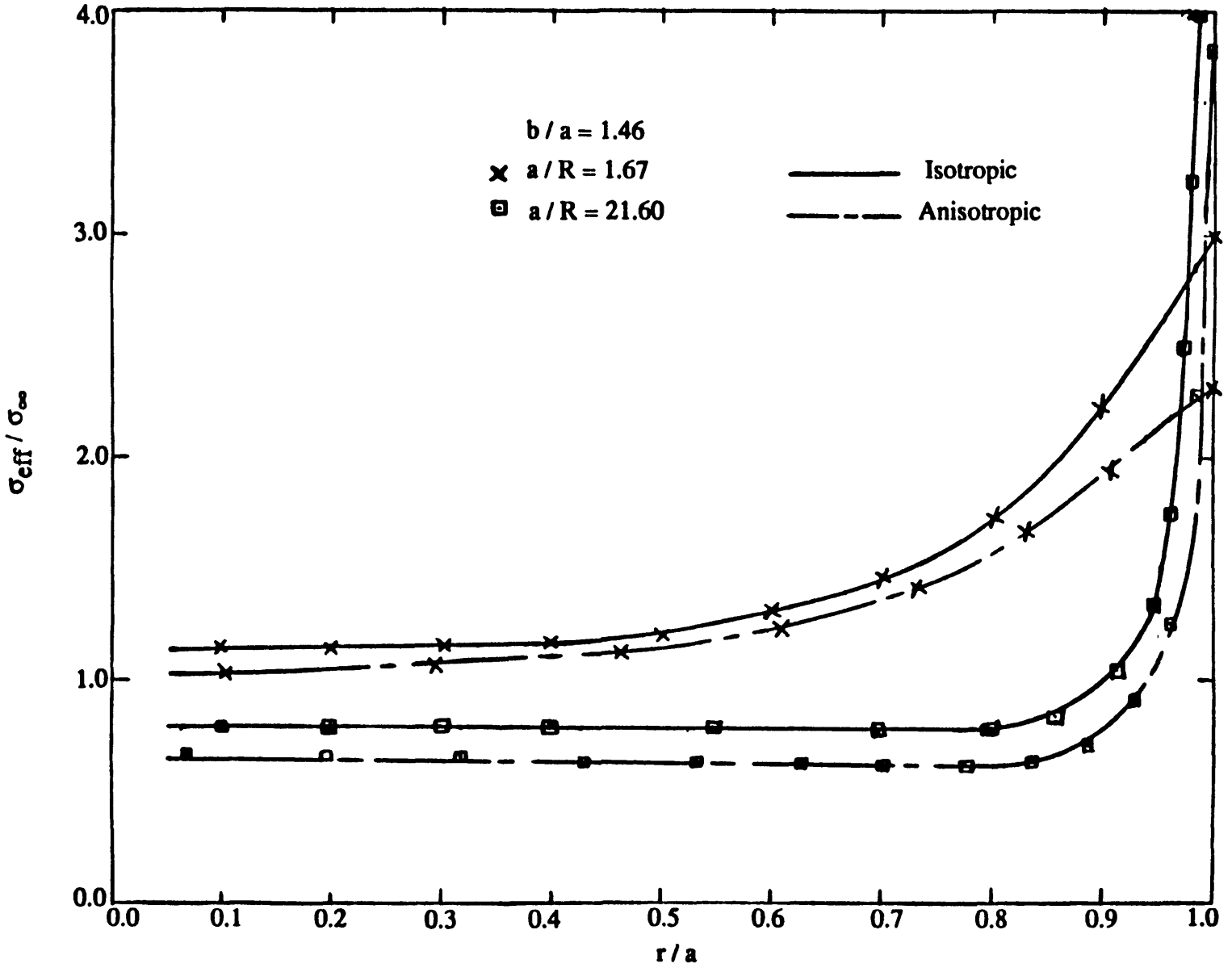


Figure 6.28 : Comparison of Isotropic and Anisotropic effective stress across a notch throat for n = 1

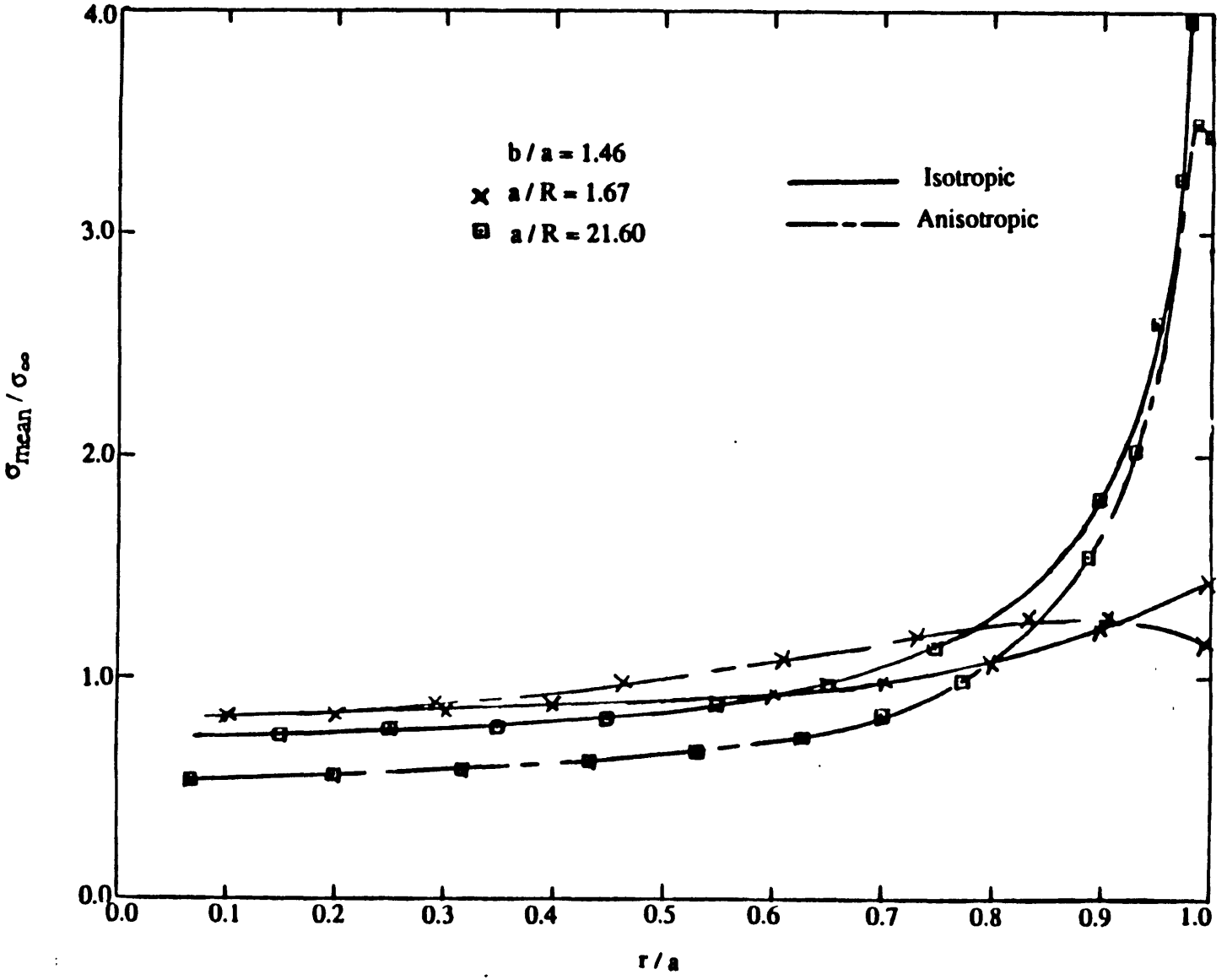


Figure 6.29 : Comparison of Isotropic and Anisotropic hydrostatic stress across a notch throat for n = 1

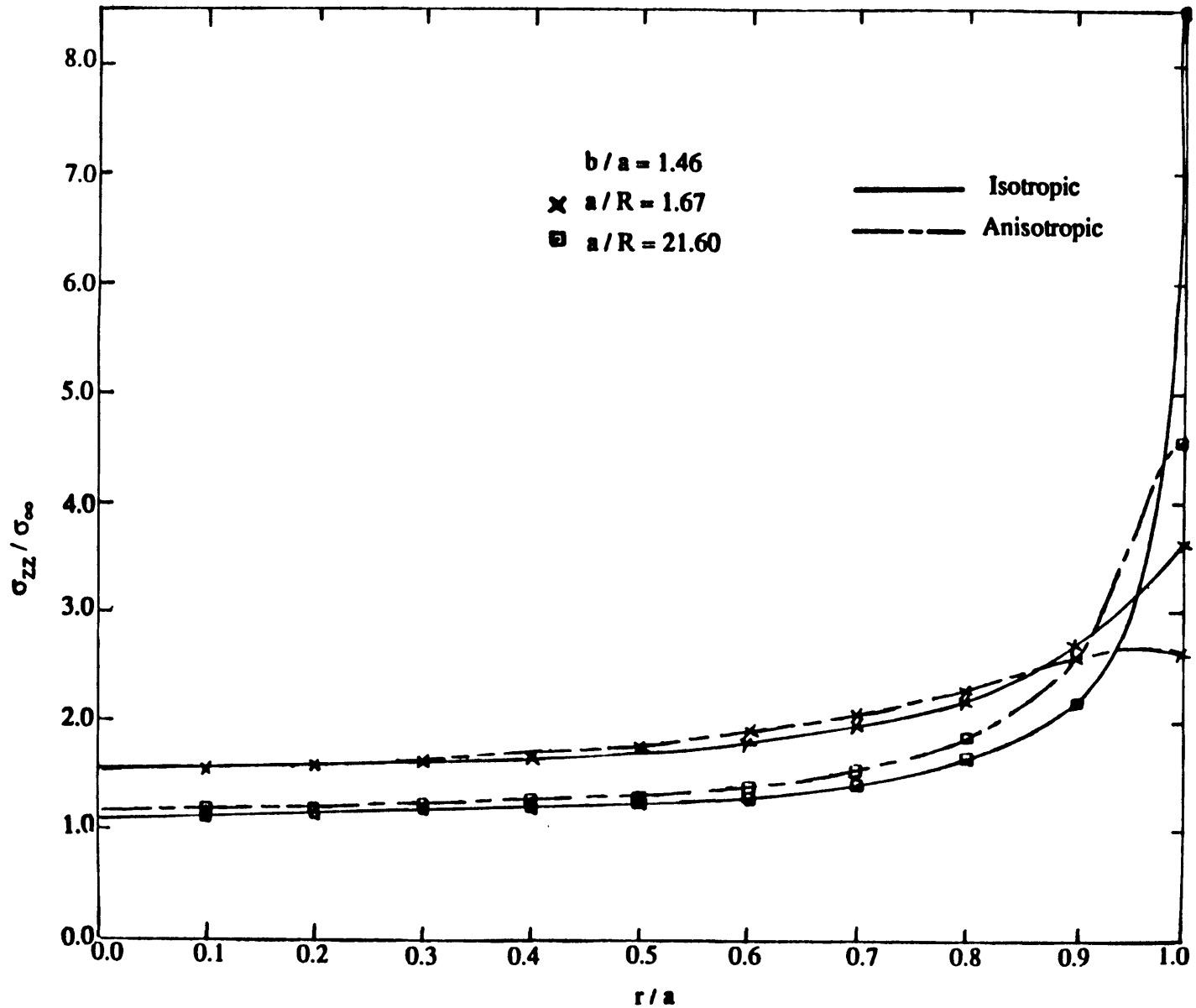


Figure 6.30 : Comparison of Isotropic and Anisotropic maximum principal stress across a notch throat for n = 1

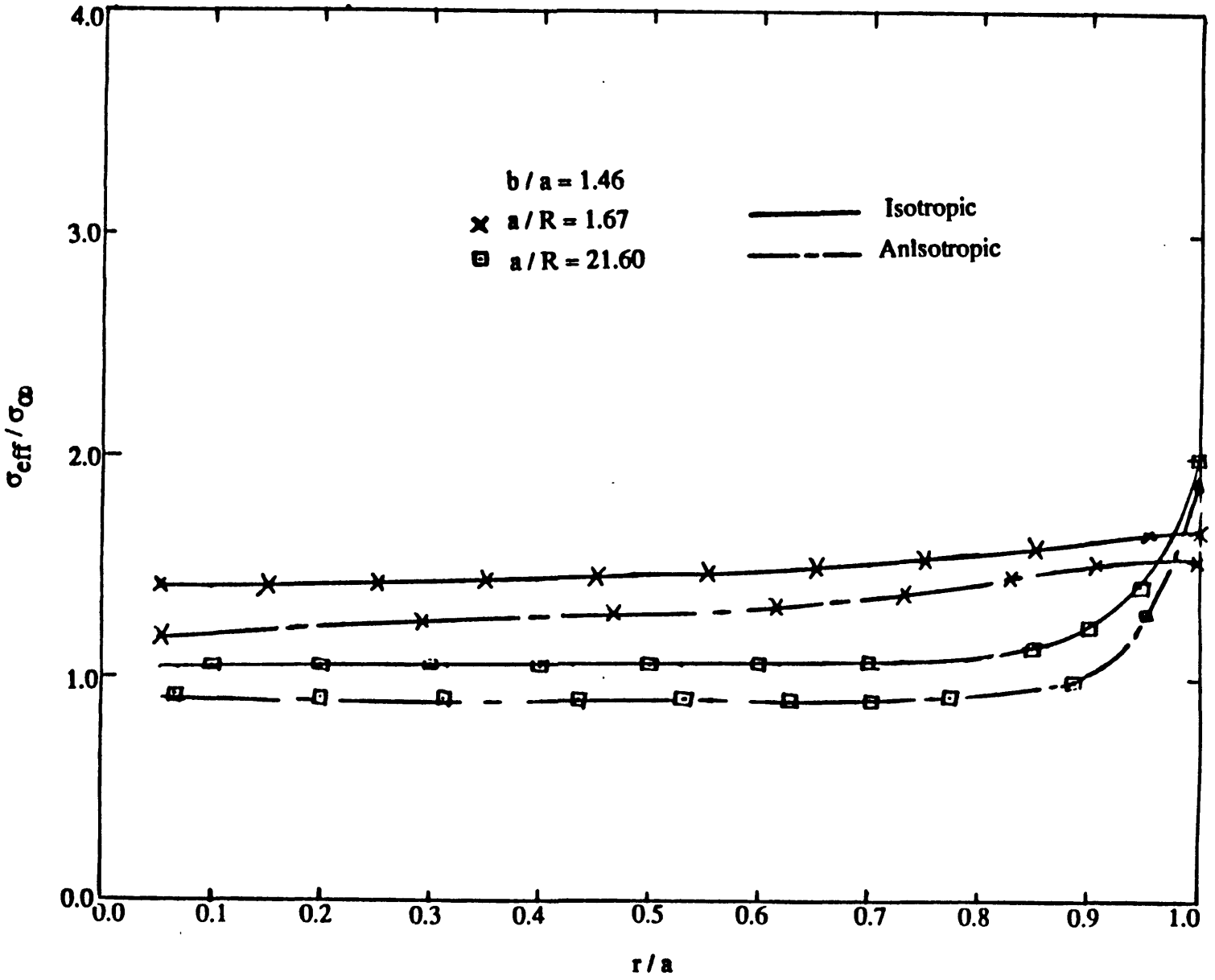


Figure 6.31 : Comparison of Isotropic and Anisotropic effective stress across a notch throat for n = 8.2

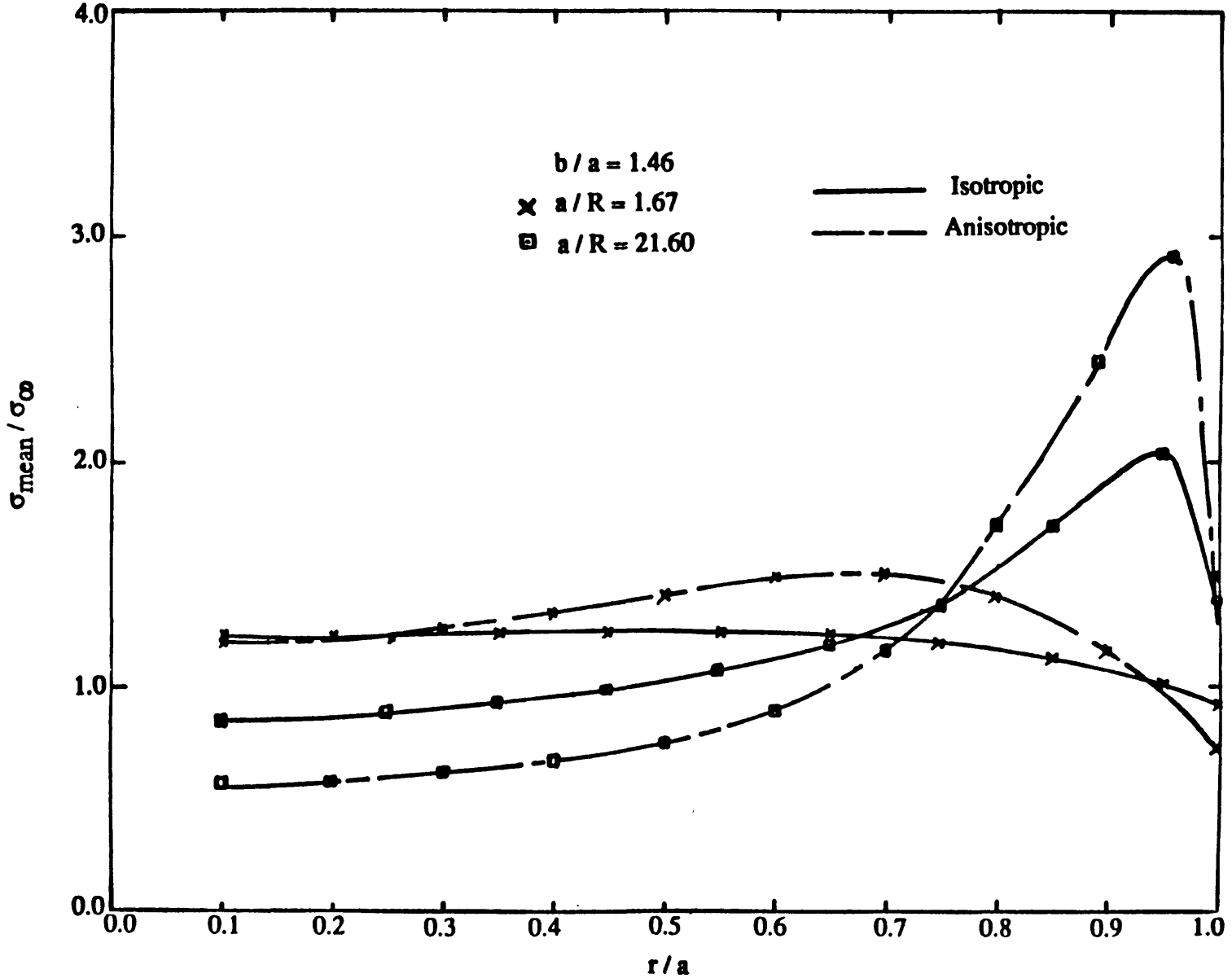


Figure - 6.32 : Comparison of isotropic and anisotropic hydrostatic stress across a notch throat for n = 8.2

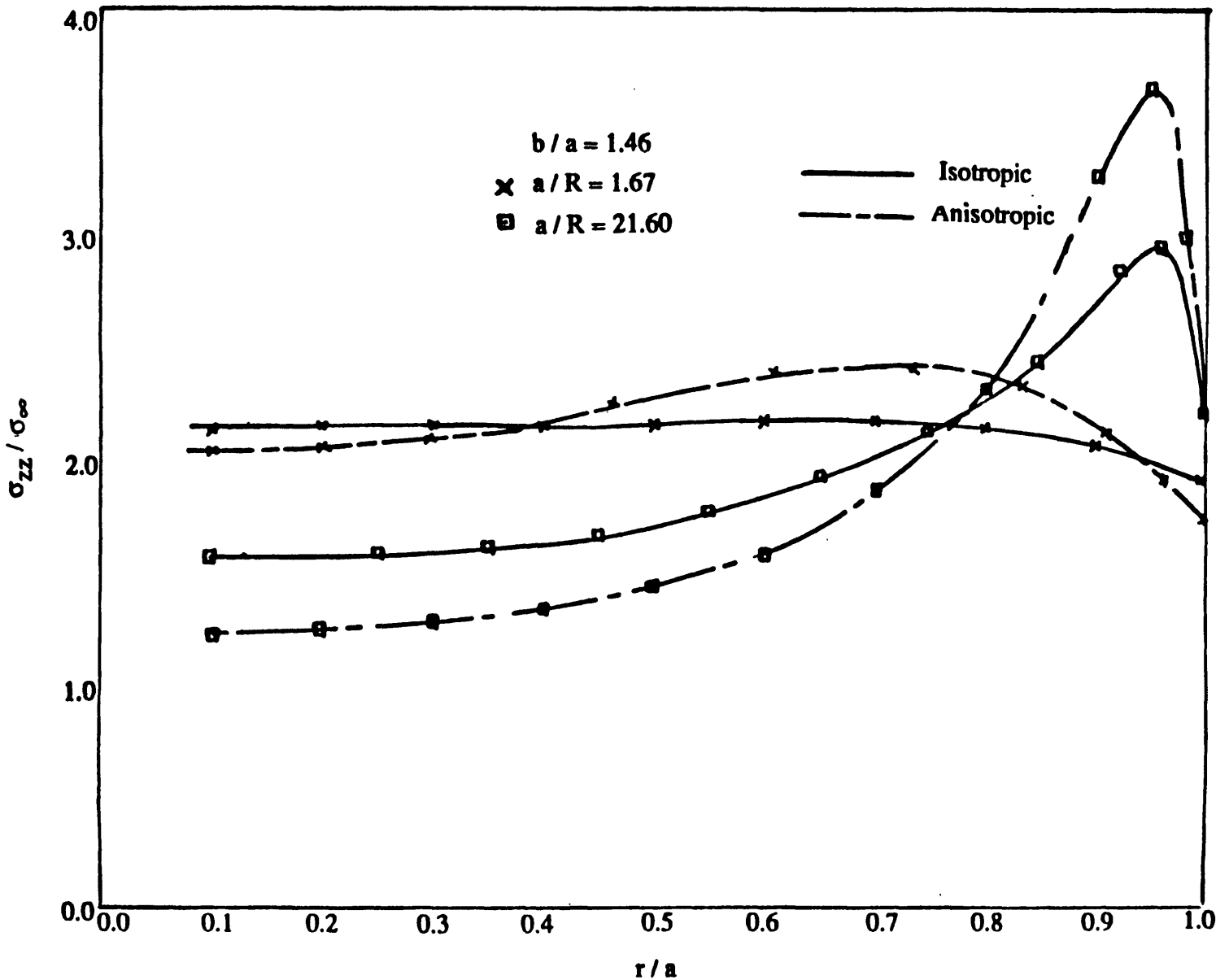


Figure 6.33 : Comparison of Isotropic and Anisotropic maximum principal stress across a notch throat for n = 8.2

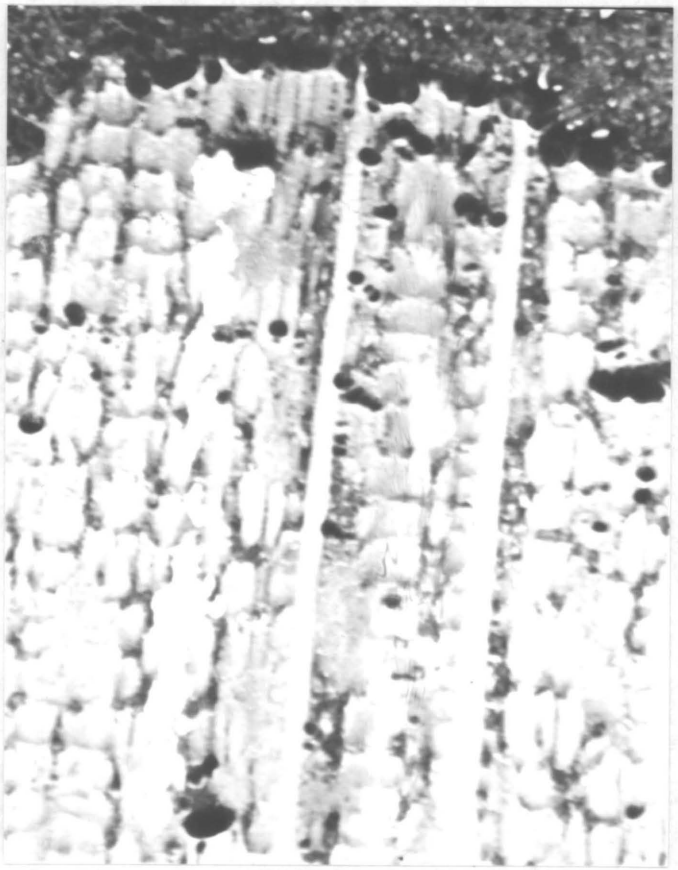




Figure 6.34 : Fracture of a plain specimen





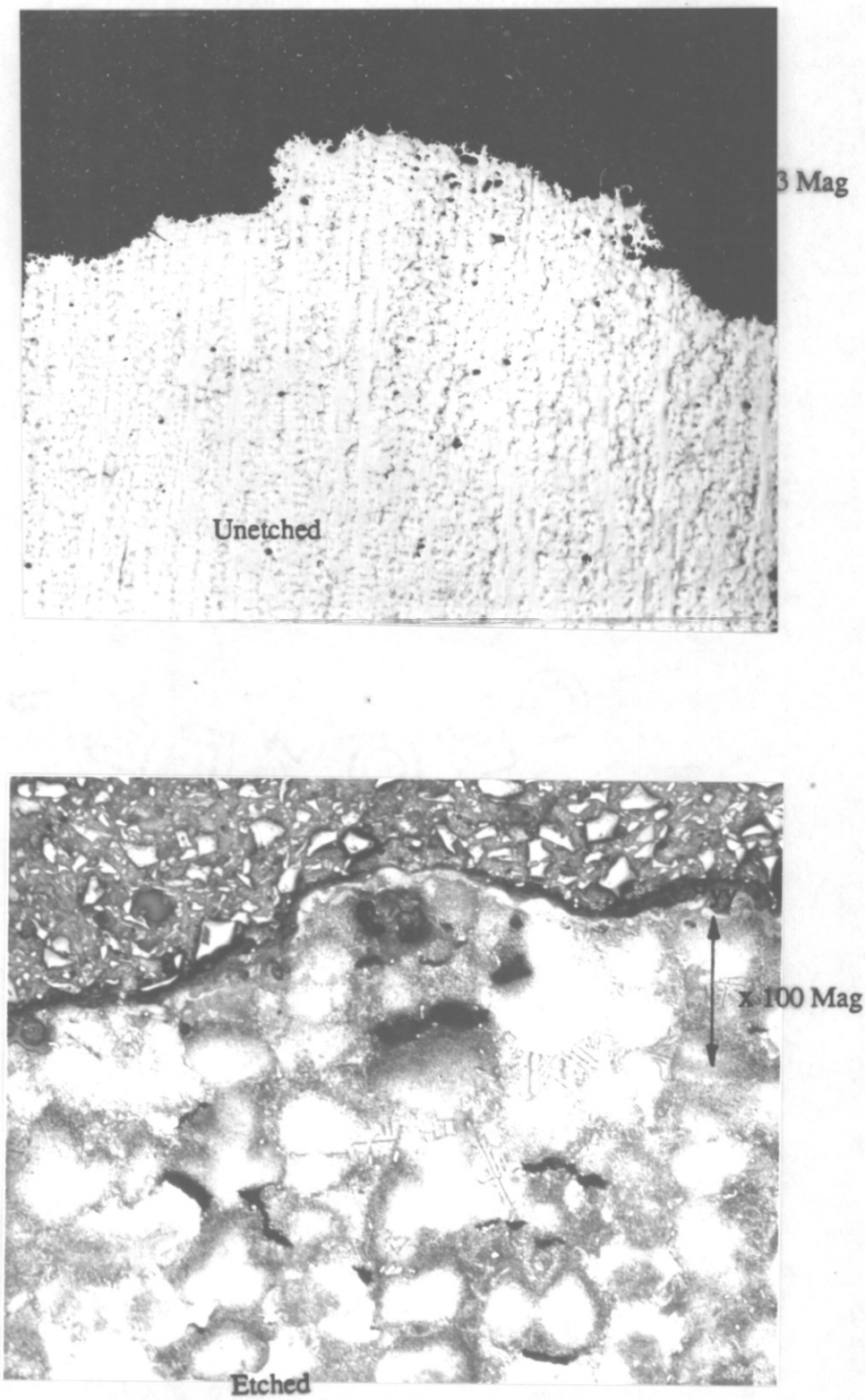
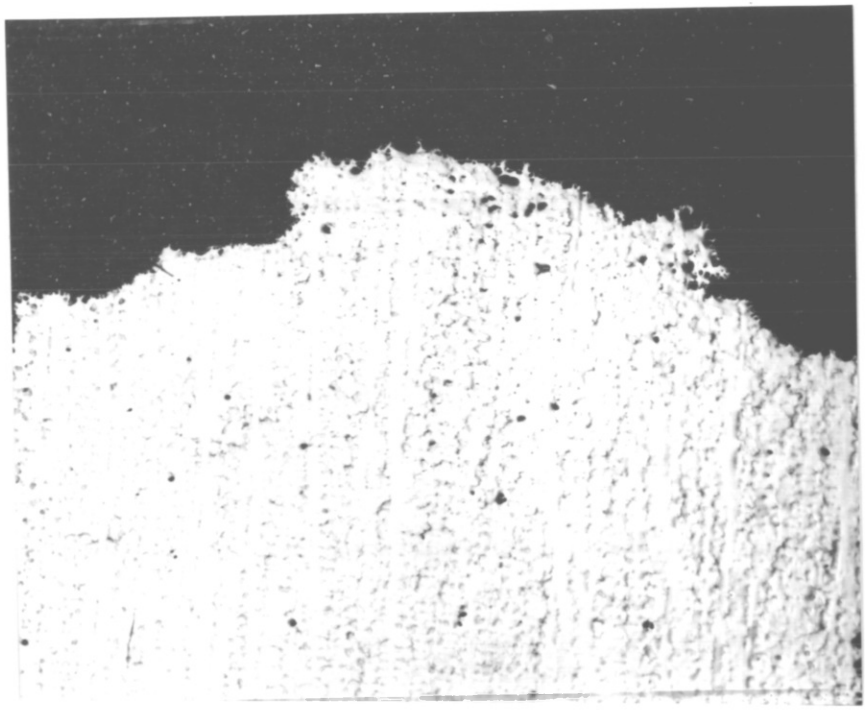
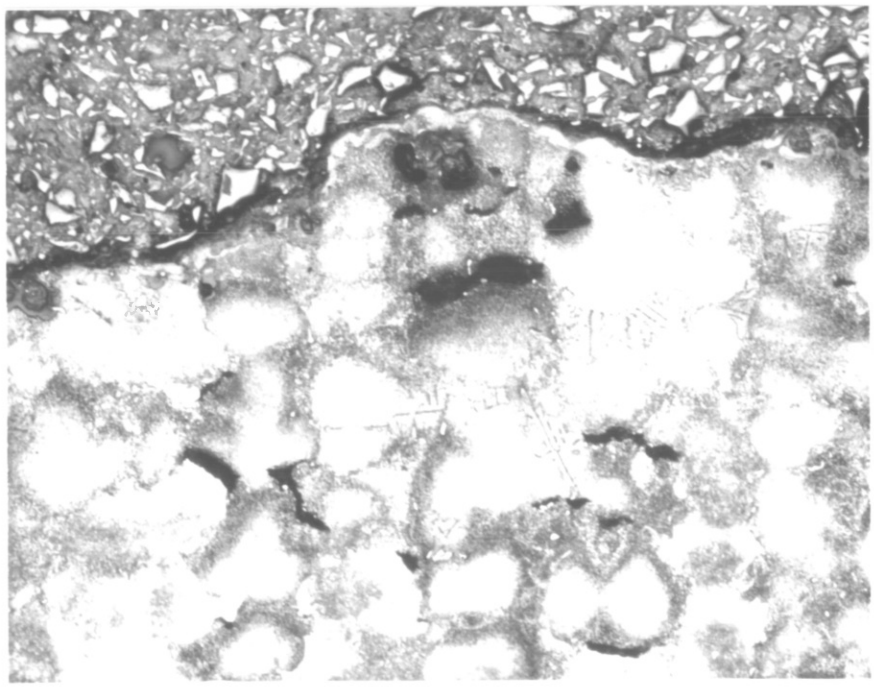
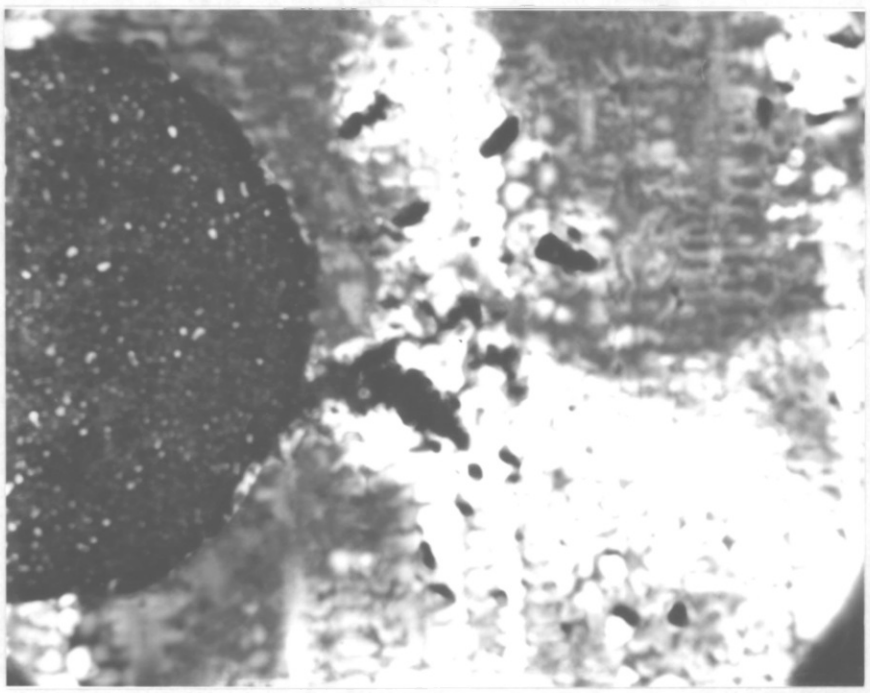


Figure 6.35 : Damage in broken notch b / a = 1.46, a / R = 4.60







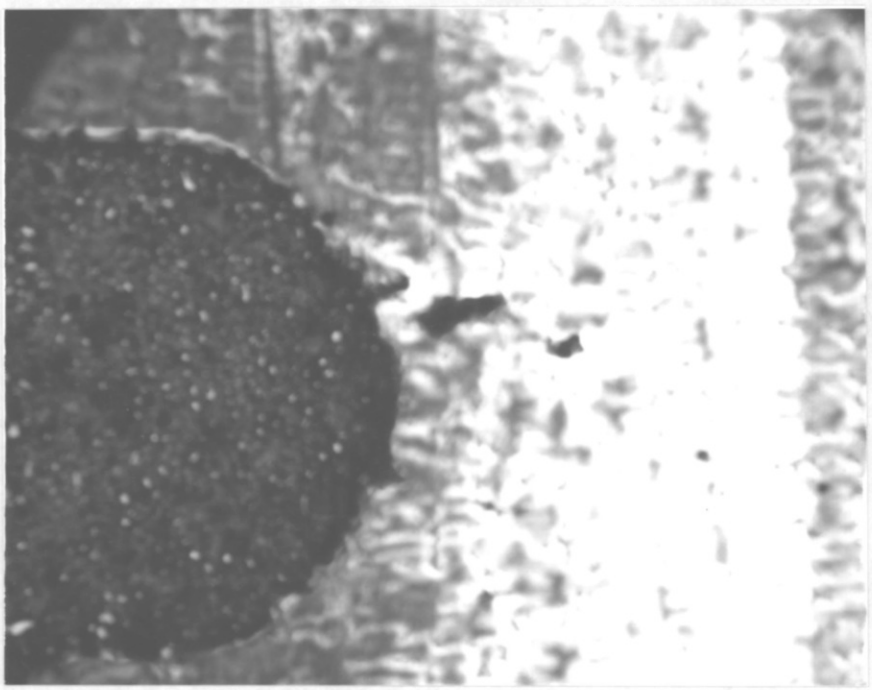
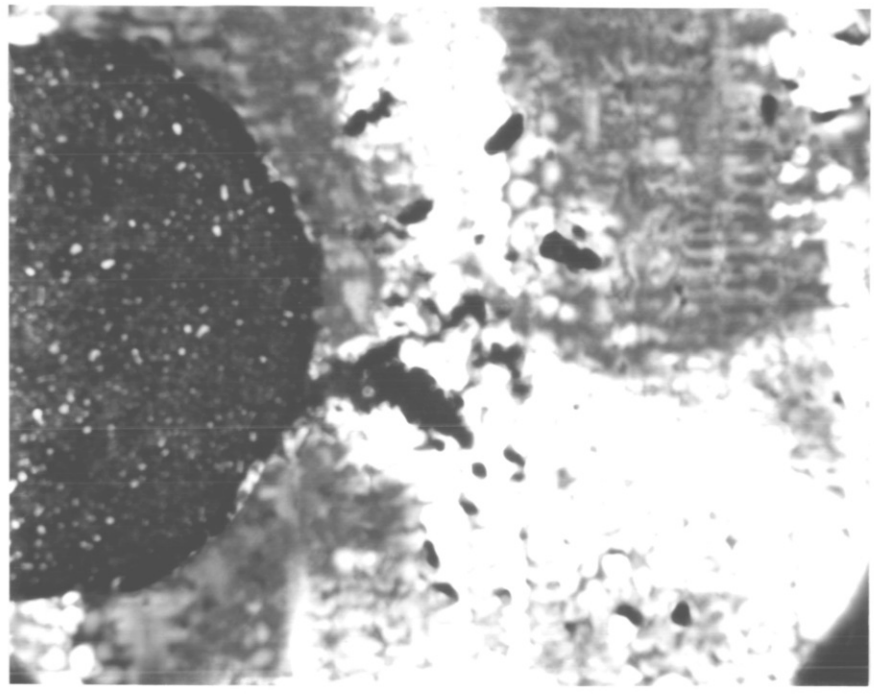
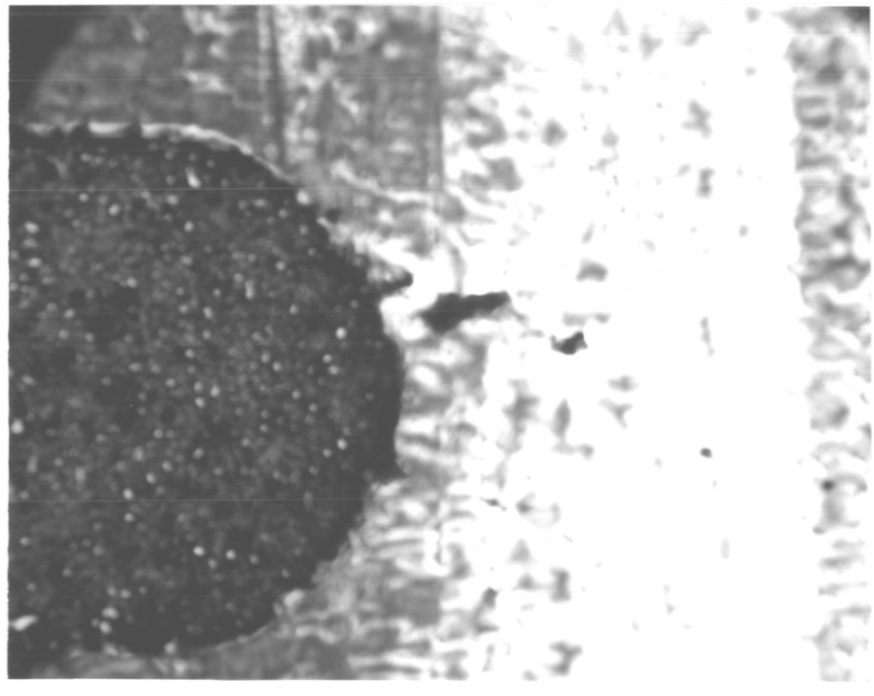
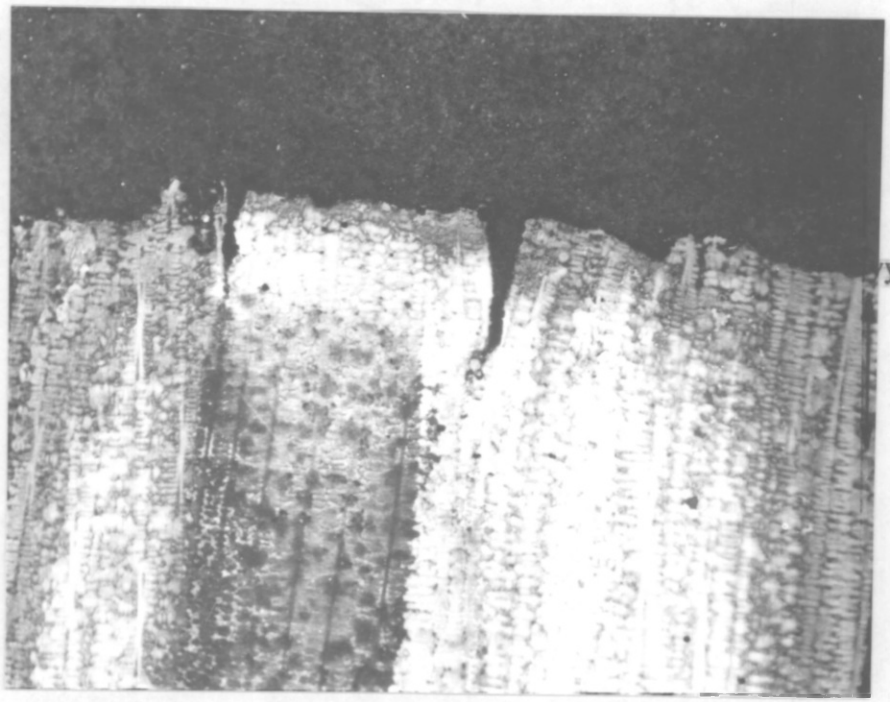


Figure 6.36 : Damage in unbroken notch b / a = 1.46, a / R = 4.60







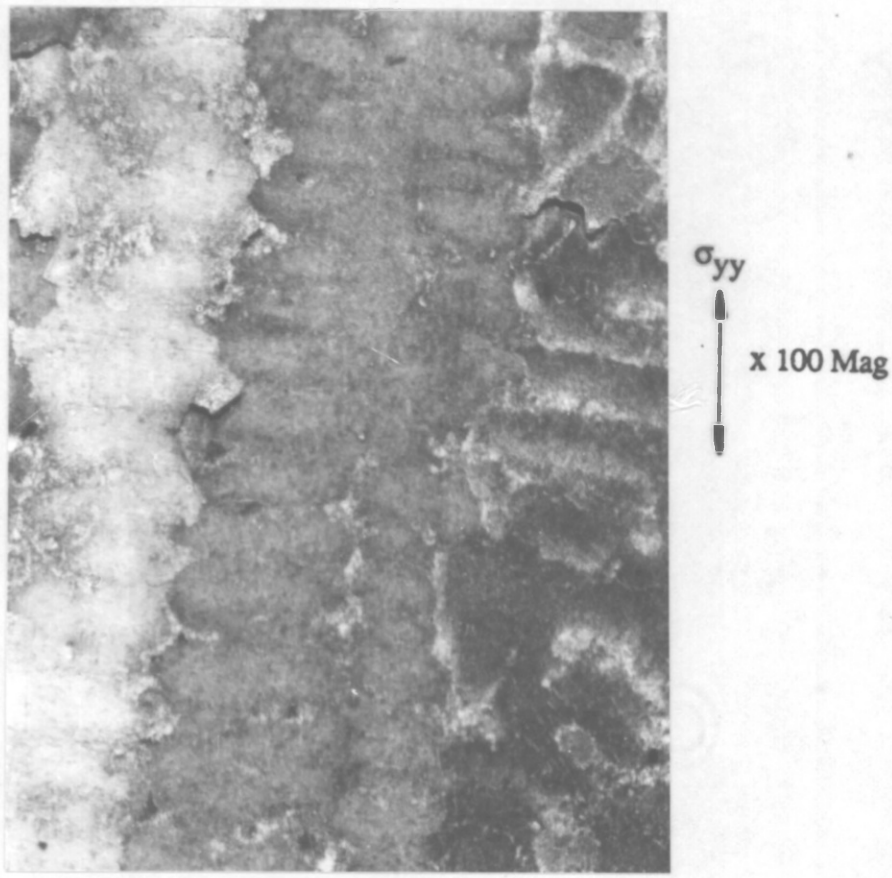
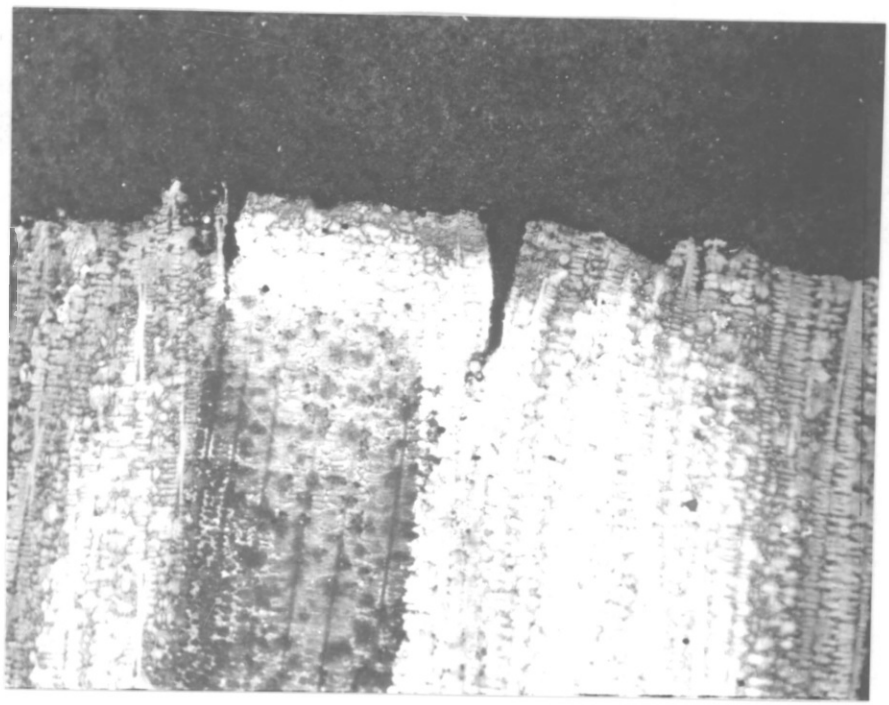
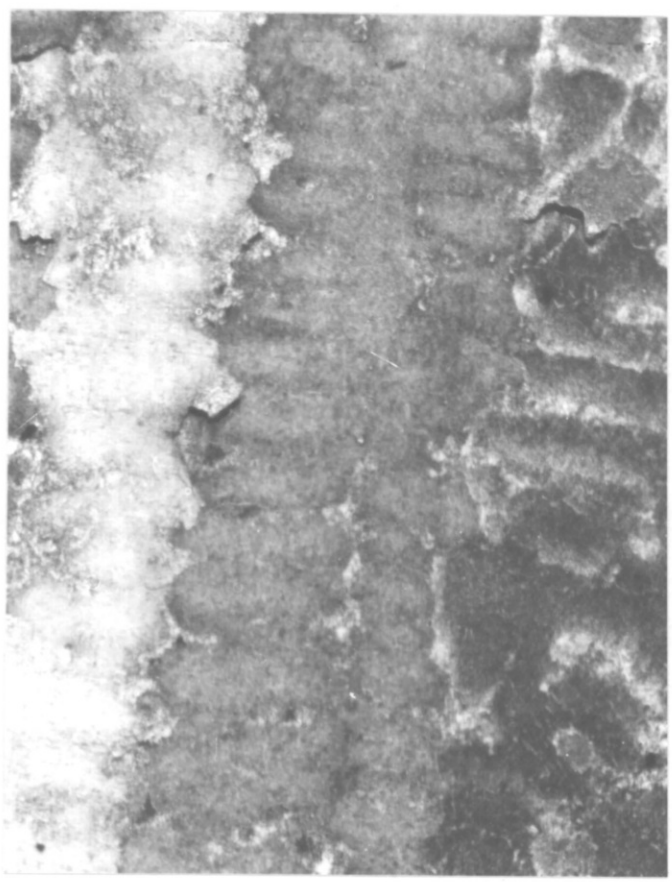


Figure 6.37 : Damage along a longitudinal grain boundary b / a = 1.46, a / R = 13.0





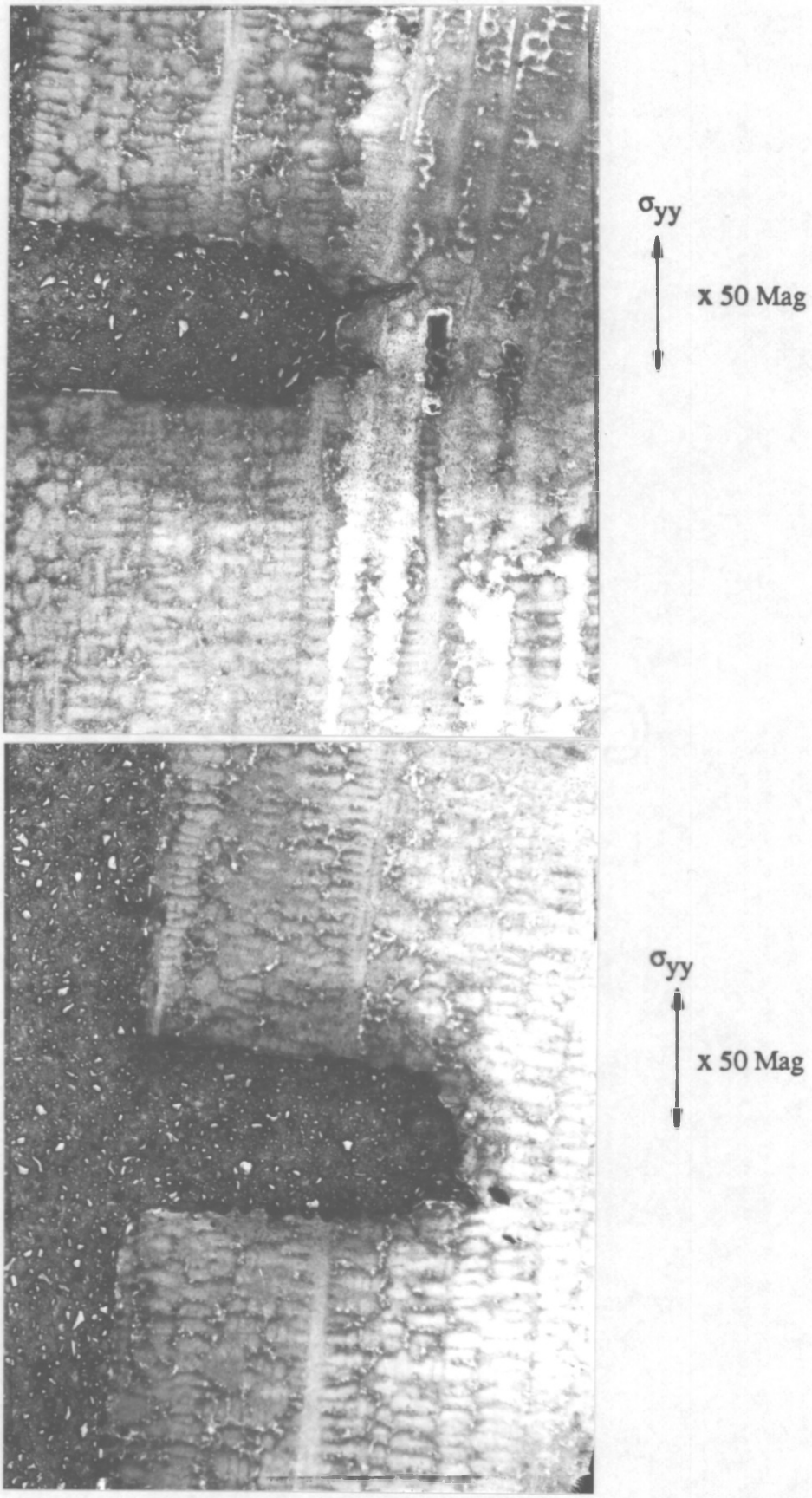
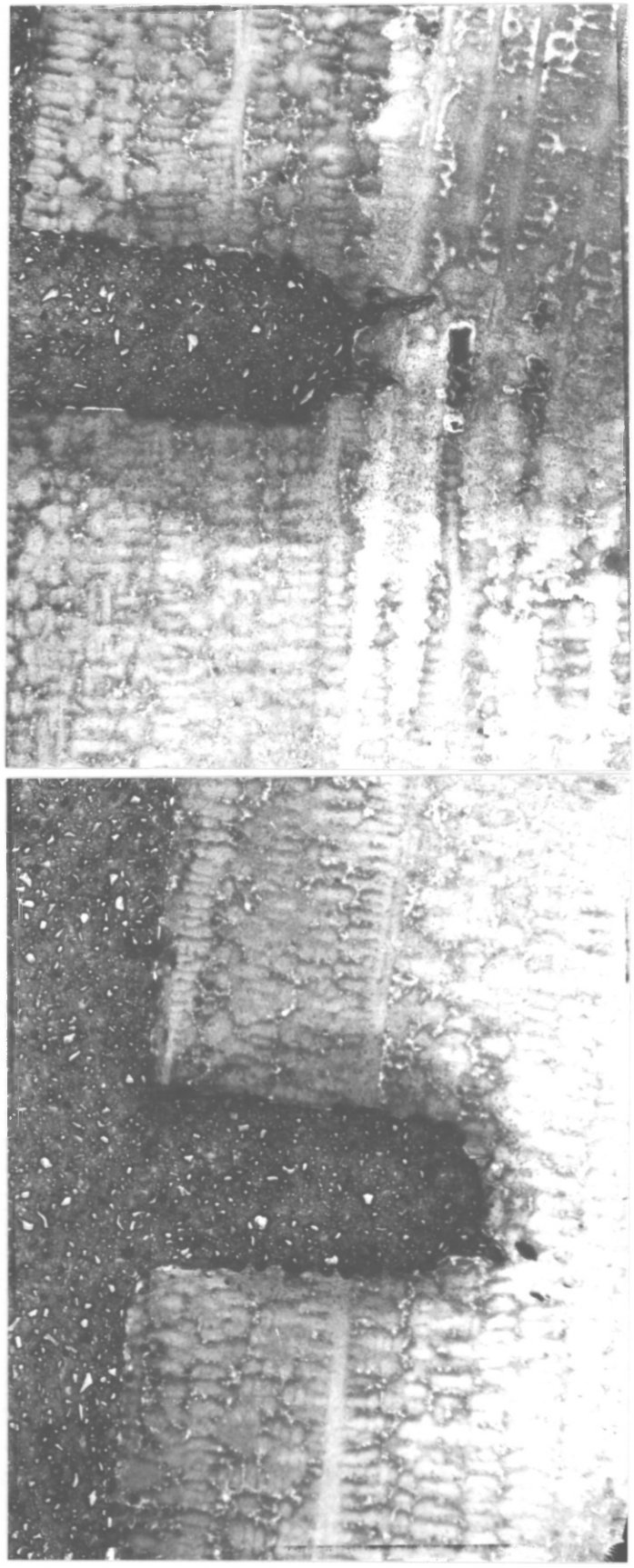


Figure 6.38 : Damage in unbroken notch b / a = 1.46, a / R = 13.0



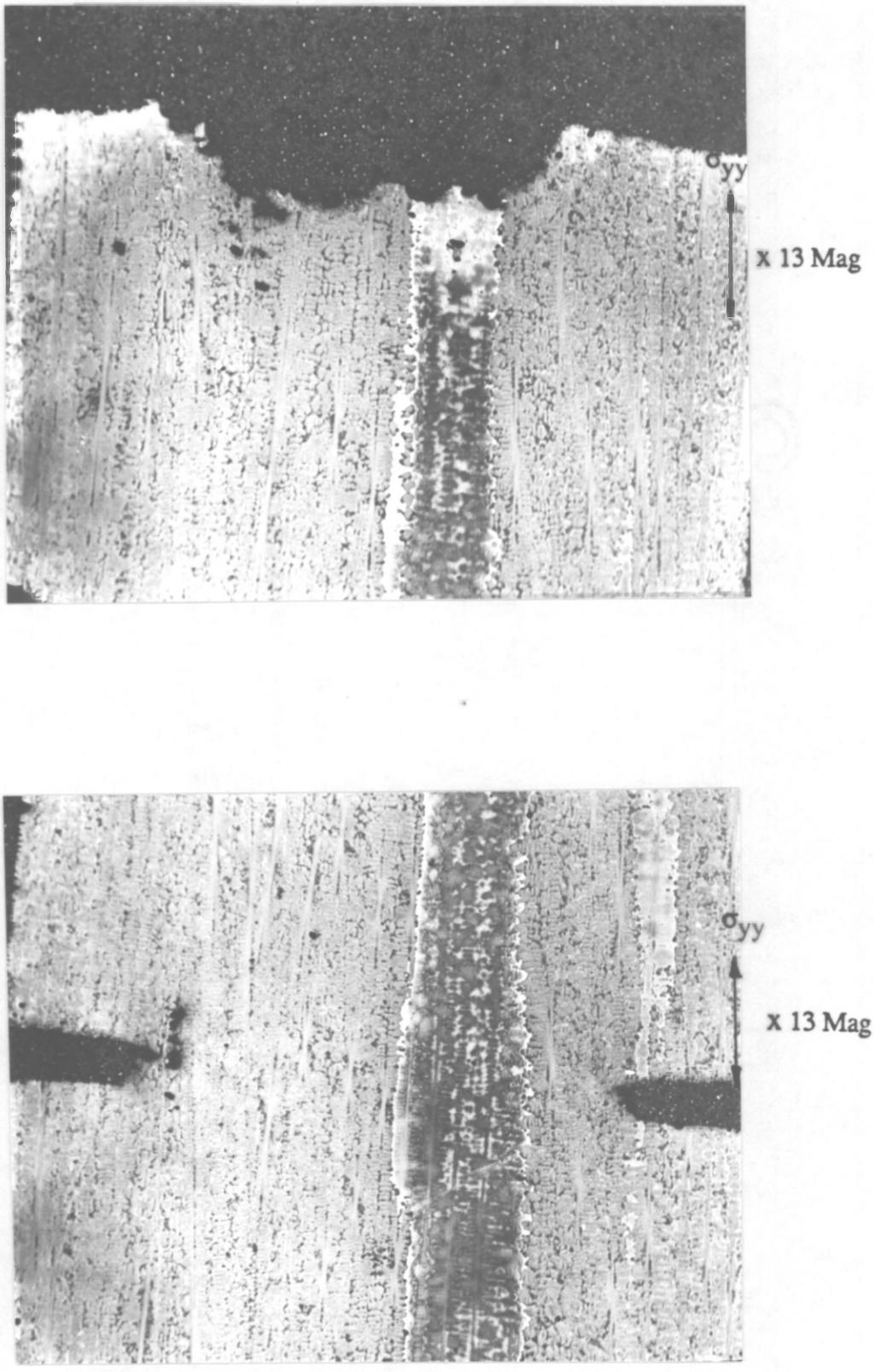
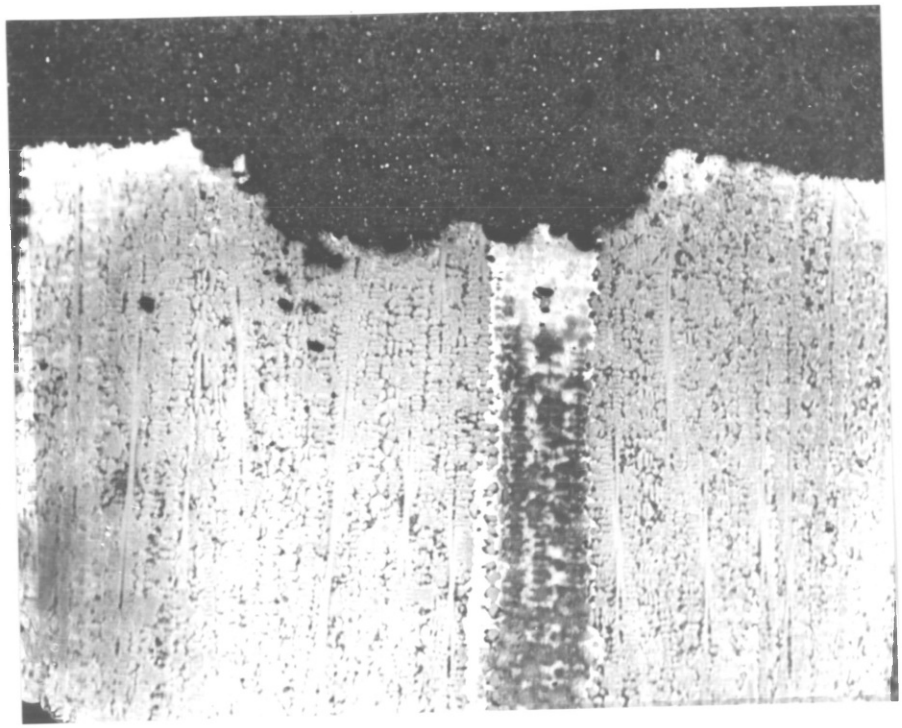
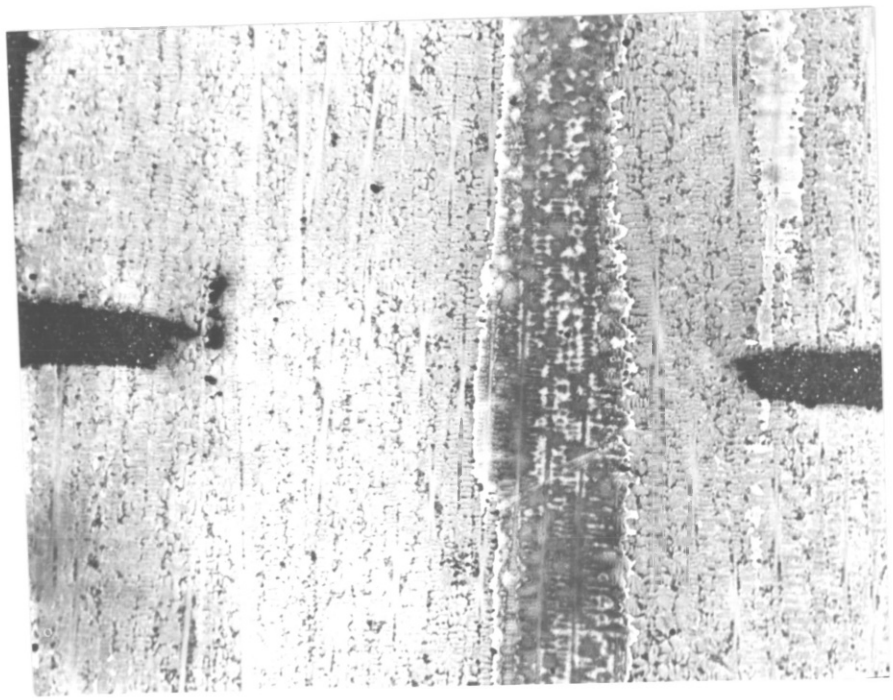


Figure 6.39 : Damage in broken and unbroken notch b / a = 1.46, a / R = 21.60





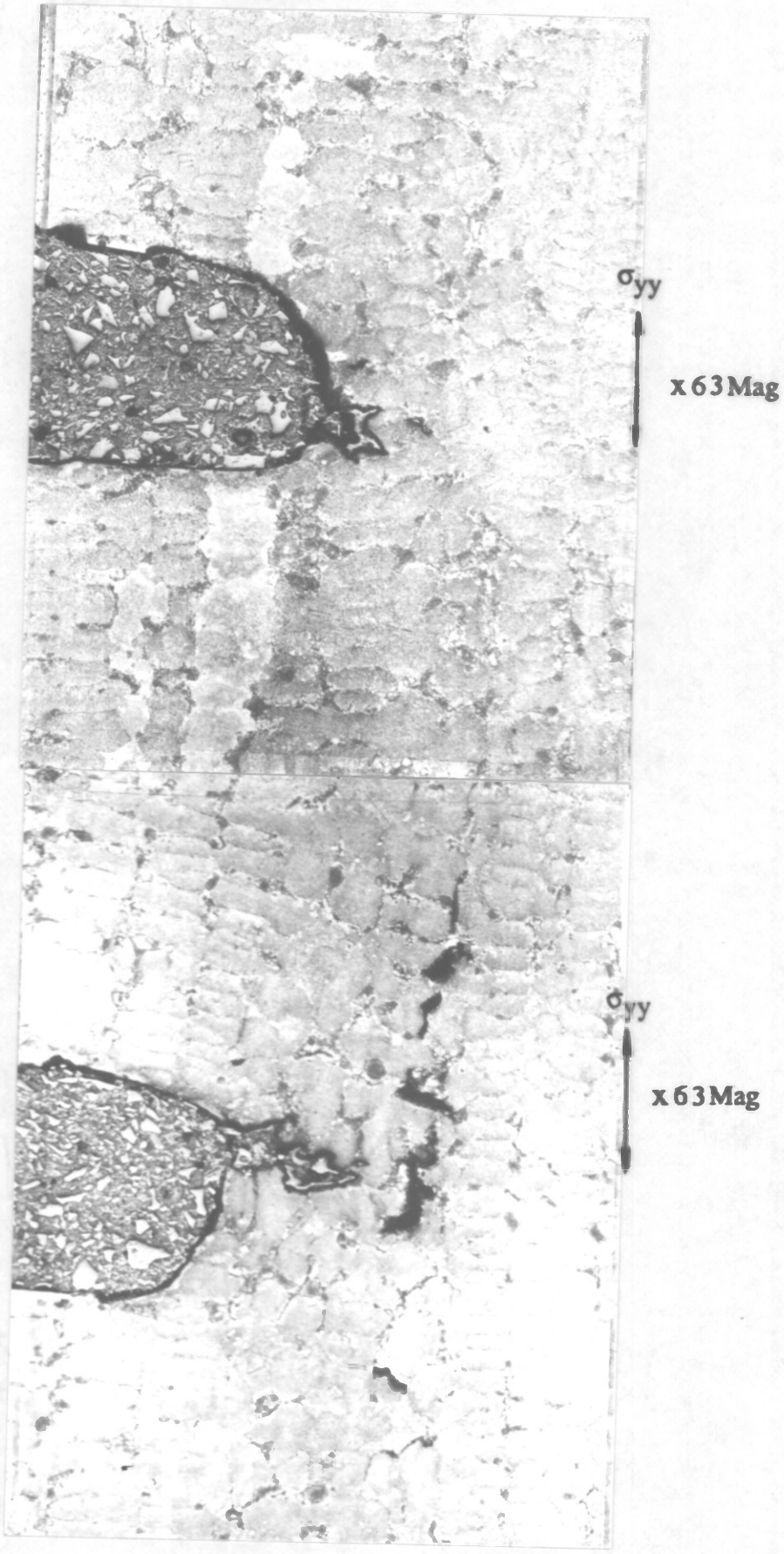
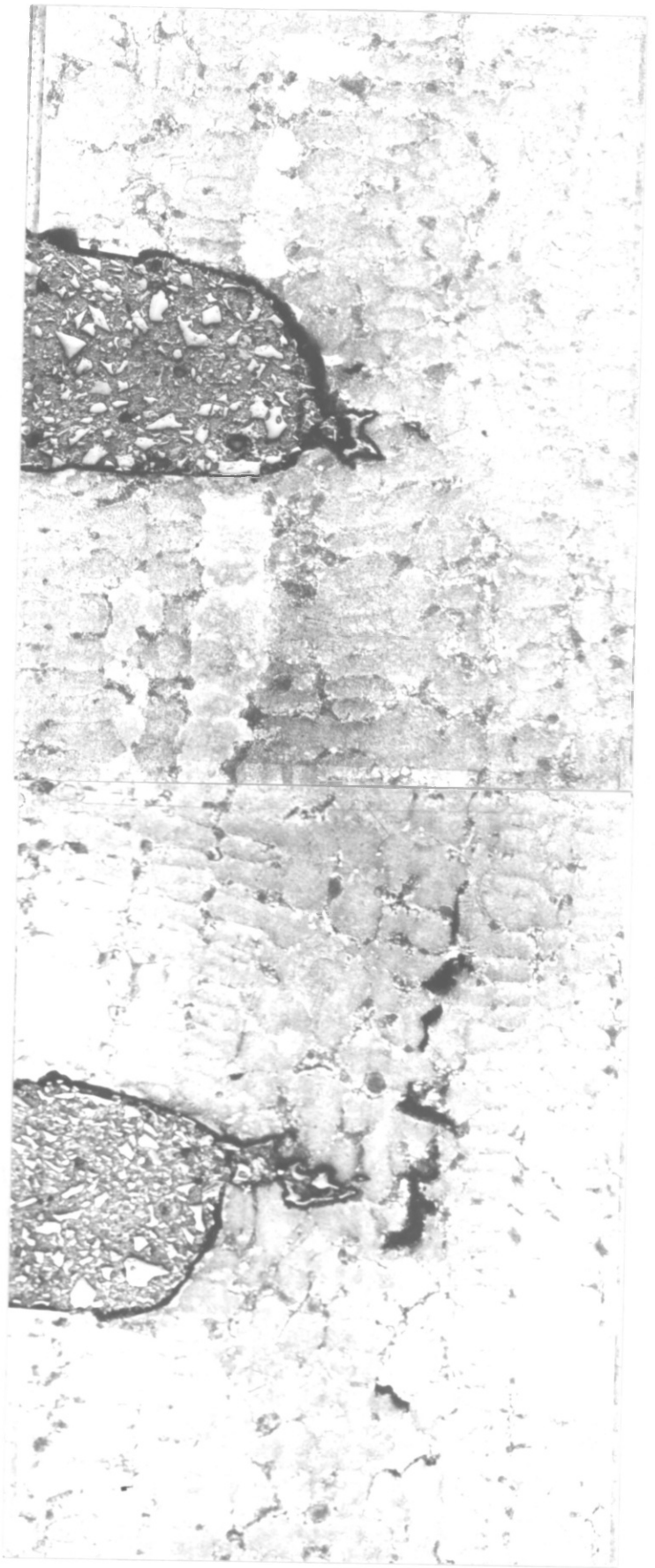


Figure 6.40 : Damage in unbroken notch b / a = 1.46, a / R = 21.60



CHAPTER-7

7.1 Conclusions

A summary of the conclusions reached from this investigation is given below.

1) A finite element program for isotropic materials has been modified to achieve a fast convergence rate for stress distributions across the notch throat of various circumferential notch geometries. Stresses across the throat of the notch have been found to be in good agreement with the stresses calculated using the ASAS-NL finite element package available at Atkins Pvt. Ltd.

2) An anisotropic effective stress and effective strain equations have been suggested, assuming the material to be stiffer elastically and because of creep in the radial direction than the axial direction. A finite element program has been adapted using these equations. The numerical solution has been verified with the analytical solution for a thick-walled cylinder, and the results have been found to be in good agreement. For comparison isotropic and anisotropic materials were considered. Major differences have been pointed out between the isotropic and anisotropic stress distributions. Firstly, the effective stress in the notch root plane in an anisotropic material has been found to be lower than the effective stress in an isotropic material for all the notch geometries studied. Secondly, the maximum effective stress in the case of anisotropic material has been found to be shifted away from the notch root plane. The other stresses are found to be localized near the notch root and significantly higher compared with isotropic materials.

3) Experiments have been carried out on 304-H stainless steel at 760± 2 ^{0}C. Experimental data on 2-1/4 Cr Mo steel at 538 ±2^{0}C is obtained from the literature. Metallographic analysis has been carried out on failed notched specimens of both the steels. A major difference between the nature of the failure of these steels has been pointed out. It has been noted that though the uniaxial ductility has been found to be the same in both the steels, multiaxial ductility showed great differences. The main reason is that the failure in 304-H stainless steel is due to void growth and coalescence, while in 2-

1/4 Cr Mo steel it is due to necking.

4) Experiments on plain and notched bars of DS Mar M002 were carried out at 900±4 ^{0}C. The notched bar results have been presented in terms of notch strengthening ratio. The experimental results have been compared with the different void growth models and the constant ductility model. It has been found that the constant ductility model obtained using the average value of the stress exponent and the average maximum effective stress away from the notch root plane, is in good agreement with the experimental results. For a / R greater than 9.30, the constant ductility model predicts constant life. But, experimental data show the drop in the life. This proves that for the notch geometries with a / R greater than 9.30 there is a change in the mode of failure.

5) To reveal the failure in DS Mar M002 , metallography has been carried out on failed plain and notched specimens. It has been found that the damage initiated and propagated away from the notch root at an angle to the notch root plane. This fact is in good agreement with the theoretical prediction of the maximum average effective stress which governs the deformation away from the notch root plane.

7.2 Recommendations for Future Work

1) A theoretical void growth model, similar to Cocks and Ashby void growth model for isotropic materials, should be developed to predict a failure of DS materials under multiaxial stress conditions. Thus, better estimation of experimental results could be made. This could be done by assuming the following assumptions,

a) Voids first nucleate at the transverse steps of the longitudinal grain boundaries.

b) Voids , once they nucleate grow by power-law.

c) Once grown to a critical size they act as a source for the cracks. Thus when the density of such cracks increases failure of the grain occurs either by a single crack or the loss of strength due to several cracks.

Hence under the assumptions made strain accumulated during nucleation, growth and crack propagation could be calculated. Thus the final failure strain and the time to failure could be calculated.

2) A cause of shifting the maximum effective stress from the notch root plane should be investigated by obtaining the different sets of material properties in the direction of anisotropy and the direction perpendicular to it. For example, the sets of material properties are, the ratio of moduli in the radial and axial direction , and the ratio of axial to radial strain rate from which the β value in the effective stress and strain equations is calculated. This could be done by running the present finite element program with a set of properties to check whether maximum effective stress shifts along the notch profile to the centre of the notch root when the isotropic condition has been reached.

3) Mostly single crystal materials possess an anisotropy in all the three directions. Thus there is a need to develop the effective stress and strain equations similar to the one developed in this work. The present equations could be modified to accommodate an anisotropy in all the three directions. This could be done by obtaining the effective stress and strain equation in all the three directions individually and combining together to provide a single equation satisfying the compatibility and equilibrium conditions.

4) Finite element analysis could be carried out using the equations mentioned in 3 to check the effect of anisotropy in all three directions on stress distribution in the notch root. This could be an important exercise to predict a failure in single crystal alloys which possess anisotropy in all the three directions.

REFERENCES

AL-FADDAGH, K. D. [1983]

Ph. D. Thesis, University of London.

ANDRADE E. N. da C. [1910]

Proc. Roy. Soc. Lond, A84, 1.

BAILY, R. W. [1929]

The engineer, 148, 528.

BEERE, W. and SPEIGHT, M . V. [1978]

Met. Sci., 4, 172.

BHATNAGAR, N. S. , KULKARNI, P., and ARAYA, V. K. [1986]

Int. J. Pres. Vess. & Piping, 23,165.

BOYLE, J. J. and SPENCE, J. [1983]

Stress Analysis for creep

Butterwoths & C0. Ltd.

BRIDGMAN, P. W. [1952]

Studies in Large Plastic Flow and Fractures

Mcgraw-Hill , New York.

BURT, H., DENNISON, J. P., and WHILSHIRE, B. [1979]

Met, Sci., May, 295.

CHABOCHE, J. L. [1984]

Nucl. Eng. Design, 79,309.

CHEN, W. H. [1971]

Int. J. Solids Structures, 7, 685.

CHUANG, T. J., KAGAWA, K.I., RICE, J.R., and SILLS, L. B. [1979]

Acta. Met., 27, 265.

COCKS, A. C. F. and ASHBY, M. F. [1980]

Met.Sci., August-Sept.,395.

BROWN, L. M.(1982)

Proc. 3rd Riso Int. Symp. on Metallurgy and Materials Science, Riso.

COUTS, W. H. JR. and FREEMAN, J.W. [1962]

Trans. ASME, June,1.

DAVIS, E. A. and MANJOINE, M. J. [1953]

ASTM, STP, 128 , 67.

DYSON, B. F., LOVEDAY, M. S. and RODGERS, M. J. [1976]

Proc. R. Soc. Lon., A349, 245.

DYSON, B. F. [1976]

Met. Sci. , 10 , 349.

DYSON, B. F. [1979]

Can. Met. Quat., 18, 31.

DYSON, B. F. and McLEAN, M. [1983]

Act. Met., 31 , 17.

ELLISON, E. G. and WU, D. [1983]

Res. Mechanica, 7, 37.

EVANS, W. J. and HARRISON, G. F. [1980]

Met. Sci., July, 262 .

EVANS, H. E. and FLEWITT, P. E. J. [1981]

Act. Met. , 29 , 867.

FENNER, R. T. [1975]

Finite Element Methods for Engineers

Macmillan, London.

FISHER, J. C. [1949]

Trans. ASME, May, 349.

FLECK, R. G., TAPLIN, D. M. R. and BEEVERS, C.J. [1975]

Act. Met. , 23, 415.

FRANKLIN, H. G.[1968]

Fibre Science and Technology, 1 (2) , 137.

FURSE, J. E. and LOVEDAY, M. S. [1981]

British Patent 8131641. JX 5782.

GAROFALO, F. [1959]

Proc. ASTM, 59, 957.

GIBBONS, T. B. and HOPKINS, B. E. [1984]

Met. Sci., 18 , 273.

GRIFFITH, J. E. and BALDWIN, W. M. [1962]

Developments in Theoretical and Applied Mechanics, 1, 410.

HAN, Y. and CHATURVEDI, M. C. [1987]

Metl. Sci. Eng., 89 , 25.

HANCOCK, J. W. and MACKENZIE, A. C. [1976]

J. Mech. Phys. Solids., 31 , 461.

HANINK, D. K. and VOORHEES, H. R. [1962]

J. Basic Eng. , June , 233.

HARRIS, J. E. [1965]

Trans. Metal Society, AIME , 233, 1509.

HAYHURST, D. R. and HENDERSON, J. T. [1977]

Int. J. Mech. Sci. , 19 ,133.

HAYHURST, D. R., LECKIE, F. A. and HENDERSON, J. T. [1977]

Int. J. Mech. Sci. 19 , 147.

HAYHURST, D. R. , DIMMER, P. R. and MORRISON, C. J. [1984]

Phil. Trans. R. Soc. Lond., A311, 103.

HENDERSON, P. J. and McLEAN, M. [1983]

Act. Met. , 31 , 1203.

HENDERSON, P. J. and McLEAN, M. [1985]

Scr. Met. , 19 , 99.

HILL, R. [1948]

Proc. R. Soc. Lond. , 193 , 281.

HOFF, N. J. [1953]

J. Appl. Mech. ,20, 105.

HOFFMAN, O. [1967]

J. Comp. Matls. , 1 (3). , 200.

HOSFORD, W. F. [1985]

Int. J. Mech. Sci. , 27 (718). , 423.

HU, L. W. [1956]

J Appl. Mech. Sept. ,444.

HULL, D. and RIMMER, D. E. [1959]

Phil. Mag. , 4 , 673.

JOHNSON, A. F. [1977]

J. Mech. Phys. Solids. , 25 , 117.

KACHANOV, L. M.[1958]

Izv. A. N. USSR, OTN, No. 8 , 26.

KEAR, B. H. and PIEARCY, B. J. [1967]

Trans. Met. Soc. AIME , 239, 1209.

KOBAYASHI, S. , CADDELL, R. M. and HOSFORD, W. F. [1985]

Int. J. Mech. Sci. , 27 (7 / 8), 509.

LECKIE, F. A. and HAYHURST, D. R. [1974]

Proc. R . Soc. Lond., A340, 323.

LEVY, A. J. [1985]

J. Appl. Mech. , 52 , 615.

LEMAITRE, J. [1985]

J. Eng. Matls. & Tech. , 107 , 83.

LIU, T. S., FIELDS, R. J., HAROW, D. G. and DELPH, T. J.[1984]

Scr. Met., 19, 299.

LOWE, M . S. J.[1987]

Stress Relaxation Due to Creep

M. Sc. Theis , Imperial College of Science and Technology, London.

McLEAN, M. [1983]

Directionally Solidified Materials for High Temperature Service

Metal Society, London.

McLEAN, M.[1985]

Act. Met., 33 (4), 545.

MARIN, J. [1957]

J. Aeron. Sci. , 24 (4), 265.

McCLINTOCK, F. A. [1968]

J. Appl. Mech. , 35 , 363.

MILES, D. E. and McLEAN, M.[1977]

Met, Sci. , December, 563.

NATHAL, M. V. and EBERT, L. J. [1985]

Met. Trans. 16A, 427.

NEEDLEMAN, A. and TVEGAARD, V. [1984]

J. Mech. Phys. Solids, 32 (6), 461.

NEWMAN, D. P., JONES, M. H. and BROWN, W. F.[1953]

Proc. ASTM , 53 , 677.

ODQVIST, F. K. G. [1953]

Int. Congr. Appl. Mech. , Cambridge 1934, Proc. Cambridge University Press

PANDEY, M. C., MUKHERJEE, A. K. and TAPLIN, D. M. R. [1985]

J. Matls. Sci., 20 , 1201.

NPL Measurement Procedures, Report D. M. A. (c) 29, August 1985.

PAI, D. H. [1967]

Int. J. Mech. Sci. , 9 , 335.

QUESTED, P. N. and OSGERBY, S. [1986]

Matls. Sci. & Tech., 2, *461.*

RAJ, R and ASHBY, M. F. [1975]

Act. Met., 23, *653.*

RAJ, R. , SHIH, H. M. and JOHNSON, H. H. [1977]

Scr. Met., 11, *839.*

RADHAKRISHNAN, V. M. [1985]

Scr. Met., 19, *259.*

RICE, J. R. and TRACEY, D . M. [1969]

J. Mech. Phys. Solids, 17, *201.*

ROBINSON, E. L.[1952]

Trans. Amer. Soc. Mech. Engrs., 74, *777.*

ROBOTNOV, Y. N. [1969]

Creep Problems in Structural Members

North-Holland publishing Co. London.

SEGERLIND, L. J. [1976]

Applied Finite Element Analysis,

Wiley, New York.

SEVENSSON, L. E. and DUNLOP, G. L. [1981]

International Metals Review, No. 2 , *109.*

SHEWFELT, R. S. W. and BROWN, L. M. [1977]

Phil. Mag., 35 (4) , *945.*

SHAHINIAN, P. [1964]

Trans. ASME. , June, *222.*

SHERBY, O. D. and BRUKE, P. M. [1967]

Progress in Materials Science, 13 , *325.*

SMITH, E. and BARNBY, J. T. [1967]

Met. Sci. J., 1 , *1.*

SPEIGHT, M. V. and BEERE, W. [1975]

Met. Sci. , 9 , 190.

STEVENS, R. A. and FLEWITT, P. E. J. [1981]

Act. Met. , 29 , 867.

SUGIMOTO, K., SAKAKI, T., HORIE, T., KURAMOTO, K. and MIYAGAWA [1985]

Met. Trans. , 16A, 1457.

SUNDERARAJAN, G. [1985]

Met. Trans. , 16A , 427.

THOMSON, R. D. and HANCOCK, J. W. [1984]

Int. J. Fract. , 26 , 99.

TVEGAARD, V. [1982]

Int. J. Solids Struct., 18 , 659.

TVEGAARD, V. and NEEDLEMAN, A. [1984]

Act. Met. , 32 , 157.

VERSNYDER, F. L. and GUARD, R. W. [1960]

Trans. ASM. , 52 , 485.

WILLIAMS, K. R. and WILSHIRE, B. [1979]

Met. Sci. J. , 7 , 176.

WU, D. , CHRISTIAN, E. M. and ELLISON, E. G. [1984]

J. Strain Analysis, 19 (4), 209.

YOSHIDA, S. and HIDEMITSU, H. [1962]

Trans. ASME. , June, 214.

YOSHIDA, M. , LEVALILLANT, C. and PINEAU, A. [1986]

Interational Conference on Creep, Tokyo, Japan.

ZENTECH CONSULTANTS

Creep Analysis of Anisotropic Notched Bar Test Specimens

Using MARC Finite Element Package

Internal Report , May 1987

APPENDIX-A

ASHBY'S THEORY OF CREEP RUPTURE BY VOID GROWTH

1. Void Growth by Boundary Diffusion Alone

When voids grow by boundary diffusion, matter diffuses out of the growing void , which remains spherical, and plates on to the grain boundary as shown in Figure-1.8a. The equations for time and strain to fracture are :

$$t_R = t_n + \frac{2}{3\phi_0\varepsilon_0}\{ f_c^{\frac{3}{2}} [\ln(\frac{1}{f_c}) + \frac{2}{3}] - f_i^{\frac{3}{2}} [\ln(\frac{1}{f_i}) + \frac{2}{3}] \} \frac{\sigma_0}{\sigma_1} \qquad \text{(A1)}$$

where

$$\phi_0 = \frac{2 D_b \delta_b \Omega}{k T l^3} \frac{\sigma_0}{\varepsilon_0}$$

or if $f_i < 10^{-2}$ and $f_c = 0.25$

$$t_R = t_n + \frac{0.17}{\phi \varepsilon_0} (\frac{\sigma_0}{\sigma_1})$$

$$\varepsilon_R = \frac{4}{3} f_c^{\frac{3}{2}} \frac{l}{d} = 0.2 \frac{l}{d} \qquad \text{(A2)}$$

2) Void Growth by Surface Diffusion Alone

When voids grow by surface diffusion, matter flows out of it at the equator, causing it to become flatter and more crack-like, as shown in Figure 1.8b. The equation for time

to fracture is

$$t_f = t_n + \frac{2\left(f_c^{\frac{1}{2}} - f_i^{\frac{1}{2}}\right)}{\varepsilon_0 \psi_0}\left(\frac{\sigma_0}{\sigma_1}\right)^3 \qquad \text{(A3)}$$

where

$$\psi_0 = \frac{1}{\sqrt{2}} \frac{D_s \delta_s \Omega \sigma_0^3}{k T l \gamma_c^2 \varepsilon_0}$$

If f_i is small and f_c is set equal to 0.25 this simplifies to

$$t_f = f_n + \frac{1 - 2 f_i}{\varepsilon_0 \psi_0}\left(\frac{\sigma_0}{\sigma_1}\right)^3$$

Because the void is flat and crack-like, it contributes almost to strain as it grows.

3) Void Growth by Power-Law Creep Alone

When voids grow by power-law creep alone, the effective stress, σ_{eff}, determines their rate of expansion. The rest of the matter containing the voids, shown as the shaded area in Figure-1.8c, extends at a rate determined by the net section stress, $\sigma_{eff} / (1-f_h)$. The equation for time to rupture and strain to rupture are :

$$t_R = t_n + \frac{\alpha}{(n+1)\varepsilon_0} \ln\left[\frac{1}{(n+1) f_i}\right]\left(\frac{\sigma_0}{\sigma}\right)^n \qquad \text{(A4)}$$

where

$$\alpha = \left\{\sinh - \left[\frac{2\left(n - \frac{1}{2}\right)}{\left(n + \frac{1}{2}\right)} \frac{\sigma_{mean}}{\sigma_{eff}}\right]\right\}^{-1}$$

and

$$\sigma_{mean} = - \frac{\sigma_1 + \sigma_2 + \sigma_3}{3}$$

At constant load the rupture time is given by ;

$$t_R^L = [(n+1) f_i]^{\frac{n}{n+1}} t_n + \frac{1 - [(n+1) f_i]^{\frac{n}{(n+1)}}}{n \varepsilon_0} (\frac{\sigma_0}{\sigma_a})^n \qquad (A5)$$

where σa is the stress at rupture defined by :

$$\sigma_a = \frac{\sigma_i}{(1 - n \varepsilon_s t)^{\frac{1}{n}}}$$

The strain to failure,

$$\varepsilon_f = t_R \varepsilon_0 (\frac{\sigma_{eff}}{\sigma_0})^n + 0.2 \frac{1}{d} \qquad (A6)$$

4) Coupled Boundary Diffusion and Power-Law Creep

A switch from void growth mechanism to another can take place if the stress field or the temperature vary with time Figure-1.9a. when the stress is low, the voids grow by diffusion, but when high they grow by power-law creep. That means when fh is small, the voids grow by diffusion , and when large they grow by power-law creep. In between , voids grow by coupling of both mechanisms. the time to fracture is given by ;

$$t_R = t_n + \frac{2 (f_t^b)^{\frac{3}{2}}}{3 \phi_0 \varepsilon_0} [\ln (\frac{1}{f_t^b}) + \frac{2}{3}] (\frac{\sigma_0}{\sigma_1}) + \frac{\alpha}{(n+1) \varepsilon_0} \ln [\frac{1}{(n+1) f_t^b}] (\frac{\sigma_0}{\sigma_{eff}})^n$$

(A7)

The strain to rupture can be obtained by using the equation (A6)in which tR is given by equation (A7)

5) Coupled Surface Diffusion and Power-Law Creep

Similar to the boundary diffusion and power-law creep mechanism, surface diffusion dominates from fi to fst and power-law creep from fst to fc Figure-1.9b. The time to fracture is given by ;

$$t_f = t_n + \frac{2 [(f_t^s)^{\frac{1}{2}} - (f_i)^{\frac{1}{2}}]}{\varepsilon_0 \Psi_0} (\frac{\sigma_0}{\sigma_1})^3 + \frac{\alpha}{(n+1) \varepsilon_0} \ln [\frac{1}{(n+1) f_t^s}] (\frac{\sigma_0}{\sigma_{eff}})^n$$

(A8)

The rupture strain is due to power-law only, since the crack-like voids contribute almost nothing to the strain. The result is :

$$\varepsilon_R = t_R \varepsilon_0 (\frac{\sigma_{eff}}{\sigma_0})^n \qquad \text{(A9)}$$

where t R is given by equation

A different criterion to the other coupled mechanisms was adopted for this coupled mechanism. It is based on using two limits of the driving force which can cause the damage to grow either by surface diffusion or boundary diffusion. When surface diffusion is very rapid, the driving force will cause the damage to grow by boundary diffusion. However, when surface diffusion is slow, the voids become crack-like and

therefore grow by surface diffusion only.

Voids cannot be considered to grow by alternative mechanisms in this type of coupled mechanism since both of them are diffusion mechanisms. However, regime exists in which one or the other totally controls void growth. The time to rupture is obtained by integrating the equations for damage rate and strain rate given by ;

$$\frac{1}{\varepsilon_0}\frac{df_h}{dt} = \Psi_0 \frac{\gamma_s^3 f_h^{\frac{1}{2}}}{\sigma_0^3 r^{*3}} \qquad \text{(A10)}$$

$$\frac{1}{\varepsilon_0}\frac{d\varepsilon}{dt} = \frac{4\Psi_0 f_h^{\frac{1}{2}} \gamma_s^3}{(1-f_h)\, d\, \sigma_0^3 r^{*2}} \qquad \text{(A11)}$$

where r* is the tip radius, defined as :

$$\frac{r_h}{r^*} = \frac{(1-f_h)^2}{\sqrt{2}\ln\left(\frac{1}{f_h}\right)\Delta_0}\left\{\left[1 + \frac{2\sqrt{2}\,\sigma_1 r_h \ln\left(\frac{1}{f_h}\right)\Delta_0}{\gamma_s (1-f_h)^3}\right]^{\frac{1}{2}} - \right\} \qquad \text{(A12)}$$

The strain to failure will be due to boundary diffusion alone and is given by equation (A2)

APPENDIX-B

The relationship between strain and stress is given by (Johnson (1977)) :

$$\dot{\varepsilon}_{11} = U^{m-1} \{ \mu \sigma_{11} - \frac{1}{2}(2\mu - \lambda)\sigma_{22} - \frac{1}{2}\lambda \sigma_{33} \}$$

$$\dot{\varepsilon}_{22} = U^{m-1} \{ -\frac{1}{2}(2\mu - \lambda)\sigma_{11} + \mu \sigma_{22} - \frac{1}{2}\lambda \sigma_{33} \}$$

$$\dot{\varepsilon}_{33} = U^{m-1} \{ -\frac{1}{2}\lambda(\sigma_{11} + \sigma_{22}) + \lambda \sigma_{33} \} \qquad \text{(B1)}$$

$$\dot{\varepsilon}_{23} = \frac{1}{2} U^{m-1} \upsilon \sigma_{23}$$

$$\dot{\varepsilon}_{13} = \frac{1}{2} U^{m-1} \upsilon \sigma_{13}$$

$$\dot{\varepsilon}_{12} = \frac{1}{2} U^{m-1} (4\mu - \lambda) \sigma_{12}$$

where 1 , 2 , 3 represents x, y , z directions respectively, μ , λ , υ are the constants

$$U = \frac{1}{2}(2\mu - \lambda)(\sigma_{11} - \sigma_{22})^2 + \frac{1}{2}\lambda [(\sigma_{22} - \sigma_{33})^2 + (\sigma_{33} - \sigma_{11})^2]$$
$$+ \upsilon(\sigma_{23}^2 + \sigma_{13}^2) + (4\mu - \lambda)\sigma_{12}^2 \qquad \text{(B2)}$$

For a uniaxial test in the fiber (Longitudinal) direction ,

$\sigma_{33} = \sigma_L$, $\sigma_{ij} = 0$, $i , j \neq 3$, the theory gives

$$\dot{\varepsilon}_{33} = \lambda^m \sigma_L^{2m-1} \qquad \text{(B3)}$$

For a second uniaxial tensile creep test in a direction transverse to the fibers,

$$\sigma_{11} = \sigma_T, \ \sigma_{ij} = 0, i, j \neq 1$$

$$\dot{\varepsilon}_{11} = \mu^m \sigma_T^{2m-1} \tag{B4}$$

$$\sigma_{13} = \sigma_S, \ \sigma_{ij} = 0, \ i \neq 1, j \neq 3$$

$$\dot{\varepsilon}_{13} = \frac{1}{2} \upsilon^m \sigma_s^{2m-1} \tag{B5}$$

Thus, λ^m and μ^m may be determined from uniaxial tensile creep tests along and transverse to the fiber direction and $1 / 2 \ \upsilon^m$ from a longitudinal shear creep test. These three uniaxial loading tests completely characterize the secondary creep response.

APPENDIX-C

From Chapter-3,the strain-strain relationship for a rigid plastic material can be written as :

$$d\varepsilon^p_{11} = d\lambda \left(\sigma_{11} - \frac{1}{2}\sigma_{22} - \frac{1}{2}\sigma_{33} \right)$$

$$d\varepsilon^p_{22} = d\lambda \left(-\frac{1}{2}\sigma_{11} + \frac{(1+\beta)}{2}\sigma_{22} - \frac{\beta}{2}\sigma_{33} \right)$$

$$d\varepsilon^p_{33} = d\lambda \left(-\frac{1}{2}\sigma_{11} - \frac{\beta}{2}\sigma_{22} + \frac{(1+\beta)}{2}\sigma_{33} \right)$$

$$d\gamma^p_{12} = (1+2\beta)\, d\lambda \qquad \text{(C1)}$$

The effective stress is written as :

$$\sigma_{eff} = \frac{1}{\sqrt{2}} \{ (\sigma_{11} - \sigma_{22})^2 + \beta (\sigma_{22} - \sigma_{33})^2 + (\sigma_{33} - \sigma_{11})^2 + 2 (1+2\beta) \tau_{12}^2 \}^{1/2} \qquad \text{(C2)}$$

The strain rate can be obtained by replacing strain in equation (C1) by strain rate the plastic constant $d\lambda$ can be written as :

$$d\lambda = \frac{\varepsilon_{eff}}{\sigma_{eff}} \qquad \text{(C3)}$$

and the creep strain rate can be expressed as :

$$\dot{\varepsilon}_{eff} = C\, \sigma^n_{eff} \qquad \text{(C4)}$$

Substituting the values of $d\lambda$ and ε_{eff} in the equation (C1) strain rate is given by

$$\dot{\varepsilon}_{11} = C\, \sigma^{(n-1)}_{eff} \left[\sigma_{11} - \frac{1}{2}\sigma_{22} - \frac{1}{2}\sigma_{33} \right]$$

$$\dot{\varepsilon}_{22} = C\, \sigma^{(n-1)}_{eff} \left[-\frac{1}{2}\sigma_{11} + \frac{(1+\beta)}{2}\sigma_{22} - \frac{\beta}{2}\sigma_{33} \right]$$

$$\dot{\varepsilon}_{33} = C\, \sigma^{(n-1)}_{eff} \left[-\frac{1}{2}\sigma_{11} - \frac{1}{2}\sigma_{22} + \frac{(1+\beta)}{2}\sigma_{33} \right] \qquad \text{(C5)}$$

For uniaxial loading in z direction we have

$$\dot{\varepsilon}_{11} = C\,\sigma_{eff}^{(n-1)}\,\sigma_{11}$$

$$\sigma_{eff} = \frac{1}{\sqrt{2}}\,(\sigma_{11}^2 + \sigma_{11}^2)^{1/2} = \sigma_{11}$$

and (C6)

Therefore,

$$\dot{\varepsilon}_{11} = C\,\sigma_{11}^{n} \tag{C7}$$

For uniaxial loading in r direction we have

$$\dot{\varepsilon}_{22} = C\,\sigma_{eff}^{(n-1)}\,\frac{(1+\beta)}{2}\,\sigma_{22}$$

and

$$\sigma_{eff} = \frac{1}{\sqrt{2}}\,(\sigma_{22}^2 + \beta\,\sigma_{22}^2)^{1/2} = \{\frac{(1+\beta)}{2}\}^{1/2}\,\sigma_{22} \tag{C8}$$

Therefore,

$$\dot{\varepsilon}_{22} = C\,\sigma_{22}^{n}\,[\frac{(1+\beta)}{2}]^{\frac{(n+1)}{2}} \tag{C9}$$

Assuming the axial strain rate as twice the radial strain rate we have

$$\dot{\varepsilon}_{11} = 2\,\dot{\varepsilon}_{22}$$

Thus,

$$\frac{1}{2} = \{\frac{(1+\beta)}{2}\}^{\frac{(n+1)}{2}} \tag{C10}$$

and β is given by

$$\beta = 2\,[\,\{\frac{1}{2}\}^{\frac{2}{(n+1)}} - \frac{1}{2}\,] \tag{C11}$$

APPENDIX-D

Calculation of the Average Effective Stress

A quarter of a geometry is modelled for the numerical analysis as mentioned before. A general example of a mesh is given in Figure-D1. Different steps for calculating the average effective stress are given below.

1) The stresses in all the elements are calculated.

2) Simple arithmatical average stress is calculated with the stresses in elements say 1and2, 3 and 4 and so on. These stresses can be named as σ_{a1}, σ_{a2}, σ_{a3} and given as :

$$\sigma_{a1} = \frac{\sigma_{e1} + \sigma_{e2}}{2}, \quad \sigma_{a2} = \frac{\sigma_{e3} + \sigma_{e4}}{2}, \quad \sigma_{a3} = \frac{\sigma_{e5} + \sigma_{e6}}{2} \text{ ———}$$

where σ_{e1}, σ_{e2}, σ_{e3}---are the stresses in element 1,2,3--------

3) The area of each annular strip is calculated as

$$a_1 = \pi r_1^2 \ , \ a_2 = \pi (r_2^2 - r_1^2) , \ a_3 = \pi (r_3^2 - r_2^2) \ \cdots\cdots\cdots$$

4) The total load is obtained by

$$P_{Total} = \sigma_{a1} a_1 + \sigma_{a2} a_2 + \sigma_{a3} a_3 \text{-----}$$

Thus the average stress is calculated by

$$\sigma_{ave} = \frac{P_{Total}}{\pi a^2}$$

Where a is the radius of the notch throat

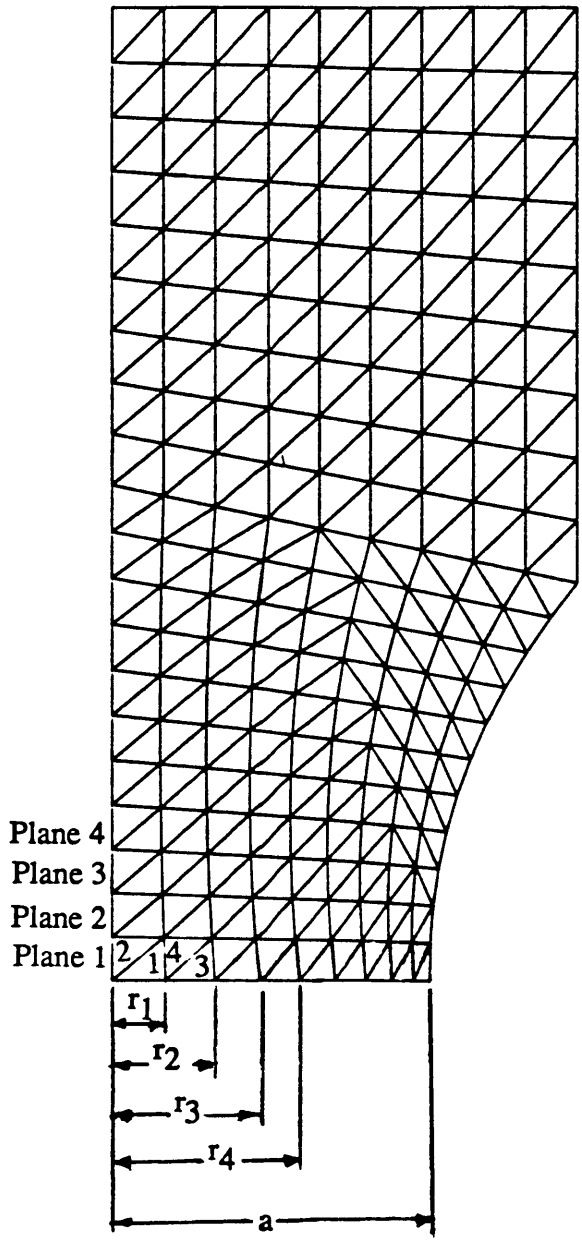


Figure- D1 : General illustration to calculate average effective stress